SINTERING AND GRAIN GROWTH
OF MgO

by

Carol Anne Handwerker

B. A. Wellesley College
(1973)

S. B. Massachusetts Institute of Technology
(1978)

S. M. Massachusetts Institute of Technology
(1978)

Submitted to the Department of
Materials Science and Engineering
in Partial Fulfillment of the
Requirements of the
Degree of

DOCTORATE IN SCIENCE

at the

MASSACHUSETTS INSTITUTE OF TECHNOLOGY

February 1983

Signature of Author______________________________
Department of Materials Science and Engineering
January 7, 1983

Certified by______________________________
R. L Coble
Thesis Supervisor

Accepted by______________________________
R. W. Balluffi
Chairman, Departmental Committee on Graduate Students

SINTERING AND GRAIN GROWTH
OF MgO

by

CAROL ANNE HANDWERKER

Submitted to the Department of Materials Science and Engineering
on January 7, 1983 in partial fulfillment of the
requirements for the Degree of Doctorate in Science
in Ceramics

ABSTRACT

The assumptions used for models of simultaneous sintering and grain growth and of pore-boundary interactions during final stage sintering were tested using MgO samples of controlled microstructure and purity. The conditions examined were pore locations, sample densities, low background impurity levels, high levels of dopants and the distributions of dihedral angles among samples.

The microstructure evolution was described in terms of the average pore size and grain size with pores attached to boundaries and the transition pore and grain sizes for pore-boundary separation. Pore-boundary separation maps and grain size-pore size trajectories were calculated from literature data and were measured for various high purity ($\sim 200\,\mu g/g$ cation basis) and low purity ($\sim 2000\,\mu g/g$) undoped MgO and Al-doped MgO samples. The pore sizes and grain sizes for the low purity undoped MgO are in good agreement with the calculated transition values for pore-boundary separation. With Al-additions, the pore sizes at separation increased relative to the conditions for the undoped MgO. The calculated trajectories for low purity undoped MgO were in poor agreement with the observed trends; increasing the ratio (assumed) of the diffusivities controlling sintering and grain growth by a factor of 10 brings the calculated and observed values into agreement.

High purity MgO was prepared using clean-room processing, liquid-liquid extraction using DDDC in $CHCl_3$, and by EDTA-masking of alkaline earth ions during hydromagnesite precipitation. The cation impurity levels were from $\sim 40\,\mu g/g$ for the DDDC-extracted hydromagnesite to $< 8\,\mu g/g$ for the EDTA-masked material. After transformation to the oxide and compact formation of the DDDC-extracted precursor, the cation contamination was $\sim 200\,\mu g/g$.

Settled compacts of high purity MgO sintered to 65-80% of theoretical density and coarsened with no discontinuous grain growth or pore entrapment, in agreement with the calculated microstructure evolution. The boundary mobilities calculated from grain growth of high density, high purity MgO were found to be two orders of magnitude lower than the values calculated from boundary diffusivities in high purity materials and four orders of magnitude lower than values calculated from boundary diffusivities in low purity MgO.

The surface-grain boundary dihedral angles from surface grooves spanned the following ranges for the materials and temperatures indicated: 97°-123° for MgO at 1520K, 85°-170° for undoped Al_2O_3 at 1870K and 95°-140° for MgO-doped Al_2O_3 at 1870K. The grooves were observed to be generally asymmetrical, the distributions of angles broad, and the median values significantly lower than earlier results based on other techniques. The observed angles from polished and fractured surfaces of sintered, hot pressed and annealed, and hot pressed and strained samples were shifted to lower values relative to the angles observed on thermally etched surfaces. The effects of a distribution of dihedral angles on sintering and pore-boundary separation are discussed.

Thesis Supervisor: Professor R. L. Coble

Title: Professor of Ceramics

TABLE OF CONTENTS

TABLE OF CONTENTS (Continued)

TABLE OF CONTENTS (Continued)

LIST OF FIGURES

LIST OF FIGURES (Continued)

LIST OF FIGURES (Continued)

LIST OF TABLES

Acknowledgements

Compared with my task in writing this section, Cecil B. deMille had it easy when he enumerated the people involved in the production of "The 10 Commandments". There is, literally, a "cast of dozens" who helped to produce this document through our discussions of science (and unrelated topics) and their labor. I must, however, limit myself to the principals. To those colleagues I do not mention directly goes my heart-felt gratitude for their support.

I was very lucky to have Professors Robert L. Coble and Rowland M. Cannon as advisors and friends through this project. Bob Coble was a constant source of new ideas and encouragement for many topics and supported my extended discursions into DIGM and MgO-doped alumina. Rowland Cannon was contagious in his enthusiasm for sintering and grain growth phenomena. Our discussions and arguments were always enlightening and he helped me see the true scope of the sintering problem.

To Pat Kearney I owe much. Over the years I have become one of his best "customers" in the ceramics "shop", both in science and in partying and have benefited by his friendship and expertise. To Toni Centorino, Al Frekor, Art Gregor, Lenny Suddenfeld, John Mara, and Dana Bryant I offer my appreciation for their help in completing many projects, including this thesis. Pat Gavagan was very patient in waiting for the final document and her help is also gratefully acknowledged.

There are many people who have shared their knowledge of particular fields with me and have made this document possible. The include, in order of appearance, Anders Henriksen, Tom Ketcham, Yet Ming Chiang, Jim Hodge (Chapter II), Walter Zamechek, Patti Morris (Chapter III), Paul Nitishin, Jack Salerno, Jimmy Carter, and Joe Dynys (Chapter IV). I am particularly indebted to Dave Gabbe for teaching me all I know about high purity chemical processing and for giving me access to the Crystal Physics clean room.

Others have been good friends during the final thesis "push"; these include my office mates, especially Ellen, Rock, Mark, and Mark, my skating buddies, especially my pairs partner Peter, who gave me special 'support', Elaine, and Sally, and Diane, Tom, and Sue. I thank them all.

My family has been a constant source of encouragement and love through my life. My parents, Ruth and Howard (without whose efforts this would not have been possible) and Granny, I thank you with all my heart.

John Blendell is my partner in life, as well as in science. Without his help in so many ways this thesis would not have been completed. I thank him most of all.

This research was supported by the Department of Energy (Contract #DE-AC02-76ER02390) and the National Science Foundation, Division of Materials Research (Contract #77-11685-DMR).

I-1 Introduction

The microstructural evolution of a material undergoing sintering and grain growth is determined by the diffusivities (surface, lattice, and boundary), the rates of evaporation and condensation, the grain boundary mobilities, the mobilities of closed pores, the pore-boundary interactions, the surface energy and grain boundary energy and their variation with orientation, and the initial sintering geometry. The effect of each of these parameters is understood quantitatively when considered separately. The effect of the total set on the microstructural evolution is understood only qualitatively.

The first generation of modelling has described sintering and grain growth separately and as a function of a single variable or a limited set of these variables. For example, the relative contributions of the surface, lattice and boundary diffusivities and evaporation/condensation can be evaluated for a simple sintering geometry to determine whether a material densifies or coarsens during the initial stages of neck growth. For a quantitative analysis of the sintering and grain growth in a powder compact, a mathematical formalism including all parameters is necessary. In this study, models based on larger subsets of the sintering variables are reviewed. These include models of simultaneous sintering and grain growth and models of the transitions from grain growth with pores attached to grain boundaries to grain growth with pores separated from grain boundaries. Particular emphasis has been placed on the effects of dihedral angle distributions on kinetics within a single material.

The microstructural evolution calculated from these models, as defined by the average pore size and grain size, and the condition of pore:boundary attachment or separation, are compared with the microstructure evolution observed in MgO compacts. The initial microstructure was controlled by hot-pressing of unconsolidated powders, by hot-pressing of a filter cast compact, and by sintering of compacts formed by settling of particles with a narrow size distribution. The solute content of the samples were varied from background cation levels of 3000 μg/g to <8 μg/g. The pore size:grain size conditions for pore separation from moving boundaries were measured for regions of uniform microstructure in low purity undoped and Al-doped MgO. The purity levels of these samples were typical of MgO samples described in the literature. High-purity MgO powder and powder compacts of uniform initial microstructure were prepared and processed under clean conditions. The sintering characteristics of the high-purity compacts are compared with the data from samples of typical low purity. The variation in the observed dihedral angle distribution in compacts undergoing sintering or in initially dense compacts undergoing desintering has been assessed. These distributions of observed dihedral angles in MgO, Al_2O_3, and MgO-doped Al_2O_3 compacts are compared with the distributions of dihedral angles as measured from grooved surfaces. The effect of the width of the dihedral angle distribution on sintering is discussed.

I.2 Microstructural Evolution

The parameters which determine the sinterability of a ceramic powder compact are: the diffusivities: D_s, D_ℓ, D_{gb} of all species; the rates of evaporation and condensation (E/C); the surface and grain boundary energies, γ_s and γ_{gb}; the average particle size and particle size distribution; the particle morphology; and the green density. The values of the diffusivities, the rates of E/C, γ_s, and γ_{gb} are functions of orientation as well as temperature and background impurity concentration. Due to the number of possible combinations of these parameters, significant simplifications are required to model the sintering process. In some cases, either sintering or coarsening is treated. In all cases, anisotropy is not treated. A single value of the dihedral angles, ψ, as defined by $\gamma_{gb}/\gamma_s = 2 \cos \psi/2$, is sometimes incorporated into the models, but is generally assumed to be 180^0.

The effect of decreasing the dihedral angle is an increase in the radius of curvature and, hence, a decrease in the driving force for sintering. Dynys, et al. (1980) estimated that with a dihedral angle of $\sim 115^0$, the sintering times would increase by a factor of 2 to 50 relative to the sintering time for $\psi = 180^0$. The time increase depends on the sintering mechanism and the neck size. However, a dihedral angle $\psi < 180^0$ is rarely incorporated into data analyses since the sintering geometries and the rate equations are approximations.

These models are frequently extrapolated to predict changes in bulk characteristics of powder compacts. Measurements of changes in the specific surface area, linear shrinkage, and pore permeability of a wide range of materials agree qualitatively with the models. Direct measurements of x/a (neck radius/particle radius) and examination of individual sintered necks often reveal that the assumptions of the models do not apply even to "model" systems. For example, in the sphere-sphere and sphere-plate experiments with large Al_2O_3 spheres by Dynys, et al. (1980), necks were frequently faceted, the dihedral angles were $<180^0$, undercutting occurred, and irregular necks and pores within the neck formed, possibly as a result of capillarity-induced instability due to undercutting. Fractured necks on an Al_2O_3 plate showing these non-ideal features are shown in Figure I-1. The orientation dependence of sintering is also shown by the pronounced neck asymmetry. It is not known whether the asymmetry is due to orientation-dependent diffusivities or a variation in surface energy around the sintered neck.

The onset of intermediate stage sintering is defined by the existence of a continuous pore network (channels) along grain edges with all pores on boundaries. The intermediate stage is generally assumed to begin at $x/a > 0.2$. In most cases, shrinkage without coarsening is modelled. The kinetics of intermediate stage sintering have been modelled as grain boundary or lattice diffusion from a right circular cylinder. The grain-pore geometry and intermediate models are presented in Figure I-2. Comparison of a sintered microstructure, shown in Figure I-3(a), and an idealized pore geometry for the intermediate stage, shown in Figure I-3(b), show substantial deviation from the assumption of cylindrical pores.

The final stage of sintering begins by the transition of the continuous pore network to isolated pores on grain boundaries. While the breakup of the complex pore network has not been analyzed, the "ovulation" into spherical pores from an infinite cylindrical void has been described by Nichols and Mullins

Figure I-1 Observed neck growth features for alumina sphere-plate sintering experiments, SEM micrographs: a) neck radius/ particle radius: $x/a \sim 0.60$ for 0.14 mm spheres, b)and c) $(x/a) \sim 0.017$ for 3.0 mm. (from J.M. Dynys et al., 1980).

Cylindrical Pore Case:

Boundary Diffusion

$$P = \frac{r^2}{l^2} = 2\,{\frac{\delta D_b \gamma \Omega}{l^4 kT}\,t}^{2/3}$$

Cylindrical Pore Case:

Lattice Diffusion

$$P = \frac{r^2}{l^2} = \frac{10 D_l \gamma \Omega}{l^3 kT}\,(t_f - t)$$

for the idealized geometry in Figure I-3(b) described by

$$P = \frac{1/3(36\pi l_p r^2)}{8\sqrt{2}\, l_p^3} = 1.06\,\frac{r^2}{l_p^2}$$ where P = fraction porosity,

r = cylinder radius, l, l_p = cylinder length (facet length),
Ω = atomic volume, t = time, γ = surface energy.

Figure I-2 Intermediate stage sintering models for grain boundary and lattice diffusion control from Coble (1961).

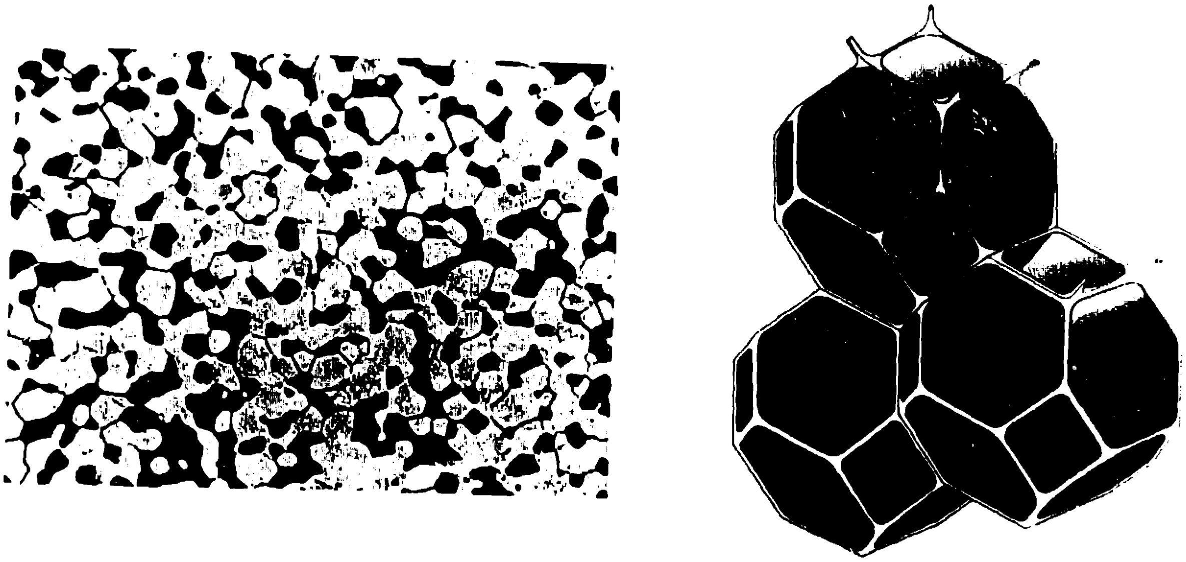

Figure I-3 (a) Typical intermediate stage microstructure of alumina at 250X (from Coble, 1961).

(b) Model geometry of intermediate stage sintering.

(1965) for surface diffusion and volume diffusion. For an infinite cylinder with sinusoidal perturbations of amplitude δ and wavelength λ distributed axially along a cylinder of radius r_o, the growth rate of the perturbation, $\dot{\delta}$, by surface diffusion is:

$$\frac{\dot{\delta}}{\delta} = B_s\left(\frac{2\pi}{\lambda}\right)^2 \left[\left(\frac{1}{r_o^2}\right) - \left(\frac{2\pi}{\lambda}\right)^2\right] \qquad \text{(I-4)}$$

where $B_s = \frac{D_s \gamma_s \Omega^2 \nu}{k\ kT}$, and ν = number of diffusing atoms/unit surface area. When $1/r_o > (\frac{2\pi}{\lambda})$, $\dot{\delta}/\delta > 0$ and the void breaks up. For breakup by volume diffusion

$$\frac{\dot{\delta}}{\delta} = A\left(\frac{2\pi}{\lambda}\right) \left[\left(\frac{1}{r_o^2}\right) - \left(\frac{2\pi}{\lambda}\right)^2\right] \left[K_1(2\pi r_o/\lambda)/K_0(2\pi r_o/\lambda)\right] \qquad \text{(I-5)}$$

where $A = \frac{D_\ell \gamma \Omega}{kT}$ and $K_1(2\pi r_o/\lambda)$ and $K_0(2\pi r_o/\lambda)$ are coefficients for the Bessel function solution. In this case, $\dot{\delta}/\delta > 0$ when $\frac{1}{r_o} > (\frac{2\pi}{\lambda})$. The wavelengths corresponding to maxima in the growth rates for the two cases are $\lambda_m = 9\ r_o$ for surface diffusion, and $\lambda_m = 13\ r_o$ for lattice diffusion, with final spacings of spherical pores with radius, r_i, $\lambda_m = 4.7\ r_i$, and $\lambda_m = 6.1\ r_i$, for surface and lattice diffusion, respectively. Studies of the breakup of cylindrical voids in Al_2O_3 (sapphire) by Yen and Coble (1972) and in LiF-doped polycrystalline MgO by Gupta (1975) were found to follow the model for surface diffusion controlled mass transport.

The critical length to diameter ratio for the transition from spheroidization to ovulation of a finite cylinder was found to be L/D = 3.36 (Gupta, 1978). From typical intermediate stage microstructures, such as the one shown in Figure I-3(a), it is seen that channels with $L/D > 3.36$ are not observed. The curvature difference between the three-sided channels and the four-sided pores made the structure inherently unstable and pore pinchoff will occur along the channel at $L/D < 3.36$. Any deviation from the model of channels and pores in an isotropic solid will change the geometry at pore pinchoff. Due to the discrepancy between modelled geometries and actual intermediate stage microstructures, fewer analyses of the intermediate stage have been performed than of initial and final stages of sintering.

In powder compacts, the transition to closed pores begins at approximately 15% volume fraction pores, V_f, and is complete at approximately $V_f =$ 5%. Gupta and Coble (1967) determined that the transition to isolated pores occurred between 85% and 95% for Cu compacts and between 90% and 95% for ZnO and Al_2O_3 compacts. This density range over which the microstructural transformation to isolated pores on grain faces, edges, and corners occurs is determined by the same factors which affect the earlier sintering stages (average grain size and grain size distribution, density distribution, anisotropy in γ_s, γ_{gb}, D's, etc.). In the intermediate and final stages of sintering, grain growth, as well as densification must be analyzed to determine the changes in pore sizes and diffusion path lengths due to Ostwald ripening and pore coalescence and for the final stage to determine the change in pore location relative to grain boundaries due to discontinuous grain growth or normal growth without pores attached to boundaries.

Two different but complementary descriptions of the simultaneous densification and grain growth processes and the transition to discontinuous grain growth have been developed in terms of the geometry of the microstructure and material parameters, such as diffusivities. The first treatment, developed by Brook and extended by Cannon, et al. and Evans, et al., involves calculation of the transitions between pore-drag controlled boundary migration to solute drag or intrinsic boundary migration controlled growth with the pores either attached to or separated from the boundary as functions of grain size and pore size. The second approach involves the calculation of pore size-grain size trajectories depending on the relative rates of grain growth/pore coalescence and sintering.

The separation of a boundary from a pore occurs when the boundary velocity, V_b, exceeds the pore velocity, V_p. The velocity, V_i, can be expressed as the product of a mobility M_i and a driving force, F_i. The separation condition, as stated by Brook (1969) is that $V_p < V_b$ for N pores on a boundary, which leads to:

$$V_p = F_p M_p < V_b = (F_b - NF_p)M_b \tag{I-6}$$

or

$$F_b > NF_p + \frac{M_p F_p}{M_b} \tag{I-7}$$

When $V_p = V_b$, the pores migrate with the boundary and

$$V_b = F_b \frac{(M_p M_b)}{NM_b + M_p} \tag{I-8}$$

The limiting cases of Equation (I-8) are when $NM_b >> M_p$ and $NM_b << M_p$. In the former, $V_b = F_bM_p/N$ and pore mobility determines the boundary velocity. In the latter case, $V_b = F_bM_b$ and the boundary mobility determines the velocity. A "semi-quantitative" map of conditions for pore separation was calculated by Brook, assuming that a single spherical pore is attached to a boundary of length G, the pore moves by surface diffusion, the maximum force on the pore exerted by the boundary is $\pi r\gamma_b$, and the force on the pore-free boundary is due to its curvature, and is $2\gamma/G$.

A schematic Brook "breakaway" map is shown in Figure I-4. The regions in the map correspond to the three types of pore-boundary interactions: pore-drag controlled migration, boundary controlled migration with pores attached, and boundary controlled migration with pores separated. Brook also considered the effect of a segregated impurity on the grain boundary mobility. The solute drag limited mobility in lower than the intrinsic mobility allowing larger pores to migrate with the boundary before separation. The "nose" of the separation curve is, thus, moved to larger grain sizes, as shown in Figure I-4.

The effects of a grain size distribution and solute drag were incorporated into this basic model by Cannon, et al. The pore-grain geometry assumed in this model (and all models) determines the conditions for pore-boundary separation. The geometry assumed in the Cannon model is the tetrakaidecahedron with spherical pores on all corners, as shown for a six-sided grain face in Figure I-5. The pore radius is related to the volume fraction pores, v_f, and average grain size $\bar{G}$ by:

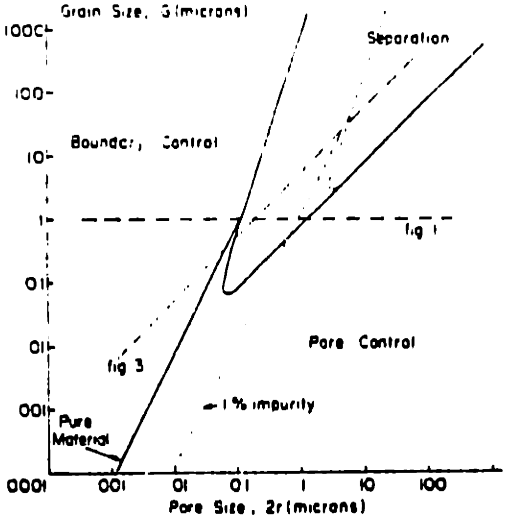

Figure I-4 Dependence of pore-boundary interaction on microstructural parameters in a pore system where pores move by surface diffusion (from Brook, 1969).

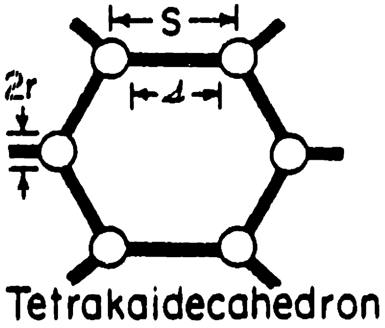

$$r = \bar{G}\left(\frac{v_f}{48}\right)^{1/3}$$

$$N = \frac{24}{\pi \bar{G}^2}$$

$$\Delta = S - 2r$$

$$\Delta = \bar{G}\left(\frac{\pi}{8} - \frac{v_f^{1/3}}{6^{1/3}}\right)$$

Figure I-5 Geometric relationships assumed for final stage sintering models.

$$r = \bar{G} \left(\frac{v_f}{48}\right)^{1/3} \quad . \tag{I-9}$$

The number of pores per boundary, N, is

$$N = \frac{24}{\pi \bar{G}^2} \quad . \tag{I-10}$$

The transition from-pore drag control to pore separation is calculated from Equation (I-7) when $M_p << NM_b$. The Hillert equation for the force on a boundary due to curvature G, in a matrix with a narrow grain size distribution is:

$$F_b = \frac{5}{2} \gamma_b \left(\frac{1}{G_c} - \frac{1}{G}\right) \tag{I-11}$$

where G_c is the critical grain size for growth. From Equations (I-10) and (I-11), the maximum restraining force due to N pores on a boundary is:

$$F_c = \pi r \gamma_b N = \frac{6.6 \, v_f^{1/3} \, \gamma_b}{\bar{G}} \tag{I-12}$$

The condition from separation becomes:

$$\frac{5}{2} \frac{\gamma_b}{\bar{G}} \left| 1 - \frac{G}{\bar{G}} \right| > \frac{6.6 \, v_f^{1/3} \, \gamma_b}{\bar{G}} \tag{I-13}$$

where $G_c = \bar{G}$. This reduced to:

$$\left| 1 - \frac{G}{\bar{G}} \right| > 2.64 \, v_f^{1/3} \tag{I-14}$$

For normal growth (Hillert criterion), $G_{max} = 2\,\overline{G}$, the critical volume fraction before breakaway from Equation (I-9), v_f*, is equal to 0.007. For $G_{max} >> G$, $v_f^* = 0.094$. The boundary to which this condition corresponds for $G_{max} = 2\,\overline{G}$, is shown in Figure I-6 as line AO. The cross-hatched region corresponds to a density of less than 65%, which is physically meaningless for the assumed geometry. Below this density, the pore diameter is greater than the facet length S, as defined in Figure I-5.

The critical force for solute drag limited migration with pores attached as calculated from Equation (I-7) is

$$F_c = \pi r \gamma_b N + \pi r \gamma_b \frac{A_n}{r^n} \alpha C_\infty \qquad \text{(I-15)}$$

where $M_b = 1/\alpha C_\infty$, the solute drag mobility, α is the impurity drag per unit velocity and per unit dopant concentration, C_∞ is the bulk concentration of solute, and the pore mobility M_p is expressed as $\frac{A_n}{r^n}$. The values of $\frac{A_n}{r^n}$ are dependent on the mechanism of pore migration; these are listed in Table I-1. The condition for pore and solute separation using Equation (I-15) and the geometric relationship between r, v_f, and $\overline{G}$ is

$$\frac{5}{2} \left| 1 - \frac{\overline{G}}{G} \right| > 6.6\, v_f^{1/3} + \frac{\pi 48^{(n-1)/3} A_n \alpha C_\infty}{\overline{G}^{n-2} v_f^{(n-1)/3}} \qquad \text{(I-16)}$$

This determines the "nose" of the curve, Line BC, in Figure. I-6.

The pores can remain attached to the boundary after the transition to the intrinsic mobility if the pore mobility is sufficiently high. To determine the range of pore sizes and grain sizes for which the pores

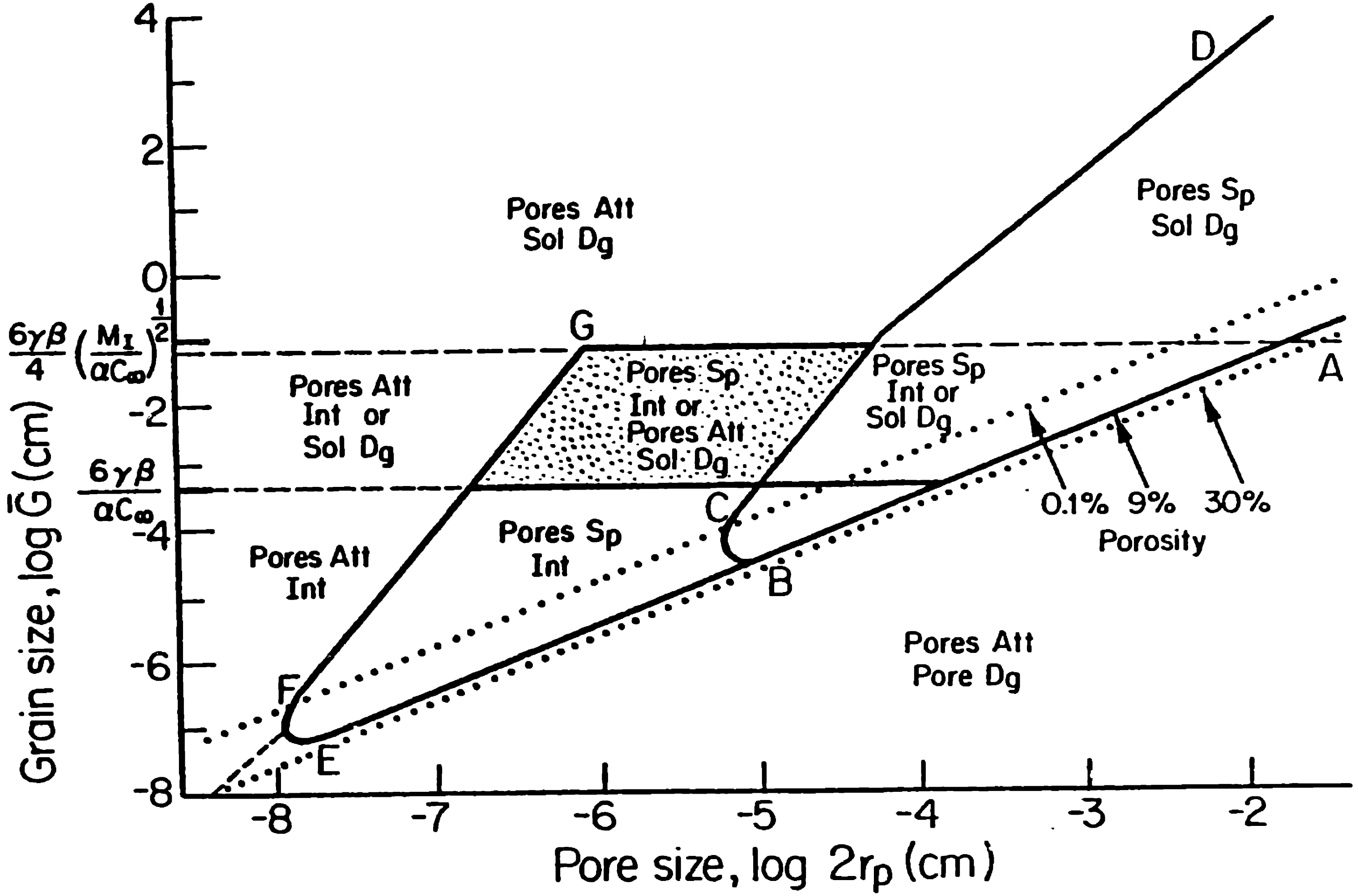

Figure I-6 Schematic of the range of pore-grain boundary interactions during final stage sintering.

Table I-1

Pore Mobilities

$$M_p = \frac{A_n}{r^n}$$

Controlling Mechanism	n	A_n
Surface Diffusion	4	$\frac{3wD_s\Omega}{2\pi kT}$
Lattice Diffusion	3	$\frac{3D_l\Omega}{2\pi kT}$
Vapor Diffusion	3	$\frac{3D_g\Omega^2P_v}{4\pi(kT)^2}$
Evaporation-Condensation	2	$\frac{3\alpha'\Omega^2P_v}{4(\pi kT)^{3/2}(2m)^{1/2}}$

where w is surface thickness; D_s, surface diffusivity; Ω, molar volume; k, Boltzmann's constant; T, absolute temperature; D_l, lattice diffusivity; D_g, vapor diffusivity; P_v vapor pressure; α', sticking coefficient; m, molecular weight.

from Nichols (1969)

remain attached, $1/\alpha C_\infty$ is replaced in Equation (I-16) by M_I, the intrinsic mobility. The "nose" of curve, line EF, in Figure I-6 is the solution in the pore separation condition. The lines CD and FG describe pore:boundary separation when the pore velocity is high, i.e., when the second term in Equation (I-16) is large. The line CD is determined by the solute drag limited boundary velocity, $\overline{FG}$, by the intrinsic mobility limited velocity. The conditions for the transition from intrinsic drag to solute drag as a function of grain size and, hence, driving force have also been derived. It has been predicted from solute drag theory that an unstable region in the velocity-driving force relationship exists as shown in Figure I-7. In this range of driving forces, transitions occur from the solute drag limited velocity to the intrinsic velocity over a range of driving forces. These driving forces can be equated to the curvature-induced driving forces for grain growth (in the absence of other driving forces).

The grain size range which corresponds to the driving forces in the unstable regime are calculated from F_{max} and F_{min} in Figure I-7 and correspond to $\frac{6\gamma\beta}{C}$ and $\frac{6\gamma\beta}{4}(\frac{M}{\alpha C_\infty})^{1/2}$, respectively. In the dotted region in Figure I-6, the pores will stay attached only if the solute stays attached.

These maps were calculated using an idealized geometry, which does not model the true microstructural evolution. For example, the assumption of $G_{max} = 2\,\overline{G}$ was derived from a different microstructure than a space-filling microstructure of tetrakaidecahedra. In the grain growth process, grains below a certain size and a certain number of sides shrink; the others grow. The treatment of Cannon, et al. assumes that pore separation

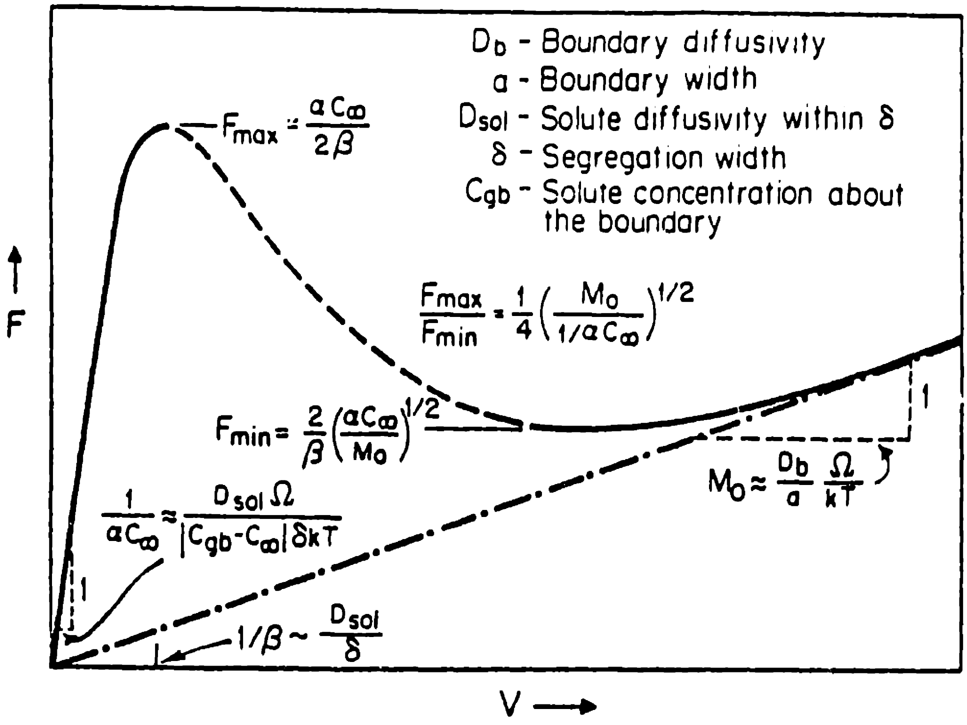

Figure I-7 Force-velocity relationship for boundary migration both in the presence of solute drag and in the intrinsic regime.

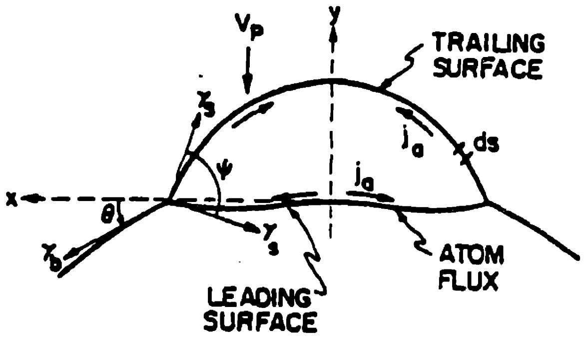

Figure I-8 Schematic of a moving pore indicating the atom flux and the inclination of the grain boundary, θ (from Hsueh et al., 1982).

occurs at a geometry close to the "equilibrium" structure, rather than during the disappearance of a grain with fewer sides than a tetrakaidecahedron.

An alternate approach has been developed by Hsueh, Evans, and Coble (1982) for the motion of pores attached to two-grain interfaces and for the motion and coalescence of pores attached to the faces of a disappearing three-sided grain. A maximum steady-state pore velocity was found which is a function of the dihedral angle. The transition from the steady-state velocity of the pore to non-steady state led to grain boundary convergence and pore separation. By comparing the steady-state pore velocity to the grain boundary velocity, critical conditions for pore separation were developed for different pore-grain configurations.

The steady-state velocity of the pore in Figure I-8 was calculated by Hsueh, et al. Equal velocities at all points along the pore surface, an invariant dihedral angle, and a continuous chemical potential at the intersection of the leading and trailing edge of the pore surfaces were required by the assumption of steady state. A normalized steady-state velocity for a pore moving by surface diffusion was found numerically from the flux equation:

$$J_2 = -\frac{D_s \delta_s \gamma_s}{kT} \frac{d(\kappa_1 + \kappa_2)}{ds} \qquad \text{(I-17)}$$

and from conservation of matter:

$$2\pi\chi Js = \pm\pi\chi^2 v_p/\Omega \qquad \text{(I-18)}$$

where κ_1 and κ_2 are the in-plane and asymmetric curvature, defined in Figure I-9 in terms of (x,y), ds is an element of pore surface in the direction of flow, γ_s is the surface energy, Ω is the atomic volume, and v_p is the pore velocity. Pore shapes predicted for the dihedral angle $\psi = 60^o$ at various velocities are shown in Figure. I-10. The solutions of the pore shape equations were found to converge over a range of pore velocities and dihedral angles; for greater distortion of pore shapes, the solutions did not converge. A maximum steady-state pore shape and velocity were determined from the maximum convergent solutions. The maximum steady-state velocity V_p, for a pore of in-boundary radius of r_p was calculated to be:

$$V_p \approx \frac{\Omega D_s \delta_s \gamma_s}{kTr_p^3} \ (17.9 - 6.24\ \psi) \qquad \text{(I-19)}$$

or, for $\gamma_b/\gamma_s = 2 \cos \psi/2$,

$$V_p = V_p^o \ \frac{(17.9 - 6.24\ \psi)}{2 \cos \psi/2} \qquad \text{(I-20)}$$

where V_p^o is the maximum pore velocity of a spherical pore of radius r_p moving by surface diffusion, as defined in Table I-I. The maximum steady-state pore velocity as a function of dihedral angle is presented in Figure. I-11(a). It should be remembered that $\delta_s D_s$, γ_s, and γ_b are assumed to be single valued in each pore-grain intersection and that $\gamma_b = 2\gamma_s \cos \psi/2$. This means that the pore is symmetrical with the boundary plane at $v_p = 0$.

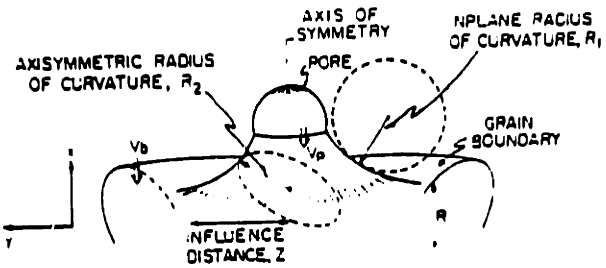

Figure I-9 The axisymmetric configuration associated with pore drag, illustrating the important curvatures, the influence distance, and the pore and grain boundary velocities (from Hseuh et al., 1982).

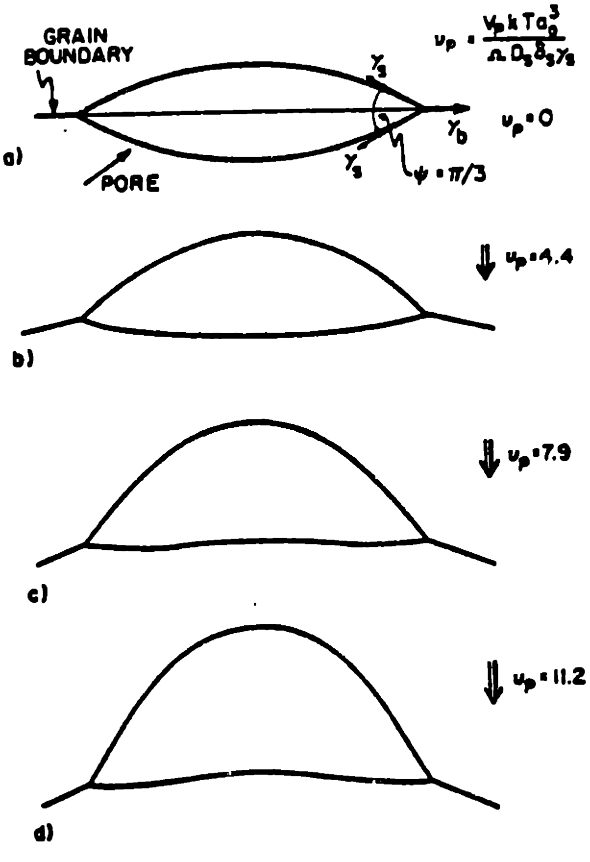

Figure I-10 Predicted pore shapes for several values of the normalized pore velocity for $\psi = \pi/3$ (from Hseuh et al., 1982).

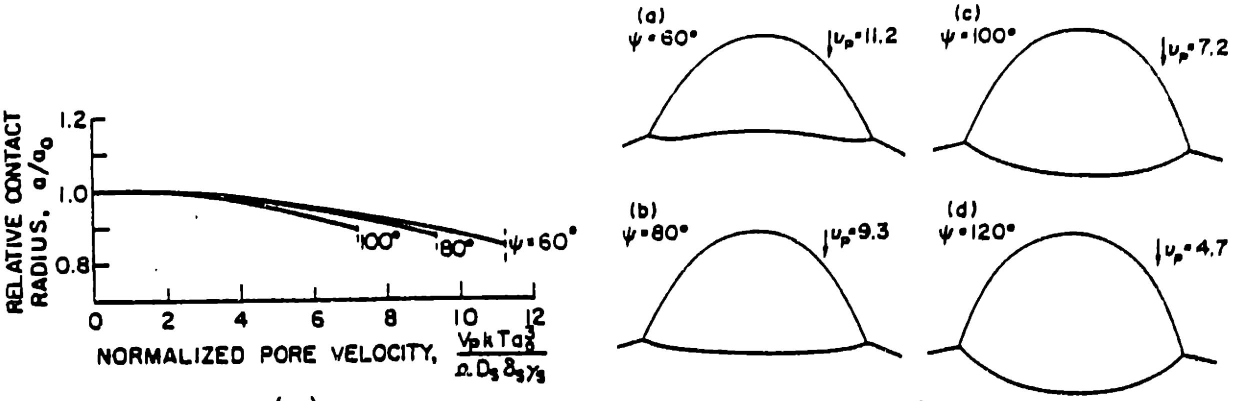

(a)

(b)

Figure I-11 (a) Plot of the grain boundary contact radius as a function of the normalized pore velocity (from Hseuh et al., 1982).

(b) The maximum steady state pore velocity (v_p) as a function of dihedral angle and the shapes of pores when the velocity attains the maximum value (from Hseuh et al., 1982).

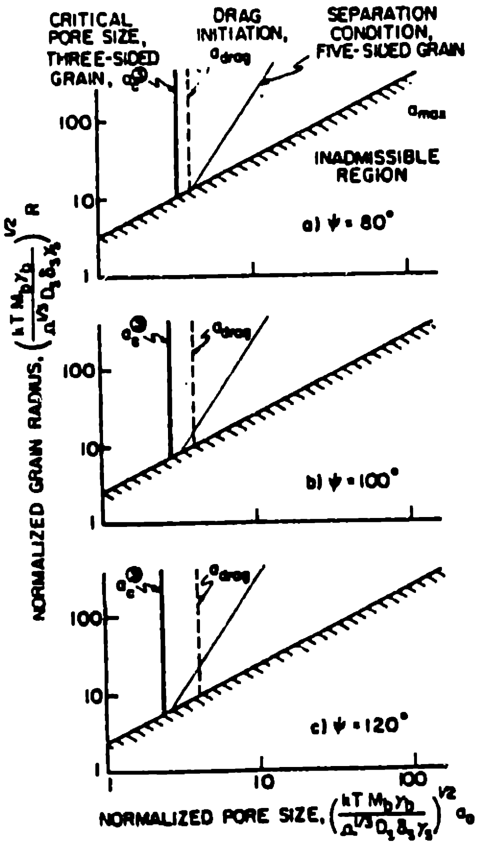

Figure I-12 The various separation and admissibility conditions plotted for three values of the dihedral angle identifie in the analysis of Hseuh et al. (1982).

The maximum velocity steady-state pore shapes for dihedral angles of $\psi = 60^0, 80^0, 100^0$, and 120^0 are shown in Figure I-11(b).

A pore size for breakaway was also calculated for a pore on one face of a three-sided grain. By equating the velocity of the boundary

$$v_b = \frac{\sqrt{3}\ \gamma_b M_b \Omega^{2/3}}{R} \tag{I-21}$$

where R is the maximum grain radius, defined in Figure I-9 to the maximum steady-state velocity, Equation (I-19), the minimum pore size for separation becomes:

$$r_o^2 \geq \left[\frac{R}{r_o}\right] \left[\frac{\Omega^{1/3} D_s \delta_s \gamma_s}{kTM_b \gamma_b}\right] \left[\frac{17.9 - 6.2\ \psi}{\sqrt{3}}\right] \tag{I-22}$$

If, for a three-sided grain, the pore becomes located at the three-grain junction before Equation (I-22) is satisfied, no separation occurs. The requirement for this condition is that $R \sim 2r_o$, so that the lower limit to the pore size for separation becomes:

$$r_o^2 = \left[\frac{\Omega^{1/3} D_s \delta_s \gamma_s}{kTM_b \gamma_b}\right] \left[\frac{2}{\sqrt{3}}\right] (17.9 - 6.2\ \psi) \tag{I-23}$$

This lower limit is plotted on a normalized pore-grain size map in Figure I-12. For a five-sided grain, the condition for pore separation is more analogous to that calculated by Cannon and shown as line CD in Figure I-6.

The pore-grain configuration at the transition from intermediate to final stage sintering was used to calculate the maximum allowable pore radius, r_{max}, relative to the facet edge-length ℓ shown in Figure I-18. This becomes:

$$\frac{r_{max}}{\ell} = 0.5\,[(1.28\,\psi - 1.42)/(1.27\,\psi - 0.556)]^{1/3} \qquad \text{(I-24)}$$

which is designated the "inadmissible region" in Figure I-12. For $\ell \sim R$ and $\psi = 80^{o}$, 100^{o}, and 120^{o}.

In addition, the pore size condition for pore drag was determined, from v_b, and r_o, when $v_p < v_b$. When $R \gtrsim 3a$ for a five-sided grain,

$$r_o^{\;2} = 16\,(\Omega^{1/3} D_s \delta_s \gamma_s / kT M_b \gamma_b) \qquad \text{(I-25)}$$

This is also shown in Figure I-12.

The analysis of Hsueh, Evans, and Coble for stable pore-boundary interactions predicts a limited region of pore size-grain size where pores remain attached. When $v_b > v_p$, a steady-state pore profile was not found for pores on two-grain faces. With decreasing dihedral angle, the maximum pore velocity increased and the critical pore radius which could remain attached to a shrinking three-sided grain increased. The region which is defined by this critical pore radius is similar to that determined by Cannon, et al. for the transition to boundary mobility controlled boundary migration with pores attached, line $\overline{FG}$ or $\overline{CD}$ in Figure I-6.

The "inadmissible" region in Figure I-12 is based on a geometrical model of isolated pore formation through "ovulation" without consideration of the actual geometry necessary for such an event to occur. As described above, the channels developed in an ideal array of sintered spheres are not cylindrical and pore pinch-off might be expected to occur at the point of closest approach in the channels, that is, at the facet mid-point. There is no reason, a priori, to choose one geometry of pore breakup over another without doing the instability analysis for channels developed by sintering for a range of dihedral angles. The "inadmissible" region of Hsueh, et al. is, therefore, arbitrary. The calculation of the "inadmissible" region shown on Figure I-6 has greater physical significance because it corresponds to the limit of isolated spherical pores as defined by Figure I-5 and Equation (I-9). This assumed geometry is also arbitrary, but the "inadmissible" region in Figure I-6 is consistent with the assumed final stage geometry.

The analysis of Hsueh, Evans, and Coble for stable pore:boundary interactions predicts a limited region of pore size-grain size where pores remain attached. When $v_b > v_p$, a steady-state pore profile was not found. A region similar to the region in which pore-drag controlled boundary motion was predicted by Cannon, et al., was deemed "inadmissible" by geometrical consideration. A single region bounded by $r_o = 0$, $r_o = r_c$ ③ and the inadmissible region was the only region in which stable pore motion with boundaries was predicted. This is in contrast to the predictions of Cannon, et al. discussed above.

The other approach to microstructural evolution during intermediate/final stage sintering is a dynamic one in which simultaneous sintering and

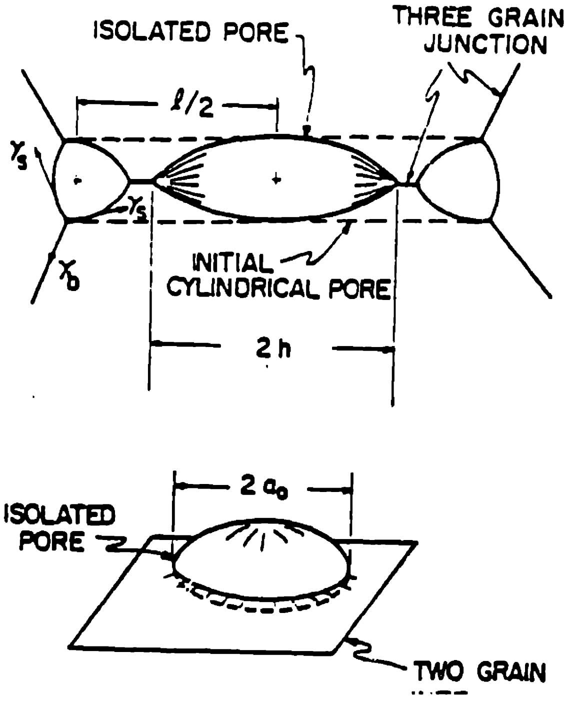

Figure I-13 A pore at a three grain junction formed by a Rayleigh instability and the corresponding pore at a two-grain interface (from Hseuh et al., 1982).

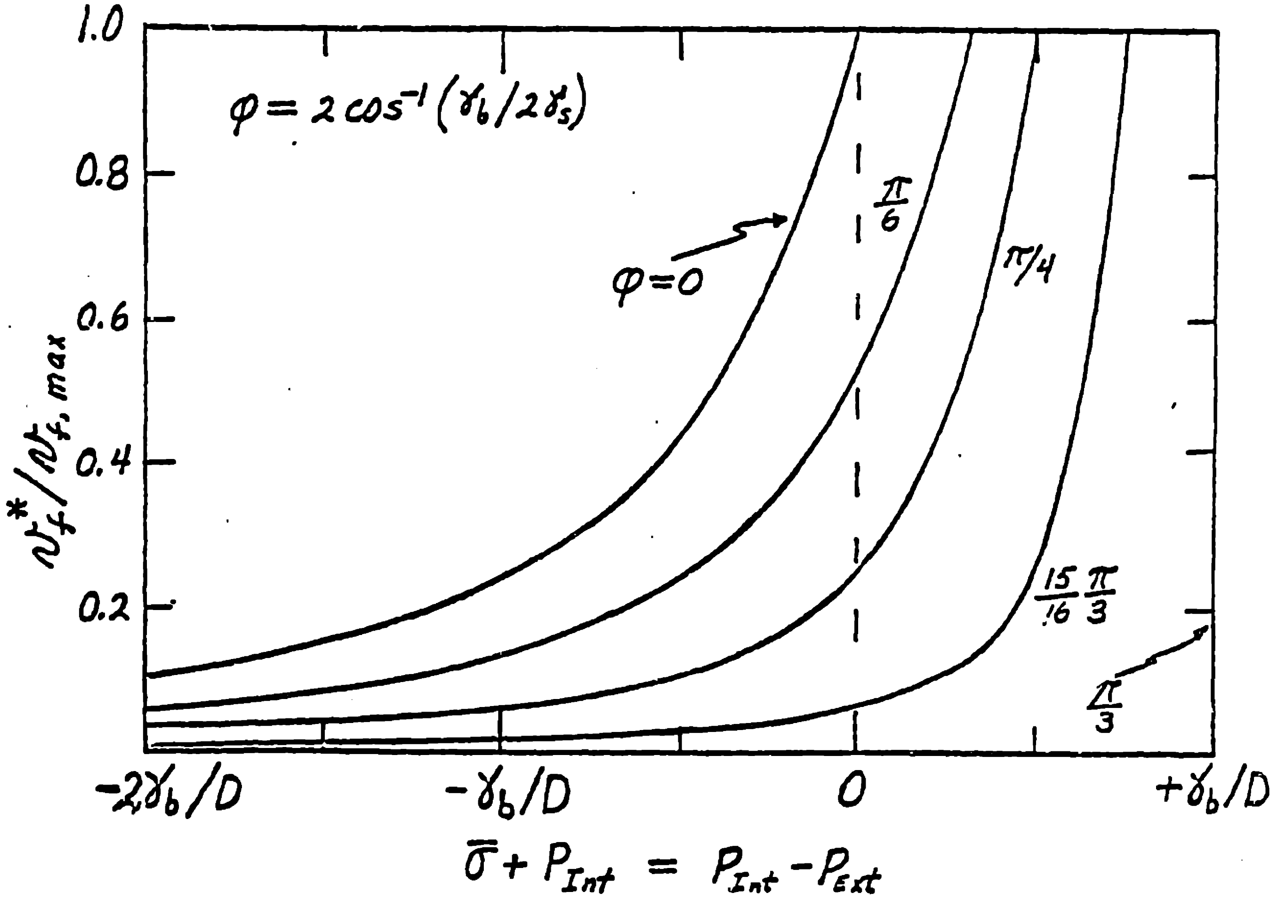

Figure I-14 The effect of dihedral angle on equilibrium porosity as a function of applied and internal pressure. (Cannon) coarsening are considered. The treatment presented here was developed by Cannon, et al. The change in the pore size with time is expressable as the sum of the change in pore size at constant volume fraction porosity and the change in pore size at constant grain size. The grain growth rate is calculated based on control by either boundary mobility of pore-drag controlled mobility. The equations for sintering and coarsening are equated through the dt terms in the rate equations, yielding relationships for $\frac{dG}{dR}$ and $\frac{d \ln G}{d \ln R}$. The various scenarios for grain growth and sintering limited by different mechanisms are presented in Table AI-1 in Appendix AI. These equations are based on the tetrakaidecahedral geometry, the final stage sintering models of Coble, and the pore mobility relations of Nichols, listed in Table I-1.

The equations shown in Table AI-1 represent trajectories in pore size-grain size maps. A further modification of this treatment yielded calculations of times to reach a given volume fraction porosity as a function of initial grain size G_o, initial pore size, r_o, initial grain density, v_{f_o}, and the coarsening parameter Γ, which is $\frac{3wD_s\gamma_{gb}}{176\delta D_b\gamma_s}$ for the case of grain growth by pore mobility (wD_s) control and sintering by grain boundary diffusion. For this case,

$$r^4 - r_o^4 = 4(K_s - S_b)(t - t_o) \qquad \text{(I-26)}$$

and

$$\frac{d \ln G}{d \ln r} = \frac{\Gamma}{\Gamma - 1}$$

where $S_b = \frac{11}{3} \frac{\delta D_b \Omega \gamma_s}{kT}$, $K_s = \frac{wD_s \Omega \gamma_{gb}}{16rT}$, and $\frac{K_s}{S_b} = \Gamma$.

This case is shown schematically in Figure AI-1 for the limiting volume fraction porosity for various values of Γ and v_{f_0}. In Figure AI-2 is shown the dependence of the time to sinter to a given final density as a function of Γ for a given v_{f_0}.

As with the other models presented here, the restrictive geometry of this model, as well as the assumed forms of the expressions for the sintering and grain growth rates, make these relationships useful only as order-of-magnitude indicators of sintering/grain growth trajectories. For the case presented above, the sensitivity of d ln G/d ln r to small change in S_b and K_s when $S_b \sim K_s$ makes this analysis difficult to apply. Only by comparison with experimental data can the value of Γ be determined for $\Gamma \sim 1$.

The models in the preceding section were presented approximately in the order in which they were originally generated. First sintering or coarsening was considered. The transition to the closed pore stage of sintering was described, followed by descriptions of the transition from boundary migration with pores attached to boundary migration with pores separated. The dihedral angle of the attached pore was considered explicitly in one boundary pore separation model. Competitive densification and coarsening were then evaluated. In these models, the dihedral angle and, hence, γ_s and γ_{gb} were assumed to be isotropic and single valued.

In the following section, a model of the relative stability of pores as a function of the dihedral angle and the number of pore sides is presented. The effects of poor grain packing and a distribution of dihedral angles in a single material are discussed.

A thermodynamic treatment of the effects of dihedral angle and pressure on the driving forces for pore growth on shrinkage has been developed by Cannon for various pore:grain configurations in 2D and extends the concepts first suggested by Kingery and Francois (1965.) Conditions for sintering, coarsening, and creep cavitation due to an internal gas pressure on an external stress were determined in terms of the differences in chemical potentials at pore surfaces and boundaries. The general expressions for the chemical potential difference for a pore of the ith type is:

$$\mu_{Pi} - \mu_b = - \left[\frac{\gamma_{gb}}{D} + \frac{\gamma_s}{R_i} + P_e - P_{P_i} \; \Omega \right] \tag{I-28}$$

where μ_{Pi} and μ_b are the chemical potentials at an ith type pore and the boundary, respectively, D is the grain size, γ_{gb} and γ_s are the specific energies associated with the boundary adjacent to and the surface of the ith type pore, R_i is a radius of curvature of the grain dependent on the dihedral angle and the number of sides of the pore, and P_e is the hydrostatic pressure of the external reservoir, P_{P_i} is the internal pore pressure, and Ω is the atomic volume. The critical radius of curvature where the grain curvature changes from positive to negative is defined by the critical angle, ψ_c, for which R becomes infinite for a pore with sides

$$\psi_c = \pi(1-2/N) \tag{I-29}$$

and

$$R_i = \frac{-D}{2} \sin \Delta \psi_i/2 \tag{I-30}$$

where $\mu_i = \mu_i - \psi_c$. An earlier analysis of this problem performed by Kingery and Francois used a form of Equation (I-28) without the $\gamma_{gb}\Omega/D$ term. When $\mu_{p_i} - \mu_b = 0$, there exists an equilibrium porosity and no further sintering or bloating (desintering) occurs. For $\mu_{p_i} - \mu_b > 0$, pores of the ith type shrink. From these stability criteria, it is seen that differences in dihedral angles between pores of equal pore volume, changes in the number of sides of a pore for a given dihedral angle, and the introduction of an internal pore pressure for different initial pore-grain geometries lead to different equilibrium microstructures. One calculation from Cannon on the effect of dihedral angle on the equilibrium porosity for different numbers of pore sides is shown in FigureI-14 for $P_p = P_r = 0$. As the number of sides of a pore increases, the dihedral angle at which $v_f{}^{\cdot\cdot}{}^{*} = 0$ increases. This stability condition indicates that as the dihedral angle decreases the number of sides per pore must also decrease in order for sintering to occur. This has significant implication for the effects of powder processing flaws on final density and also for the effects of grain boundary mobility on final density. For a dihedral angle of 90^{o}, the number of nearest neighbors/pore sides must be less than four in the dimensions for densification to continue. In three dimensions the critical dihedral angle for a four-sided pore is 70.5. Calculations of the effects of internal pore pressure on equilibrium porosity has been performed for different angles and the results are presented in FigureI-15. For small dihedral angles, the applied stress necessary for pore growth in an equilibrium structure is small because an internal pressure and an equilibrium porosity exists on boundaries with

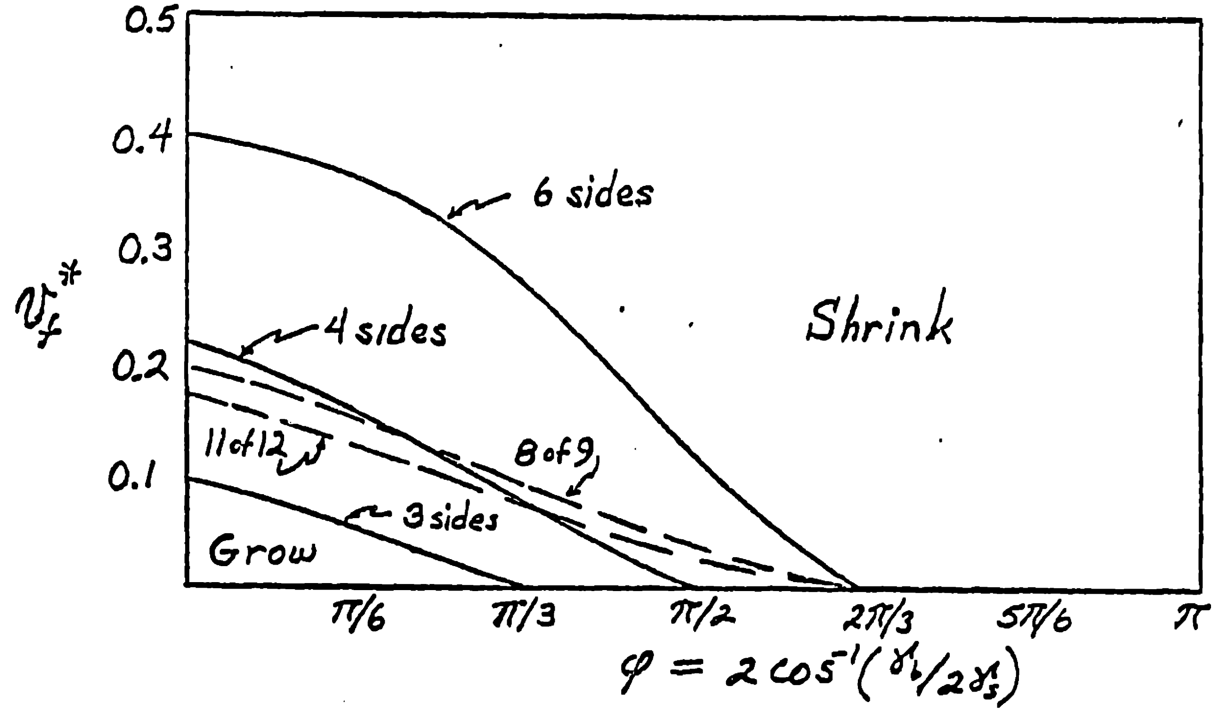

Figure I-15 The effect of dihedral angle and particle packing on equilibrium porosity. (Cannon) low dihedral angles. This implies no barrier to cavity nucleation in a dense material formed by a technique other than sintering, such as hot-pressing or plastic deformation.

In a material with a wide distribution of possible dihedral angles undergoing densification (or desintering due to an external tensile stress or an internal pore pressure), the range of observed dihedral angles at pore-grain intersections will, therefore, be narrower than the total possible range of angles and will be skewed to smaller angles.

As are the models in the previous section, this analysis is too simple since it does not include the coupling between dihedral angles, diffusivities, especially δD_{gb}, and grain boundary mobility. A boundary structure effect on grain boundary diffusivities and grain boundary mobilities has been reported for metals (Gleiter and Chalmers, 1972). For metals when the surface energy anisotropy can be neglected, the dihedral angle can be related to grain boundary energy and, hence, diffusivities and mobilities.

Low angle grain boundaries in metals are observed to have large dihedral angles, low diffusivities and mobilities. "Special" high angle boundaries are observed to have low diffusivities, high mobilities, and intermediate dihedral angles. The remaining high angle boundaries (usually unspecified with respect to structure) are observed to have high diffusivities, mobilities intermediate between special and low angle boundaries and the lowest dihedral angles.

These combined effects may moderate the effect of low dihedral angles and a wide dihedral angle distribution by increasing the diffusivities of high energy boundaries and decreasing the mobilities and diffusivities of low energy boundaries. The variation of diffusivities, energies, and mobilities with grain boundary structure for ionic materials is not known. The variation in grain boundary and surface energies with structure are discussed in greater detail in Chapter IV.

I. 3 Summary

The complexity of a real sintered microstructure has not been adequately represented by any single model. In small volumes, the assumptions of the models may be fulfilled locally, but in general, the simplified geometries and the single-valued relationship $\gamma_b/\gamma_s = 2 \cos \Psi /2$ are only approximations. The more difficult conditions to model in a powder compact sintered to the closed pore state are: a distribution of dihedral angles; asymmetrical pores due to asymmetrical and variable dihedral angles; a wide distribution of grain sizes; a range of grain boundary mobilities due to boundary structure differences and differential solute contents among boundaries; and entrapped gases.

In this study some of the assumptions of the models are tested by examining samples of controlled, close-to-ideal microstructure and purity at various stages of the sintering process. The primary conditions leading to pore separation from boundaries to be tested were the geometry of the pore-boundary intersections, the effects of low background impurity levels, higher levels of dopants on the microstructure, and the variation of dihedral angles within a sample. Both breakaway maps and sintering/grain growth trajectories were to be determined.

In the following three chapters, three different sets of experiments are described which test different models and their critical assumptions. In Chapter II, breakaway maps and grain size-pore size trajectories were calculated from data from the literature and were constructed from data for samples of various low purity 'pure' and Al-doped powder sources formed by either hot pressing and annealing or sintering. In Chapter III, the techniques for preparing high purity powder and powder compacts are presented. Techniques for controlled doping of the high purity powder and for minimizing contamination during heat treatment used in this study are presented that their effects on green and sintered microstructures are discussed. The results from sintering studies of this powder are discussed. In Chapter IV, the total populations of dihedral angles are presented for three materials: high purity MgO, undoped Al_2O_3, and MgO-doped Al_2O_3. These distributions are compared with measured distributions from samples undergoing sintering and desintering due to internal gas evolution or creep cavitation.

Chapter II. Sintering and Grain Growth in Low Purity MgO

II.1 Calculation of Microstructure Evolution for MgO

An extensive data base is required to calculate the pore:boundary separation conditions and the sintering trajectories described in the previous section. A complete set of diffusivities, boundary mobilities, vapor pressures and interfacial energies are needed for each temperature and composition of interest.

The data base on MgO is the most extensive for ceramics, and MgO was chosen for this study for this reason. The best diffusivity data for various purity levels as a function of temperature are from creep experiments (boundary and lattice diffusivities), tracer diffusion experiments (lattice diffusivities) and grain boundary grooving experiments (surface diffusivities). Grain boundary mobility data are derived from the results of grain growth experiments for undoped ("pure") and Fe-doped MgO. The intrinsic boundary mobility was estimated by Yan, et al. (1976), using the simplified Turnbull relation (1951) and the boundary diffusivities deduced from creep experiments on Fe-doped MgO. The most extensive data for MgO grain growth and creep are available only near 1620 K. Vapor pressure data for MgO are available over a wide temperature range. Because of inaccuracies in the calculated activation energies for these processes, the calculated values of the coarsening parameter, Γ, and the pore:boundary separation condition may be in error at temperatures where the diffusivity data do not overlap.

Pore size-grain size maps for "pure" and Fe-doped MgO at 1620 K were calculated by Chowdry, et al. (personal communication) from the data for grain growth, diffusion, and vapor transport listed in Table II-1. The data for "pure" MgO describes material with at least 100 ppm cation impurities. However, the chemical compositions of the MgO samples described in the literature are not generally reported. Comparison and combination of data from different sources become equivocal due to the probable composition differences.

The data anlysis and map construction are outlined here. The pore mobility as a function of pore radius and temperature is shown in Figure II-1(a). The pore mobilities were calculated using the equations listed in Table I-1 for spherical pores of radii r_p.

Transitions from surface diffusion to gas diffusion control (1920 K) and lattice diffusion control (1470 K and 1620 K) are found. Boundary mobilities for undoped MgO intrinsic and doped MgO (0.05 and 0.25 cation % Fe) calculated from grain boundary diffusion and grain growth data are shown in Figure II-1(b). The calculated maps are shown in Figure II-2(a) and II-2(b). In the "pure" MgO map are seen all main features described generally above. There exists a primary region for which pores are separated and the boundary moves with the solute-drag limited velocity. The similar pore separation region is found for the intrinsic mobility determined velocity. A narrow region defined by the grain sizes for which solute drag to intrinsic transition can occur are found. For the case of MgO with 0.25 mole % Fe, only the primary solute drag-pore separation region was found.

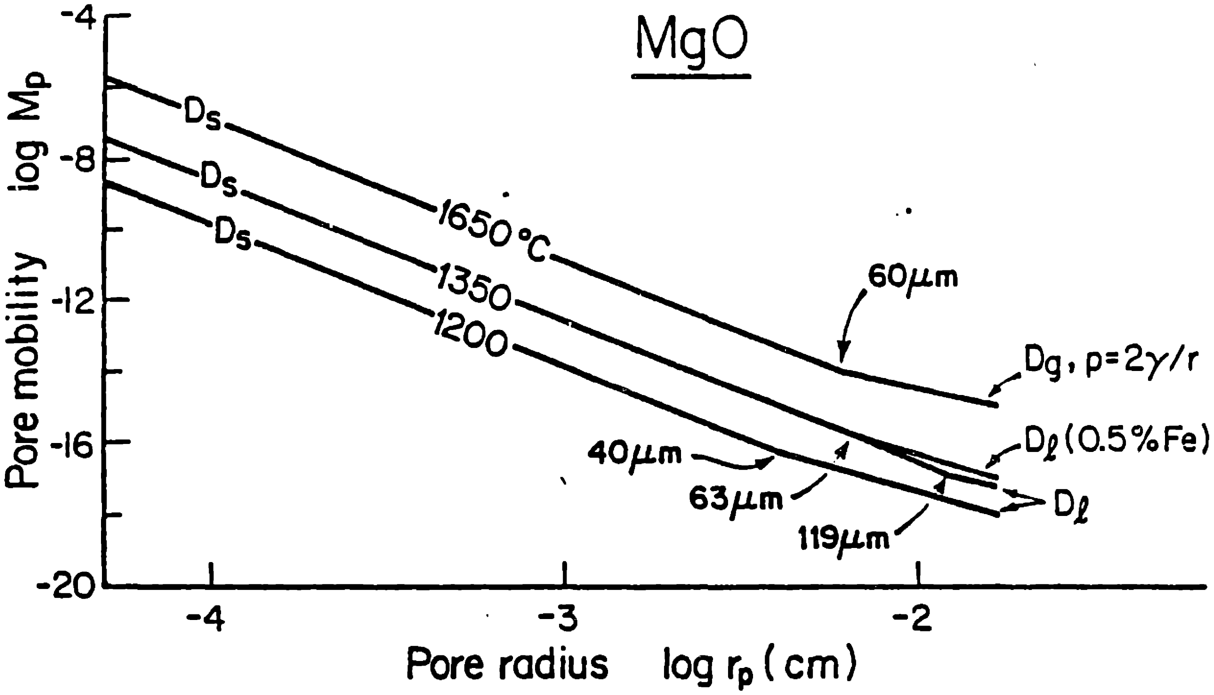

Figure II-1 (a) Pore mobility as a function of pore radius and mobility controlling mechanism at 1200°, 1350°, and 1650°C. (Chowdry et al.)

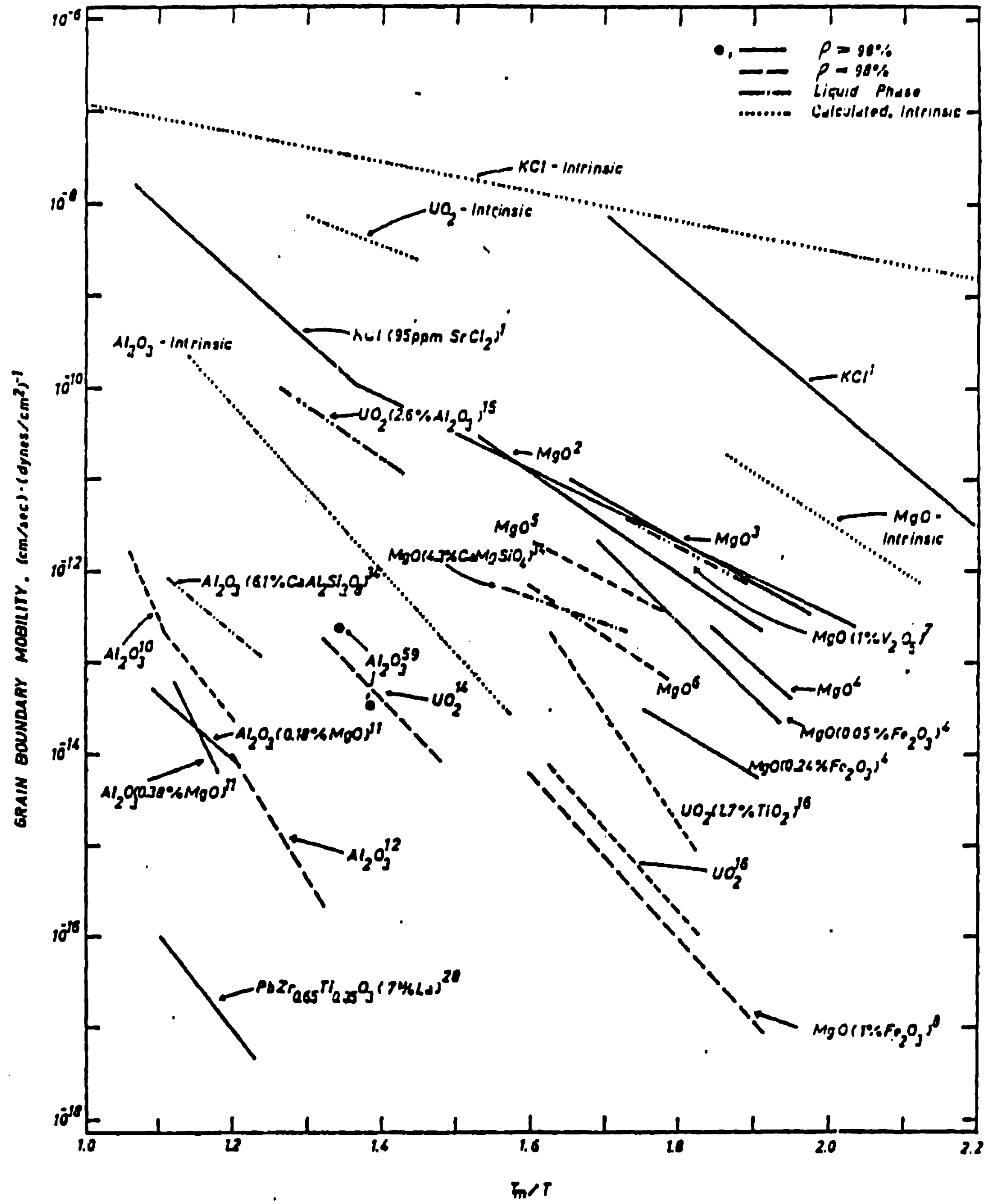

Figure II-1 (b) Grain boundary mobility as a function of temperature for a range of materials (from Yan et al., 1976).

Table II-1

Data for Pore-Boundary Separation and Sintering-Grain Growth Calculations

Diffusivity Data		
wDs (grain boundary grooving in air)	6.9×10^{-3} exp(-90 kcal/RT)(cm^3/sec)	Robertson (1967)
D_{ℓ}^{Mg} (tracer in Ar)	4.19×10^{-4} exp(-63.5 kcal/RT)(cm^2/sec)	Wuensch, Steele, and Vasilos (1973
+0.53% Fe (creep)	1.04×10^{4} exp(-117 kcal/RT)	Tremper et al. (1974)
+2.65% Fe (creep)	5.06×10^{4} exp(-117 kcal/RT)	Gordon (1975)
D^{Mg} (creep of undoped)	3.6×10^{-13} cm^2/sec at 1620 K	Hodge and Gordon (1978)
δD_b^{Mg} (creep of undoped)	$<10^{-18}$ cm^3/sec at 1620 K	Hodge and Gordon (1978)
+0.53% Fe (creep)	$2.13 \overset{x}{z} 10^{-8}$ exp(-55.8 kcal/RT)	Gordon (1975)
δD_b^{o} + 0.53% Fe (creep)	1.06×10^{-6} exp(-55.8 kcal/RT)	Gordon (1975)
Vaporization Data		
MgO(s) Mg(g) + 1/2 O_2(g)	$p_{Mg} = 3.15 \times 10^{-9}$ atm at 1620 K, 0.2 atm O_2	Altman (1963)
Boundary Mobility Data		
$M_{intrinsic}$	1.21×10^{-11} cm/sec/dyne/cm^2	Gordon et al. (1970)
+0.05 cation % Fe	4.64×10^{-14}	Gordon et al. (1970)
+0.25 cation % Fe	6.75×10^{-15}	Gordon et al. (1970)

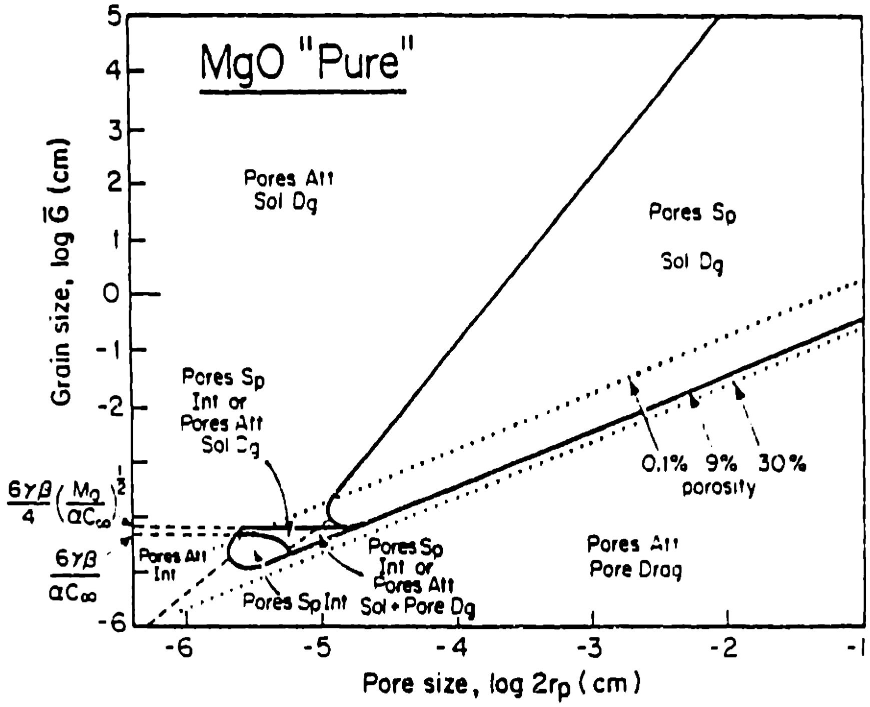

Figure II-2 (a) The pore-boundary interaction map for a wide grain size distribution for 'pure' MgO at 1350°C.

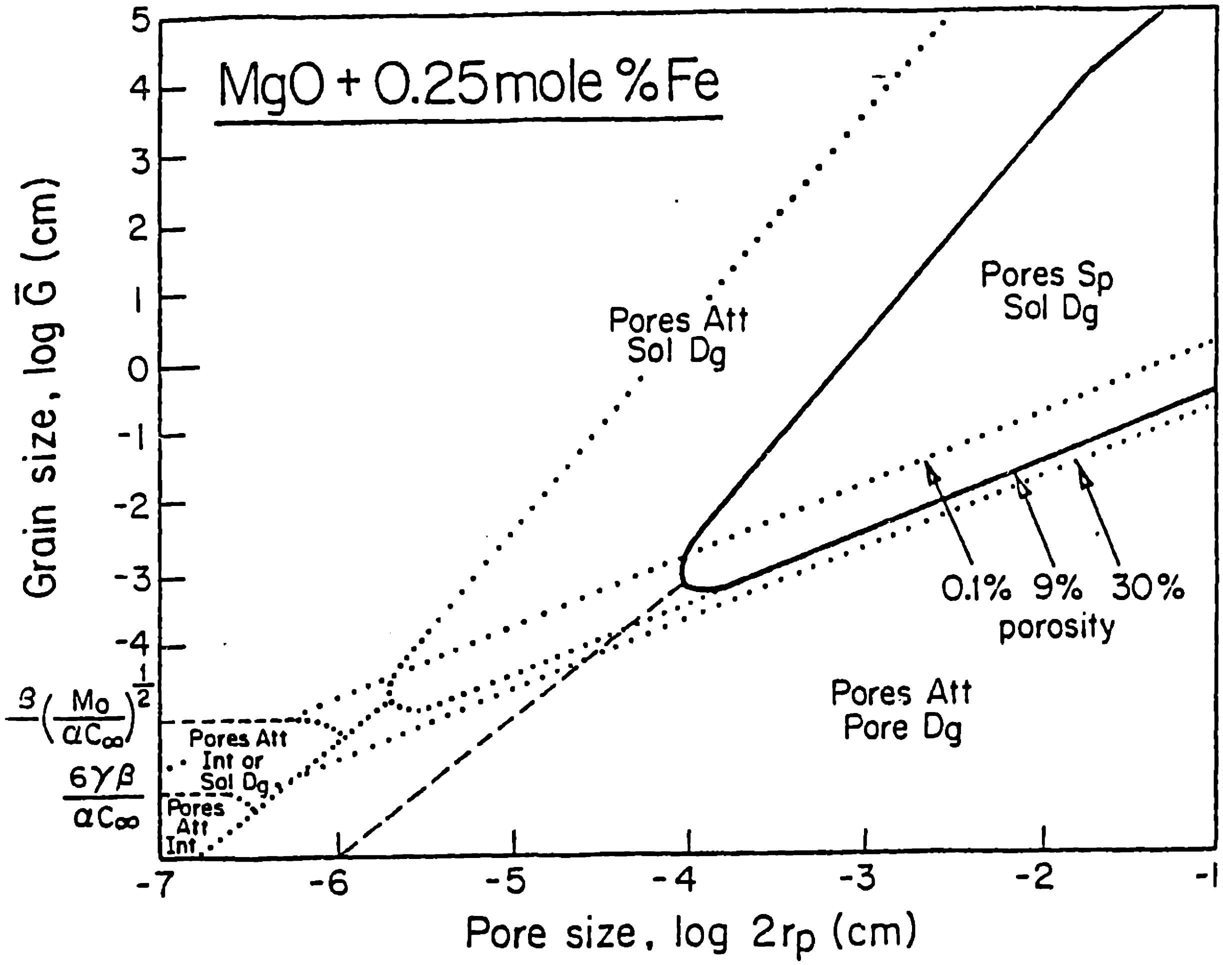

(b) The pore-boundary interaction map for a wide grain size distribution for Fe-doped Mgo at 1350°C.

In the analysis of Hsueh (1982) for the pore velocity as a function of the dihedral angles, the steady-state pore velocity for a pore with $\psi = 60^o$ on a grain face was greater by a factor of 11.6 than a spherical pore with the same initial in-boundary radius. With a decrease in dihedral angle, the pore size at which separation occurs increases for a given grain size. This type of analysis is not easily applied to more complex pore-grain geometries, such as pores at 4-grain corners.

The simultaneous sintering and coarsening relations for MgO were calculated using equations as listed in Table A1-1. The sintering rates of "typical" purity MgO due to grain boundary and lattice diffusion during final stage were compared using the Coble sintering models and the data in Table II-1. The change in spherical pore size with time at constant grain size is:

$$\frac{dr}{dt} = -\frac{22}{6}\,\frac{\delta D_b^{Mg}\Omega\gamma_s}{kTr^3} - 2\,\frac{\delta D_\ell^{Mg}\Omega\gamma_s}{kTr^2} \qquad \text{(II-1)}$$

Using the magnesium boundary and lattice diffusivities at 1623 K, Mg grain boundary diffusion is predicted to control shrinkage for pore radii less than 10 μm. At this temperature, oxygen grain boundary diffusion is about a factor of 50 greater than magnesium grain boundary diffusion. For high-purity MgO, the diffusivities are not known. As listed in Table II-1 there is a value for δD_b^{Mg} at 1623 K for undoped MgO (∿ 100 ppm) which is orders of magnitude lower than the data for the lower purity material. This limiting value was calculated from creep of undoped MgO undergoing substantial grain growth (Hodge and Gordon, 1978).

Using this single δD_b^{Mg} value and D_ℓ^{Mg} for "normal" purity MgO, Equation (II-1) can be evaluated. It was calculated that at $r_p < 0.01$ μm, sintering is controlled by grain boundary diffusion; at $r_p > 0.01$ μm, sintering is by Mg lattice diffusion.

Although no surface diffusion data are available for high-purity MgO, the surface diffusion data for the lower purity material were used to allow some estimation of shrinkage and coarsening. The calculations are presented in Appendix I. At 1623 K and 1673 K, the values for the coarsening parameter, Γ, for normal purity MgO are 0.15 and 0.20, respectively. This implies that the material will sinter without significant coarsening. The times to close 1 μm pores on grain boundaries are 1.3×10^5 sec (35 h) and 8.5×10^4 sec (25 h) for 1623 K and 1673 K, respectively. For higher purity MgO with smaller pore sizes ($r_o < 0.01$ μm) grain boundary diffusion is predicted to dominate coarsening. In this case, the coarsening parameter is large, $\Gamma = 107$, indicating significant coarsening but little densification before the transition to lattice diffusion controlled densification occurs. This transition in densification mechanism corresponds to a vertical line on the $\overline{G}$-$2r_p$ diagram for 1623 K. For higher purity MgO densifying by lattice diffusion, $\Gamma > 1$ for a pore size below a critical size, r_p^* determined by the ratio of the controlling diffusivities. As shown in the calculations in Appendix I, $r_p^* = 1.5$ μm and $r_p^* = 1.9$ μm at 1623 K and 1673 K, respectively.

Because it is assumed that the microstructure is described by Equation (I-9), lower limits for pore size and grain size at a given density exist for which densification is significant compared with coarsening/grain growth. At $v_f = 0.20$ and $r_p^* = 1.5$ μm, $\overline{G}^* = 9.3$ μm. At $v_f = 0.005$ and $r_p^* = 1.5$ μm, $\overline{G}^* = 32$ μm. As shown in Appendix AI the time dependence of the pore size for $\dot{v}_f(D_l)$ and $\dot{G}(wD_s)$ case is not as simple as the situation where $\dot{v}_f(D_b)$ and $\dot{G}(wD_s)$

The preceding calculations were based on pore mobility-controlled coarsening. If grain growth/coarsening is controlled instead by the grain boundary mobility, the microstructure evolution ($\overline{G}$, $2r_p$ trajectory) will be different and the time to retain a specific density from an initial microstructure (v_o, $\overline{G}_o$, $2r_{p,o}$) will decrease.

For MgO powder of "normal" purity, compacted to high green density wit- near-ideal packing, the sintering/coarsening analysis predicts sintering to high density ($\Gamma < 1$). The calculated values of Γ for "normal" purity MgO are not much less than 1. Changes in the sintering geometry or in the diffusivities (by a factor of ten) can lead to $\Gamma > 1$ and coarsening will be predicted to dominate microstructure evolution. For MgO powder of high purity, identically compacted, the microstructure will coarsen to $r \sim r_p^*$ and $G \sim G^*$ at 1623 K and 1673 K regardless of the starting pore size and grain size (up to $r_o \sim r_p^*$ and $G_o \sim G^*$).

Because of the geometrical approximations of this model and the sensitivity to small changes in diffusivities, these calculated values of Γ are used to suggest trends rather than predict specific r and G values.

The calculated values of Γ and d ln G/d ln r are compared with sintering/coarsening data for "normal" purity MgO in Chapter II and for high-purity MgO in Chapter III.

II.2 Sintering and Grain Growth Experiments

In this chapter, two sample types are described which were prepared from two powder precursors and formed using two different processing techniques. The first experiment to determine breakaway conditions was performed using hot-pressed and annealed $Mg(OH)_2$-derived undoped and Al-doped MgO samples. A constant valence ion, aluminum, was added to MgO to change the grain boundary mobility by solute drag. Kingery et al. (1976) determined that Al segregates to boundaries in MgO. Chiang (1981) determined that Sc^{3+}, (an ion similar in size and solubility to Al^{3+}), Ca^{2+}, and Si^{4+} segregate to MgO grain boundaries up to 3 nm away from the boundaries. (Samples without Ca and Si were not available.) The second set of experiments for breakaway determinations used sintered, $MgCO_3$-hydrate-derived MgO samples prepared by settling sized powders. Hot-pressing was chosen initially to produce samples with narrow grain size distribution and densified to the closed pore stage. Sintering was later chosen to avoid the bloating problems associated with annealing hot-pressed samples.

II.2.1 $Mg(OH)_2$-derived MgO

II.2.1.1 Experimental Procedures

Magnesium oxide was prepared by the hydrothermal conversion of 99.99% Mg metal turnings* into $Mg(OH)_2$ in saturated steam at a temperature of 620 K

---

*Atomergic Chemetals Corp., Plainview, N.Y.

and pressure of 16.3 MPa. The reaction is exothermic so that the vessel temperature rose above 1250 K. To avoid thermally shocking a ceramic crucible, a stainless steel crucible was used for transforming the standard batches of 20g Mg. The processing parameters to produce single phase $Mg(OH)_2$ from the autoclaving of Mg were provided by Dr. R. Tremper* and Dr. A. F. Henriksen**. This process for powder production was originally chosen by Dr. Henriksen for a study of the solubility of Al in MgO (1978). The solubility of Al in MgO as a function of temperature is shown in Figure II-3. The same powder processing variables were chosen for this study because of the known solubility limits.

The hydrothermal conversion process produces hexagonal platelets (<1 μm wide) agglomerated into a wide distribution of agglomerate sizes. The specific surface area of the $Mg(OH)_2$ was ∿ 11 m^2/g. The hydroxide powder was suspended in methanol and deagglomerated by placing the hydroxide methanol mixture in an ultrasonic bath for 1 h.

The Al concentrations chosen for this study were ∿500 ppm and 1000 ppm, cation basis, which are 1/6 and 1/3 the solubility limit at 1670 K. The Al-dopant, $Al(OC_3H_7)_3$***, was dissolved in trichloroethylene and added dropwise to the stirred $Mg(OH)_2$-methanol suspension. The "pure" and Al-doped powders were air-dried at 320 K for 24 h and transformed to the oxide at 1270 K in air for 2 h. Phase analyses by x-ray diffraction of the hydroxide, and the "pure" and doped calcined powders indicated that all were single phase.

---

*General Electric Co., Cleveland, Ohio.

**M.I.T.

***Alfa-Ventron Corp., Danvers, MA, Chemical Assay 99.9%, Metallic Assay 6N.

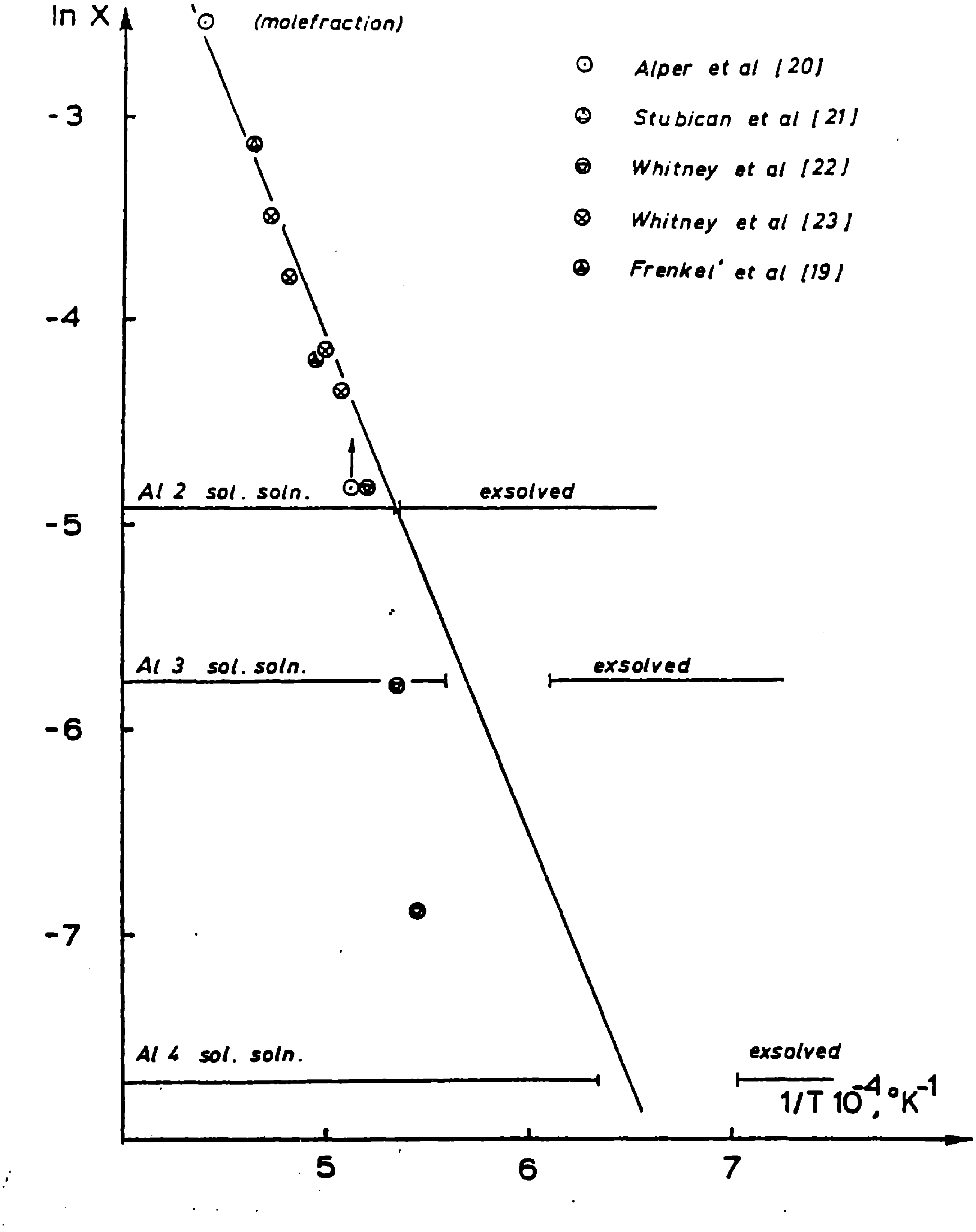

Figure II-3 Solid solubility of Al in MgO as a function of temperature as determined by Henriksen (1978).

The specific surface areas of the "pure" and Al-doped oxide powders are ∿40 m^2/gm and 10 m^2/gm, respectively. The semi-quantitative chemical analyses of one "pure" and one Al-doped powder are listed in Table II-2. Chemical composition, both with regard to background and Al-dopant levels, vary from sample to sample.

The hydroxide-derived powders were ground using a mortar and pestle and vacuum hot-pressed into disks of >90% ρ_{th} and approximately 0.5 cm high in a 5 cm diameter graphite die. The graphite was lined with graphite foil, preannealed in vacuum at 1700 K. The pressing temperature was measured by optical pyrometry.

The surface of the hot-pressed disks were ground on coarse SiC paper to remove adhering graphite foil and were annealed at 1300 K in air for 24 h to oxidize the surface carbon. The hot-pressed disks were cut into cubes of approximately 5 mm and divided according to the region of the disk from which they were cut. The samples from the center of the disks were annealed to an alumina tube resistance furnace; temperature was controlled to $\pm 10^{o}$C. The heat-treatments were performed at 1670 K in air or O_2 for various times up to 184 hours.

Densities of annealed samples were measured before sectioning by the Archimedes method. The samples were mounted in epoxy, ground using SiC paper (200 to 1000 grit), and polished with 0.25 μm diamond paste. The fraction porosity and the average pore size and pore size distribution were determined from photographs of the polished but unetched samples using automati

Table II-2

	MgO from $MgCO_3$ (Mg turning)[1]	Al-doped MgO[2]	MgO from $Mg(OH)_2$ (Mg turnings)[3]	Mg turnings[4]
Ag*	VFT	--	--	--
Al	VFT-FT	FT	VFT-FT	VFT-FT
B	--	FT	FT	--
Be	VFT	--	--	--
Ca	FT	FT	FT	FT
Cu*	VFT-FT	VFT-FT	VFT	VFT
Fe	FT	VFT	FT	VFT
Mn	FT	FT	FT	VFT-FT
Mo*	FT	FT	FT	--
Pb	VFT-FT	VFT	--	--
Pt*	FT	FT	FT	--
Si	FT-T	FT-T	FT	FT
Sn*	VFT	--	--	--
Sr	VFT	--	--	--
Ti	VFT-FT	--	--	VFT

<u>Key</u>: VFT - 1-10 ppm by weight

FT - 10-100 ppm by weight

T - 100-1000 ppm by weight

[1] MgO described in Appendix ; MgO-2

[2,3] MgO described in Section II. ; MgO-1

[4] Source of Mg for 1,2, and 3

Sporatic contamination during sample preparation for chemical analysis quantitative metallography. The polished sections were etched in a solution of $HCl:H_2O$ (10:1). Concentration HCl was determined by Hamano and Kamizono (1977) to etch MgO grain boundaries but not dislocations. The average grain size, $\overline{G}$, was determined from the average line intercept, $\overline{\ell}$, where $G = 1.5\overline{\ell}$. Grain size distributions were measured from photographs of fracture surfaces of the lower density hot-pressed compacts.

The polished surfaces were examined for evidence of pores entrapped within grains. In areas of uniform density, microstructures were classified as either having or not having pores entrapped. Only in uniform regions were average pore sizes and grain sizes categorized according to a "yes-no" classification of entrapment. These data were used to construct breakaway maps.

II. 2.1.2 Results

Micrographs of polished surfaces of the undoped and Al-doped MgO samples are shown in Figure II-4. Although the as-hot pressed disks were $\gtrsim$90% of II-4 theoretical density, all samples have large, well defined bands of different densities. The lower density bands characterized by open proposity were grey after hot-pressing and remained grey during subsequent annealing at 1670 K. After additional heat-treatment, these density gradients persist; they are evident in the microstructures of multiple samples annealed at the same temperature and times. Superimposed on this large, but local density variation is a variation in grain size, pore size, and density due to the action of the die and the non-uniform temperature gradient during hot-pressing.

---

*Magiscan, Joyce-Loebl Ltd., Gateshead, U.K.

Figure II-4 SEM and optical micrographs of hot-pressed Mg(OH)$_2$-derived MgO: (a) undoped MgO; (b) MgO with 500 ppm Al; and (c) MgO with 1000 ppm Al after various annealing times at 1673K.

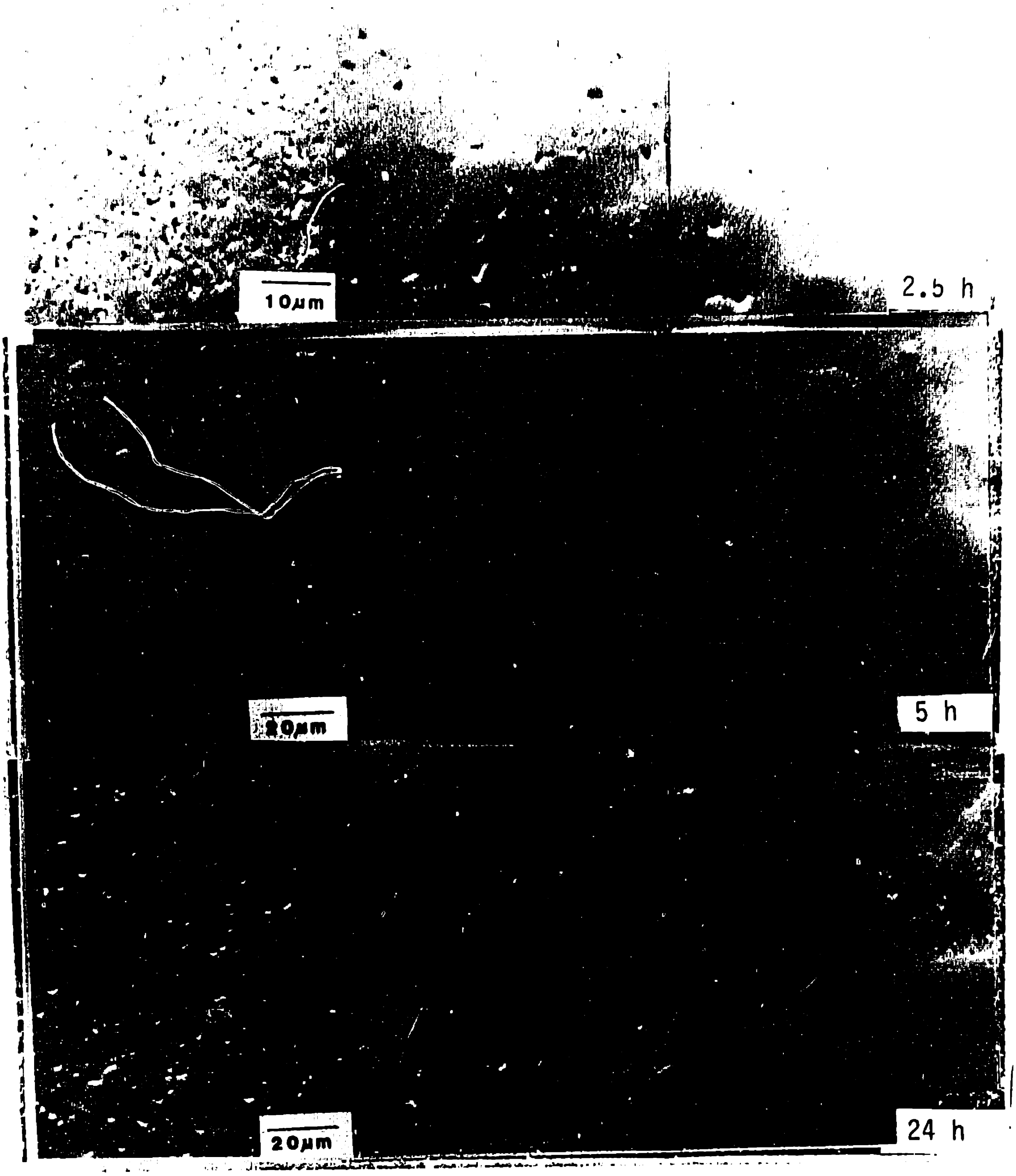

(b)

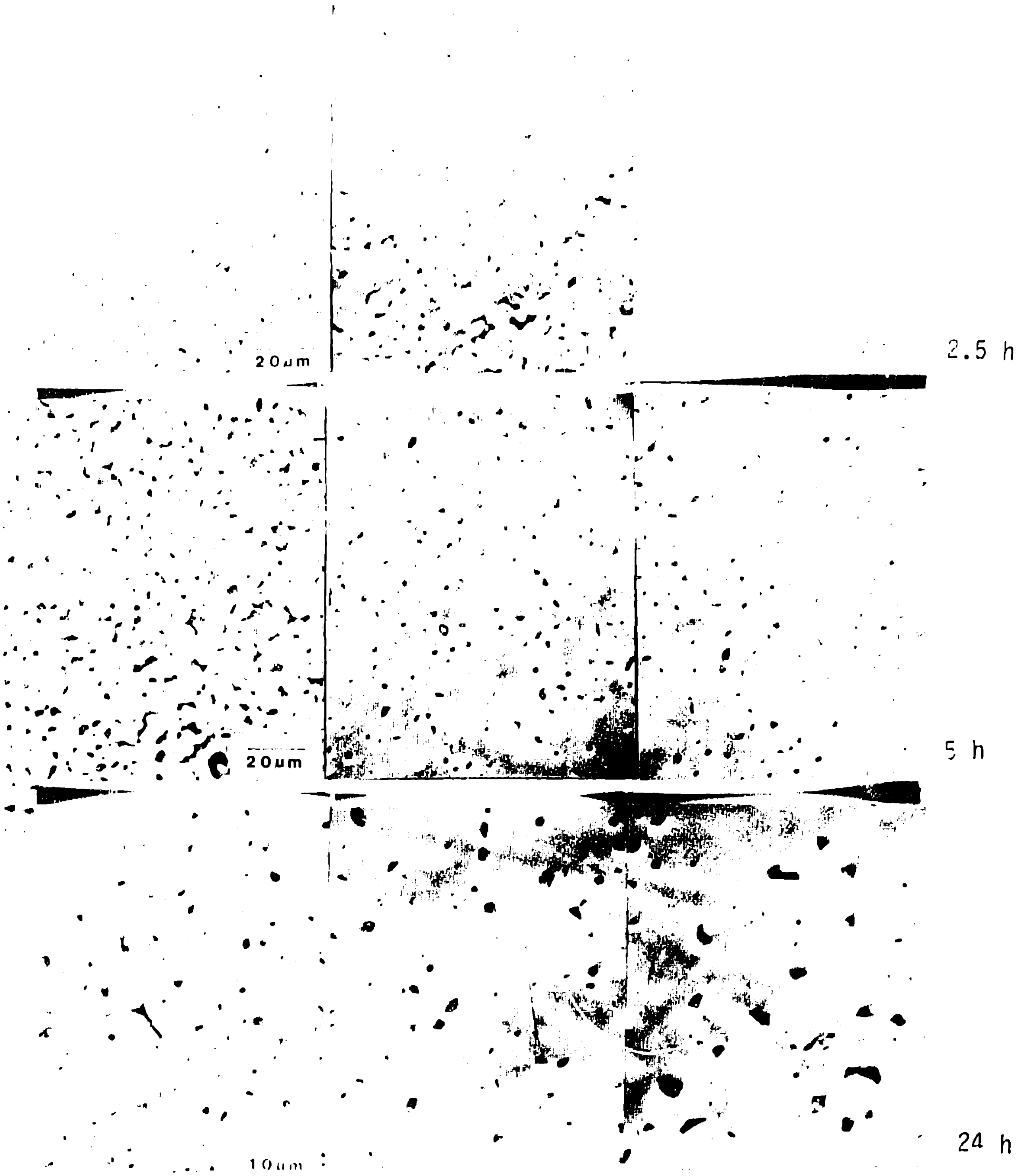

(c)

No systematic changes in the mean grain size, density, and number of pores per area for various samples nor in grain size distributions were noted with increasing time at 1670 K.

An examination of a fracture surface of hot-pressed samples by Auger spectrosocpy showed elemental carbon (graphite) present at the grain boundaries. Ion sputtering of the surface removed the elemental carbon. Due to C contamination from the graphite die, the microstructural evolution is probably affected by gas evolution (CO, CO_2) during annealing in air; the magnitude of the effect is not known.

The gross density variations precluded any kinetic analysis. Only local area analysis of pore:boundary breakaway was possible for these "pure" and Al-doped samples. These boundary breakaway data are presented in Figure II-5(a) and (b).

II 2.2 Discussion

Before the results of this final stage sintering study are discussed, the results of a STEM study by Chiang (personal communication) of grain boundary segregation in the Al-doped MgO samples are presented. Typical TEM microstructures of the Al-doped MgO samples are shown in Figure II-6 (a)-(C). Large microstructural and compositional variations were observed that were not seen by optical microscopy or SEM. Some triple points were precipitate- and pore-free; others contained a glassy phase, a crystalline second phase, or pores. In addition, solute segregation of Al, Si, Ca, and Ti to MgO boundaries was observed at different ratios and different total levels from boundary to boundary, as illustrated in Figure II-6(b) and (d).

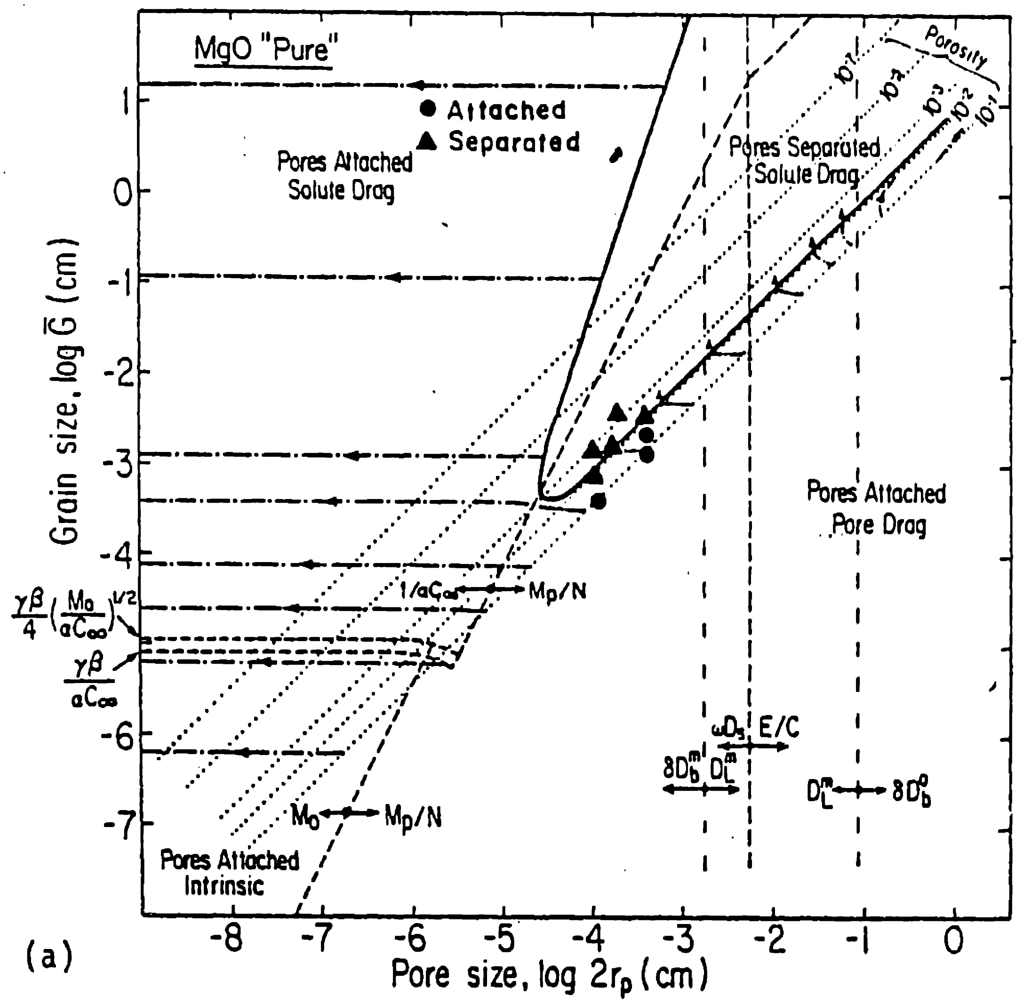

Figure II-5 Grain size-pore size data for boundary-pore attachment and separation plotted on interaction maps for a narrow grain size distribution: (a) undoped MgO; and (b) MgO with 500 ppm Al.

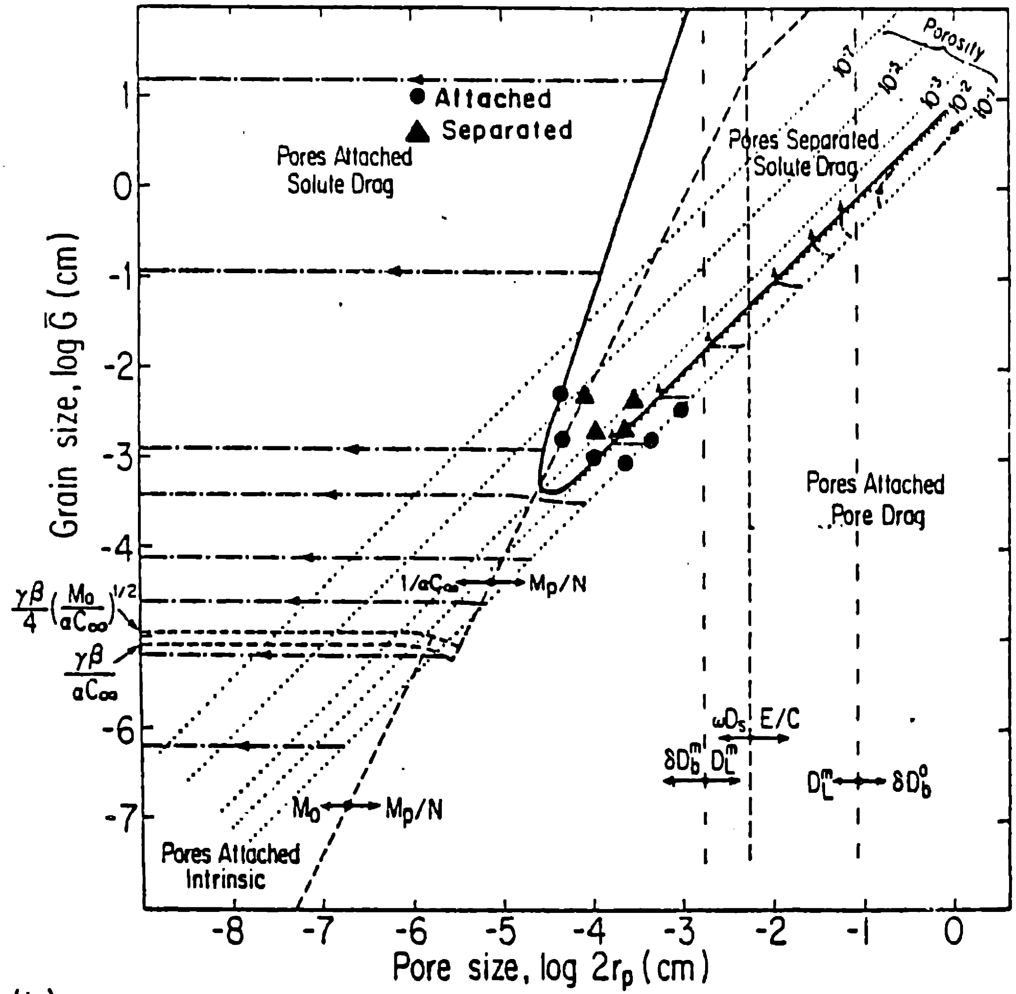
● Attached
▲ Separated
Pores Attached
Solute Drag
Pores Separated
Solute Drag
Pores Attached
Pore Drag
Pores Attached
Intrinsic
Porosity
10^{-1}
10^{-2}
10^{-3}
10^{-2}
10^{-1}
$1/aC_\infty \leftrightarrow M_p/N$
$M_0 \leftrightarrow M_p/N$
$\frac{\gamma\beta}{4}\left(\frac{M_0}{aC_\infty}\right)^{1/2}$
$\frac{\gamma\beta}{aC_\infty}$
ωD_s
E/C
δD_b^m
D_L^m
$D_L^m \leftrightarrow \delta D_b^0$
Grain size, log $\bar{G}$ (cm)
Pore size, log $2r_p$ (cm)
1
0
-1
-2
-3
-4
-6
-7
-8
-7
-6
-5
-4
-3
-2
-1
0

(b)

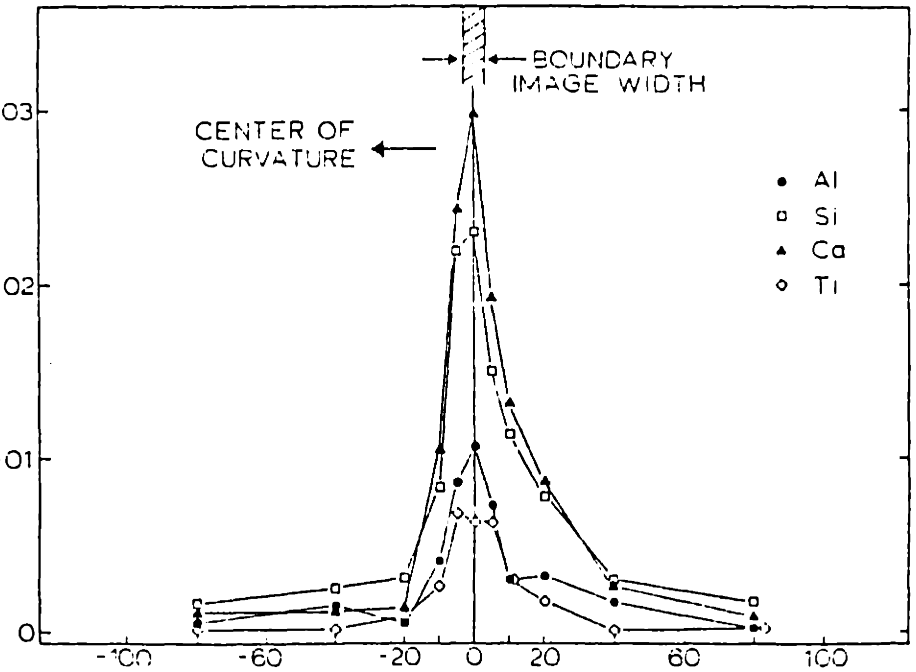

(a) STEM profile

(b) Boundary for (a)

Figure II-6 STEM segregation profiles and bright field micrographs of areas from which profiles measured. Samples are hot pressed Al-doped (1000 ppm) MgO annealed at 1670K for 72h.

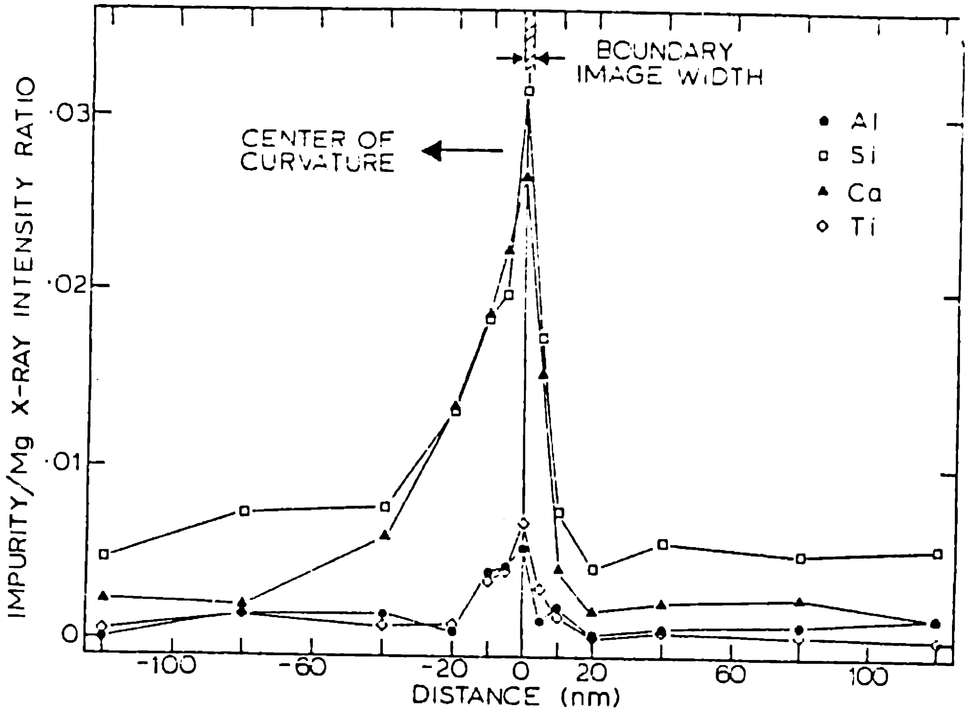

(c) STEM profile

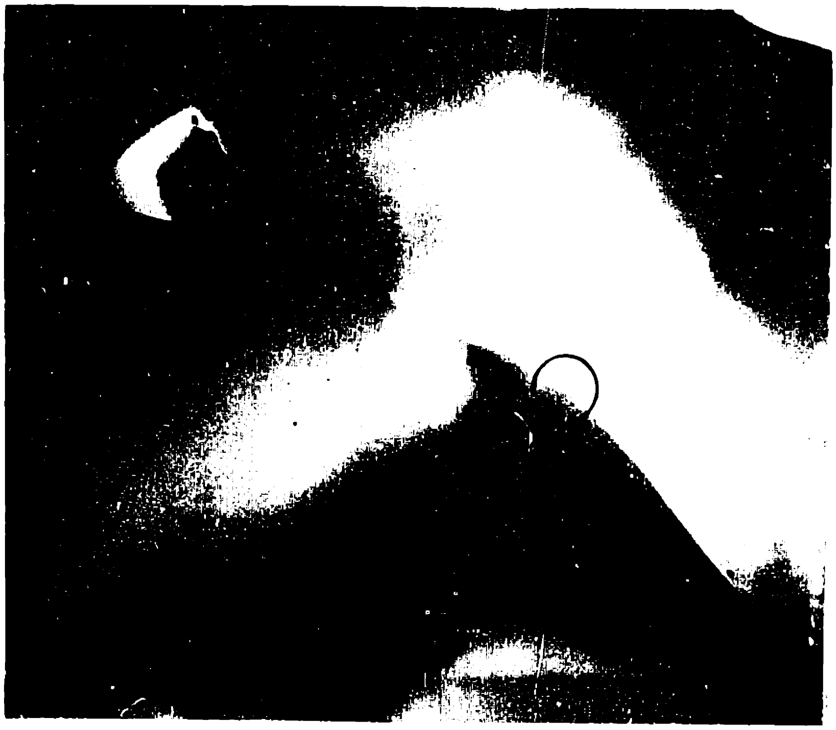

(d) Boundary for (c)

sizes of pores) and grain size. These regions were excluded from the measurements.

The data from which the plots in Figure II-5(a) and (b) were calculated were gathered on samples of high background impurity levels, perhaps similar to the samples examined here. As described in Section II.1, the data needed for these analyses are diffusivities (D_g, δD_s, D_l) and grain boundary mobilities for undoped and doped MgO). In this analysis it was assumed that oxygen boundary diffusion of oxygen diffusion through a vapor phase is sufficiently fast to make magnesium transport rate-limiting. The Mg lattice diffusivities from ^{26}Mg tracer measurements on single crystals containing at least 300 ppm impurities (possibly up to 2000 ppm) (Wuensch, et al. 1973) and from creep of LiF-doped MgO (total impurities not measured) (Hodge and Gordon, 1978) were 1.3×10^{-12} and 1.5×10^{-12} cm^2/sec, respectively, at 1623 K. The two sets of ωD_s data from thermal grooving in air of exposed MgO surfaces of unspecified composition are also similar (Robertson, 1967); Henney and Jones, 1968). The grain boundary mobilities for undoped and Fe-doped MgO were calculated from grain growth studies of hot-pressed MgO and magnesiowustite (0.10 and 0.48 wt % Fe_2O_3) (Gordon, et al. 1970). While the nominal composition of the as-hot pressed MgO was 99.99+% Mg, cation basis, no special procedures were employed to maintain the low level of cation impurities and, therefore, contamination was probable (see Chapter III). In this study, chemical compositions of the undoped samples prepared from nominally 99.99+% MgO were found to vary from sample to sample but, generally, contained 2500 ppm (by weight) total cation impurity, predominantly Si, Ca, Fe, and Ti. The Ti contamination was found by Chiang using STEM analysis but not using semi-quantitative emission spectroscopy.

There exists a window of measurable pore sizes and grain sizes on the attachment-separation map due to the limits of resolution of SEM and optical microscopy and to the size of the uniform density regions. The resolution limit is ∿ 0.5 μm with optical microscopy. However, the practical limit varies from microstructure to microstructure. For example, pores of 0.5 μm adjacent to 1 μm grains are difficult to resolve; well dispersed 0.5 μm pores adjacent to 10 μm grains are easier to identify and measure. The resolution limit of SEM is much lower (∿0.01 μm); however, the good depth of field in SEM leads to a practical limit of ∿0.1 μm for pores. At pore sizes less than 0.1 μm and grain sizes less than 0.5 μm, little information on the microstructural evolution can be obtained. At small initial pore sizes and grain sizes, several cycles of normal growth and pore attachment followed by pore separation could occur without detection by optical microscopy and SEM. Therefore, the data presented here describe only a small part of the G-$2r_p$ space through which microstructures evolve. The upper limits of grain size and pore size in this study were determined by the gross density variation in the samples, caused by the powder type and the fabrication technique. In the undoped samples, the thickness of the high-density lenticular regions vary from 20 to 200 μm perpendicular to the pressing direction. In the Al-doped MgO samples, the lenticular regions are larger (40-500 μm) but also occur throughout the entire sample thickness.

The measurement limits for pore size ($2r_p$) and grain size ($\overline{G}$), 40 μm for $\overline{G}$, and 5 μm for $2r_p$ are drawn on the $\overline{G}$-$2r_p$ plot shown in Figure II-5 When the $\overline{G}$-$2r_p$ values in a compact sintered to intermediate-final stage fall into this range, the microstructural evolution can be determined.

In a study of intermediate and final stage sintering, Kamizono and Hamano (1978) determined the average pore size-average grain size and the pore location for ordered MgO hot-pressed at 1170 K and annealed at 1670 K. As shown in Figure II-7 the pore size-grain size ranges for pore attachment-separation overlap for the Kamizono and Hamano study and this study.

In a study by Vieira and Brook (1980) on fast firing of $MgCl_2 \cdot 6H_2O$ derived, undoped, and Al-doped MgO, coarsening but no sintering was observed. The powder particles were agglomerated cubes and contained 1600 ppm Cl. The deleterious effect of Cl on the sintering and hot-pressing of MgO has been observed by Leipold and Kapadia (1973). In the Virella study, the effects of Cl and the cuboid morphology dominated evidently the sintering behavior. The morphological effect is discussed in Section IV.3.2 in terms of the experimental and calculated values of grain boundary and surface energies in rock-salt structure materials.

The lenticular shape of the regions of different density is due to uniaxial deformation of agglomerates. Similar microstructural variations were found for undoped $Mg(OH)_2$-derived MgO by Rhodes, et al. (1972a, 1972b) and Henriksen (personal communication). No such gross microstructural variations were observed by Rhodes for hot-pressed or sintered samples of

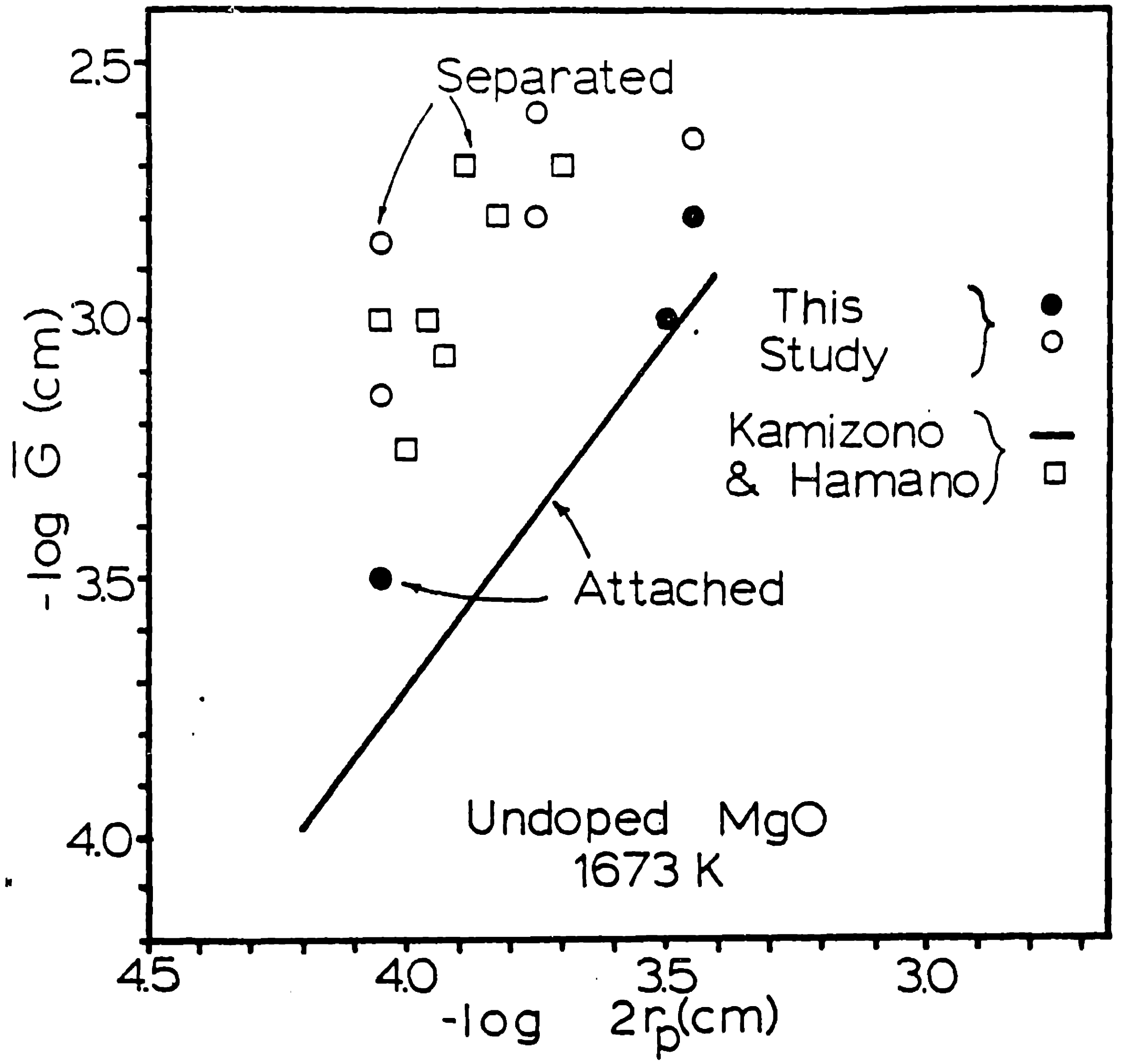

Figure II-7 Comparison of pore-boundary separation and attachment conditions from this study with data from Hamano and Kamizono (1978).

$MgCO_3$-derived MgO. With similar initial particle sizes, and crystallite sizes, the microstructures developed were uniform for the $MgCO_3$-derived MgO and duplex for $Mg(OH)_2$-derived MgO. This result was also obtained in this work.

In a recent study by Watanabe (1982), magnesium carbonate, sulfate fluoride, and oxalate powders were added to magnesium hydroxide, calcined at 1173 K, isostatically compacted and sintered at 1673 K. The additions of $MgSO_4 \cdot 7H_2O$ and $MgC_2O_4 \cdot 2H_2O$ led to duplex microstructure formation in MgO compacts at 1673 K similar to that observed in this study. In an earlier study, Leipold and Kapadia (1973) showed that additions of S, Cl, F, and OH to MgO decreased final hot-pressed density in the order $(\rho_{OH} > \rho_F > \rho_{Cl} \sim \rho_S)$. While it is suggested that the carbon from the hot-pressing die and sulfur from the grafoil or other local chemical differences may have induced the duplex microstructure formation, the cause of the microstructural inhomogeneity is undetermined.

II.2.2 $MgCO_3$ n-Hydrate Derived MgO

II.2.2.1 Experimental Procedures

The second set of experiments on low-purity MgO was performed using reagent grade, hydrated magnesium carbonate. The commercial process involves bubbling CO_2 gas through a magnesium nitrate aqueous solution*. The carbonate precipitate is hydromagnesite with an approximate chemical composition of $4MgCO_3 \cdot Mg(OH)_2 \cdot 4H_2O$. A quantitative chemical analysis

---

*J. T. Baker Corp.

by plasma-coupled emission spectroscopy* is listed in Table III-4. The physical and chemical properties of this powder in the carbonate and oxide forms are described in Chapter III and in greater detail in Handwerker, et al. (1982) and O'Connor (1982). The carbonate was transformed to the oxide by heating in air to 1270 K. The agglomerated oxide powder was suspended in methanol and ultrasonically deagglomerated at 100 watts (20KHz) for 4 min. The resulting particle size distribution is shown in Figure II-8 as measured by a Sedigraph**. The powder suspension was allowed to settle for 25 h and the remaining suspension was decanted. The particle size distribution of the decanted suspension ranged from 0.13 μm to 0.4 μm. The suspension was allowed to settle in a glass container and the alcohol was evaporated at 300 K to form a compact of approximately 60% ρ_{th}. The top surface of the as-cast sample is seen in Figure II-9. The term "top surface" refers to the side of the compact containing the last particles to settle by gravity and the "bottom surface" to the first part of the compact to form, therefore, containing the largest particle sizes. These designations correspond to particle sizes of 0.13 μm and 0.4 μm, respectively. The samples were heated at approximately 10^{0}/min to 1620 K, 1740 K, and 1870 K and annealed for times up to 170 h in O_2. The grain sizes and pore sizes on the top and bottom as-fired surfaces of the samples were measured. Fracture surfaces were examined to determine the amount of porosity through the sample thickness. "Yes-no" decisions of boundary breakaway were also made for these samples based on entrapped pores on free surfaces and on fracture surfaces.

---

*Union Carbide Corp.
**Sedigraph, Micromerities

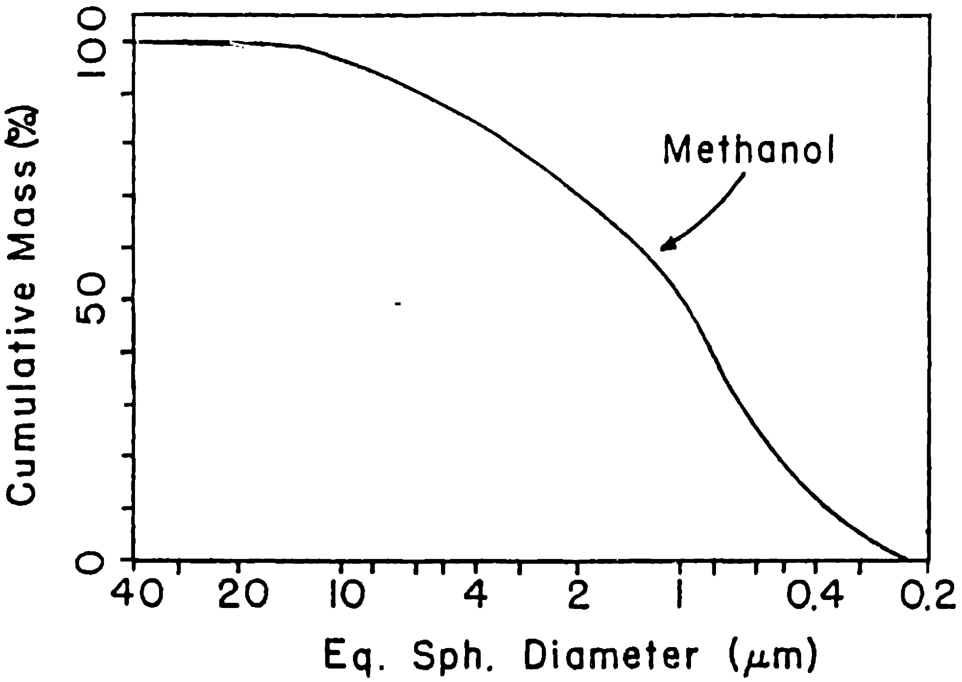

Figure II-8 Distribution of equivalent spherical diameters for deagglomerated, reagent grade, carbonate derived MgO.

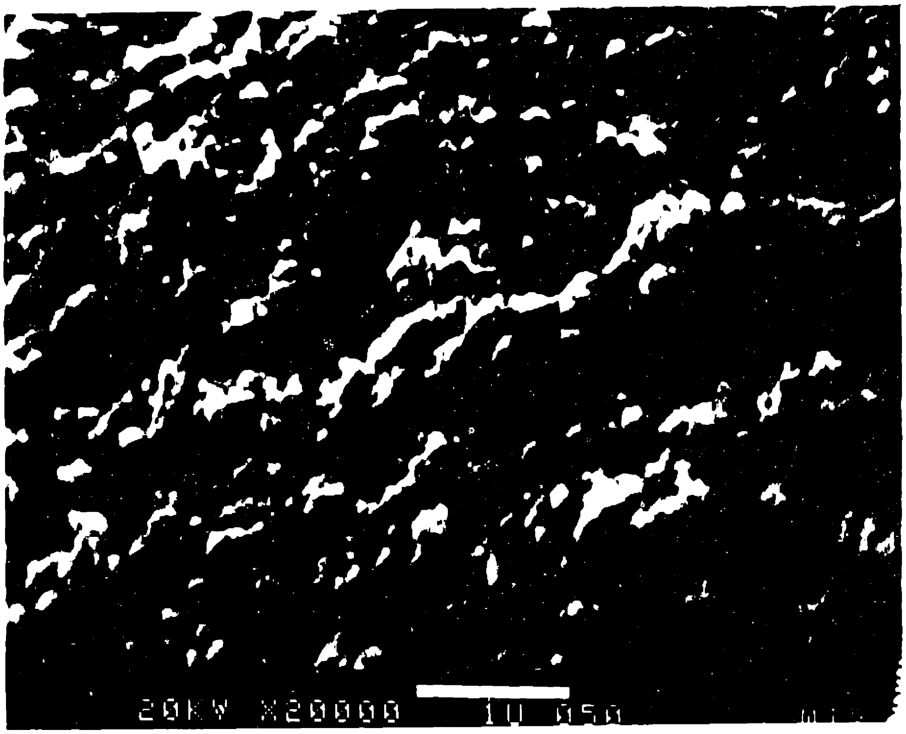

Figure II-9 SEM micrograph of the as-cast top surface of MgO compact.

II.2.2.2 Results

In Table III-3 are shown the initial particle sizes of the top (0.13 μm) and the bottom (0.4 μm) of the compact as calculated from Stokes equation and measured by SEM and the grain and pore sizes after annealing. Two regimes were observed: small grain and pore sizes with no observable pore separation and large grain sizes and intermediate pore sizes with pores attached predominantly to two-grain intersections. At 1620 K and 1740 K for times up to 4 h, no change in microstructure was observable by SEM. At 1620 K for 8 and 24 h, the samples had sintered to the closed pore stage and the grain sizes were similar: 0.7 μm (top surface) and 0.5 μm (bottom surface). The pore sizes were <0.2 μm for both surfaces. No pore separation from boundaries was observed. At 1740 K for 21 h, the average grain sizes of the compact were 28 μm (top) and 15 μm(bottom). Entrapped pores and pores at grain intersections were observed on the as-fired bottom surface but not on the as-fired top surface. Examination of the fracture surface through the compact thickness revealed entrapped pores through the thickness up to approximately one grain diameter from the top surface. At 1740 K for 170 h, the average grain sizes increased to 35 μm (top surface) and 30 μm (bottom surface). From 71 h to 170 h at 1740 K, $G_{max}/\overline{G}$ at the top surface changed from 2.5 to 4. The bottom surface showed entrapped pores and pores attached to 2- and 3-grain intersections. Along fracture surfaces of the 170 h, 1740 K sample, pores ranging from 3 μm to 0.4 μm were attached to all boundaries (7-25 pores per grain face); pores entrapped inside grains were

Table II-3

Grain Size-Pore Size Relationships in Settled and Sintered $MgCO_3$-Derived MgO

Grain Size (μm)

1620 K	t = 0	t = 4h	t = 8h	t = 24h	pores
top	0.13*	N.C.	0.7	N.C.	$r_p < 0.3 \mu m$
bottom	0.4*	N.C.	0.4	N.C.	
1740 K	t = 0	t = 71h	t = 170h		3-0.4 μm pores attached along grain faces; 0.8-0.4 μm pores within grains
top	0.13	28	35		
bottom	0.4	15	30		
1870 K	t = 0	t = 6h			0.3-0.1 μm pores attached along grain faces; entrapped pores on top and bottom surfaces
top	0.13	15			
bottom	0.4	15			

*from Sedigraph; in reasonable agreement with SEM

N.C. = no observed change from shorter annealing time smaller: 0.8-0.4 μm. At 1870 K for 6 h, the compacts sintered to the closed pore stage. The grain size was uniform through the sample and entrapped pores were observed in both top and bottom surfaces. Pores of $2r_p \sim 0.3$ μm were also attached to boundaries predominantly along 2-grain intersections with approximately 10 pores (>0.1 μm) per grain face.

II.2.2.3 Discussion

In the graded MgO samples examined in this study, the tendency toward pore separation from boundaries increased with increasing temperature and increasing initial particle size. At 1870 K, pore entrapment was evident on both as-fired surfaces (G_o = 0.13 μm, and G_o = 0.40 μm) and in the bulk. Pore attachment was evident on grain faces indicating reattachment during grain growth At 1740 K, pore entrapment was observed only on the (G_o = 0.40μm) surface. Pore reattachment to grain faces was observed through the sample thickness up to ∿ 10 μm from the top surface (G_o = 0.13 μm). At 1620 K, no pore separation was observed.

As calculated from the simultaneous sintering/coarsening expressions (Appendix I), the times at these temperatures to sinter pores associated with 0.13 μm and 0.40 μm grains are small at 1670 K, t ∿ 1 sec. This is obviously not the situation found for MgO-settled compacts. Coarsening is much greater than predicted from these models and the available diffusivity data.

Either the model or the data lead to an underestimation of the coarsening/sintering rates. Coarsening can be enhanced by poor particle packing in the green state, by decreasing the dihedral angle, or by increasing wDs. The powder size distribution was narrow and powder packing in these samples was good; $\rho_0 \sim$ 66-65%. It is suggested that a lower dihedral angle is the dominant factor. (Increasing wDs leads to the same calculated change in Γ as decreasing ψ.)

A rough estimate of the effect of dihedral angle on coarsening rate can be made from the results of Hsueh (1982). For $\psi = 90^0$, the pore velocity is a factor of 8 greater than the pore velocity for a spherical pore of the same in-boundary radius. As shown in Section IV, $\psi = 90^0$ is a typical average value for MgO sintered to final stage. Substitution of this factor into the expression for Γ yields $\Gamma > 1$ for 1623 K, 1743 K, and 1873 K. The calculated grain size-pore size trajectories are shown in Figure II-10 for (G_0 = 0.13 μm, r_0 = 0.028 μm, v_f = 0.40) and (G_0 = 0.40 μm, r_0 = 0.08 μm, v_f = 0.40). The pore separation map is for 1620 K only; the trajectories for 1740 K and 1870 K can be qualitatively used to estimate the breakaway conditions. At 1620 K neither trajectory intersects the primary pore separation region. At 1740 K and 1870 K the trajectories for (G_0 = 0.13 μm) intersect the pore separation region at larger grain sizes than the (G_0 = 0.40 μm) trajectories. At 1870 K, the difference in grain size at which pore separation occurs for (G_0 = 0.13 μm) and (G_0 = 0.40 μm) is small, leading to little difference in grain size through the compact. Pore reattachment at larger grain sizes occurred. This situation is not easily depicted in a "breakaway" diagram because of the more complex microstructural evolution.

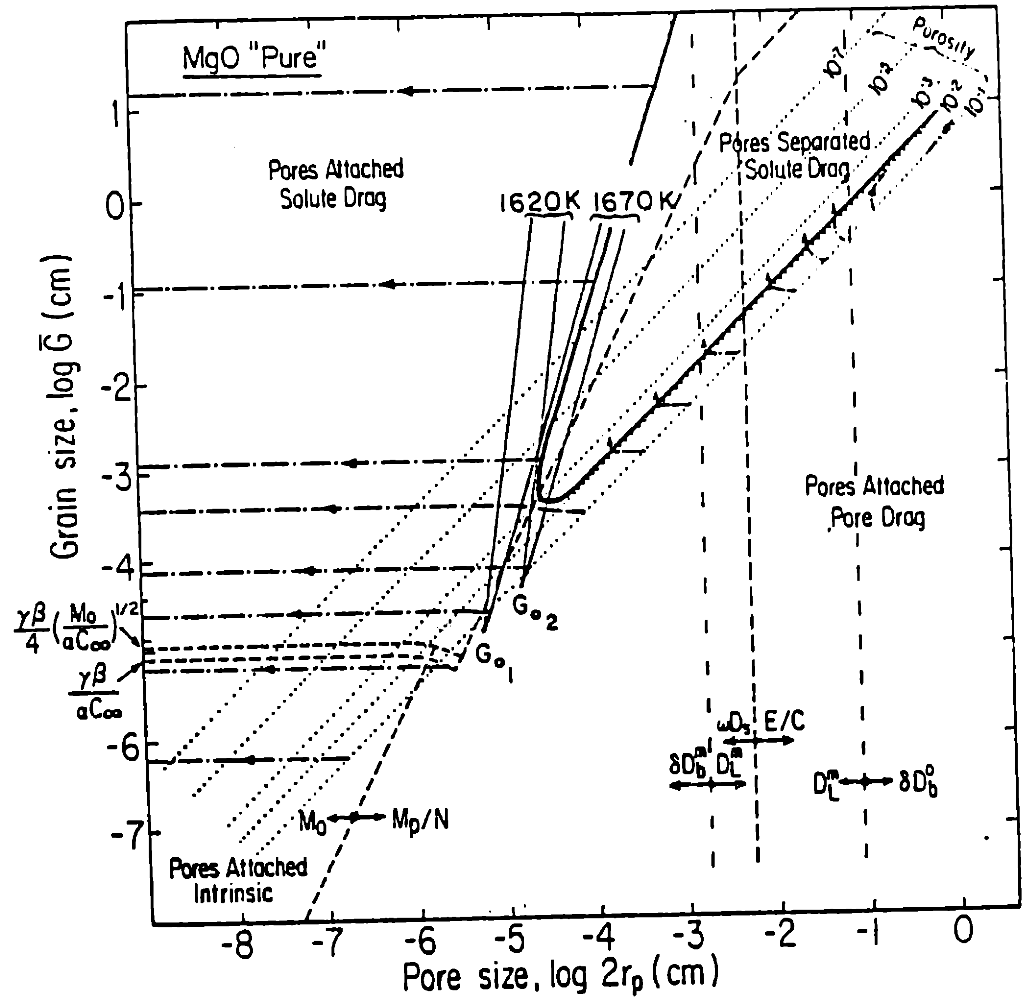

Figure II-10 Calculated trajectories of grain size-pore size during sintering of MgO.

The averages and the ranges of pore sizes and the average grain sizes after reattachment are plotted in Figure II-11 with pore growth data during grain growth in MgO (Gupta, 1973). Gupta determined the average pore size, grain size, and number of attached pores for isostatically pressed and sintered MgO undergoing coarsening-induced bloating. As in samples examined in this study, the microstructures examined by Gupta had many pores in two grain intersections and the pore radii varied by a factor of ∿10 along a single fracture surface. The smallest average grain size examined by Gupta was 9 μm (1823 K), indicating breakaway at smaller grain sizes. The grain sizes exactly at breakaway were not measured.

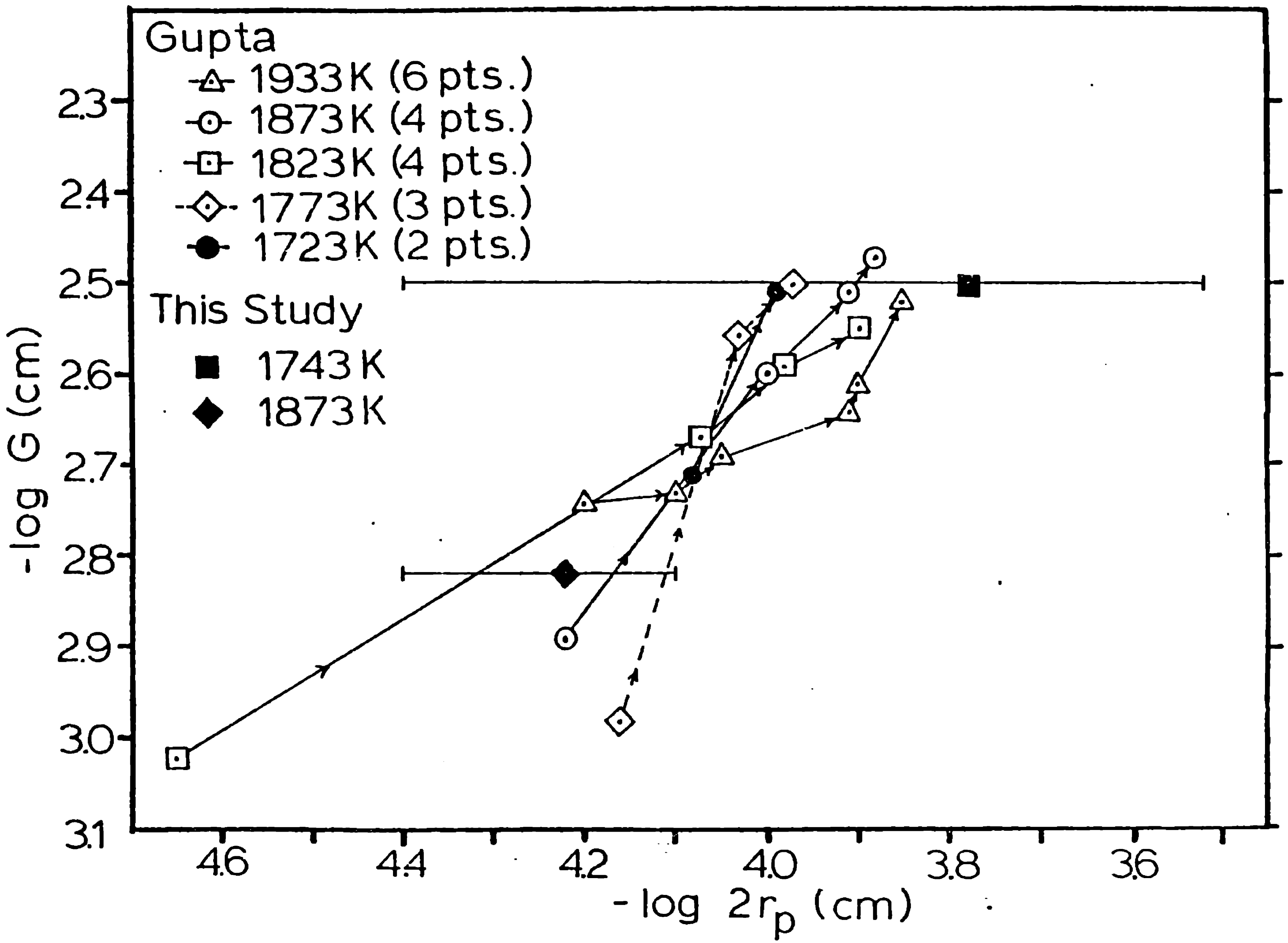

Figure II-11 Comparison of pore reattachment data from this study with data from Gupta (1971).

II.3 Conclusions

In hot-pressed and annealed samples of $Mg(OH)_2$-derived MgO, the pore sizes and grain sizes at which boundary separation from pores occured are in good agreement with the transition values calculated from literature data using the model of Cannon, Yan, and Chowdry. With Al additions, the pore sizes at separation increased relative to the separation conditions for undoped MgO, as expected from lower boundary mobilities due to the solute drag of Al.

For 'normal' (typical) purity MgO, sintering to theoretical density with negligible coarsening is predicted from the data with no boundary-pore separation at the experimental temperatures. Experimentally, this is not the case. An increase in the surface diffusivity by 10x or an increase in pore mobility by 10x would be in better agreement with the observed behavior.

Chapter III

High Purity MgO: Production, Sintering, and Grain Growth

III.1 Introduction

High purity was the primary criterion for materials selection for this set of sintering and grain growth experiments. There is considerable literature on the effects of high concentrations of dopants on kinetic processes in metal and ceramic systems. There is no information on the effects of low levels of total impurities--cations, anions, and organics in the bulk and on the surface--on the physical and chemical properties of ceramic materials. This has been due, in part, to a lack of samples of high initial purity with which to experiment.

The goals of this study were to prepare such a high-purity compact, and cation-doped compacts without changing background impurity levels for subsequent studies of grain growth and other kinetic processes. A high-purity magnesium carbonate precursor was prepared and the starting high purity was maintained to a great extent during the production of the oxide compact. Controlled doping of high-purity MgO powder with Ca and Al was also performed without changing the background impurity level. The cationic, anionic, and organic contamination was minimized by design of special procedures to be carried out under clean conditions. Each processing step was examined for its effect on the purity and the physical and chemical properties on the powder and the powder compact. Compacts were formed without plastic deformation by settling and evaporation of a narrow particle size MgO dispersion. The high-purity compacts were sintered at various times in air at 1670 K, 1740 K, and 1870 K. The sintering behavior of the high-purity material is compared with the sintering behavior of low-purity MgO, which was presented in the previous chapter. To obtain high-density samples for grain growth experiments, a few compacts were cold-pressed with high pressures and annealed at 1670 K, 1740 K, and 1870 K.

III.2 Powder Production and Compact Formation

III.2.1 Precursor Selection

In this study, total impurity levels-cations, anions, and organics were assessed at each processing step to minimize contamination. Even slight contamination can have dramatic effects on the kinetic processes, especially boundary migration. The magnitude of the effect of extremely low background cation concentrations on boundary migration in LiF has recently been assessed; in a study of secondary recrystallization, Glaeser, (1981.) found that the boundary mobility was often governed by sub-part-per-million levels of aliovalent cations or by unidentified anions rather than by MgF_2 additions of as much as 300 ppm. The effects of anions have only been measured indirectly through studies of hot-pressing, grain growth, and sintering in the presence of a high concentration of the anionic species. For example, the sintering of MgO was determined to be enhanced by ~24 mole % MgF_2 (Ikegama, et al., 1980) and by high partial pressures of H_2O (Hamano et al 1977). The effects of lower levels are not known.

Since the detection limit of anionic impurities is higher than the levels of interest (ppm), the verification of the removal of anions from a potentially contaminated material is difficult. The precursor was, therefore, chosen to minimize contact of the MgO with anions, such as Cl^- and S, and to allow purification with respect to cations to the ppm level. Only the cation concentrations were measured.

Residual organics on the surface, or carbon, or hydroxyls, on the surface and/or dissolved in the bulk, can produce an insoluble gas during heat-treatment. Bloating/desintering is sometimes observed in reannealed polycrystalline bodies formed by solid-state sintering and is often found in bodies produced by hot-pressing, as described in Chapter II and Appendix II. Ketcham (1981) observed that the density of hot-pressed ThO_2/ZrO_2 compacts decreased from >99% of theoretical to less than 80% upon annealing in air at high temperature. Annealing the hot-pressed samples in CO/C environments produced no bloating. Musikant, et al. (1971) observed a small CO_2 absorption peak in the IR spectra of partially stabilized ZrO_2 sintered to closed porosity in air.

An extreme example of carbon contamination has been noted by Freund, et al. (1980) for arc-fused single crystal MgO (99.99% Mg-cation basis) which contained approximately 900 ppm H and 300 ppm C. This suggests that carbon and hydrogen could also remain after transformation to the oxide from C- and H-containing precursors such as carbonates, oxalates, and hydroxides. In this study, the amounts of retained ^-OH or C and other adsorbed species associated with each processing step were monitored by the weight loss (TGA) during heating to 1270 K, the DTA temperature scan during heating to 1770 K and by specific surface area measurements. No absolute measurements of the H or C content were performed. In a companion study by O'Connor (1982) and in a report by Handwerker, et al. (1982), are more detailed descriptions of the gas desorption experiments, including infrared spectroscopic data.

The species of precursor to the oxide phase determines the purification techniques and, hence, the lowest possible background levels of foreign cations and anions in the oxide. The MgO precursors considered for this study are listed in Table III-1. The direct production of the final phase from the reactants is the preferred technique in many cases. The first two reactions produce cubes of MgO smoke. The smoke particles produced by Vieira (1980) from $MgCl_2 \cdot 6H_2O$ decomposition, contain ∿2000 ppm Cl and do not densify. From the studies of Chaudhari and Matthews (1971) on the grain misorientation relationships between cuboid smoke particles produced from the reaction of Mg with O_2, it is not certain that the MgO particles will form <001> twist boundaries in the absence of water vapor. (See Section IV.3.4.) These two techniques were rejected on the bases of Cl^- and OH^- contamination and their unsinterability. The hydroxide precursor was rejected due to the duplex microstructure found in this study (see Chapter II) and by Rhodes, et al. (1972) for $Mg(OH)_2$-derived MgO. Rhodes also observed that using carbonate and oxalate precursors, uniform high-density MgO compacts could be formed. The typical oxalate reaction shown in Table III-1 requires four ionic complexes. Magnesium oxalate

Table III-1

MgO Precursors

1. Mg metal + O_2

2. $MgCl_2 \cdot 6H_2O$ decomposition

3. $Mg(NO_3)_2^{*}(aq) + 2NH_4OH \longrightarrow Mg(OH)_2 + 2NH_4NO_3(aq)$

4. $Mg(NO_3)_2^{*}(aq) + (NH_4)_2C_2O_4(aq) \longrightarrow MgC_2O_4 + NH_4NO_3(aq)$

5. $Mg(NO_3)_2^{*}(aq) + (NH_4)_2CO_3(aq) \longrightarrow MgCO_3 + 2NH_4NO_3(aq)$

6. $Mg(HCO_3)_2(aq)$ decomposition

*$Mg(NO_3)_2$ can be replaced by other compounds soluble in water, such as $MgCl_2$, $MgSO_4$, etc.

precipitates leaving two ionic complexes in solution. These reactions were rejected for this study because of the possible incorporation of those foreign complexes or some of their constituent elements into the oxalate. Formation of magnesium carbonate from a similar two-solution/four-ion complex reaction was, likewise, rejected.

The decomposition of $Mg(HCO_3)$ aqueous solutions to form a hydrated magnesium carbonate precipitate was chosen for the study. Precipitation occurs at 1 atm (0.1 MPa) by heating the highly supersaturated solution which is prepared by applying a high CO_2 pressure to a magnesium carbonate powder-water mixture. The decomposition reaction limits the number of elements in contact with the carbonate to three: H, C, and O. In addition, the basic $Mg(HCO_3)_2$ solution (pH $\sim$10) allows easy extraction of cations by liquid-liquid extraction of metal chelate complexes.

III.2.2 Clean Room Facilities

The purification procedures, and powder and powder compact handling described here were performed under Class 100 clean room conditions. Vertical laminar flow hoods containing high efficiency particulate air filters (HEPA) were used to maintain the Class 100 rating, that is, fewer than 100 particles greater than 0.5 μm per cubic foot. Bench tops were fabricated from an acid-cleanable glass-ceramic. Ultrapure water of 18×10^6 Ω-cm at 25°C was obtained by mixed-bed ion-exchange of distilled CO_2. Lint-free clothing and towels and talc-free disposable gloves were used for intrusion in the laminar flow air space.

The use of glassware was minimized due to the high corrosion rate of glasses at room temperature (∿0.1 $mg/cm^2/day$) in strong alkali, strong chelate, and strong acid aqueous solutions as well as in ultrapure water (Adams, 1972). The pressure reaction vessels and the four-liter separatory funnels were the only glass containers used in this study. Residence time in these vessels was kept to a minimum. Polymethylpentene (PMP, Nalgene®) and Teflon® containers and accessories were used for solution transfer, storage, and heating.

Glassware was cleaned by rinsing in concentrated HCl, boiling in concentrated reagent grade HNO_3 and rinsing in ultrapure water. All filters were washed with concentrated reagent grade HCl and ultrapure water before use. All non-glass containers and accessories were cleaned by soaking in concentrated HCl and washing in ultrapure water.. All glassware, plasticware, and accessories were used only for purification of magnesium bicarbonate solutions. During the course of this work, the clean room facilities were used solely for the processing of magnesium bicarbonate solutions and precipitation of the hydrated carbonate to eliminate cross-contamination.

II.2.3 Chemical Analysis

At the part-per-million level, chemical analysis must be performed under clean conditions similar to the initial processing facilities and procedures. The chemical analyses reported here were performed by Dr. Walter Zamechek using plasma-coupled emission spectroscopy under such conditions. Typical detection limits for high-purity MgO are listed in

Table III-2. The detection limits are functions of the cleanliness of the chemical analysis laboratory and the procedures needed to dissolve the samples. Because MgO and its precursors dissolve readily in HNO_3 and HCl, sample preparation for analysis contributes little contamination under clean conditions.

In this study, chemical analysis was used only to indicate trends in contamination. To obtain statistically significant quantitative chemical analyses at the trace element level (1-100 ppm), the American Chemical Society standards (1981) for trace analysis must be used. The tests include, for example, multiple testing, blank testing, spiked blank testing, and multiple laboratory testing of the "same" sample. Because of the low yields of carbonate and oxide, the ACS standards for multiple testing for trace analysis were not followed.

III.2.4 Purification Techniques

The purification techniques used in this study are filtration of insoluble precipitates from aqueous solution, liquid-liquid extraction of metal-chelate complexes, precipitation of the hydrated magnesium carbonate in the presence of a soluble masking (complexing) agent, and washing of the precipitate with high-purity water.

Filtration removes insoluble particulate primarily, SiO_2 and Al_2O_3, introduced during chemical processing and the packaging operation. The primary separation method for transition metal ions was liquid-liquid extraction of metal-chelate complexes. The extraction is possible due to

Table III-2

Detection Limits of Elements by Plasma Coupled Emission Spectroscopy

(μg/g Mg metal basis)

Al	< 1	Fe	< 1	Sb	< 1
As	< 1	Ga	< 1	Se	< 1
B	< 0.4	La	< 0.3	Si	< 2
Ba	< 0.3	Li	< 0.3	Sn	< 1
Be	< 0.2	Mn	< 0.2	Sr	< 0.2
Ca	< 0.1	Mo	< 1	Ti	< 0.3
Cd	< 0.3	Na	< 0.2	V	< 0.2
Co	< 1	Ni	< 1	Zn	< 0.5
Cr	< 1	P	< 1	Zr	< 0.3
Cu	< 1	Pb	< 1	K	< 1

the solubility difference of metal chelate complexes in organic media and aqueous solution. The reaction between a metal N of charge N, with a chelating agent HA in the organic solvent, forms a metal-chelate complex MA_N highly soluble in the organic phase and insoluble in the aqueous phase:

$$(M^{N+})_{aq} + N(HA)_{org} = (MA_N)_{org} + N(H^+)_{aq} \qquad \text{(III-1)}$$

with an extraction constant, K:

$$K = \frac{[MA_N]_{org}[H^+]^N_{aq}}{[M^{N+}]_{aq}[HA]^N_{org}} \qquad \text{(III-2)}$$

For a constant $[HA]^N_{org}$, the distribution coefficient, q, of the metal impurity becomes:

$$q = \frac{[MA_N]_{org}}{[M^{N+}]} = \frac{K}{[H^+]^N_{aq}} \qquad \text{(III-3)}$$

and is a function of only the pH of the aqueous solution and temperature. A typical value of K for dithiocarbonate extraction is 10^{-12} for N=3. At a pH of 3 and [HA] = 0.1, q = 10^{-6} and essentially no extraction of trivalent ions occurs. At a pH of 10 and [HA] = 0.1, q = 10^{15} and the concentration of cations of +3 charge in the aqueous phase is zero. The pH of the magnesium bicarbonate solution is approximately 10, at ∿300 K which, therefore, tends toward the maximum distribution coefficient for these solutions (Stary, 1964).

For the extraction of impurity metal ions to the part-per-billion level from $Mg(HCO_3)_2$ (aq), diethylammonium diethyldithiocarbamate (DDDC) in chloroform was used. The hydrogen in the chelating agent formula HA is replaced by the ion $(NH_2(C_2H_s)_2)^+$. The chelate former is the dithiocarbonate ion, $NCS_2(C_2H_5)$, as shown schematically in Table III-3. Dithiocarbonate ions have been found to form highly stable complexes with the cations listed in Table III-3 (Stary, 1964).

The three techniques for eliminating the alkaline earth impurities examined in this study were multiple precipitations/recrystallizations, low supersaturation growth of single crystals and chemical masking using a complexing agent which changes the solubilities of the alkaline earths in the aqueous phase. The masking agent used in this study was ethylenediamine tetracetic acid (EDTA), which forms Ca-EDTA complexes and Mg-EDTA complexes with different stability constants (K_{Ca},K_{Mg}) in the aqueous phase. Log K_{Ca} is 10.7; log K_{Mg} is 8.7 (Welcher, 1958). The yield of hydrated $MgCO_3$ decreases slightly due to complexing with EDTA. However, in this study and a previous study by Debska-Horecka, et al. (1973), a high yield in the absence of EDTA was associated with almost total incorporation of the Ca in the precipitate; precipitation in the presence of EDTA decreased the yield by ∿10% and caused 99+% of the Ca to remain in the aqueous solution. The efficiencies of three techniques are discussed in the following section.

The DDDC and EDTA were purified in the clean laboratory. The preparation procedure for EDTA is described below.

Table III-3

Diethylammonium Diethylodithiocarbamate

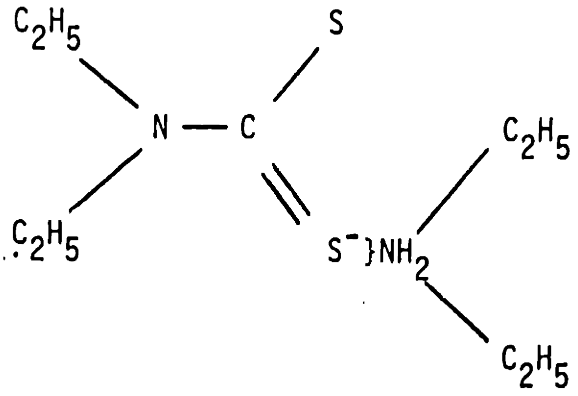

Metals Extracted by Dithiocarbamate Ion

Ag
As (III)
Au
Bi
Cd
Co
Cr (VI)
Cu
Fe
Hg
In
Mn
Os
Ni
Pb
Pd
Pt (II)
Sb (III)
Se
Sn (II)
Te
U
V
W
Zn

Metals Not Extracted by Dithiocarbamate Ion

As (V)
Cr (III)
Nb (V)
Pt (IV)
Rh (III)
Sb (V)
Sn (IV)
Alkalis
Alkaline Earths
Rn (III)

The solubility of alkaline elements in aqueous solution is high and is low in the precipitated magnesium carbonate. However, adsorbed alkalis on the precipitate surfaces can lead to significant contamination (100-1000 ppm). By multiple washing of the precipitate with ultrapure water, a large fraction of the alkalis can be removed.

III.2.5 Precipitation Procedures and Purity Results

The basic purification and precipitation techniques are shown in the flow chart in Figure III-1.Modifications to these procedures to remove the alkaline earth ions are presented in the latter part of this section. All procedures described here were performed under Class 100 conditions. A reagent grade hydrated magnesium carbonate obtained commercially[†] was used as the magnesium source. The starting carbonate powder is shown in Figure The commercial powder, prepared by bubbling CO_2 through a magnesium nitrate aqueous solution, was hydromagnesite, approximate composition $4\ MgCO_3 \cdot Mg(OH)_2 \cdot 4H_2O$ (40 wt % MgO). A typical chemical analysis of this powder is listed in Table III-4.

Batches of approximately 300 grams of the hydrated carbonate were dissolved in ultrapure water under CO_2 pressure ($P_{CO_2} = 1.6$ MPa) to form a 0.6M $Mg(HCO_3)_2$ (saturated) solution. A slight excess of $MgCO_3 \cdot$ n-hydrate was added to suppress dissolution of the less solubleless pure material. A stainless steel pressure vessel was used and the powder was stirred with a Teflon® coated stirring bar. The dissolution process takes approximately 12 h at room temperature.

[†] J. T. Baker Co.

Figure III-1

MgO Purification Techniques

Reagent grade basic
$MgCO_3 + H_2O$ (Ω = 18 Mohm·cm) $\xrightarrow{P_{CO_2} = 1.6\ \mathrm{MPa}}$ $Mg(HCO_3)_2$ (aq) $\longrightarrow$

DDDC in H_2O
centrifuge
filtration
$\longrightarrow$
DDDC in $CHCl_3$
filtration
$\longrightarrow$
purified
$Mg(HCO_3)_2$ (aq)

The solution which is metastable at room temperature and CO_2 pressure is siphoned into PMP liter bottles to which approximately 0.1 gm DDDC is added to form undoluble precipitates. The solutions are centrifuged at 1000 rpm for 1/2 hr to remove particles greater than 1 μm. The solutions are filtered through 0.25 μm Teflon® filters and transferred to 4 liter separatory funnels. Multiple extractions of transition metal ions were performed by shaking the solutions with a chloroform (250 ml) - DDDC (1 gm) solutions until the chloroform remained uncolored. The solution was then extracted with pure chloroform to extract the unreacted chelating agent.

The purified solution is filtered through a 0.25 μm Teflon® filter to remove magnesium carbonate precipitates. The purified solution can then be heated to 350 K to precipitate hydromagnesite. Because the bicarbonate solution is highly supersaturated at room temperature, precipitation occurs readily. Two hydrated magnesium carbonate phases occur: nesquhonite, $MgCO_3 \cdot 3H_2O$, at $\sim$300-325 K and hydromagnesite, $4MgCO_3 \cdot Mg(OH)_2 \cdot 4H_2O$ at high temperatures (Dell and Weller, 1969). It was expected that both phases would form during heating of the solution from room temperature to 360 K.

The resulting precipitate is washed with ultrapure water and filtered by vacuum filtration through a Teflon® filter supported in a PMP funnel. The funnel assembly with the precipitate is centrifuged at 1000 rpm for 30 min to remove the excess water.

A typical chemical analyses of the precipitate is listed in Table III-4. The amount of K and Na detected are functions of the number of

Table III-4

Chemical Analyses

(μg/g Mg metal basis)

	Reagent Carbonate	DDDC Extraction Only
Ba	1	0.6
Ca	33	20
Mn	3	<0.2
Na	430	11
Ni	2	<1
Sr	1	1
K	5	<1

No other elements detected.

precipitate wash cycles and intermittent recontamination. The initial concentration of the alkaline earth ions is high relative to the concentration of the transition metal ions. All elements extractable by DDDC are below the detection limit and, by visual inspection of the chloroform, are at the extraction limit. Although the extraction limits are in the ppm range, recontamination of the solutions during clean room processing raises the possible level to less than 0.1 ppm.

The alkaline earth ions complexed with EDTA remained in aqueous solution during precipitation of magnesium carbonate as shown schematically ir Figure III-2. The EDTA was purified by dissolution of reagent grade EDTA in a purified $Mg(HCO_3)_2$ solution and acidifying with HCl to precipitate Mg-EDTA salt. This process removes Na from the reagent EDTA. The purified Mg-EDTA is dissolved in a purified $Mg(HCO_3)_2$ solution and precipitation is induced by heating to 350 K. The resulting powder is washed with ultrapure water as described above. The chemical analysis of the EDTA-masked precipitate is listed in Table III-5 along with the chemical analyses of hydrated $MgCO_3$ produced by three dissolution-precipitation cycles and by room temperature low supersaturation growth of single crystal $MgCO_3 \cdot 3\ H_2O$. Complexing of Ca , Ba, and Sr by EDTA lowered the Ca content to approximately 0.4 ppm from 20 ppm for DDDC extraction alone. Multiple precipitation (3x) did not significantly lower the Ca content; low supersaturation growth did decrease the Ca concentration to 4 ppm, but this concentration is an order of magnitude higher than the EDTA-masked precipitate. All three techniques produced powder with all other cations, except Na, at concentrations lower than the detection limit.

Figure III-2

Separation of Calcium

EDTA Purification

$$\begin{matrix}\text{EDTA dissolved in}\\ \text{purified MG(HCO}_3)_2\text{ (aq)}\end{matrix} + \text{HCl} \longrightarrow \text{Mg-EDTA salt (s)}$$

Precipitation

$$\text{Purified Mg(HCO}_3)_2\text{ (aq) + Mg-EDTA salt (aq)} \xrightarrow[350\text{ K}]{} \text{hydrated MgCO}_3$$

Figure III-3

Doping Procedures

$$1.\quad \begin{matrix}\text{MgCO}_3\cdot n\text{H}_2\text{O}\\ +\\ \text{CaCO}_3\end{matrix} \xrightarrow{P_{\text{CO}_2} = 1.6\text{ MPa}} \begin{matrix}\text{Mg-Ca(HCO}_3)_2\\ \text{solution}\end{matrix} \xrightarrow{T} \text{Ca-doped MgCO}_3$$

$$2.\quad \text{MgCO}_2\cdot n\text{H}_2\text{O} \xrightarrow{P_{\text{CO}_2} = 1.6\text{ MPa}} \begin{matrix}\text{Mg(HCO}_3)_2\text{ (aq)}\\ +\\ \text{Al(NO}_3)_2\text{ (aq)}\end{matrix} \xrightarrow{T} \text{Al-doped MgCO}_3$$

Table III-5

Chemical Analyses of Hydrated $MgCO_3$ Powders

(μg/g Mg metal basis)

	DDDC Extraction Only	EDTA Masked	Multiple Precipitation	Low Supersaturation Growth
Ba	0.6	<0.5	<0.5	<0.5
Ca	20	0.4	16	4
Sr	1	<0.2	<0.2	<0.2
Na	11	<2	<2	2

The hydrated magnesium carbonate produced by EDTA masking contained less than 8 ppm total cation impurities with less than 1 ppm detectable (Ca only). These cation levels are lower than in commerially available high-purity Mg and MgO as determined by plasma coupled emission spectroscopy shown in Table III-2. High-purity magnesium[†] and MgO[††] were found to contain Fe, Mn, Zr, Na, and K and Cu, Na, and K, respectively. In addition, the background levels of all elements were higher, raising all detection limits by approximately a factor of 5.

In no case are anion levels known. Although the MgO precursor prepared using DDDC complexing, liquid-liquid extraction, and EDTA masking contains only Mg, O, C, and H by phase analysis, it has been in contact with Cl- and S-containing compounds and the Cl and S concentrations are not known.

III.2.6 Controlled Doping with Al and Ca

As described in Section III.1, the ability to dope high-purity materials without changing the precipitated phase, the morphology, and the background levels of cations and anions is critical to a study of the effects of dopants on sintering and grain growth. Only the chemical analyses are presented and discussed below. The cations Ca and Al were chosen as dopants because they both segregate to grain boundaries in MgO. Segregation of Ca^{2+} in MgO is determined largely by the radii difference between Ca and Mg: segregation of Al^{3+} is due predominantly to space charge at boundaries.

[†] Johnson Matthey

[††] Spex

The doping procedures for Al and Ca in hydromagnesite prepared under Class 100 conditions are shown in Figure III-3. The $CaCO_3$ was purified from a CO_2-supersaturated $Ca(HCO_3)_2$ solution using DDDC and liquid-liquid extraction. The purified magnesium and calcium carbonate were dissolved under CO_2 pressure (1.6 MPa) and coprecipitated by heating the solution at 350 K. The aluminum was added in the form of an aqueous nitrate solution to a $Mg(HCO_3)_2$ purified solution. The magnesium carbonate powders used in this phase of the study were prepared by DDDC complexing, liquid-liquid extraction, and precipitate washing only. No EDTA-masking was used.

The chemical analyses of the doped powders are presented in Table III-6. The intended dopant levels were 2000 ppm Ca and 1000 ppm Al. The levels of Sr and Na in the Ca-doped materials are high relative to the total dopant level. This amount of Sr indicates that the Sr concentration in $CaCO_3$ was 0.5 wt %. The Al-doped material is cleaner than the starting powder with respect to background Ca, Sr, and Na levels and as clean as the EDTA-masked material with respect to all cations.

III.2.7 Transformation to the Oxide

Due to fabrication costs of the high-purity material, the reagent grade carbonate from which it was prepared was used as a prototype for the high-purity powder. The effects of each processing step on these physical and chemical characteristics were first determined for the lower purity material. The complete range of experiments was not performed with the high-purity powders, except when the powder characteristics were sensitive

Table III-6

Chemical Analyses

(μg/g Mg metal basis)

	EDTA-Masked Precipitate	Ca-doped	Al-doped
Al	<1	<1	0.09%
Ca	0.4	0.15%	0.2
Sr	<0.2	4	<0.2
Na	<2	6	<2

to slight changes in the processing parameters. Some of this work was reported previous in a report by Handwerker et al. (1982) and is described in detail in a companion study by O"Connor (1982).

The processing procedures and the evaluation techniques subsequently used are listed in Figure III-4. The carbonate was transformed to the oxide at various temperatures; the oxide was deagglomerated in various solvents by ultrasonic disruption using a high-power ultrasonic probe immersed in the suspension; compacts were formed by settling and evaporation; and the residual organics and surface species were removed by heating the compacts.

The anionic and organic contaminants due to a processing step were assessed by measurements of the weight loss and thermal changes upon heating, by changes in the specific surface area and average crystallite size, by detection of surface species by Fourier transform infrared spectroscopy, and by phase analysis by x-ray diffraction. Changes in the powder morphology and particles size distribution were measured by direct microscopic observation using the SEM and by particle settling experiments.

The purity with respect to cations was measured for the reagent grade and high-purity carbonates, and for the high-purity powder after transformation to the oxide and after compact formation. The results for the reagent grade material are discussed in detail in Handwerker et al.(1982) and O'Connor (1982) and are not presented below.

From these results a series of clean-room processing procedures for high-purity MgO was chosen which was determined to minimize total contamination

PROCESSING STEPS	CHARACTERIZATION TECHNIQUES
2 Types of hydrated $MgCo_3$ Reagent Grade and High Purity	X-Ray Diffraction
MgO Powder	X-Ray Diffraction, DTA, TGA, X-Ray Line Broadening Observation by SEM, BET Surface Area, IR Spectroscopy Sedigraph
Ultrasonic at Power Level P For Time t in Alcohol A	Sedigraph
Settle and Decant	Sedigraph Sedimentation Volume
Dry in Air	Observation by SEM IR Spectroscopy
Heat to Desorb/ Decompose/Sinter	TGA, DTA, BET Surface Area Observation by SEM

III-4 Clean Room Processing Steps and Characterization Techniques Used in This Study

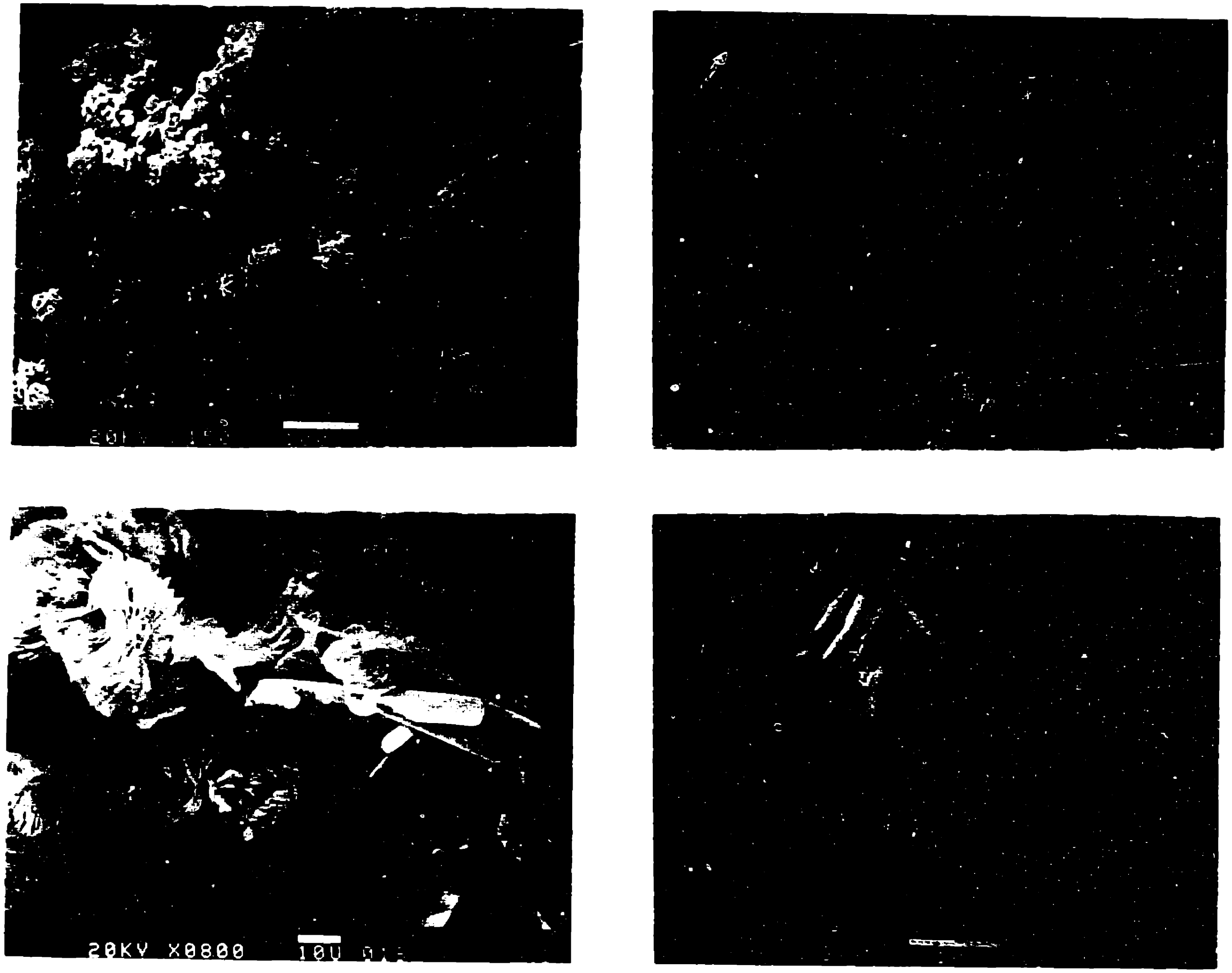

(a)

(b)

Figure IV-5 Morphologies of high purity carbonate and oxide powders: (a) before transformation and (b) after decomposition to MgO at 1273 K.

and produce an uncracked, high-density green body. The high purity carbonate used for compact formation was purified by DDDC extraction alone.

The high purity magnesium carbonate material prepared under clean conditions from a magnesium bicarbonate solution contains approximately 20 wt% MgO. Adsorbed water in the high-purity material accounts for the difference in oxide content from the fraction MgO predicted from the hydromagnesite composition ($\sim$ 40 wt% MgO), the phase detected by x-ray diffraction.

The high-purity hydromagnesite, shown in Figure III-5, has particles of two distrinct morphologies: single crystal needles ($\sim$ 60%) and spherulites ($\sim$ 40%). The average agglomerate size of the high-purity spherulites and the average needle length are approximately 100 μm,based on SEM inspection. Dell and Weller (1969) determined that two powder morphologies of hydrated Mg-carbonates correspond to two distinct phases--spherulites to hydromagnesite* and needles to nesquehonite, $MgCO_3 \cdot 3H_2O$. However, the x-ray diffraction data does not indicate the presence of nesquehonite which would have been detected at 10 volume percent.

Surface area, x-ray line broadening, and sedigraph measurements were difficult to interpret due to the residual water in the carbonate.

To transform the carbonate to MgO, batches of approximately 50g. of carbonate were placed in covered MgO crucibles† (98% MgO, 1.2% SiO_2, [Si]/[Ca]=29 heated in O_2 in an RF furnace with a Pt susceptor at 10°C/minutes to 770 K, 1070 K, and1270 K, held at temperature for two hours and cooled at 10° C/minute. The surface areas and x-ray diffraction phase analyses, are listed in Table III-7.

---

* $4\ MgCO_3 \cdot Mg(OH)_2 \cdot 4H_2O$

† Honeywell

Table III-7

Phase Analyses, Specific Surface Area, and Crystallite Size as a Function of Heat-Treatment

MgO (High Purity)	Phases Identified	Surface Area (m^2/g) Calc. Eq. Sph. Diameter (nm)	Particle Size by X-ray Line Broadening (nm)
As-Precipitated	$4MgCO_3 \cdot Mg(OH)_2 \cdot 4H_2O$	74	--
500°C	$MgO + MgCO_3 + Mg(OH)_2$	158	--
800°C	MgO	38 (46)	31
1000°C	MgO	18 (95)	39

The magnesium carbonate powder in approximately 2 mg batches was transformed in the TGA and DTA according to the heating schedules listed above. Representative TGA and DTA data are shown in Figure III-6. The broad endotherms at 400 K, 570 K, and 700 K indicate loss of CO_2 and H_2O to form various amorphous hydrated magnesium carbonates and, at 800 K to form magnesium oxide. The exotherm at 780 K corresponds to the crystallization of magnesite, $MgCO_3$, followed by evolution of CO_2 and H_2O at $T > 780$ K.

From the DTA and x-ray diffraction study of Dell and Weller (1969), it was found that the formation of $MgCO_3$ and the crystallization exotherm at 780 K can be avoided by slower heating rates and by more efficient removal of the CO_2 and H_2O evolved at $T \sim 670$ K to avoid the conditions under which $MgCO_3$ is stable.

Thus, considering the poor gas-flow condition with a large batch size (50 g for the high purity), it is not surprising that the carbonate and hydroxide phases identified by x-ray diffraction were formed during heating to 770 K.

The hydrated $MgCO_3$ was treated in a low temperature (∿400 K) oxygen plasma[†] as a cleaner alternative to transformation to the oxide in a standard furnace. The DTA curves of the plasma-treated powder heated to 1270 K showed fewer features than the untreated powder but the carbonate was not completely transformed to the oxide. This method of treatment was not used.

[†] LFE Corporation, Low Temperature Asher


鈴木春信画

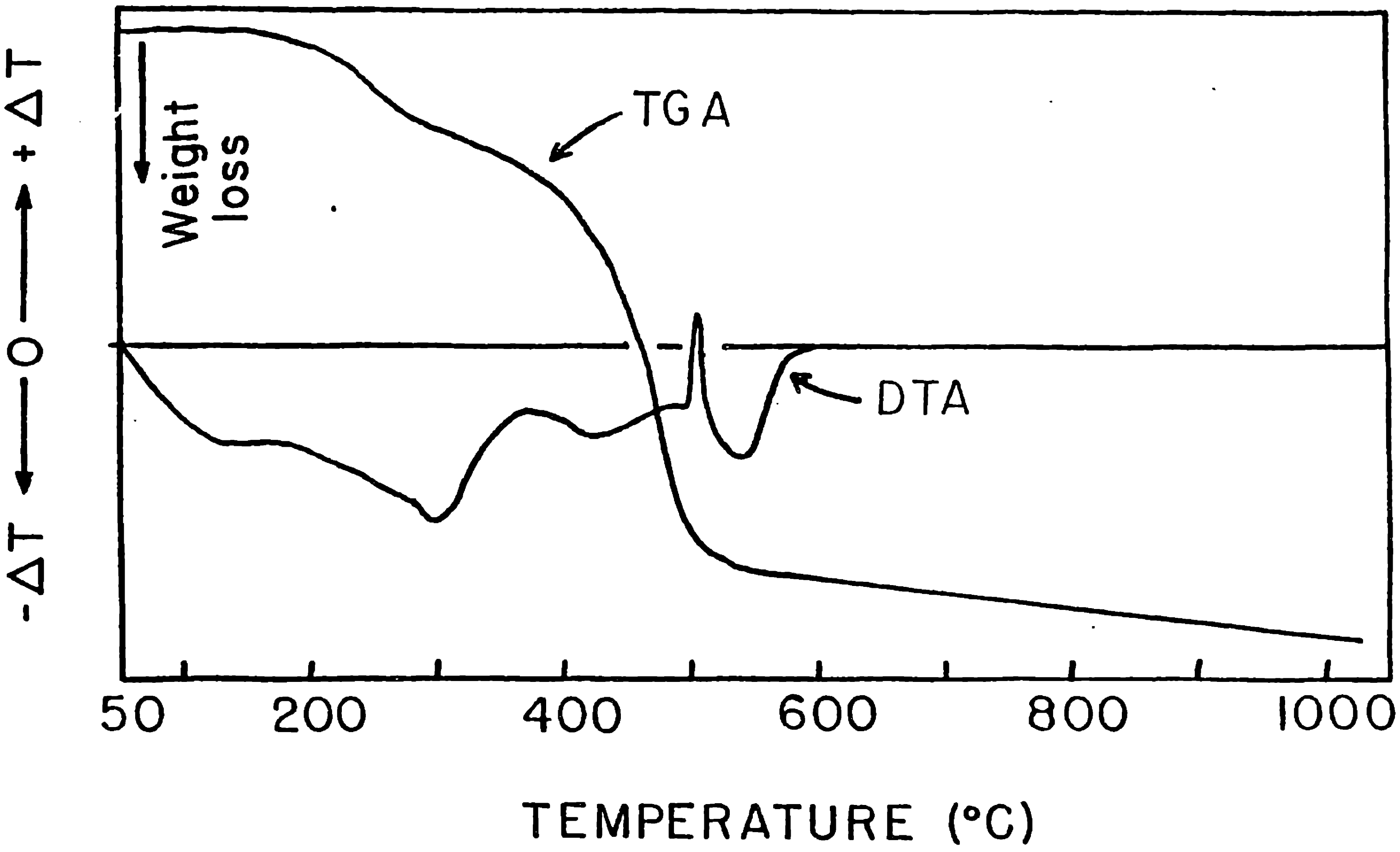

Figure III-6 Representative TGA and DTA curves for the transformation from the hydrated carbonate to the oxide.

The measured weight loss (TGA) was approximately 80% on transformation to the oxide, whereas for the weight loss in the transformation of the compound $4MgCO_3 \cdot Mg(OH)_2 \cdot 4H_2O$ to MgO is expected to be 57% of the initial weight. The actual H_2O and CO_2 content varies as a function of the temperature and partial pressure conditions of the precipitation and the subsequent drying and calcination cycles. Adsorbed water on the surface can also contribute to weight losses greater than 57%.

Although weight loss may continue to higher temperatures ($T > 1270$ K), sintering occurs concurrently, leading to significant agglomeration as determined from calcination investigations not reported here. Therefore, the maximum transformation temperature was kept at 1270 K.

The transformation to MgO did not significantly change the gross morphology from that of the precursor for all transformation temperatures. Representative microstructures are shown in Figure III-5. The needles of the high-purity hydromagnesite break up upon transformation, whereas the spherulites show no change.

The surface areas and the average crystalline sizes are listed in Table III-7. The hydromagnesite transformed at low temperature retains water and carbon dioxide as evident from phase analysis and DTA and weight loss measurements at higher temperatures. The high-purity powder transformed at 1270 K was, therefore, the highest powder with respect to H_2O and CO_2 used for the compact formation experiments.

III.2.8 Compact Formation

As indicated in FigureIII-4the as-transformed powders must be deagglomerated before compact formation, followed by settling and evaporating to form a green body and heated to desorb and decompose the adsorbed species before high temperature heat-treatment.

The degree of agglomeration is shown in the particle size distribution of the high-purity oxide in FigureIII-7.Fordeagglomeration, the oxide was placed in a PMP container; the container was half-filled with isopropanol, and a flexible polyethylene shield was used to cover the isopropanol suspension. Additional isopropanol was placed inside the polyethylene shield. The suspension was deagglomerated by ultrasonic disruption using an ultrasonic probe inserted in the exterior isopropanol, but not in direct contact with the MgO.

The oxide was settled for various times and decanted to form graded compacts, as described in Chapter II.

Infrared spectroscopy, DTA, TGA, and specific surface area were used to characterize the adsorption of isopropanol and ambient species (OH^-, CO_2) on MgO. These data on the high-purity oxide and the sensitivity of adsorption to sample purity are presented in O"Connor (1982) and will not be described here.

High-purity MgO compacts were formed for the following particle-size ranges: 4 μm - 0.5 μm and <0.5 μm. The powder with >4 μm particle sizes did not form a compact upon drying. Chemical analysis of the as-transformed

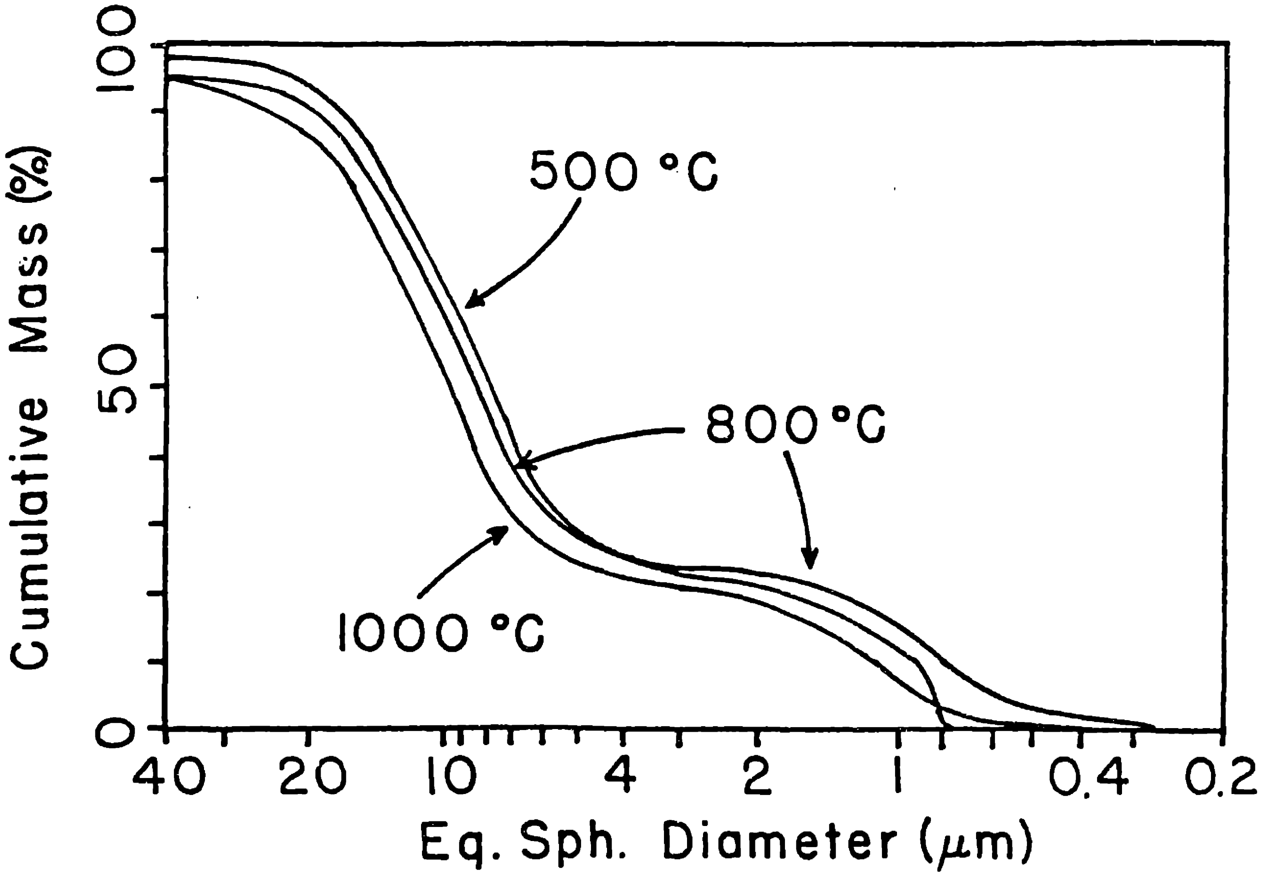

Figure III-7 Distribution of equivalent spherical diameters for agglomerated high purity oxide powders as a function of decomposition temperature oxide and the as-dried compacts are listed in Table III-8. Significant degradation has occurred in the sample purity (Ca, Na). It is uncertain whether this degradation is due to contact with the crucible during transformation, or to airborne particulate or vapor species or whether the high concentrations of Ca and Na were present in the original carbonate batch. It should be remembered that the oxide in these experiments were prepared from DDDC-extracted carbonate, precipitated without EDTA-masking. The Ca concentration in one batch of the as-precipitated materials was 20 ppm but could conceivably have been a factor of five higher in the carbonate batch from which the MgO compact was formed. Without more extensive chemical analyses, this issue of the variation of contamination from batch to batch and within a batch cannot be resolved.

The calcium contamination was probably not due to particles of the crucible material in the transformed high-purity material. The value of Si/Ca in the crucible was 29, as reported by the manufacturer. No concurrent increase in the Si concentration suggests that solid particulate from the crucible was not the contamination source.

Although this has not been demonstrated, the use of high-purity hydromagnesite prepared by EDTA complexing in conjunction with high-purity MgO curcibles and a cleaner heat source (laser, for example) should maintain the initial purity of the carbonate.

Anion impurities, with the exception of hydroxyls, were minimized by the choice of an MgO precursor which contains only CO_2 and H_2O as

Table III-8

Composition Analysis by Plasma Coupled Emission Spectroscopy[*] Reported in ppm. Cation Basis (µg/g of Mg)

	Reagent Grade $MgCO_3 \cdot$ N-Hydrate	High Purity $MgCO_3 \cdot$ N-Hydrate	MgO	MgO Compact
Ba	1	0.6	2	3
Ca	33	20	109	123
Na	430	15	60	54
Sr	1	1	3	4
Mn	3	<0.6	<0.6	<0.6

Below Detectability Limit for Al, As, B, Be, Cd, Co, Cr, Cu, Fe, Ga, La, Li, Mo, Ni, P, Pb, Pd, Sb, Se, Si, Sn, Ti, V, Zn, Zr, K

---

[*] Union Carbide Corporation

as foreign species. The suspension medium, isopropanol, was chosen both for its simple chemical formula, containing only C, H, and O, and for the good compact quality obtained using this liquid. From DTA and TGA, the MgO powders must be heated to approximately 1270 K for the transformation and 870 K for the re-heating after deagglomeration to remove most of these species. Residual OH^- and C after these heat-treatments have not been measured directly. Use of DDDC in chloroform may cause Cl and S contamination during precipitation. The amount of Cl and S contamination and the degree to which these species are removed during transformation to MgO or re-heating of the compact are not known.

The amount of residual H and C in the transformed MgO is not known. Use of a cold wall furnace and an O_2 atmosphere is the only option for transformation of the carbonate to the oxide. Vacuum calcination seems initially to offer the advantage of removing more hydroxyl/water or CO_2 from the powder. However, contamination of the sample from the vacuum system oil may occur. In addition, incomplete oxidation of adsorbed carbon containing species may leave elemental carbon on the surface. Therefore, vacuum calcination was not used.

III.3 Sintering and Grain Growth of High-Purity MgO

III.3.1 Experimental Procedures

The fabrication procedures for settled compacts of high-purity MgO were described in Section III.2. Only the compact with particle sizes from 4 μm (bottom surface) to 0.5 μm (top surface) and $\sim$ 60% ρ_{th} was used for sintering experiments.

The compacts composed for particles <0.5 μm was cracked and was of lower density than the larger particle size compact. The individual samples were surrounded with high-purity MgO and packed in a low purity MgO crucible (98% MgO)[†] which had been etched in HF and HCl, soaked in ultrapure water, rinsed in ethanol, and air-dried under clean conditions. The crucible was covered with 98% MgO[†] lead and placed on a high Al_2O_3[††] sample carrier, and surrounded with MgO powder. The samples were annealed in a Mo-resistance furnace (H_2 protective atmosphere) inside a high Al_2O_3[††] tube which had been previously annealed at 1970 K for 48 h. This furnace tube preheating was found to decrease the furnace-generated contamination (Coble, personal comm.). Furnace temperature was controlled by a Variac to ±10°.

As reported in Section III.2.7, heating the as-settled compact to 900 K was needed to decompose the adsorbed alcohols and the alcoholates. The sample assembly was heated at $\sim$ 900 K for 30 minutes in O_2 then heated to the sintering temperature in $\sim$15 minutes. The sintering temperatures were 1620 K, 1930 K, and 1970 K.

[†] Honeywell, 98% MgO

[††] Morganite, 99% Al_2O_3

Grain growth samples were prepared by cold-pressing high-purity MgO powder at 200,000 psi (1.4 GPa) in a WC die under clean conditions. The disks were 1/4" in diameter and ∿200 μm thick; as-pressed sample densities were >98% ρth. These samples were heated to the same temperatures and using the same procedures as for the settled samples.

The microstructure evolution was assessed by examining as-fired and fracture surfaces by SEM.

III.3.2 Results

From an initial density of 60% ρth, the MgO compacts sintered at 1620 K, 1730 K, and 1870 K up to 114 h in O_2 reached densities of approximately 65-80% of theoretical. Exact measurement of density by either the Archimedes method or point counting from polished surfaces was precluded due to the small sample sizes.

The average grain size did not change significantly after short times (∿ 5 h) and were uniform through the sample thickness. The grain sizes for the compacts were 4 μm (1620 K), 6 μm (1930 K), and 10 μm (1870 K). Typical microstructures are shown in Figure III-8. As seen in Figure III-8 for MgO at 1873 K for 114 h, there are small groups of grains (∿ 3-4 grains) which have sintered in the closed pore stage. Grain boundaries are evident in these higher density agglomerates. This suggests that the grain boundary mobility is low.

Figure III-8 Microstructures of settled and sintered high purity MgO after annealing at 1873 K for 114 h.

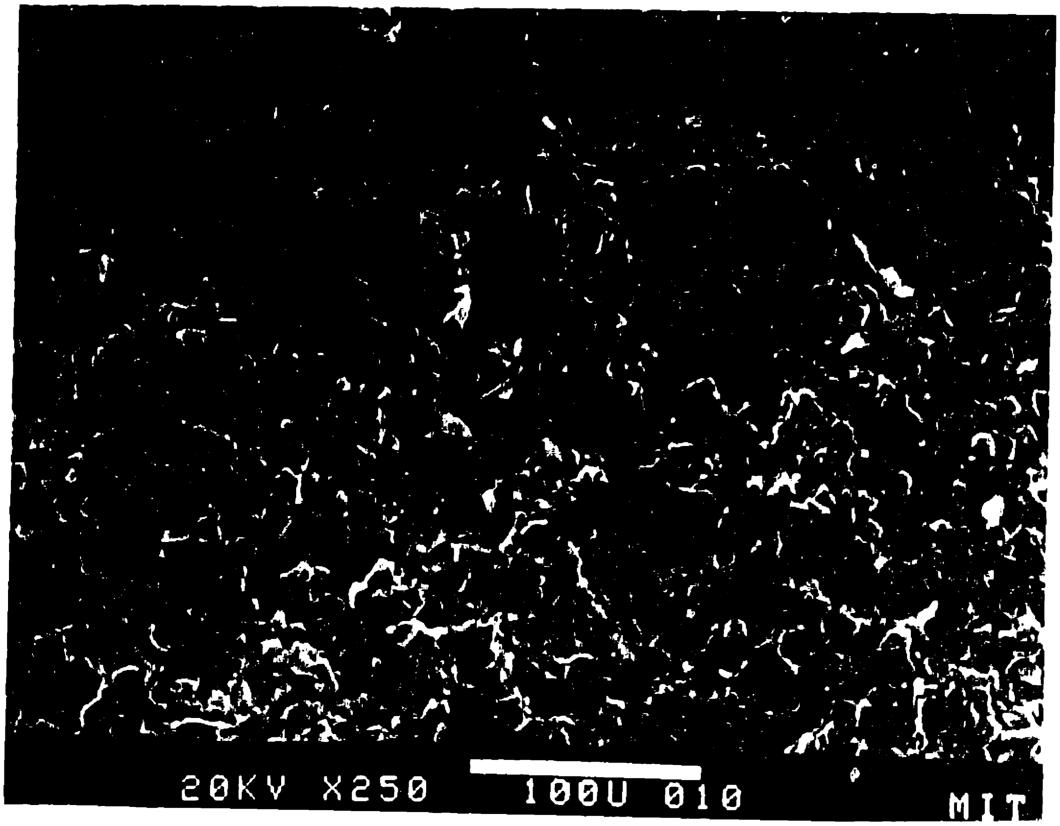

Three grain growth experiments were performed with the cold-pressed samples. The thermal histories of the samples are: (1) 39 h at 1620 K; (2) 39 h at 1620 K, 54 h at 1733 K; and (3) 39 h at 1620 K, 54 h at 1733 K, and 16 h at 1873 K. Grain sizes were measured for each sample and the effective mobility calculated form the grain growth rate.

Porosity was evident along grain boundaries after annealing.

For grain growth described by the equation:

$$G^2 - G_o^2 = K_2 t \qquad \text{(III-4)}$$

the effective mobility can be calculated by:

$$M_{eff} = \frac{V}{F} = \frac{K_2}{\frac{4G}{\gamma/G}} = \frac{K_2}{4\gamma} \qquad \text{(III-5)}$$

For grain growth described by:

$$G^3 - G_o^3 = K_3 t \qquad \text{(III-6)}$$

the effective mobility becomes:

$$M_{eff} = \frac{K_3}{3\gamma\bar{G}} \qquad \text{(III-7)}$$

The grain sizes and the calculated values for M_{eff}, K_2 and K_3 are tabulated in Table III-10. The values of M_{eff} based on Equations (III-5) and (III-7) are of the same order of magnitude. The calculated values of M_{eff} are

Table III-10

Effective Mobilities

	G_o	$\overline{G}$	t	K_2 $(\frac{cm^2}{sec})$	M_{eff} †	K_3 $(\frac{cm^2}{sec})$	M_{eff} †*
1620 K	<1 μm	5 μm	39 h	1.8×10^{-12}	1.5×10^{-15}	8.9×10^{-16}	2.0×10^{-15}
1730 K	5 μm	25 μm	54 h	3.1×10^{-11}	2.5×10^{-14}	8×10^{-14}	3.6×10^{-14}
1870 K	25 μm	50 μm	16 h	3.3×10^{-10}	2.7×10^{-13}	1.9×10^{-12}	4.2×10^{-13}
2030 K	<1 m	12	20	1.2×10^{-9}	1×10^{-12}	1.4×10^{-12}	1.3×10^{-12}

† M_{eff} units: cm/sec $(dyne/cm^2)^{-1}$

* M_{eff} calculated using $\overline{G}$ in Equation (III-7) and $\gamma = 300$ ergs/cm^2

plotted with the other M_{eff} values calculated by Yan, Cannon, and Bowen in FigureIII-9.The values of M_{eff} calculated in this study are not significantly different from previously determined values for lower purity MgO and are orders of magnitude lower than the calculated values for the intrinsic boundary mobility of MgO using δD_b for low-purity MgO (Cannon, 1978).

III.3.3 Discussion

The chemistry of the MgO powder forming the settled compact played a larger role in the microstructural evolution than did the original powder morphology. The morphology of the as-transformed high-purity MgO was not uniform; the acicular and spherulitic forms of the precursor and the wide size distribution remained after transformation. After deagglomeration by ultrasonic disruption, the particle size distribution shifted to smaller particle sizes, which were fragments of the needles and spherulites. Upon sintering/annealing of the MgO compact at high temperature, little evidence of the original particle morphology remained. The same deagglomeration, compact formation,and sintering procedures were used for a study of the sintering of lower purity carbonate-derived MgO, as discussed in Section II.

The agglomerated MgO particles were agglomerates of plates, which were themselves agglomerated. The as-settled compacts were composed of plates and agglomerated plates. However, for lower purity MgO, the compacts remained in the open pore stage at times up to 114 h at 1870 K. It is concluded that the diffusivities to the higher purity MgO are decreased such that sintering is inhibited relative to the low-purity MgO.

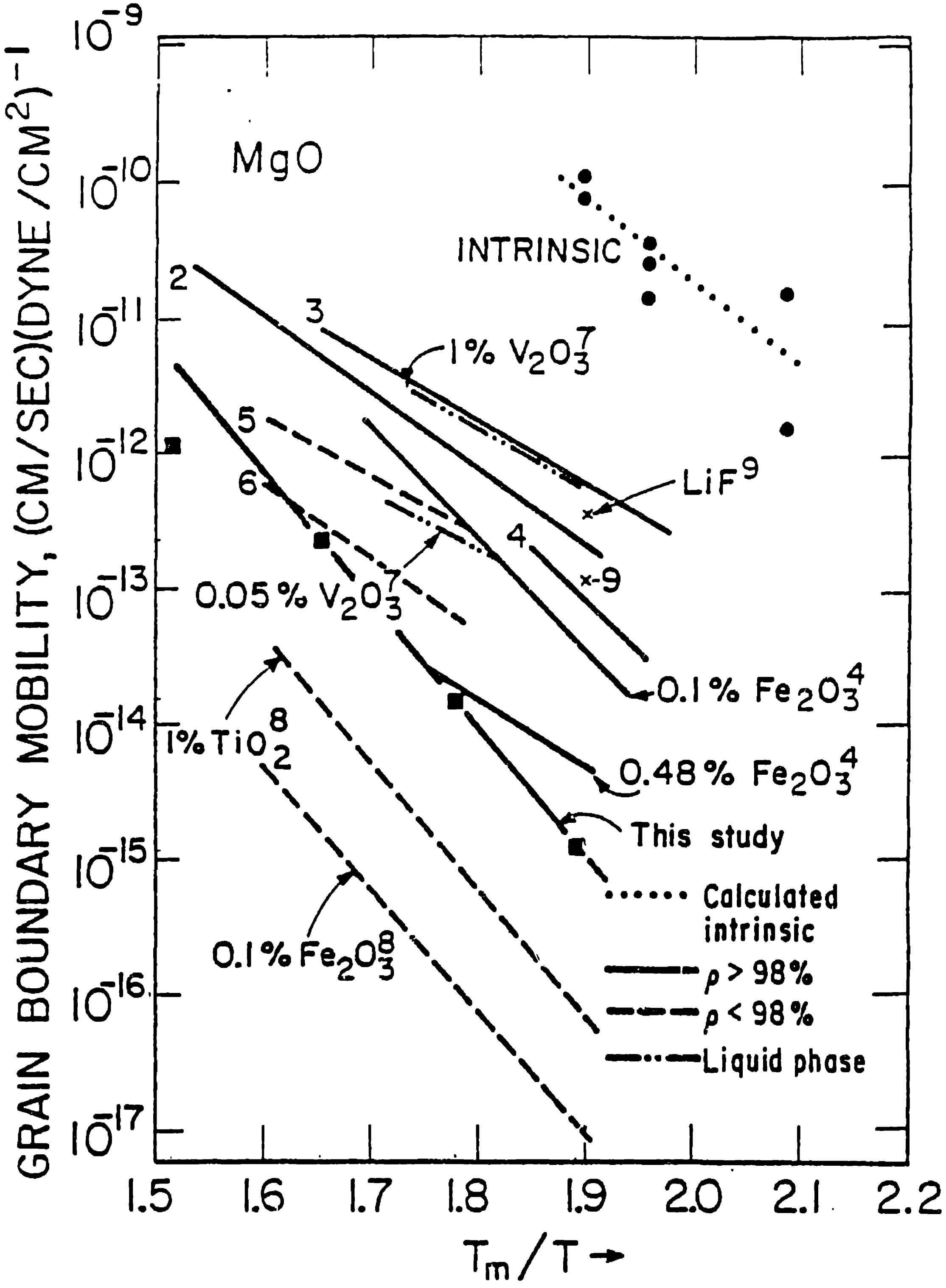

Figure III-9 Grain boundary mobilities calculated from grain growth data from this study and previous studies as a function of temperature.

The settled MgO compacts heated to 1620 K, 1740 K, and 1870 K for times up to 114 h did not sinter in the closed pore stage. The particle/grain sizes reached "limiting" values at each sintering temperature and were uniform through the sample thickness although initial particle sizes varied from 4 μm to 0.5 μm. Because grain size changes as $t^{1/2}$ or $t^{1/3}$, a factor of 2 change in the grain size corresponds to a factor of 4-8 increase in annealing time. This leads to an apparent "limiting" grain size at long times.

These observations of a "limiting" uniform grain size through the sample thicknesses are in good agreement with the microstructural evolution calculated from the expressions in Section II.1 and Appendix I for simultaneous sintering and coarsening. For low background impurity levels, sintering of MgO is slow relative to coarsening. Coarsening was predicted to dominate up to a grain size and density at which sintering is significant relative to coarsening. This is a direct result of sintering controlled by lattice diffusion and coarsening by surface diffusion. As observed in Section II.1, sintering by grain boundary diffusion and coarsening by surface diffusion yield a grain size/pore size independent trajectory (d ln G/d ln r) on the $\bar{G}$-$2r_p$ graph.

The calculations of (d ln $\bar{G}$/d ln r), from Section II.1, were based on a lower value of δD_b for the higher purity material and no change in D_l from that measured for lower purity material. However, if D_l and D_s decrease as the concentration of background impurities decreases, evaporation/condensation may determine microstructure evolution. From this study, it is not possible to evaluate Γ.

These sintering and grain growth results are also in good agreement with the results of Brown (1965) for sintering and grain growth in high-purity MgO. In the study by Brown, cold-pressed compacts of high-purity MgO were sintered at temperatures ranging from 1570 K to 2000 K for times up to 100 h and were examined optically. No change in grain size was observed for samples heated to T < 1770 K for T < 100 h. At 1870 K "slight" grain growth was observed; at 2000 K, discontinuous growth occurred.

Although this study does not extend to T > 1870 K, there is a datum at 2030 K for the high-purity MgO produced for this work. Shaw and Brook fast-fired green tubes of the high-purity MgO prepared for this study to 2030 K following the procedures as described by Vieira (1980). The green compact was not uniform and the fast-fired compact contained both open and closed porosity. The material had undergone discontinuous grain growth and pores were entrapped, in good agreement with the results of Brown.

It is possible that the original unsintered microstructure was not ideally stratified from 4 μm at the sample bottom to 0.5 μm at the sample top and instead was a mixed structure of 4 μm to 0.5 μm particles through the sample thickness. This uniform microstructure could result in a lack of grain size difference through the sample thickness after annealing. Settling of a suspension with a bimodal particle size distribution can produce a load-bearing network of large particles with smaller particles deposited in the interstices. The reagent grade settled compacts, described in Chapter II.3.4, had particle size gradients through the sample thicknesses (as determined by SEM observation). No SEM examination of the gradient in the high-purity compact was possible because of charging of the MgO compact in the electron beam.

From the single experiment by Shaw and Brook, the grain size (12 μm) and the time at 2030 K (20 min) were used to calculate K_2, K_3, and the corresponding effective mobilities. The calculated values are listed in Table III-10 and M_{eff} is included in Figure III-9. This value of M_{eff} is approximately the value extrapolated at lower temperatures.

The values of the effective boundary mobility are similar to those determined from studies of doped and "normal" purity MgO. The concentrations of total cationic impurities are estimated to be 100 ppm, primarily Ca from calcination, as described in Section III.2. Contamination of the MgO samples by transition metal ions was not evident from visual inspection of the color of solutions of MgO dissolved in concentrated HCl. Visual inspection of these solutions can detect total transition metal ions at ~10 ppm (Gabbe, personal communication).

The low mobilities are unexpected based on consideration of the total background cation levels. However, in light of the results of Glaeser (1981) on trace element (Al^{3+}) effects on grain boundary migration in LiF, the similarity between the calculated mobilities of Fe-doped MgO and of high-purity MgO suggests the dominance of low levels of cationic impurities. Alternately, the level of anionic impurities may be the dominant factor in determining the LiF mobilities as well as the MgO boundary mobilities. The total anionic impurity levels may be high but were not measured either in the LiF samples or in the MgO samples used in this study.

The Turnbull analysis of the correlation between grain boundary diffusion and grain boundary mobility (1951) yielded the following expression:

$$M_b = \frac{D_b \Omega}{\delta k T} \qquad \text{(III-8)}$$

Using the estimated value of the grain boundary diffusivity at 1620 K of $D_b < 10^{-18}$ cm^3/sec, for undoped MgO (Hodge and Gordon, 1978), and $\delta = 3 \times 10^{-8}$ cm, the calculated mobility is $\sim 4 \times 10^{-13}$ (cm/sec)$(\frac{\text{dyne}}{\text{cm}^2})^{-1}$. The effective mobility calculated from grain growth at 1620 K is $\sim 1.5 \times 10^{-16}$ (cm/sec)$(\frac{\text{dyne}}{\text{cm}^2})^{-1}$. Although M_{eff} from grain growth is smaller by two orders of magnitude than M_b from Equation (III-8), the value of δD_b is only an upper limit and could be two orders of magnitude smaller.

From STEM studies of grain boundary segregation in MgO (Chiang, et al. 1981; unpublished research), the width of the segregated layer can be as large as 50 nm. In this layer the defect concentration can be much larger than in MgO boundaries without segregants. Higher diffusivities and mobilities could be associated with highly doped, highly defective boundaries. Conversely, low mobilities and low grain boundary diffusivities could be associated with clean boundaries. However, from consideration of the effects of solute drag on boundary mobility, the mobilities of the higher purity boundaries are expected to be higher than in the "doped" material.

III. 4 Conclusion

III. 4.1 Preparation of High Purity MgO

The maximum total cationic impurity level in the MgO precursor was significantly reduced by clean room processing, by liquid-liquid extraction of the aqueous solution using DDDC in $CHCl_3$, and by EDTA-masking of alkaline earth ions during hydrogmagnesite precipitation. The levels decreased from 470μg/g (Mg metal basis) for the Mg-source material to $<$ 8μg/g for the EDTA-masked hydromagnesite, which is signficantly lower than for commercially available high purity MgO and Mg, especially with respect to Si, Ca, Fe, and Mn.

During incorporation of Al into DDDC-extracted hydromagnesite, the cation impurities did not increase. With Ca doping, Sr and Na increased to 12μg/gm.

During transformation of the DDDC-extracted precursor to the oxide, Ca increased from 20 to 130 μg/g and Na from 15 to 60μg/gm. Deagglomeration and compact formation did not significantly increase cation contamination beyond the increase attributed to the transformation to the oxide.

III. 4.2 Sintering and Grain Growth

Settled compacts of high purity MgO sintered to 65-80% of theoretical density and exhibited significant coarsening. The microstructures were observed to be uniform through the sample with no discontinuous grain growth or pore entrapment. This is consistent with the calculated evolution based on the literature data and Cannon's model of simultaneous sintering and coarsening.

The calculated boundary mobilities were found to be two orders of magnitude lower than values calculated using δD_b from creep experiments on high purity

MgO and four orders of magntidue lower than the values calculated using δD_b from creep experiments of low purity MgO.

Chapter IV. Dihedral Angles (Surface and Grain Boundary Energies in MgO and Al_2O_3)

IV.1 Introduction

In the first-order modelling of sintering phenomena, the solid-vapor surface energy (γ_s) has been used as the driving force for neck growth between particles and for densification, while the grain boundary energy (γ_b) has been used as the driving force for grain growth. Both γ_s and γ_b have been assumed to be isotropic. The densification rate relative to the grain growth rate at the final stage of sintering has been modelled by Cannon, et al. and by Hsueh, et al.. (1982), and the criterion for pore separation from boundaries by Hsueh, et al.; these may be expressed in terms of the ratio of γ_b/γ_s or of the dihedral angle. In both of these treatments, γ_s and γ_b were still assumed to be isotropic. However, the basic theory dictates and various experimental results demonstrate the need for the inclusion of the variability and anisotropy of each for more accurate modelling of sintering from initial to final stage and, in particular, of pore-boundary separation during final stage sintering.

It seems clear from Cannon's and Hsueh, et al.'s modelling that the distribution and the extremes in the values of the ratio γ_b/γ_s for a given material will affect the local pore stability. Breakaway of boundaries from some pores while others migrate with grain boundaries may be expected. An additional driving force for migration may be introduced by the change in γ_b with misorientation and γ_s with surface orientation Thus, local variations in the pore breakaway criterion from point to point in the structure are expected.

The differences in the stability and in the pore-boundary migration characteristics of pores with different dihedral angles make it probable that the dihedral angle distribution for a material will change from the initial stage in the final stage of sintering and, likewise, during the desintering of an initially dense body due to internal gas evolution. A similar process is cavity nucleation and growth during creep of an initially dense material. In this case, the direction of applied stress, the distribution of grain orientations, and the distribution of possible dihedral angles determine the dihedral angles observed during creep cavitation. As described in Chapter I, either cavities will nucleate first on boundaries with low dihedral angles or cavities remaining from previous processing which also have low dihedral angles will grow.

Due to the lack of data on the variability of γ_{gb} and γ_s or the dihedral angle for any ceramic, inclusion of the effect of a range of these values into models of sintering or pore-boundary interactions has not been important.

The magnitudes of the surface energies and the grain boundary energies are difficult to measure independently to yield values for specific surfaces and boundaries. However, the surface-boundary energy ratios can be evaluated from groove angles (dihedral angles) that form on the solid-vapor interface at boundary intersections during heat-treatment or that exist at pore-grain boundary intersections. By performing many measurements on a polycrystalline surface with randomly distributed grain surfaces and grain boundaries, the total distribution of dihedral angles for a material can be determined.

By comparing the distribution of dihedral angles from thermally grooved surfaces with the distribution from a compact undergoing sintering, bloating or creep cavitation, the effects of the variations of γ_{gb} and γ_s on microstructure development can be assessed.

In this study the distributions of dihedral angles from grain boundary grooves were measured for several polycrystalline ceramic materials using different measurement techniques. The orientations of the grain boundaries intersecting free surfaces were assumed to be random. A new technique using metal reference lines has been used to determine the distribution of dihedral angles on the surfaces of thermally grooved polycrystalline samples of MgO, undoped Al_2O_3, and MgO-doped Al_2O_3. The data for MgO-doped Al_2O_3 are compared with distributions determined by interferometry for the same thermally grooved surface. The dihedral angle distribution for thermally grooved MgO-doped Al_2O_3 is compared with the distribution of apparent dihedral angles characterizing creep cavities in a TEM foil of the same composition. The apparent dihedral angles from creep cavities in MgO due to internal gas evolution and from pores in a sintered body are also compared with the distributions from thermally grooved MgO.

In different materials with different dopants or impurities, greater variations in γ_{gb} and γ_s are expected than in a single material; this originates from changes in the bond type and segregation effects. Although the ratio of some "average" values (γ_b/γ_s) may be expected to be of order $(\sim 1/2)$ because each scales with the bond strength, the extremes of the ratios may vary significantly for materials whose bonding is described by central forces (metals, ionics) or by highly directional bonds (covalents).

Numerous experimental and theoretical studies of metals and alloys have been reported on the variations of the surface energy and the grain boundary energy with composition, orientation, and temperature. In ceramics, the data base is much smaller, consisting of limited studies of MgO, NiO, UO_2, Al_2O_3, and the alkali halides. In the following sections, literature on surface and boundary energies is reviewed and comparisons are made between the magnitudes of the interfacial energies in metals, ionics and covalents. Theoretical calculations of these energies and equilibrium atomic structures based on structural and molecular dynamics models, are compared with experimental results. The effect of the ranges of dihedral angles on sintering and pore-boundary interaction are discussed for each material type.

IV.2 Literature Review

IV.2.1 Grain Boundary Groove Formation

Most experimental measurements described in this chapter are based on the balance of forces at the intersection of three interfaces to form a line. In a plane perpendicular to the intersection line, the line forces associated with the three forces most sum to zero at the point of intersection. During heating of smoothly polished polycrystalline material, "grooves" will form along the boundaries to establish the force balance. In general form, the balance of forces can be written (Herring, 1951):

$$\sum_{i=1}^{3} \gamma_i t_i + (t_i \times \ell)\left(\frac{\partial\gamma_i}{\partial\psi_i}\right) = 0 \qquad \text{(IV-1)}$$

where γ_i is the energy of the ith interface and t_i is the unit vector in the plane of the ith interface, normal to the line of intersection of the three interfaces and pointing away from this line, $(\partial\gamma_i/\partial\psi_i)$ is the orientation dependence of γ_i and n is the unit vector normal to the line of intersection, ℓ, such that $n = t_i \times \ell$. The force balance for the intersection of a general grain boundary with a vapor species is shown schematically in Figure IV-1(a). The groove geometry illustrated in Figure IV-1(b)is based on the assumptions generally made in measurements of ψ, the dihedral angle; the surface energies are single valued and isotropic, and the boundary meets the surface at 90^0. In this case, grooving is symmetrical with respect to a general surface normal and Equation (IV-1) reduces to:

$$\gamma_{gb} = 2\gamma_s \cos\frac{\psi}{2} \qquad \text{(IV-2)}$$

and the grain boundary to surface energy ratio is measurable from the dihedral angle alone. Except in special cases, where the orientation of the grains are symmetrical with respect to the grain surfaces and the grain boundaries are normal to the surface, the groove is asymmetrical, changes in energy with orientation $(\partial\gamma_i/\partial\psi_i)$ are non-zero, and the use of Equation (IV-2) is not justified.

Another special case of force balance is shown in Figure IV-1(c) for twin boundary-surface intersections. Using the equation presented

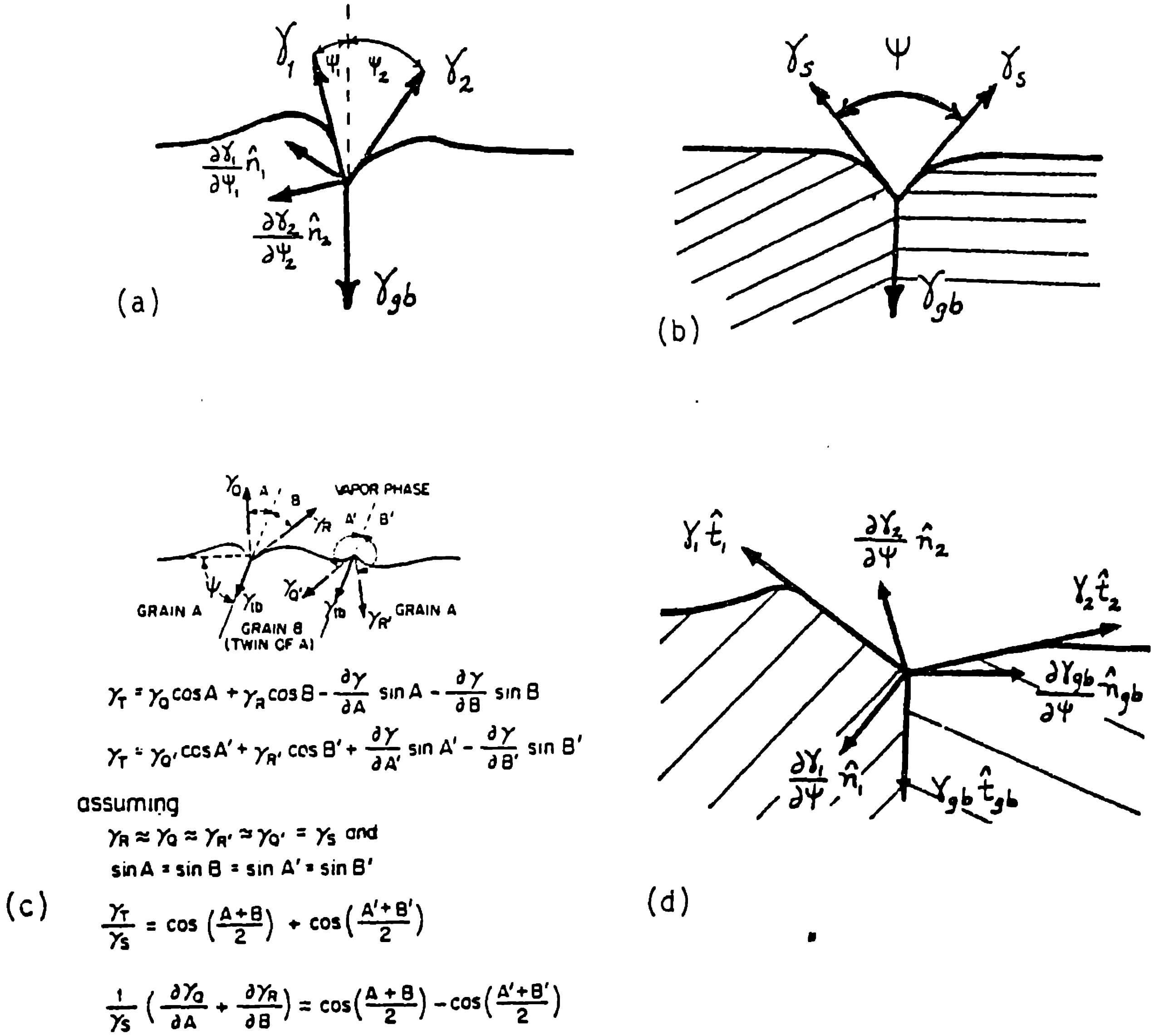

$$\gamma_T = \gamma_Q \cos A + \gamma_R \cos B - \frac{\partial\gamma}{\partial A}\sin A - \frac{\partial\gamma}{\partial B}\sin B$$

$$\gamma_T = \gamma_{Q'} \cos A' + \gamma_{R'} \cos B' + \frac{\partial\gamma}{\partial A'}\sin A' - \frac{\partial\gamma}{\partial B'}\sin B'$$

assuming

$\gamma_R \approx \gamma_Q \approx \gamma_{R'} \approx \gamma_{Q'} = \gamma_s$ and

$\sin A = \sin B = \sin A' = \sin B'$

$$\frac{\gamma_T}{\gamma_s} = \cos\left(\frac{A+B}{2}\right) + \cos\left(\frac{A'+B'}{2}\right)$$

$$\frac{1}{\gamma_s}\left(\frac{\partial\gamma_Q}{\partial A} + \frac{\partial\gamma_R}{\partial B}\right) = \cos\left(\frac{A+B}{2}\right) - \cos\left(\frac{A'+B'}{2}\right)$$

Figure IV-1 Grain boundary configuration and force balance for (a) the intersection of a general grain boundary with a vapor species; (b) grain boundary perpendicular to surface and an isotropic surface energy; (c) twin boundary-surface intersection; and (d) an asymmetrical groove with modified force balance.

in Figure IV-1 an expression is given for the $\partial\gamma_s/\partial\psi_i$ terms.

In the absence of data for the $\partial\gamma_i/\partial\psi_i$ terms, Equation (IV-2) is used. For consideration of surface energy anisotropy, Equation (IV-1) can be modified for asymmetrical grooves as shown in Figure IV-1 (d).

$$\gamma_{gb} = \gamma_{s_1} \cos \psi_1 + \gamma_{s_2} \cos \psi_2 \qquad \text{(IV-3)}$$

and

$$\psi_{s_1} \sin \psi_1 = \gamma_{s_2} \sin \psi_2 \qquad \text{(IV-4)}$$

IV 2.2 Measurements of Grain Boundary Groove Angles

IV 2.2.1 Thermal Groove Angles

In this study an experimental technique based on photoresist masking process was used for measuring the distribution of dihedral angles from thermally grooved surfaces. A photoresist is formed on the surface and exposed using a monochromatic light source and a diffraction grating. The exposed photoresist is stripped from the sample surface leaving bonds of photoresist whose sides are perpendicular to the sample surface. Metal is evaporated on top of the remaining photoresist and directly onto the sample surface between the lines of photoresist. The photoresist is dissolved leaving a metal grating which conforms to surface features, such as facets and grain boundary grooves.

At a specimen stage tilt angle of 0° where the projection plane is parallel to the grooved surface, the metal grating appears straight as shown in Figure IV-2(a). When a grain boundary groove which is crossed by a metal line is observed in the SEM at a specimen stage tilt angle greater than 0°, Figure IV-2(b), an apparent groove angle, ψ', is observed where $\psi' = \psi'_1 + \psi'_2$. From projective geometry, the true dihedral angle can be calculated from measurements of ψ'_1 and ψ'_2 from SEM photomicrographs for most orientations of the boundary relative to the metal line.

The projective geometry of a metal line perpendicular to a grain boundary groove is shown in Figure IV-2(c). At a SEM tilt angle of 60°, the metal line-grain boundary groove angle measured at the groove root is $\psi'_1 + \psi'_2$. At a SEM tilt angle of 90°, the observed angle is the true angle. The true angles can be calculated from observed angles at a known degree of stage tilt from

$$\tan \psi_i = \sin (\text{stage tilt angle}) \tan \psi_i' \qquad \text{(IV-8)}$$

This equation is derived in AppendixAII. For metal lines not perpendicular to the boundary, the angle ψ_1' and ψ'_2 can be constructed geometrically from the observed groove profile and the angle which the boundary makes with the metal line.

This technique has many advantages over other techniques used to measure dihedral angles. The most common technique is interferometry of grooved surface. A second technique used by Gaddapati on twin boundary grooves in Al_2O_3 is the production of carbon contamination reference lines in the SEM on a thermally grooved surface (Achutaramayya (Goddapati) and Scott, 1973).

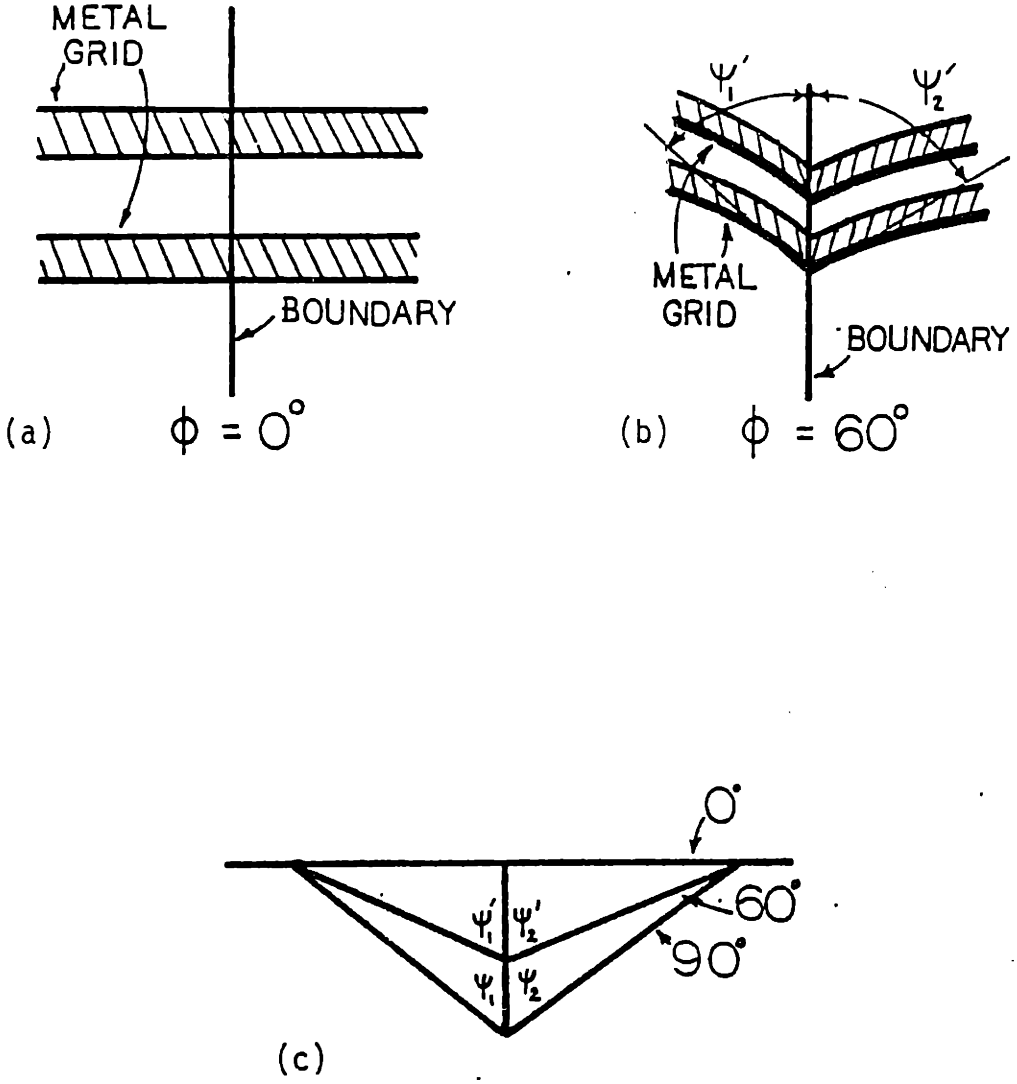

Figure IV-2 Metal reference line geometry (a) metal grid and sample surface observed at a tilt angle of 0°; (b) metal grid and sample surface observed at a tile angle of 60°; and (c) projection geometry of metal grid- grain boundary intersection at 0°, 60°, and 90°.

(Gaddapati) and Scott, 1973). The metal reference line and the carbon contamination line technique are based on the same geometry. These techniques are evaluated below, with special emphasis on interferometry since in this study the same sample has been examined by both interferometry and the metal line technique. In the interferometric measurement of grain boundary grooves, the true dihedral angle, ψ, is calculated from the interfringe spacing, a, and the measured angle between the fringes ψ', by the following equation:

$$\tan \frac{\psi}{2} = \left(\frac{2a}{M\lambda}\right) \tan \frac{\psi'}{2} \qquad \text{(IV-6)}$$

where M is the magnification, and λ is the wavelength of the monochromatic light source (Amelinckx, et al., 1953).

Equation (IV-6) has been corrected by Tolman and Wood for the effects of oblique rays on the measured fringe spacing at high magnifications. It was found empirically that the fringe spacing was greater than $\lambda/2$ by approximately 10% (Tolman and Wood, 1956). The corrected equation is:

$$\tan \frac{\psi}{2} = \left(\frac{2a}{1.1\ \lambda M}\right) \tan \frac{\psi'}{2} \qquad \text{(IV-7)}$$

The correction factor is not necessary at low magnifications and when the oblique rays are removed by stopping down the objective aperture.

When dihedral angles are large ($> 160^{\circ}$), interferometry can be used effectively to measure surface profiles. The ranges of angles measured between interference fringes ranging from 20° to 160° correspond to true dihedral angles from 160^0 to 180^0 for typical light sources and magnifications. For example, when $(\frac{2a}{1.1\ \lambda M}) = 50$, and $\psi = 160^0$, $\psi' = 13^0$; when $(\frac{2a}{1.1\ \lambda M}) = 30$, and $\psi = 160^0$, $\psi' = 21^0$. The true dihedral angles from 80^0 to 160^0 produce the following ranges of fringe angles: $(\frac{2a}{1.1\ \lambda M}) = 50$, 2^0 to 13^0; and $(\frac{2a}{1.1\ \lambda M}) = 30$, 3^0 to 21^0.

For $(\frac{2a}{1.1\ \lambda M}) = K = 24$, which was the minimum value obtainable by Gjostein, and for a known measurement error of $\pm 2^0$ in ψ', the true angle lies in the range from 118^0 to 137^0 for $\psi' = 10^0$. When $\psi' = 20^0$, $K = 24$, and $\Delta\psi' = \pm 2^0$, the true angle is in the range of 161^0 to 163^0. An error analysis of the interferometric technique as determined by Gjostein (1958)is presented in Appendix III. The effect of measurement error on the accuracy of angles is shown in Figure IV-3 for K = 24 and ψ' from 1^0 to 20^0. For small groove angles, interferometry is, therefore, not the appropriate technique for groove angle measurement. At groove widths <1 μm and for wide and deep grooves, interferometry is not appropriate due to optical resolution problems.

The carbon reference line technique is based on the same principle as the metal reference line technique used in this study. The contamination line is formed by scanning the SEM electron beam along a line normal to the sample surface and to the grain boundary groove at a specimen stage tilt angle of 0^0. The sample is tilted and the observed angle at the grain boundary delineated by the carbon line, which follows the surface groove, can be used to calculate the dihedral angle. Carbon reference lines have been successfully used for measurements of several twin boundary angles in

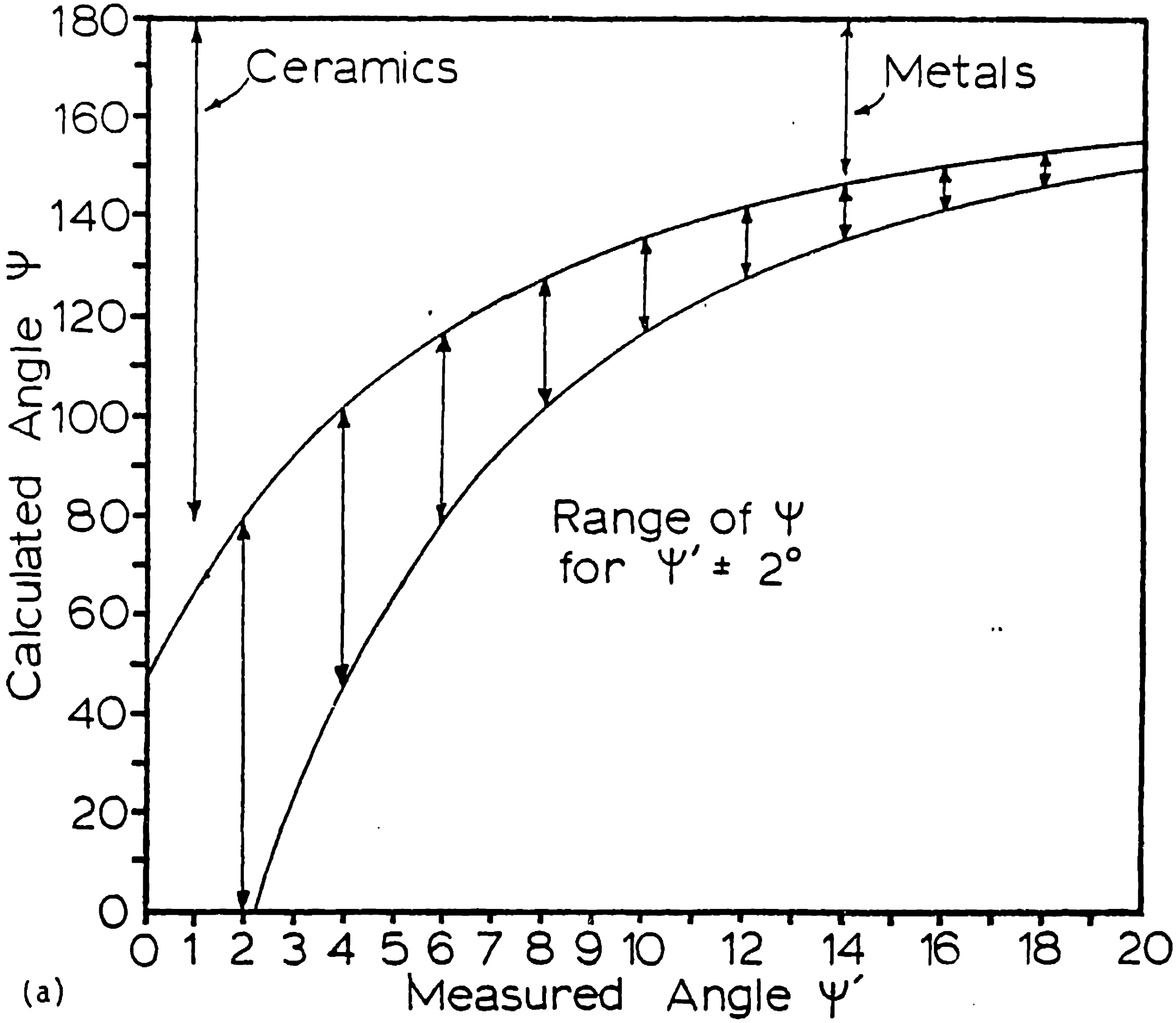

(a)

Figure IV-3 Range of calculated dihedral angles possible with a known measurement error of ± 2° (a) for interferometry and (b) for the metal reference line technique.

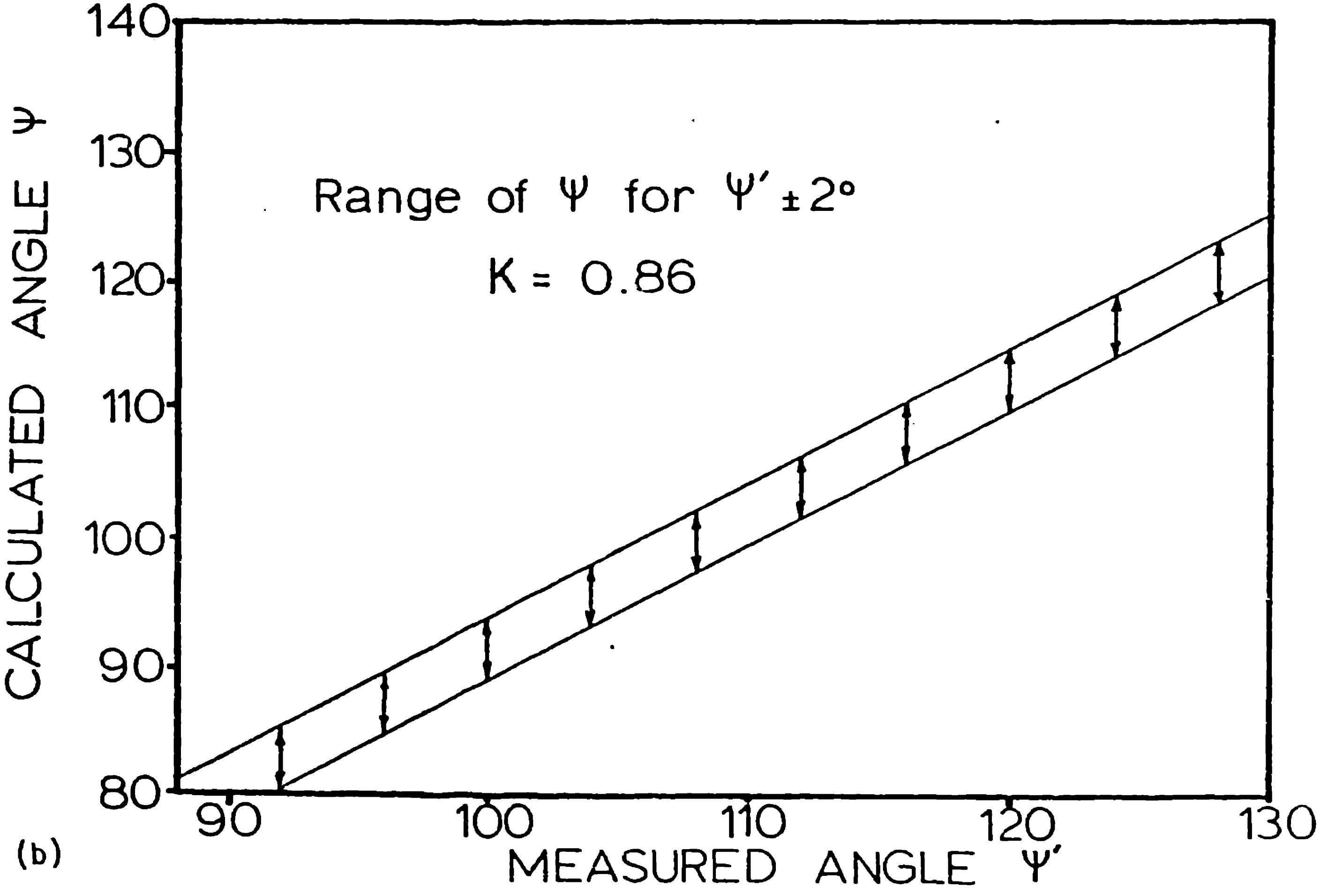
Range of Ψ for Ψ′ ± 2°
K = 0.86
CALCULATED ANGLE Ψ
140
130
120
110
100
90
80
90
100
110
120
130
MEASURED ANGLE Ψ′

(b)

Al_2O_3. However, there are major problems in implementing this technique . With a clean microscope and sample, the contamination line will not form. If the sample or specimen chamber is contaminated to allow line generation the resolution deteriorates. In practical terms, it is difficult to tilt a sample from 0° to 60° in the SEM at high magnifications without having the carbon reference line move out of the field of view.

In the metal reference line technique errors are due, predominately to poor ceramic metal adhesion. The ceramic-metal bond may be poor for some samples leading to metal grating pull-off during removal of the photoresist. For narrow grooves, the photoresist may not penetrate to the groove root, producing apparent dihedral angles which are too large. In addition, a second phase at the grain boundary, undetectable by SEM, could determine the groove profile at the groove root.

The range of calcualted angles produced by a $\pm 2°$ error in ψ' is shown in Figure IV-3(b) for measured angles from 90° to 130° at a tilt angle of 60°. The error bars doe not vary significantly with measured angles, as compared with those for the inteferometric technique.

IV 2.2.2 Groove Angles on Porous, Polished Sections

The apparent dihedral angle distribution from random sections through a single free surface-boundary intersection has been analyzed by Harker and Parker (1945). The apparent dihedral angle distributions for single-valued true dihedral angles are shown in Figure IV-4 (a) for $\psi = 15° - 165°$.

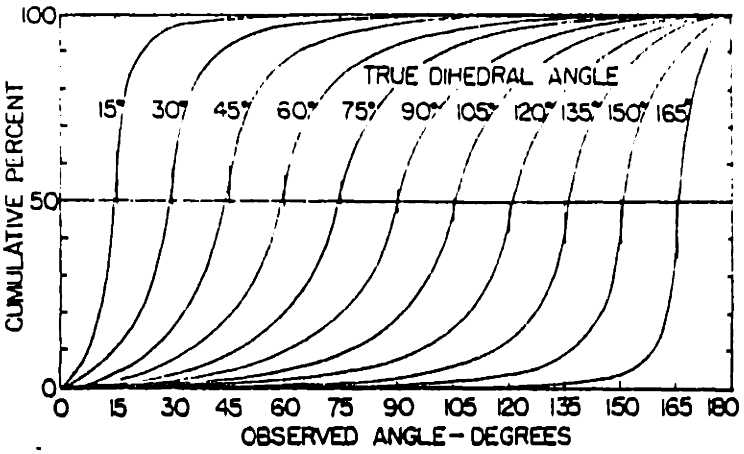

(a)Cumulative distributions of the observed dihedral angles for various true angles (from Riegger and Van Vlack).

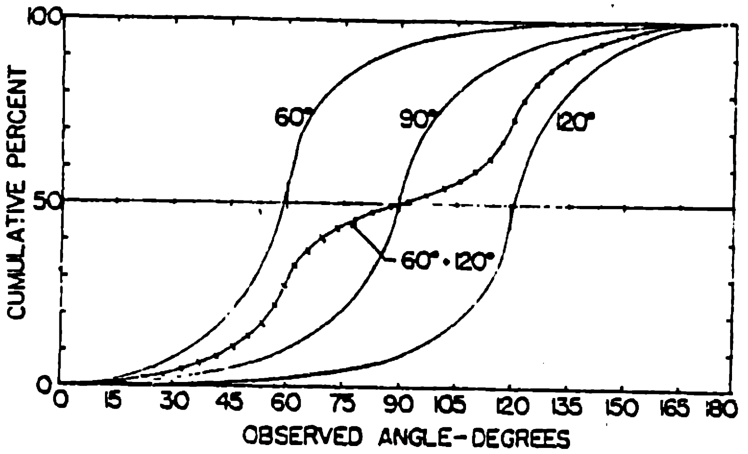

(b)Bimodal distribution for equal numbers of 60° and 120° true angles.

Figure IV-4

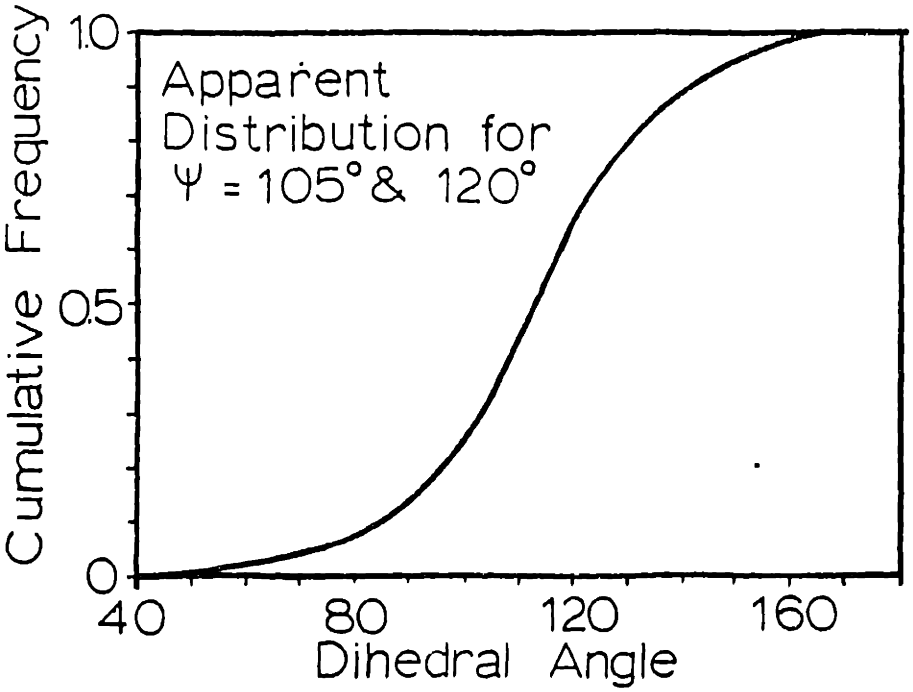

(c)Bimodal distribution for equal numbers of 105° and 120° true angles.

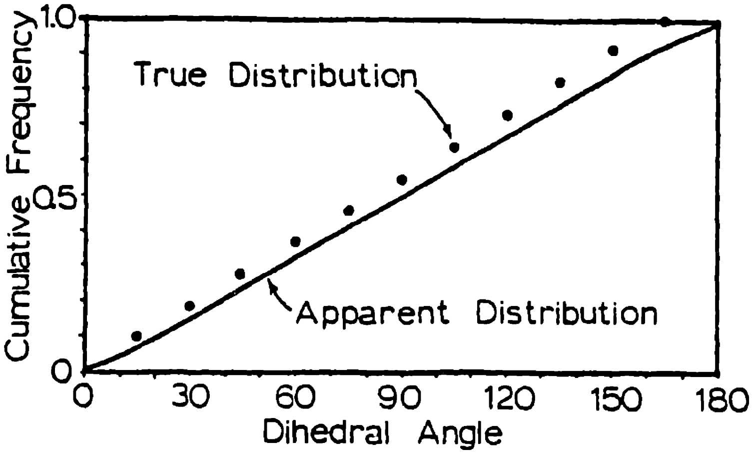

(d)Flattened distribution due to a range of true dihedral angles.

For all values of ψ, the apparent dihedral angle varies from 0^o to 180^o with the median value approximately equal to the true value. The case of two dihedral angles of equal frequency was considered by Riegger and Van Vlack (1960). The distribution of apparent dihedral angles for a solid with equal numbers of true angles of 60^o and 120^o is compared with the apparent distribution for a solid with a true dihedral angle of 90^o in Figure IV-4(b). While the distributions have the same median angle, the distribution for the mixed angles is clearly the sum of two random distributions. For a narrower distribution of true angles, the distribution of apparent angles is flattened relative to the distribution for a single true dihedral angle with the same median value. This is illustrated in Figure IV-4(c) for two true angles: 105^o and 120^o. The combined apparent distribution is flatter than the distribution of $\psi = 112^o$ but the two modal values at 105^o and 120^o correspond to true values of ψ. For a broad but uniform distribution of true angles (15^o-165^o), the apparent distribution is also flatter than the distribution for $\psi = 90^o$, the median value, as shown in Figure IV-4(d). This distribution is also compared in Figure IV-4(d) with the distribution of true angles assumed in the determination of the distribution of apparent angles, i.e., one each of $\psi = 15^o$, 30^o, 45^o, 60^o, 75^o, 90^o, 105^o, 120^o, 135^o, 150^o, and 165^o. The distributions of apparent angles and true angles are similar and have the same median. This is of special significance when comparing angles from grooved surfaces ("true" angles) with angles from random sections through porous samples ("apparent" angles). If the distributions of angles do not have the same median and do not overlap significantly, then the populations of angles in the two samples are different.

For dihedral angle measurements from planes of polish of porous solids the deconvolution of angular data is complicated by the coupling between pore shape and size and apparent dihedral angle. A simpler problem has been analyzed by Gokhale, Iswuran, and DeHoff (1981) for lenticular-shaped pores (pores on grain faces) of various sizes with a single dihedral angle or for lenticular pores of the same in-boundary radius but different dihedral angles. An example of a polished section through lenticular pores of the same size with a single dihedral angle is shown in Figure IV-5(a). In Figure IV-5(b) is shown a pore of ψ and in boundary radius of r*. Planar cuts through the pore yields pores with apparent dihedral angles greater than ψ(AA' ($\psi' = 180^0$), BB' ($\psi = 180^0$), EE'), equal to ψ (DD'), and less than ψ (CC' and FF'). There are pores in planes of polish with ψ' greater than or less than ψ which have projected areas less than a given area. For a single pore size and shape, the distribution of apparent dihedral angles is, therefore, a function of the resolution unit of the microscope used to examine the planes of polish. To properly determine the relationship between location of pore (2-, 3-, or 4-grain intersections) size of pore, and dihedral angle, construction of a three-dimensional image of the microstructure through serial sectioning is required. This is beyond the scope of this study. The distributions of apparent angles in polished sections presented in this study are, therefore, used to suggest trends in the distributions of true angles rather than to represent a complete apparent distribution.

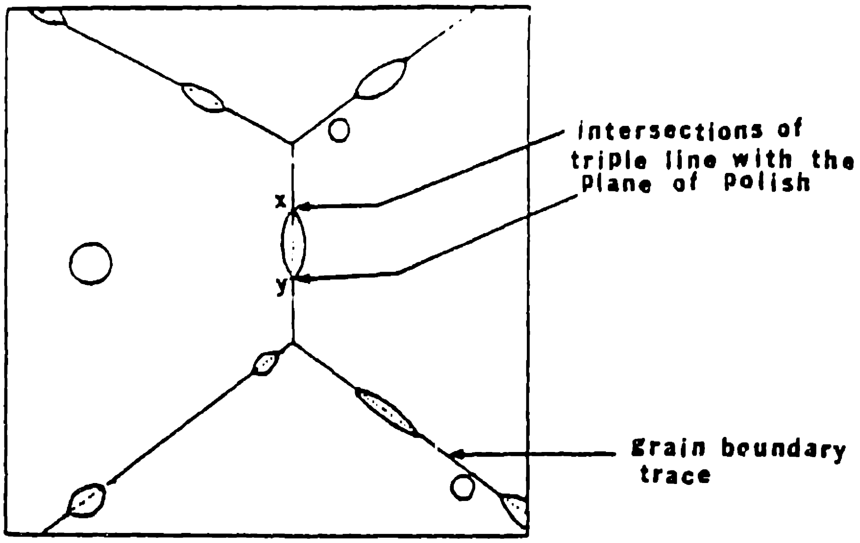

Figure IV-5 (a) Schematic of plane of polish of a microstructure consisting exclusively of single-sized lenticular pores located on grain faces. (from Gohkale et al., 1981).

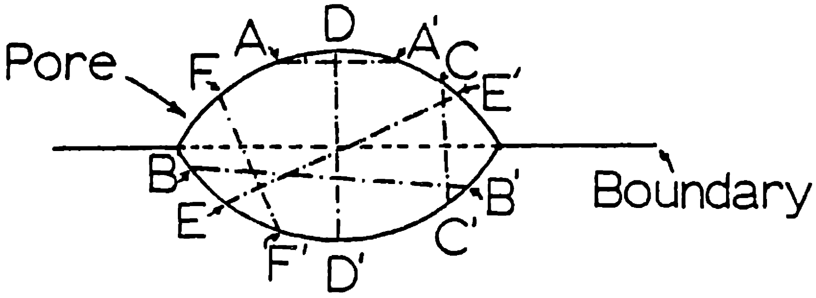

(b) Observed dihedral angles generated by different planes of polish for a lenticular pore.

Poor polishing and non-random pore distribution in the samples can also introduce significant error in the measurement of apparent dihedral angles. In this study, polishing defects such as grain pull-out, pore rounding, and scratches were eliminated by careful polishing at small grit size (0.25 μm diamond) and light loads. Fracture surfaces which were approximately planar were also used for apparent angle measurements.

IV.2.3 Surface Energy

The range of surface energies varies with crystal structure, chemical composition and temperature. The formalisms describing the surface energy and its variations with these parameters are given below.

For a given material system at constant temperature, the variation in surface energy, γ_s, can be easily visualized by reference to the Wulff plot. The Wulff plot is the projection of the three-dimensional variation of γ_s with orientation for a single or multiple component system at constant temperature. A Wulff plot is derived form projecting the vector $r(\theta,\phi) = \gamma(n)n$ onto the θ plane, where n is a unit vector defined by the origin of the axes and the direction normal to the crystal surface in terms of θ and ϕ and $\gamma(n)$ is the surface energy whose orientation is "defined" by n. The Wulff plot should be used with caution because the complete specification of a surface requires three parameters rather than the two defining the surface normal. This implies that the lowest energy plane perpendicular to n has been determined and used in the construction of the Wulff plot. Although the position and structure of this plane can, in principle, be found experimentally or by molecular calculations, it is not represented in the Wulff construction. With this caveat understood, the Wulff plot will be used in discussing theoretical and experimental surface energy results.

The change in surface energy with other species in solid solution or adsorbed on the surface has been treated by Gibbs and is, for i species, with chemical potentials, μ_i,

$$d\gamma = -S^X dT + \Delta x dP - \sum_i \Gamma_i d\mu_i \tag{IV-8a}$$

where γ is the specific interfacial free energy, S^X is the interfacial entropy per unit area of interface, and Γ_i is the surface excess of the ith component, and Δx is the interface width. At constant T and P, Equations (IV-8a) reduces to:

$$\frac{d\gamma}{\partial\mu_i}_{T,P,\mu_i\neq j} = \Gamma_i \tag{IV-8b}$$

For a positive surface excess (adsorption or segregation of the ith species), the surface energy decreases. The effect of adsorption on the Wulff plot for any crystal structure or material is not currently predictable.

Some details of the Wulff plot are discernible through transitions in faceting accompanying composition changes. The transition from a non-faceted to a faceted surface for cubic materials has been described by Herring in terms of a tangent construction on the Wulff plot. The Herring construction and the stability equations are presented in Figure IV-6. For faceting to occur, the values of γ_B and $(\frac{\partial\gamma}{\partial\psi})_B$ reach a critical value relative to γ_A and $(\frac{\partial\gamma}{\partial\psi})_A$.

The temperature dependence of the surface energy of a single component at constant volume is:

$$\left(\frac{d\gamma}{dT}\right)_V = -S \qquad \text{(IV-9)}$$

where S is the entropy. Since S is always positive, $\frac{d\gamma}{dT}$ is negative. For a multicomponent system, $\frac{d\gamma}{dT}$ is a function of the surface excesses and the partial molar entropies of the components and can be either positive or negative.

From a simple bond breaking treatment, anisotropy in γ_s is expected. Nicholas (1968) has calculated relative surface energies for fcc and bcc metals as a function of surface orientation in terms of the broken first and second nearest neighor bonds using Morse and Lennard-Jones potentials and no relaxation. The results are shown on a stereographic triangle for an fcc metal based on the Lennard-Jones potential in Figure IV-7.(a) for 0^oK. Although the predicted order of energies for low index planes for all fcc metals is $\gamma_{111} < \gamma_{100} < \gamma_{110}$ based on bond breaking of nearest neighbors, the ranking varied with potential. The maximum anisotropy for fcc and bcc metals, regardless of the potentials used, was 1.13 and the (111), (100), and (110) were found to be local minima.

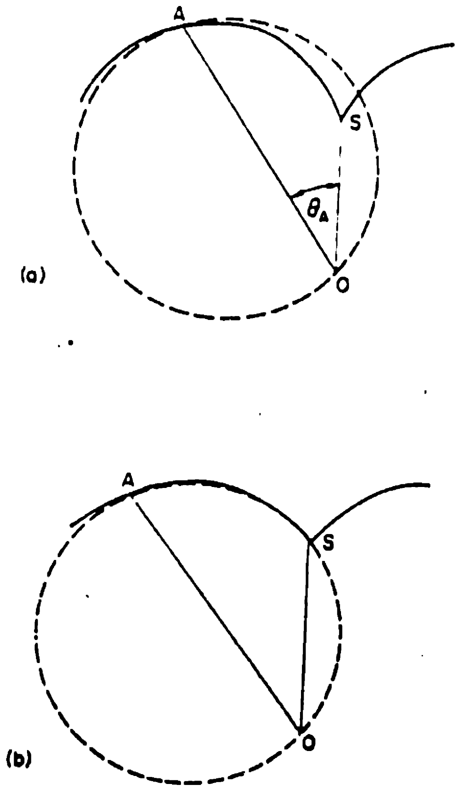

$$\left(\frac{\partial\gamma}{\partial\theta}\right)_S \geq \gamma_A \sin\theta_A + \left(\frac{\partial\gamma}{\partial\theta}\right)_A \cos\theta_A,$$

$$\gamma_S \geq \gamma_A \cos\theta_A - \left(\frac{\partial\gamma}{\partial\theta}\right)_A \sin\theta_A.$$

Figure IV-6 Tangent sphere criterion for stability of a particular surface with respect to faceting. OA represents the surface tension and orientation of a surface A close so some surface S at which a γ-plot cusp occurs. A is unstable with respect to faceting of the sphere through the origin and tangent to the γ-plot at A is pierced by the γ-plot as shown in (a); (b) represents the limiting condition for stability of a surface with respect to forming facets of S. The sphere tangent at A passes through S. (from Blakely, 1973).

The experimental studies of the surface energy variation with orientation have used dihedral angle measurements of twin boundary grooves and of bamboo-structure wires. The calculated orientation dependence of surface energy is a strong function of the assumptions used in the data analyses. Three determinations of the $\gamma_s(\theta,\phi)$ function are: (1) Mykura's interferometric study of Ni twins (Mykura, 1961); (2) Winterbottom and Gjostein's analysis of Au twins by interferometry (Winterbottom and Gjostein, 1966); and (3) McLean and Gale's study of bamboo-structure Cu wire (McLean and Gale, 1969). A critical evaluation of these studies can be found in a review by Murr (1975).

The polar projections of the calculated $\gamma_s(\theta,\phi)$ plots are presented in Figure IV-7(b)-(d) with all values relative to the energy of the (111) surface. By reference to the calculated plots by Nicholas, it is evident that the orientations of the extreme in the experimental plots for Ni and Au do not correspond to the predicted orientations. Adsorbed species have been invoked to explain this discrepancy; however, no specific adsorbed species was identified in these studies. Regardless of the shape of the $\gamma_s(\theta,\phi)$ plot, the important features are the values of maximum anisotropy: 1.085 for Ni at $T/T_m = 0.74$, 1.077 for Au at $T/T_m = 0.97$, and 1.021 for Cu at $T/T_m = 0.95$, the fact that the anisotropy is small at high temperature, that (111), (100), and (110) are local minima, and that the maximum anisotropy is approximately the same as that predicted from bond breaking calculations for 0^oK.

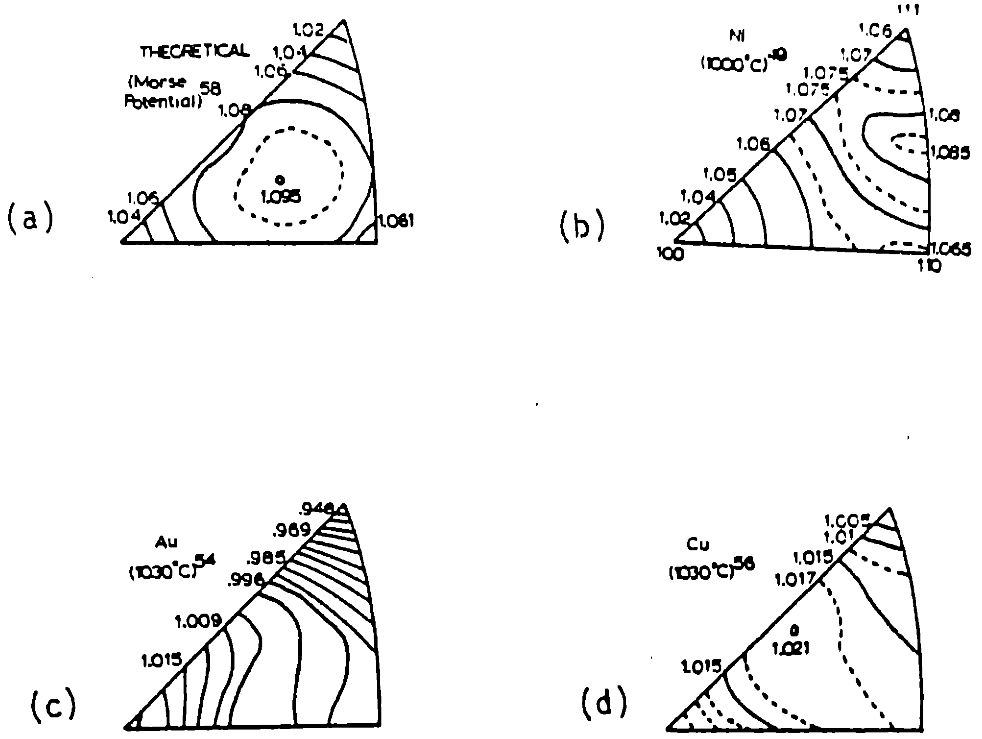

(a) Calculated γ_s-plot for an fcc metal (from Nicholas(1968)).

(b) for Ni (Mykura, 1961); (c) for Au (Winterbottom and Gjostein, 1966); and (d) for Cu (McLean and Gale, 1969).

Figure IV-7

The differences in the ranking of local minima can be explained by adsorption effects. Surface energy measurements of Cu as a function of oxygen adsorption in Cu were performed by Robertson and Shewmon (1963) and by Hondros and McLean (1970). In both experiments, the anisotropy increased with increasing P_{O_2} to approximately 1.04. At low P_{O_2} (10^{-22} atm), $\gamma_{111} < \gamma_{100} < \gamma_{110}$ as predicted in Nicholas' bond breaking analysis. At higher P_{O_2} (10^{-13} atm), $\gamma_{100} < \gamma_{110} < \gamma_{111}$.

For pure metals with the exception of γ-Fe, $\frac{d\gamma}{dT} \sim -0.45$ ergs/cm^{2}K, there are two results for multicomponent metal systems: for Fe-3 w/o Si, $\frac{d\gamma}{dT} = -0.36$ ergs/cm^{2}K and for 304 stainless steel, $\frac{d\gamma}{dT} = -1.76$ as compared with Fe (γ phase), $\frac{d\gamma}{dT} = -3.0$ (Murr, 1975).

The calculated surface energies of metal surfaces (Lang and Kohn, 1970, Beloguroy, 1963) have been in poor agreement with experimentally determined average surface energy values. To date, no calculation has succeeded in matching the maximum anisotropy of ~ 1.1 determined from experiment and relative energy calculations. "Reasonable agreement" of calculated values with average experimental values is usually taken as γ_s (calculated) $\pm 20\%$.

In summary, the maximum surface energy anisotropy at any temperature for metals was found to be less than 1.2 by both experiment and theoretical calculations (Nicholas). Although surface energies vary vary from 100 ergs/cm^2 for Cs to 2800 ergs/cm^2 for W, the magnitude of anisotropy seems characteristic of all metals.

In nonmetallic solids, estimates of surface energies come primarily from cleavage data. Examples of such data are listed in Table IV-1. Since

Table IV-1

Surface Energies from Cleavage Experiments

Material	T (K)	Estimated γ_s (ergs/cm^2)	References
MgO (100)	77	1,500	Ref. in Cannon et al. (1982)
BaF_2 (111)	77	280	Gilman (1960)
CaF_2 (111)	77	500	Gilman (1960)
LiF (100)	77	340	Gilman (1960)
NaCl (100)	77	300	Kingery
KCl (100)		110	Class & Machlin (1966)
Al_2O_3 (10$\bar{1}$2)	298	6,000	Ref. in Cannon, et al. (1982)
(1010)	298	7,300	"
(0001)	298	>40,000	"
SiC (11$\bar{2}$0)	298	20,000	"
$MgAl_2O_4$ (100)	298	3,000	"
(111)	298	5,600	"

cleavage occurs most easily along the lowest energy plane, these data usually represent only the lowest surface energies. For fcc (rock salt) ionics the cleavage plane is (100); for the fluorite structure, cleavage occurs on the (111) plane. For sapphire there is no pronounced cleavage plane. As illustrated by the range of energies for MgO, LiF, and NaCl, the strength of the bonding plays a significant role in determining the surface energy.

No Wulff plot exists for any ionic material although faceting has been observed for a variety of materials and conditions. The surface energies of low index planes of rock salt and fluorite structure ionics and sapphire have been calculated by Tasker (1979a, b; 1980; 1982) An estimate of the surface energy anisotropy in ionics can be made by comparing the calculated γ_s values for different low index planes.

Tasker (1979c) has classified ionic surfaces into three types: Type I surfaces are planes of zero net charge, such as the (100) and (110) in the rock salt structure. Type II surfaces have a net surface charge, but are grouped into repeating units with no net dipole moment perpendicular to the surface, such as the (111) in the fluorite structure terminating at the surface with an anion plane or the (0001) sapphire surface with Al^{3+} ions at the surface (1/2 of atoms originally on plane. Type III surfaces have a net surface charge and a net dipole moment perpendicular to the surface. The three surface types are shown schematically in Figure IV-8.

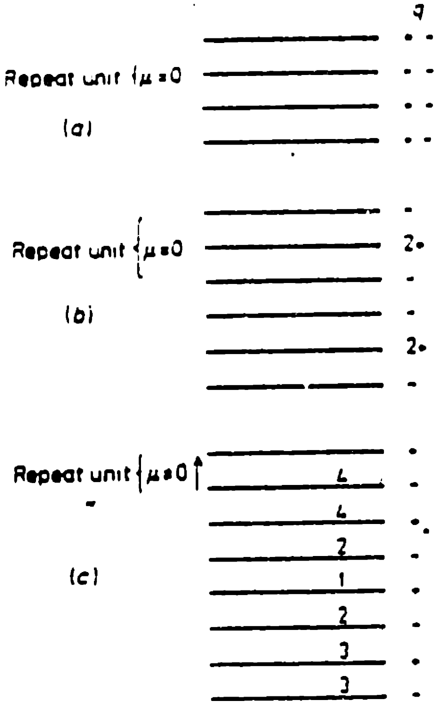

(a) Distribution of charges q on planes for 3 stacking sequences parallel to surface (a) type 1 with equal anions and cations on each plane; (b) type 2 with charged planes but no net dipole moment perpendicular to surface; (c) type 3 with charged planes and dipole moment normal to surface. (from Tasker, 1979).

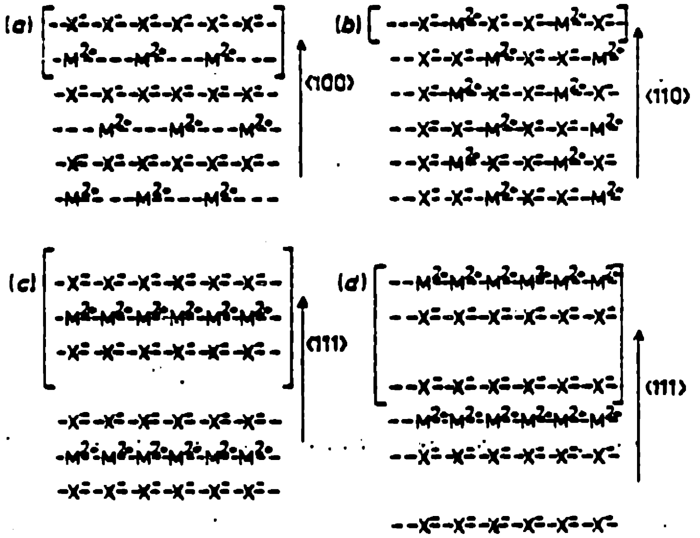

(b) Schematic representation of the stacking sequences in the fluorite structure MX_2 : (a) for (100) surface, type 3; (b) (110) surface, type 1; (c) (111) surface with terminating anion plane, type 2; (d) (111) surface with terminating cation plane, type 3. Square brackets indicate repeat unit for planar charge density. (from Tasker, 1979).

Figure IV-8

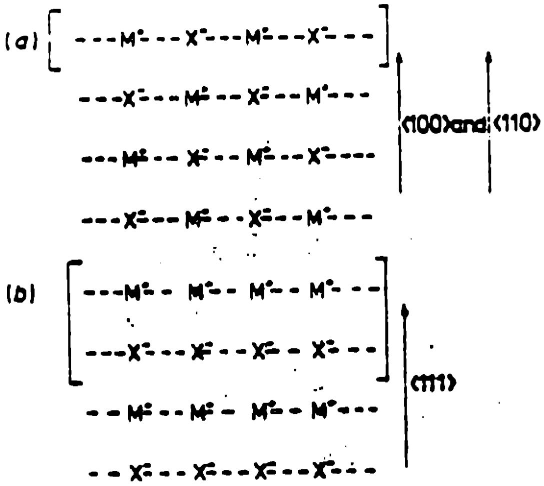

(c) Schematic representation of the stacking sequences in the rock salt structure, MX: (a) for (100) or $(\bar{1}10)$ surfaces, both type 1; (b) for $(\bar{1}11)$ surface, type 3. Square brackets indicate repeat unit for planar charge density. (from Tasker, 1979).

The static lattice calculations for surfaces by Tasker are based on the computation of the long range coulombic contribution to the energy in conjunction with the energy contribution due to short-range forces over a two-dimensionally periodic structure. The ions are represented by polarizable shells and cores of opposite signs and the short-range potentials empirically determined by Mackrodt (1977). In a defined surface region, the polarizable ions are relaxed and the energies compared before and after the "relaxation". An additional region of rigid, unpolarizable ions whose energy is characteristic of the bulk is included to ensure that the energy summation converges. These static calculations are most applicable at 0 K.

Reasonable agreement was found for the calculated surface energies with experimental data, primarily cleavage data, presented in Table IV-2. However, the surface energy for sapphire determined by cleavage along the (0001) plane was found to be >40,000 ergs/cm^2 at 298 K. The calculated value by Tasker (personal communication) for an unrelaxed (0001) surface with one-half of the Al^{3+} ions on the surface at 0 K was 6.520 ergs/cm^2. Relaxation lowered the surface energy to 2.970 ergs/cm^2. The cleavage results are, thus, in poor agreement with the calculated surface energies. No other calculations for sapphire have been made.

For the alkali halides, $\gamma_{(110)}/\gamma_{(100)} \sim 2$. For the alkaline earth fluorides, $\gamma_{(11)}/\gamma_{(111)} \sim 1.5$. For the fluorite structure oxides, $\gamma_{(110)}/\gamma_{(111)} \sim 1.45$. The calculations for unreconstructed Type III

Table IV-2

Calculated Surface Energies for Alkali Halides and Fluorite Structure Materials (ergs/cm^2)

	γ_s (100)	γ_s (110)	γ_s (110)/γ_s (100)
LiF	480	1047	2.34
NaCl	212	425	2.18
KCl	170	350	1.98
KBr	154	311	1.96

	γ_s (111)	γ_s (110)	γ_s (110)/γ_s (111)
CaF_2	476	760	1.6
SrF_2	407	630	1.55
BaF_2	349	492	1.41
UO_2	1064	1561	1.47
ThO_2	1016	1451	1.42

surface, such as the rock salt (111) and the fluorite (100), did not converge. Tasker has suggested that Type III surfaces may be stabilized by structural changes/deviations from stoichiometry, although no calculations have been made for these modified surfaces. It is interesting to note that Type III surfaces have only been observed in transition metal oxides and for (0001) surfaces on Al_2O_3 after long thermal anneals.

These calculated variations in the surface energy with orientation indicate that the anisotropy is significantly greater than metals and approaches ∞ for unreconstructed Type III surfaces. The measurable γ_s values for the cubic ionics, i.e., the energies of the lowest energy planes are in the range 140 ergs/cm^2 for KI to 1500 ergs/cm^2 for MgO.

The temperature dependence of the surface energy for any ionic solid has not been measured independently of the grain boundary energy. These results are described below in Section IV.2.5. The effects of adsorbing species/annealing atmosphere or impurity additions on the surface energy or the surface energy anisotropy have, likewise, not been measured.

For ionic systems with more covalent bonding and for covalent systems (Si, GaAs), the requirements of localized bonds leads to substantial reconstructuion of the surface relative to a simple bulk termination (Duke, 1978). For covalent systems, the surface energy is frequently estimated using a quasi-chemical model of bond breaking of first nearest neighbors. In its simplest form,

$$\gamma = 1/2 \sum_{ij} N_j n_i^j \phi_j \qquad \text{(IV-10)}$$

where N_j is the number of j-type atoms per unit area, n_i^j is the number of bonds of type i broken for surface atoms of type j, and ϕ_j is the bond energy of atom type j which is estimated as $(\frac{2H_s}{2})$, where H_2 is the heat of sublimation and 2 is the bulk coordination number. This model produces an upper limit since reconstruction and relaxation of the surface as well as entropy terms lowers the surface energy (Blakely, 1973). The calculated anisotropies are approximately 1.75 considering the (100) and (111) planes.

For metals, the maximum anisotropy is $\sim$1.2. For ionic solids, the maximum anisotropy is at least 2 and approaches ∞ for unreconstructed/stoichiometric Type III surfaces. Due to the instability of high energy surfaces to faceting, these surfaces will never be observed under equilibrium conditions. For covalently bonded solids, the anisotropy is $\sim$1.75. The data are not sufficient to set a closer limit on the anisotropy for covalent solids.

Table IV-3

Estimates of Surface Tension for Some Covalently Bonded Crystals

	Surface Tension (ergs/cm^2)		
Crystal	(100)	(110)	(111)
C (diamond)	3064	2170	1770
Si	2513	1781	1451
Ge	1927	1365	1113
InSb	1100	750	600
GaAs	2200	1500	1300
InAs	1400	1000	840
GaSb	1600	1100	910
InP	1900	1300	1100
AlSb	1900	1300	1100
AlAs	2600	1800	1500
GaP	2900	2000	1700
AlP	3400	2400	2000

The experimental values for the $\{111\}$ planes of germanium and silicon are 1060 and 1230 ergs/cm^2 respectively (R. J. Jaccodine, Surface energy of germanium and silicon, J. Electrochem. Soc. 110, 524 (1963)). The estimates for the III-V compounds are from J. W. Cahn and R. E. Hanneman. (III) Surface tensions of III-V compounds and their relationship to spontaneous bending of thin crystals, Surface Sci. I, 387 (1964). The numbers for $\{111\}$ refer to the mean of (111) and $(\bar{1}\bar{1}\bar{1})$ surfaces. The estimates for diamond, germanium, and silicon are based on cohesive energies quoted in C. Kittel, Introduction to Solid State Physics, Wiley, New York, 1966, p. 78 (from Blakely, 1973).

2.4 Grain Boundary Energy

The structures of the simplest boundaries, low angle grain boundaries, have been described in terms of the dislocation content of the boundaries. The energy variation of low angle grain boundaries with misorientation, θ, can be calculated based on the dislocation energy using the Read-Shockley expression:

$$E = E_0 \ (A - \ell n \ \theta) \qquad \text{(IV-11)}$$

where E_0 and A are functions of the Burger's vector, Poisson's ratio, the shear modulus, the type of lattice, and the type and direction of dislocations. The agreement between experimental and predicted energies of low angle grain boundaries from the Read-Shockley expression are qualitatively very good. For higher angle grain boundaries, a simple geometrical model is not sufficient to describe the structure or the associated energy.

A geometrical model for high angle boundaries based on periodic structural units was proposed by Brandon et al. (1964). With this model, the boundary energy is expected to decrease as the structural unit size and the period decrease. For special boundary structures with a large number of boundary sites shared by each lattice, the energy was predicted to be low. These 'special' boundaries lead to 'cusps', local minima, in the energy variation with misorientation. A purely geometrical model does not, however, lead to true atomic positions or energies because of atomic relaxation in the boundary.

Computer modeling of three dimensional relaxation has been used to compute the structure and energy of grain boundaries. In a recent review of the structure of high angle grain boundaries in metals and ceramics by Balluffi et al. (1981); the modelling techniques and recent experimental results are summarized. Only those studies in which the grain boundary energy is separable from the surface energy are discussed in this section. In many studies, dihedral angles are measured and γ_{gb} is calculated from Equation (IV-2) using a single value of γ_s. These results are discussed in Section IV. 2.5.

It should be noted that in many experimental studies of grain boundary energy as a fuction of boundary orientation, the grain boundary structure is incompletely specified. Nine parameters are required to uniquely describe a general grain boundary. In the studies described below, the orientation dependence of the grain boundary energy is frequently shown as γ_{gb} or as a dihedral angle change with an orientation parameter, θ. This θ is the angle between the same crystallographic direction in the two crystals such that at $\theta = 0$, a single crystal is formed. This approach is acceptable for [001] and [011] tilt and [001] twist boundaries for single component cubic materials. In general, the grain boundary plane has not been specified. In the most recent TEM and electron and x-ray diffraction studies, the boundaries are described uniquely.

Another common description of grain boundaries includes the number of atomic sites in the boundary coincident to both lattices. This is expressed in terms of the inverse of the fraction of coincident sites. For example, 1 coincident site in 5 is $\Sigma 5$. The ΣN nomenclature along with boundary type is used below.

The grain boundary energy as a function of misorientation for symmetrical [001] tilt boundaries in Al has been calculated by both Pond , et al. (1977), and Hasson, et al. (1972). The calculated variations in energy which apply at 0 K are plotted in Figure IV-9. In spite of differences

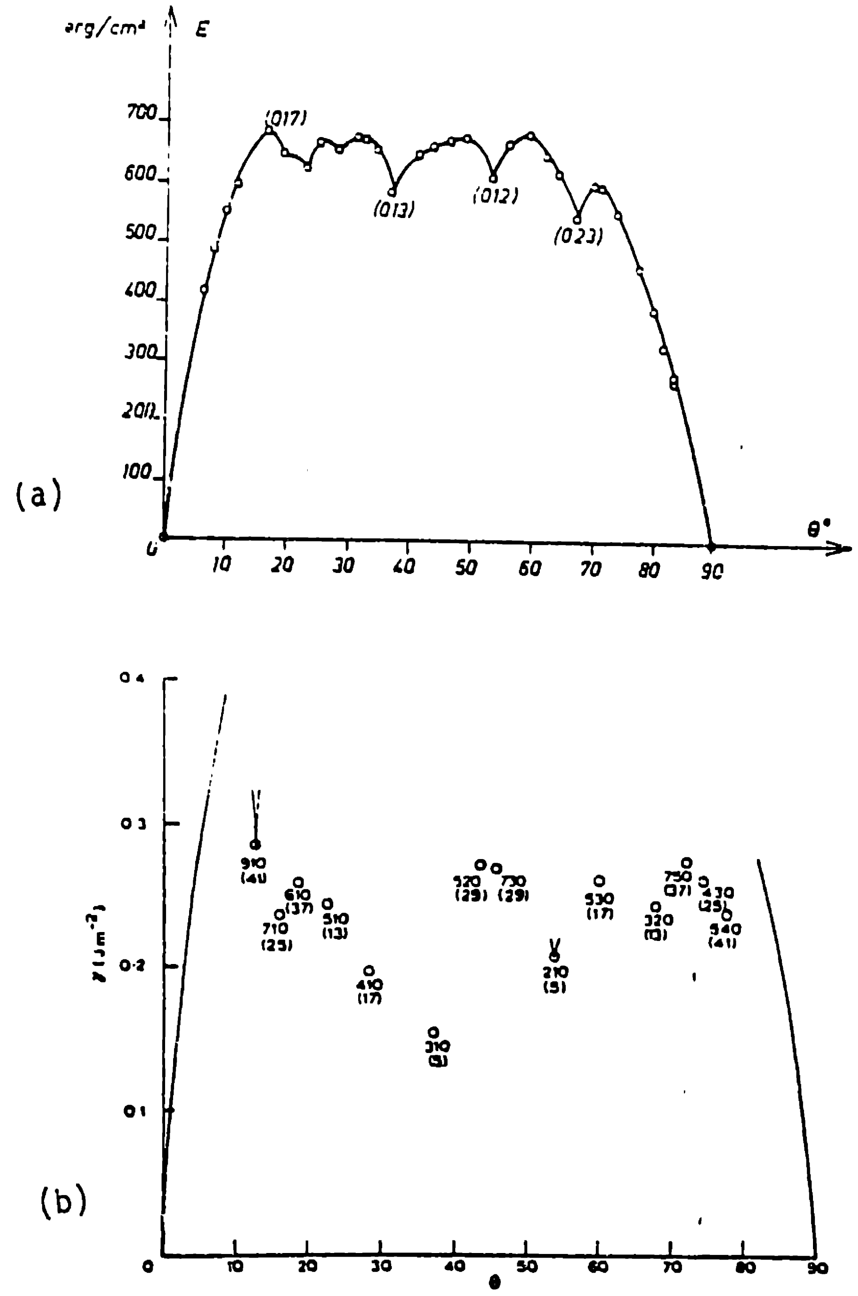

Figure IV-9 Calculated energies of⟨001⟩symmetrical tilt boundaries in coincidence orientation with $\Sigma \leq 41$ for Al; (a) from Hasson et al., 1972; and (b) from Smith et al., 1977.

in the boundary conditions and the atomic potentials used for the calculations, both plots show minima for the twin misorientations (013), (012), and (023). For both calculations, the relaxed atom positions in the boundary structure are close to but different from those predicted by purely geometrical coincidence models. The calculated energies for high angle boundaries were found to vary by a factor of 2 with a maximum value of 270 $ergs/cm^2$ ±40% for $10° < \theta < 80°$ by Smith et al. and by approximately 20% with maximum value of 700 $ergs/cm^2$ for $10° < \theta < 70°$, by Hasson et al.

The experimental evidence for the variation of γ_{gb} with misorientation for high angle grain boundaries in metals comes from three sources: from experiments on particle rotation, from calculations based on observed dihedral angles at boundaries of known orientations in polycrystalline wires and bicrystals, and from electron and x-ray diffraction and TEM structural studies.

In the experimental study by Gjostein and Rhines (1959) of symmetrical [001] tilt boundaries in Cu at 1338 K ($T/T_m \sim 1$), the energies of low angle grain boundaries followed the Read-Shockley equation up to $\theta \sim 5°$-$6°$ and little variation of energy with misorientation was found for high angle grain boundaries. However, it was assumed that the simplified form of the Herring equation, Equation (IV-2) applied and that γ_s was single valued. If the difference between the energies of boundaries with high and low densities of coincident atoms were small, consideration of the surface energy anistropy may be requried to determine the γ_{gb} relationship with misorientation.

Metal spheres sintering to a single crystal plate have been observed to rotate to several low energy orientations relative to the plate orientation. In experiments by Hermann et al. on Cu (1976), by Sauter et al. (1977) on Ag-1 wt% Au, Ag-20 wt% Au, and Ag-0.2 wt% Bi, and by Mykura on Cu (1979), orientations corresponding to calculated local minima dominate the distributions as determined by pole figure analyses. Bristowe and Sass (1980) found excellent agreement between the structures of a $\Sigma 13$ (22.6°) [001] boundary and a $\Sigma 337$ (23.8°) boundary in Au determined by x-ray diffraction techniques and the calculated structures modelled by molecular statics.

Schober and Balluffi (1970) found that (001) twist boundaries in Au which deviated slightly from low Σ misorientations relaxed into structures consisting of low Σ boundaries and grids of secondary screw grain boundary dislocations, of lower energy than the unrelaxed structure.

McLean determined the grain boundary energy of individual grain boundaries from grain boundary grooving data for Cu annealed at 1303 K ($T/T_m = 0.96$) by taking into account the surface energy anisotropy. (1973) A histogram of the incoherent twin boundaries and high angle grain boundaries observed is hown in Figure IV-10. The frequency data are plotted for γ_{gb} relative to the (100) surface energy. The single high coincidence boundary orientation ($\Sigma 11$-(110)) found in 19 high angle grain boundaries examined had a lower energy than the other high angle grain boundaries, $\gamma_{\Sigma 11}/\gamma_{s(100)} = 0.26 \pm 0.01$. Incoherent twin ($\Sigma 3$) boundaries are of lower energy than $\Sigma 11$: $\gamma_{\Sigma 3}/\gamma_{s(100)} = 0.21 \pm 0.01$. Not included in this distribution are coherent twins whose energy is $\gamma_{coherent}/\gamma_{s(100)} = 0.02$. From these relative energy data, an estimate of the anisotropy of high angle boundaries from $\gamma_{max}/\gamma_{\Sigma 3}$ is 1.7. When ($\Sigma 3$) coherent twins are

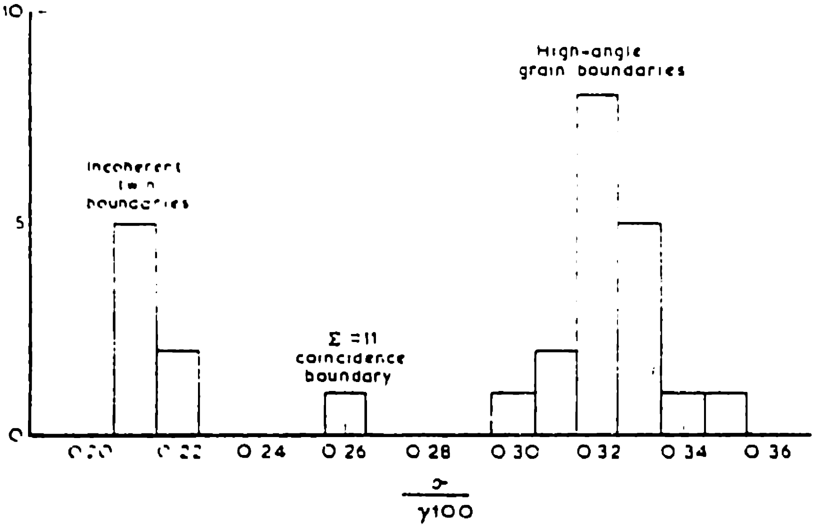

Figure IV-10 Histogram of incoherent twin and high angle grain boundaries in Cu (McLean, 1973).

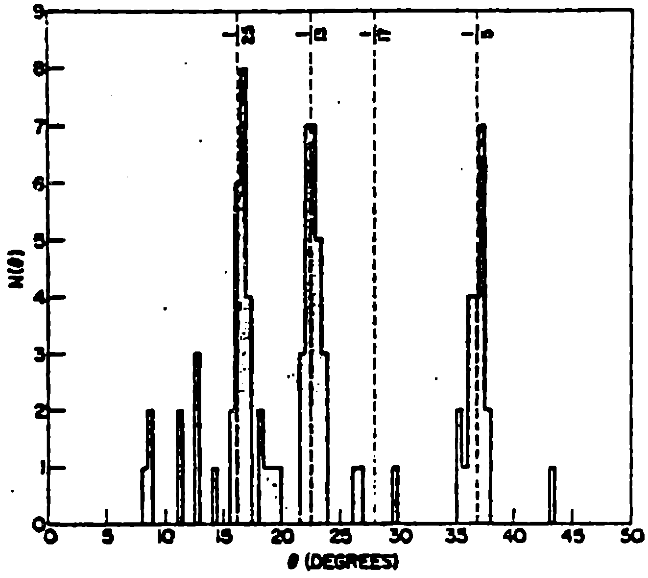

Figure IV-11 Histogram of <001> twist boundary misorientation for 'wet' MgO smoke (from Chaudhari and Matthews, 1970).

included in the grain boundary energy distribution, $\gamma_{max}/\gamma_{min} \approx 20$. As $\theta \rightarrow 0$, $\gamma_{min} \rightarrow 0$ and $\gamma_{max}/\gamma_{min} \rightarrow \infty$.

The preceding literature review describes experimental and theoretical studies of the structure and energy of "pure" metals. The data on particle rotation in nominally single component and binary systems were included in this category because the chemical composition were not well characterized during the studies. It was later reported that the Cu spheres (Hermann, et al. 1976) contained high levels of sulfur (Wolf, personal communication). No composition data are available for the "binary" systems examined by Sauter or for the Cu examined by Mykura. As with surfaces, solute segregation to boundaries leads to a decrease in the boundary energy. The degree of segregation and the resulting boundary energy are determined by the boundary structure. Boundaries are composed of regions of tensile and compressive stress and solutes which minimize the strain energy. Anisotropy of grain boundary segregation has been reported for Cu-Bi (Powell and Woodruff, 1976), Fe-S and Fe-Sn (Seah and Hondros, 1973), and Fe-Si (Watanabe, Murakami and Karoshima, 1978). No data on the changes in grain boundary energy with adsorption/segregation to specific boundary have been reported.

For ionics, the calculation of grain boundary energies are complicated by the requirements of electroneutrality and stable coulombic interactions. The most recent calculations of the grain boundary energy for high-angle boundaries in NiO and MgO have been performed for [001] twist boundaries by Wolf and Benedek (1981) and by Tasker (personal communcation), for [001] tilt boundaries by Tasker (private communication), and for [011] tilt boundaries by Wolf (1980). It was found by Wolf and Benedek and by Tasker that [001] twist boundaries were only marginally stable

($\gamma_{gb}/2\gamma_s$ = 0.97, Wolf and Benedek). The [011] twist boundaries were found to be much less than for the two corresponding free surfaces. According to Tasker's calculations, the surface energy for the general MgO surface is approximately twice the cleavage energy, that is, γ_s general $\approx 2\gamma_{s(100)}$. It was also calculated that γ_{gb}([100] tilt) $\approx 2\gamma_{s(100)} \approx \gamma_s$ general. Because $2\gamma_{s(100)} \approx \gamma_{gb}$([100] twist), γ_{gb}([100] tilt) $\approx \gamma_{gb}$([100] twist). These calculations imply that for [001] twist and tilt boundaries, the surface energy anisotropy is much greater than grain boundary energy variation and γ_s determines the values of γ_{gb}/γ_s.

The results of Chaudhari andMatthews (1970, 1971) on the frequency of low Σ(001) twist boundaries for MgO smoke seem to conflict with the calculated energies for these boundaries.

The frequency plot for boundaries between MgO smoke particles (cubes) is shown in Figure IV-11. The low Σ boundaries dominate the distribution. However, in a later study by Chaudhari and Charbeau (1972), it was reported that under dry conditions, few low Σ boundaries and (111) twins were observed. Cowley et al. (1979) reported that MgO (111) twins are only formed under wet conditions and suggest that preferential adsoprtion of water vapor or a charged species (H^+, OH^-) or the formation of a brucite surface could stabilize the {111} twin. It is suggested that adsorption under wet conditions could also stabilize [001] twist boundaries.

Experimental studies of grain boundary structure in fcc ionics have been performed using TEM techniques and mechanical properties testing on fabricated bicrystals and using particle rotation experiments. The results for ionics are more difficult to interpret than similar results for metals due to the possible impurity effects.

Intrinsic grain boundary dislocations have been observed by Sun and Baluffi (1979) for boundaries near low Σ orientations for [001] twist boundaries in MgO. While these results support the possible occurrence of low energy, low Σ boundaries, these boundaries may have been made energetically acceptable due to segregated impurities or water vapor present during bicrystal fabrication.

A partical rotation experiment was performed by Peterson et al. for NiO in air at 1660K (T/Tm = 0.73) after which the crystallographic misorientation between spheres and single crystal plates was found to be random.(1980)The 'spheres' were irregularly shaped and faceted on (111) planes during annealing, neck growth could have occurred by surface diffusion or evaporation/condensation rather than grain boundary or lattice diffusion leading to no sphere rotation, and possible changes in the stoichiometry for NiO boundaries may decrease the energy variation with orientation, and, hence, no driving force for rotation.

Fracture experiments on fabricated bicrystals have shown a correlation between grain boundary misorientation and fracture energy. A study of the change in crack extension force along KCl [001] twist boundaries has been performed by Class and Machlin (1966) using the double cantilever technique. For brittle materials, the crack extension force, G_c, can be related directly to the surface energy and the grain boundary energy by

$$G_c = 2\gamma_s - \gamma_{gb} \qquad \text{(IV-12)}$$

As shown in Figure IV-12 the crack extension force decreases from the $2\gamma_{s(100)}$ value as predicted qualitatively by the Ready-Shockley equation and shows shallow maxima as a function of twist boundary misorientation; the

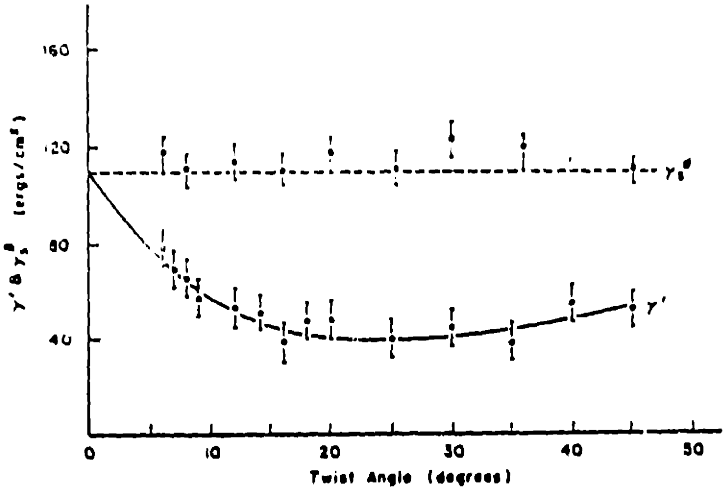

(a) Conjugate true γ_s^θ and apparent surface energies γ' for KCl as a function of twist angle θ for [001] twist boundaries. (from Class and Machlin, 1966).

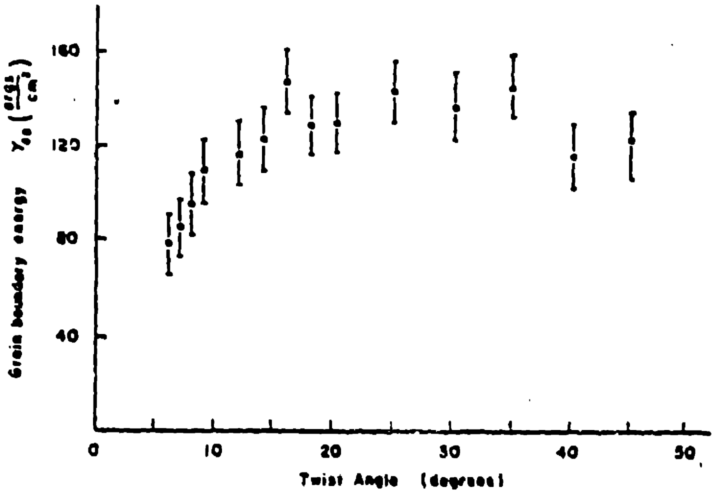

(b) Calculated variation of grain boundary energy with twist angle θ for KCl. (Class and Machlin, 1966).

Figure IV-12

maxima occur at approximately 20°, 30°, and 40°. The geometrically derived low Σ boundaries occur at 16.5°, 22.6°, 28.1°, and 36.6°. These cleavage data show little correlation between predicted and measured γ_{gb} values.

In summary, the variation of grain boundary energy with orientation is well documented for low angle grain boundaries in metals. For low angle boundaries in ionics and high angle grain boundaries in metals and ionics, the variation of energy with grain boundary structure is poorly documented. The grain boundary structure has been observed to vary systematically for certain special boundaries; however, the energy difference between these boundaries and more general boundaries is not known for metals or ionics. The effects of impurity adsorption and of temperature on grain boundary stability in ionics may be important but is currently poorly documented.

IV. 2.5 Dihedral Angles

From the anisotropy in γ_s, $\gamma_{s_{max}}/\gamma_{s_{min}} \sim 1.2$ for metals, >2 for ceramics, and 1.75 for covalent materials. From the calculated variation of γ_{gb} with boundary structure, $\gamma_{gb_{max}}/\gamma_{gb_{min}} \sim 2$ for "special" high angle boundaries in metals. For low angle boundaries, $\gamma_{gb} \rightarrow 0$ as misorientation decreases. For MgO and NiO [001], twist boundaries, $\gamma_{gb}/\gamma_{s_{(100)}} \sim 2$. For [001] tilt boundaries in MgO and NiO $(\gamma_g/\gamma_s)_{max} \sim 1.28$. From these data and calculations, the dihedral angle distributions for metals are expected to be narrow. From the sparse data on ceramics, dihedral angle distributions are expected to be much wider than on metals and to have some boundary surface combinations where $\psi \rightarrow 0°$. These will rarely be observed because of boundary migration due to energy minimization

($\partial\gamma_g/\partial\psi_i$ terms in Equation IV-1).

As described in Section IV.2.2, dihedral angle measurements from polished and grooved surfaces are frequently used in conjunction with Equation (IV-2) to calculate distributions or averages of γ_{gb}/γ_s. These data for grooved surfaces from the literature are presented here in terms of the measured dihedral angle rather than the derived γ_{gb}/γ_s or γ_{gb} values.

2.5.1 Measurements from Grooved Surfaces

Typical average values of dihedral angles, ψ, for undoped metals are in the range 155° to 165° for high angle grain boundary vacuum/H_2/inert gas interfaces. Assuming that $\partial\gamma_i/\partial\psi_i = 0$, that the grooves are symmetrical, and that the boundaries are perpendicular to the surface, these angles correspond to γ_{gb}/γ_s values of 0.43 to 0.26. Several values of $\bar{\psi}$ are listed in Table IV-4. Two examples of the typical distributions of dihedral angles are shown in Figure IV-13 (a) and (b). The distribution of angles chosen randomly along the circumference of Chromel-A (NiCr) bamboo structure wire were measured from TEM micrographs by Murr et al. (1971). Low angle grain boundaries and twins, with dihedral angles $\sim 180°$, were excluded by Murr from the distribution shown in Figure IV-13 (a). The total distribution of observed angles from grooved Ni surfaces as determined by optical interferometry by Hodgson and Mykura (1973) is shown in Figure IV-13 (b). In both cases $\bar{\psi} \sim 160°$.

The effects of an adsorbed species on the dihedral angle distribution is illustrated by the distribution of angles from Cu surfaces exposed to Pb vapor (unsaturated) at 1220K (Fullman, 1951). The ranges of angles span from 115° to 160° for high angle grain boundaries and from 177° to 180° for

Table IV-4

Average Dihedral Angles in Metals at $(T/T_m)^*$

(HA = High Angle) (TB = Twin Boundaries)

Material	$\bar{\psi}_{HA}$ (T/T_m)	$\bar{\psi}_{TB}$ (T/T_m)
Cr	157° (0.76)	
Cu	159° (0.83)	179.4° (0.94)
Au	165° (∿ 1)	
Ni	158 (0.77)	179° (0.74)
Pt	161 (0.68)	177° (0.68)
Ag	166 (0.1)	
In	162 (0.89)	

* calculated from $\frac{\gamma_b}{\gamma_s} = \cos\frac{\bar{\psi}}{2}$ using $\frac{\gamma_b}{\gamma_s}$ values

from Murr (1975)

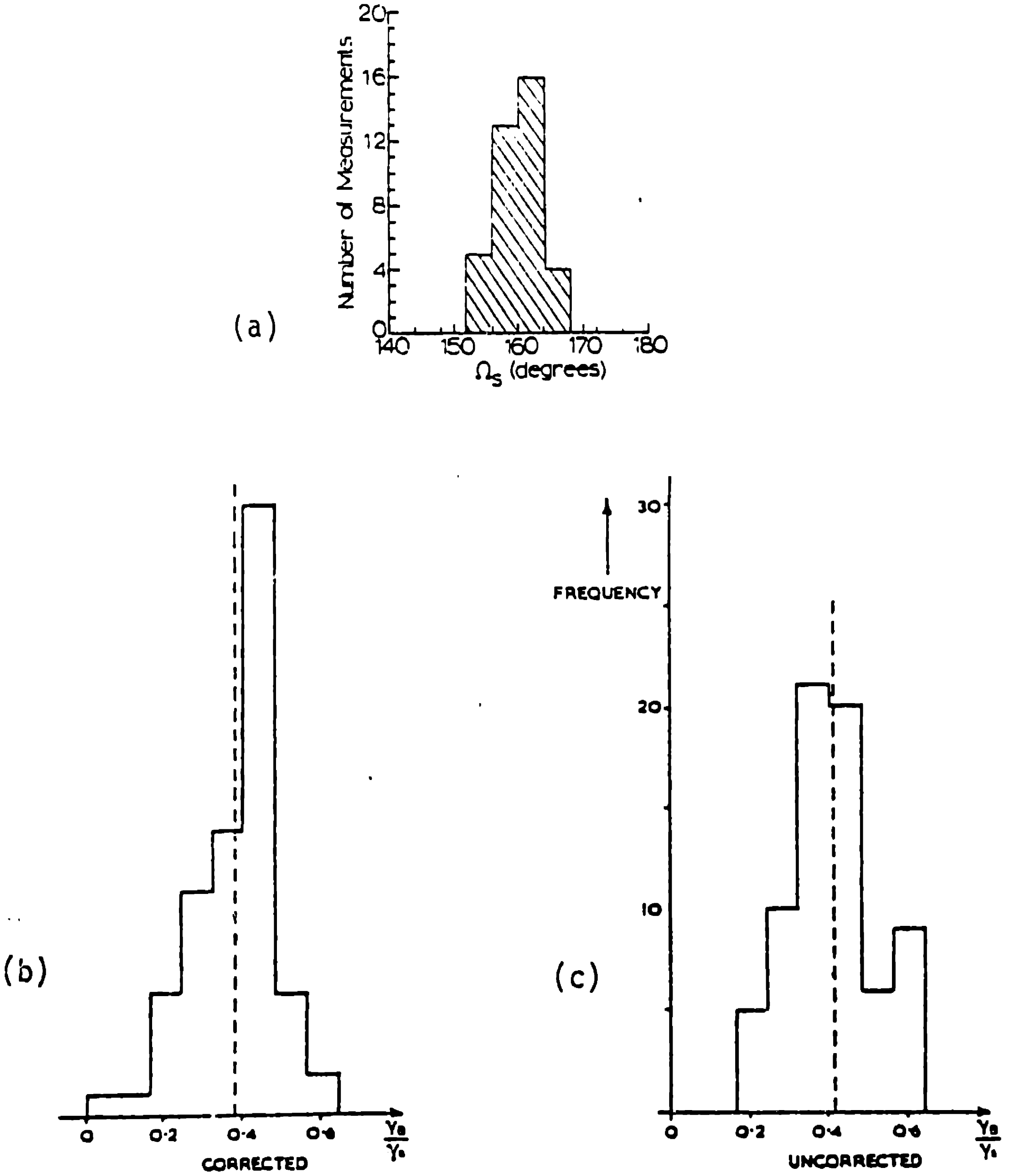

Figure IV-13 Dihedral angle histograms for metals: (a) Chromel-A at 1600 K from Murr et al, 1971; (b) Ni at 1270 K from Hodgson and Mykura, 1973 and (c) data in (b) corrected for boundary torque terms.

low angle boundaries and twins. The minimum observed angle for undoped Cu at 1340 K was 160° as measured by Gjostein and Rhines (1959). The value of $\bar{\psi}$ for Cu at 1220 K was 164°, as measured by Inman and Tipler (1963).

The dihedral angle data for ionic systems are sparse and the techniques used to measure the angles are inaccurate. The techniques used in the studies described below are: interferometry, profilometry, and optical microscopy of surfaces perpendicular to grooved surfaces. The errors in $\Delta\psi$ for $\psi <$ 160° due to errors in angle measurements by interferometry were discussed in SEction IV.2.2.1. As seen below, all measured dihedral angles in ionics have been less than 160°. Profilometry makes faceted grooves appear smoothly curved and does not examine the angle at the groove root, leading to a larger apparent dihedral angle. Polishing surfaces perpendicular to the grooved surface can widen the groove or can make the groove crack-like. Even in the absence of polishing effects, there is a coupling between microscope resolution and apparent dihedral angle. Small angles may not be detected. Grooves cut at other than 90° to the grain boundary plane have larger apparent dihedral angles, and thus, are easier to resolve. Each of these three techniques may move the dihedral angle distribution to larger values.

The average dihedral angle of groove polycrystalline Al_2O_3 at 2123K was 152° as measured by Kingery (1954) using optical microscopy of samples sectioned and polished perpendicular to the grooved surface. Similar experiments by Kingery on Ca-stabilized ZrO_2 at 2123 K yielded $\bar{\psi}$ = 154°. The greatest uncertainty in these measurements is the effect of polishing and measurement techniques on the measured angles.

The most extensive dihedral angle data are from the studies of Hodkin et al. (1973, 1977, 1980) and of Nikalopoulos et al. (1977) on UO_{2+x} and UC. Dihedral angles were measured for several types of interfaces: grain boundary-argon, grain boundary-vapor (argon + Cu; argon + Ni), grain boundary liquid metal (Cu, Ni), and polycrystalline surface-liquid Cu (sessile drop). In these studies, interferometry was used to determine $\overline{\psi}$ for the grain boundary vapor (argon; argon + metal vapor) interfaces. Because the degree of reactivity between the metal and the oxide is not known, only the argon data are presented here. The values of $\overline{\psi}$ as a function of nominal stoichiometry are listed in Table IV-5. The values of $\overline{\psi}$ vary from 141° to 159°. The stoichiometry of these samples was measured before thermal grooving; actual compositions corresponding to the measured values of $\overline{\psi}$ are not known (Hodkin, personal communication). Two examples of the change in dihedral angle distribution with temperature are shown in Figure IV-14 for $UO_{2.053}$ and $UO_{2.001}$. The distributions are narrower than for typical metals (see the Ni distribution shown in Figure IV-13) and are shifted to smaller dihedral angles than observed in pure metals. In spite of the inaccuracy of interferometry at small angles, these results constituted the largest data base of dihedral angles in any ionic system.

The changes in dihedral angle with misorientation have been measured on fabricated symmetrical bicrystals of NiO and Al_2O_3. The results of Ready and Jech ([001] tilt boundaries in NiO (1968)), of Shackelford and Scott ([$\bar{1}$100] tilt boundaries in Al_2O_3 (1968)) and of Dhalenne et al. ([001] and [011] tilt boundaries in NiO (1979, 1982)) are presented in Figure IV-15. In Figure IV-15 (a)-(c), the dihedral angle decreases as misorientation angle, θ, increases and becomes constant for $\theta > 20°$. In Figure IV-15 (d), the dihedral angle variation with θ for NiO [011] tilt boundaries shows local minima at the (221), (111), and (113) twins

Table IV-5

Median Groove Angles from Thermal Grooves at the Free Surfaces of Unirradiated Nuclear Ceramics (from Hodkin, 1980)

Material	Grooving Atmosphere	Temperature (°C)	Median Thermal Groove Angle (degrees)
UC	Argon	1100-1600	156.5-159.2
$UO_{2.001}$	Argon	1400-1700	140.8-148.8
$UO_{1.998}$	Argon	1700	148.6
$UO_{2.053}$	Argon	1100-1700	141.3-149.0
$UO_{1.999}$	Argon	1900	148.8
$UO_{2.006}$	Argon	1750	146.1
$UO_{2.025}$	Argon	1500	148.2

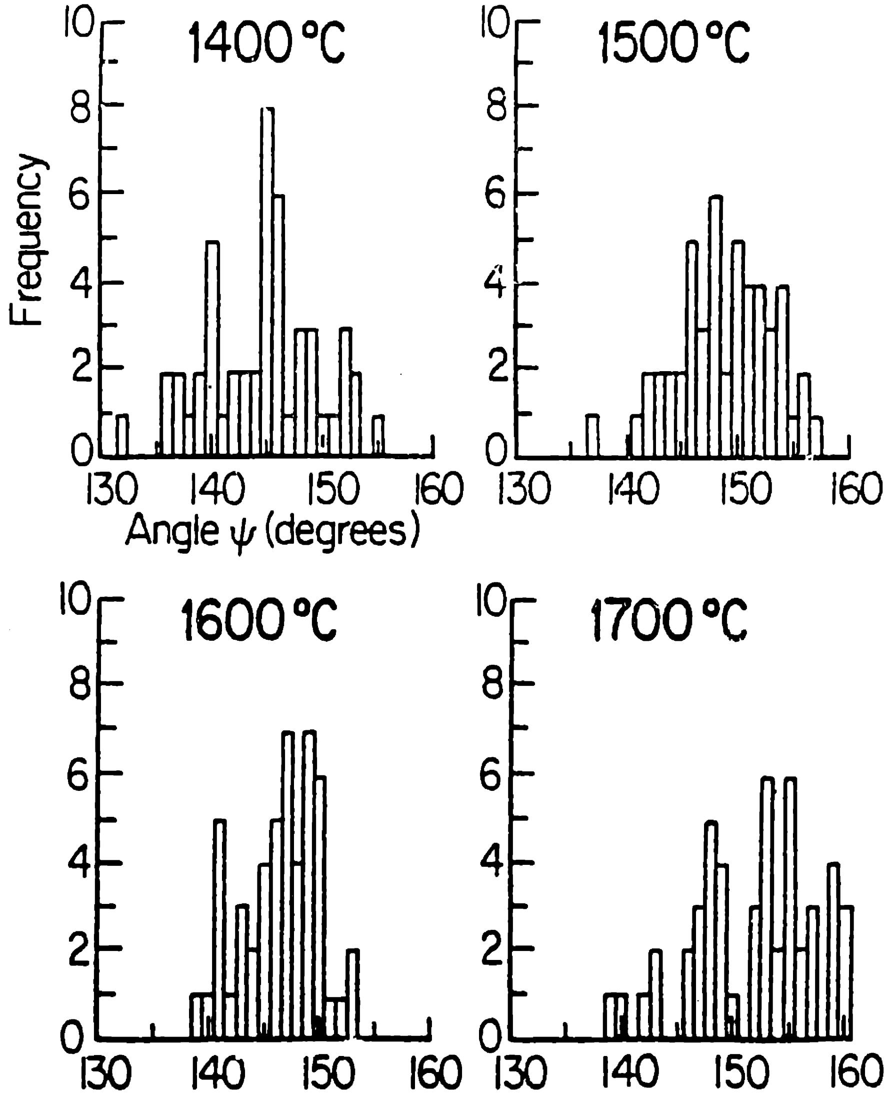

(a)

Figure IV-14 Histograms calculated from interference fringes by Hodkin (personal communication): (a) for $UO_{2.001}$ and (b) $UO_{2.053}$.

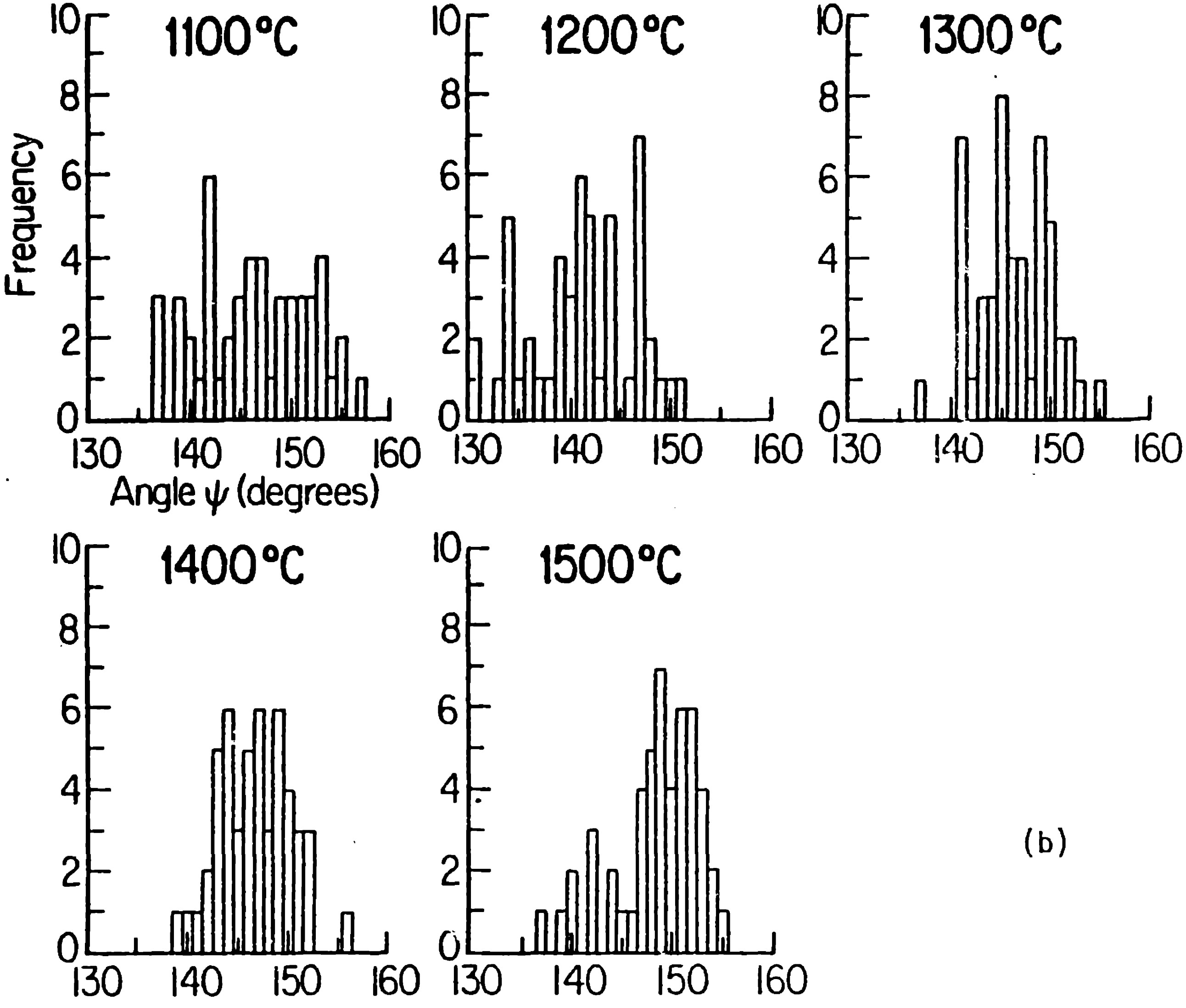
1100°C
1200°C
1300°C
1400°C
1500°C
Frequency
Angle ψ (degrees)
0
2
4
6
8
10
130
140
150
160

(b)

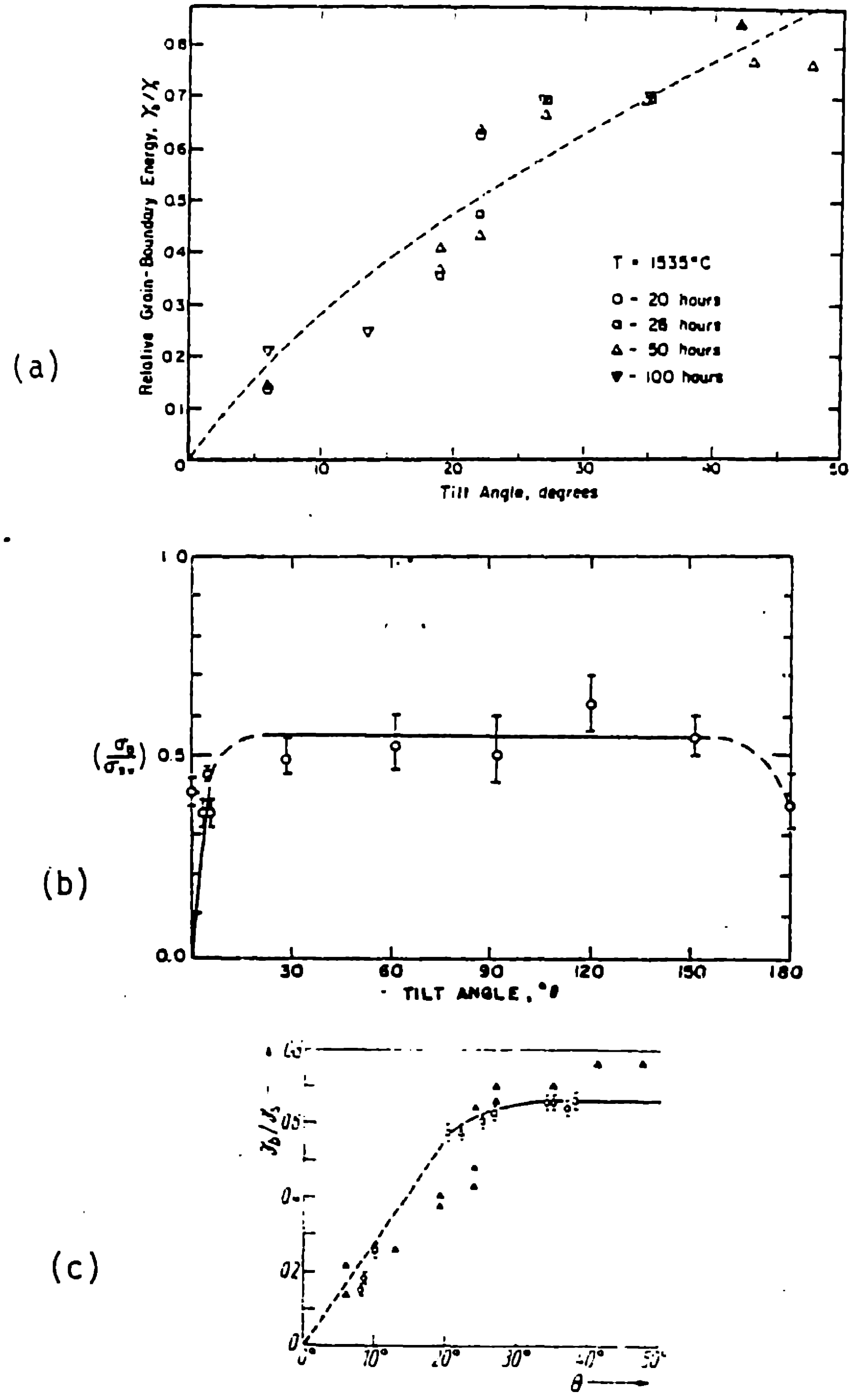

Figure IV-15 Misorientation dependences of dihedral angles:

(a) for<001>tilt boundaries in NiO, 1800 K, from Ready and Jech, 1968. (b) for $[\bar{1}100]$ tilt boundaries in alumina, from Skackelford and Scott, 1968.
(c) for<001> tilt boundaries in NiO at 1800 K, from Dhalenne, et al., 1979. o 100h, □ 50h, △ 20h.
(d) for<011>tilt boundaries in NiO at 1800 K, from Dhalenne, et al., 1982.
(e) for<001>tilt boundaries in Al, calculated by Hasson et al., 1972.

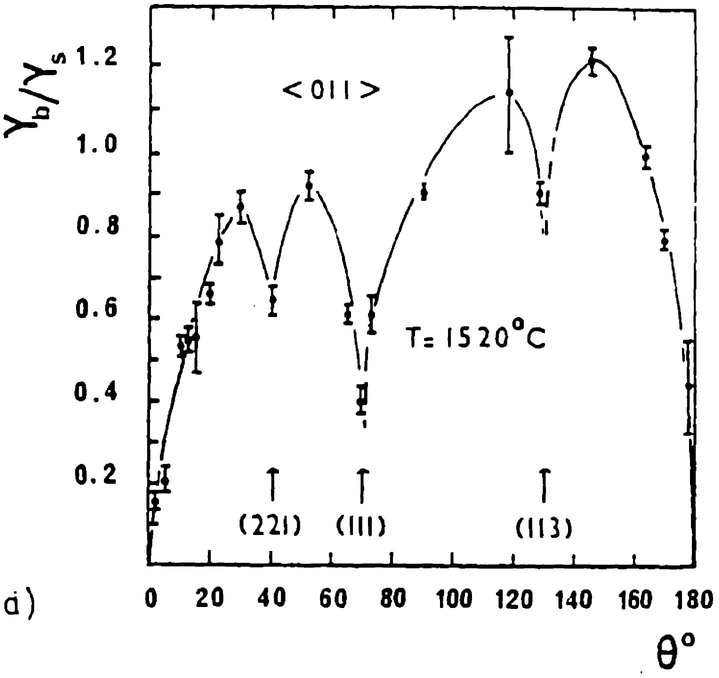
γ_b/γ_s
1.2
1.0
0.8
0.6
0.4
0.2
<011>
T= 1520°C
(221)
(111)
(113)
0
20
40
60
80
100
120
140
160
180
θ°

(d)

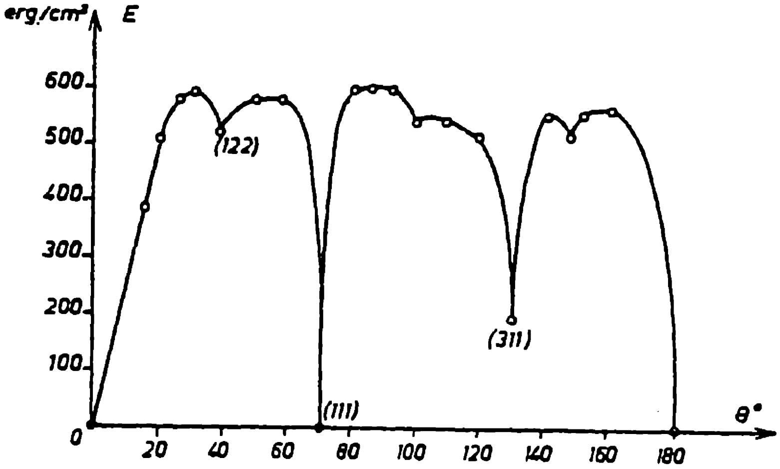
erg/cm²
E
600
500
400
300
200
100
0
(122)
(111)
(311)
20
40
60
80
100
120
140
160
180
θ°

(e)

corresponding to the misorientations of 39° (Σ=9), 70°30' (Σ=3) and 129°30' (Σ=11), respectively. For comparison, the energies of Al[011] symmetrical tilt boundaries as calculated by Hasson et al. are shown in Figure IV-15 (e). The two shallower minima at the (112) twin (θ= 109°28') and at θ ∿145° are not observed in the ψ-θ plot for NiO [011] tilt boundaries. This omission can be due to coulombic repulsion at these misorientations, to variations in γ_s with orientation obscuring variations in γ_{gb} with θ, or to insufficient resolution of angles in this range due to the interferometric technique.

The dihedral angles varied from 106° to 171° for NiO, with smaller angles for [011] tilt boundaries than for [001] tilt boundaries, and from 142° to 160° for [$\bar{1}$100] tilt boundaries in Al_2O_3. The range of ψ values for for NiO is significantly broader than the values for metals.

There have been no measurements of boundary vapor dihedral angles from grooved surfaces of covalent solids. However, Wagner and Chalmers (1960) measured the dihedral angle variation for twin boundary-grain boundary intersections in Ge. The results for [001] and [011] tilt boundaries and [001] twist boundaries are shown in Figure IV-16. Except for the Read-Shookley region for low angle boundaries, no energy/dihedral angle variation with miscrientation was observed.

As expected from the orientation dependences of the surface energy (Section IV.23) and the grain boundary energy (Section IV.2.4), the distributions of dihedral angles for metals, ionics, and covalents, are wide: 120° - 180° for metals with ψ from 140° - 180° for pure metals, and 100°-160° for ionics. In the following section, the values of $\bar{\psi}$ and the dihedral angle distributions measured from grooved surfaces are compared with measurements from pores on planes of polish.

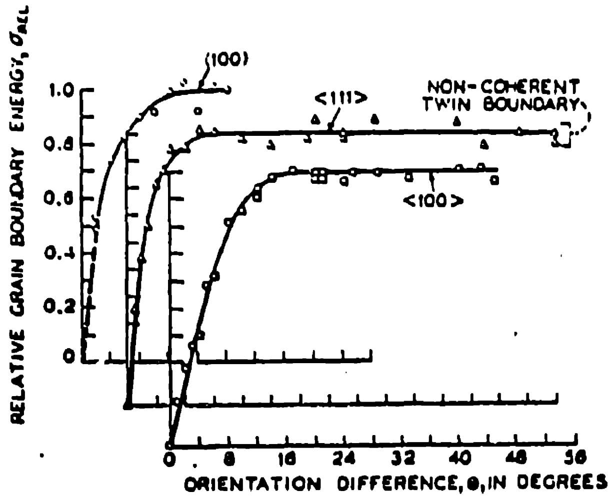

Figure IV-16 Orientation dependence of dihedral angles for<001> and<111>tilt boundaries and(001)twist boundaries in Ge, from Wagner and Chalmers, 1960.

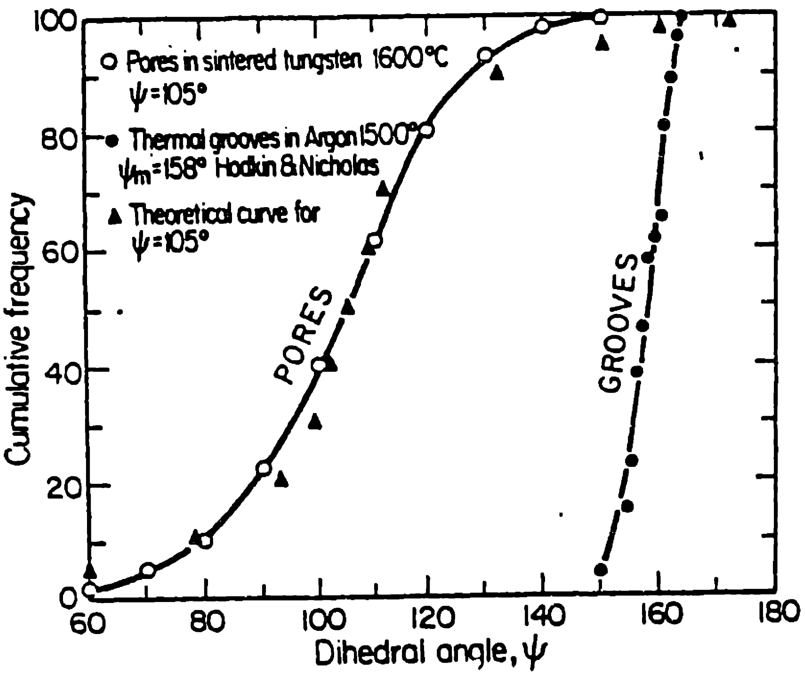

Figure IV-17 Cumulative distributions of apparent dihedral angles from surface grooves and internal pores in W, from Hodkin (personal communication).

2.5.2 MEASUREMENTS FROM POROUS COMPACTS

The distribution of dihedral angles in a sintered or hot pressed compact or in a polycrystalline compact undergoing creep cavitation is expected to be a subset of the possible dihedral angles determined by random boundary-surface combinations. Data from porous W and UO_2 compacts support this theory.

Dihedral angle data from porous sections of W sintered at 1870K are compared in Figure IV-17 with the distribution of angles measured by interferometry of W surfaces grooved at 1770K in argon (Hodkin and Nicholas, unpublished research). On porous sections $\psi_m = 105°$; on grooved surfaces, $\psi_m = 158°$. Comparison of the groove data from the porous compact with the calculated apparent distribution for $\psi = 105°$ reveals that the distribution for the porous compact is similar to the $\psi = 105°$. This range does not include the range of angles measured by interferometry (150°-164°). These results suggest that populations of dihedral angles in porous sintered compacts and on grooved surfaces for W are substantially different. This result is discussed below in terms of the implication for sintering.

Several dihedral angle distributions from polished sections of sintered unirradiated compacts of UO_2 , UO_2/5wt% PuO_2, UO_2/15 wt% PuO_2 and UC/15 wt% PuC are shown in Figure IV- 18 (a)-(f) (Hodkin, 1980). The theoretical curves for single-valued dihedral angles are also plotted for several of the curves. The sample histories and the median values for these curves are tabulated in Table IV-6 with the values of ψ for grooved surfaces of similar composition. Because these data were obtained on small pores near the limit of resolution (500x-1000x), the smaller apparent angles are not represented in the curves.

Table IV-6

Median Pore Angles from Polished Sections of Unirradiated and Irradiated Nuclear Ceramics (from Hodkin, 1980, unless otherwise noted)

Material	Angles Measured	Median Pore Angle (degrees)	Sample History
Unirradiated			
UO_2	50	93.2	Sintered after jet-milling at 1550°C for 8 h in H_2
UO_2		92	Sintered 5 h at 1600 C plus 50 h at 1800°C in H_2 containing 2-3% H_2O (Francois and Kingery; 1965)
UO_2/5wt%PuO_2	20	99.6	Sintered 1550°C for 4 h in wet H_2
UC/15wt%PuC+ M_2C_3	36	98.6	Sintered in argon at 1650°C for 4.5 h
UC/15wt%PuC+ MC_2	25	93.2	Sintered in argon at 1650°C for 4.5 h
Irradiated			
UO_2	50	94	WAGR solid pellet irradiated 0.5-1.0% burn-up; T = 1100-1300°C
UO_2/15wt%PuO_2 equiaxed grain structure	32	93	Annular mixed oxide pellets, irradiated in Harwell MTRS to 7.4-8.6% burn-up
UO_2/15 wt%PuO_2 columnar grain structure	110	77	"
UC/15wt%PuC 0.2%O_2	50	94.6	Sintered and crushed fuel feed vibropacked; burn-up 4.4-5.5%; 1198°C =PCFT; from structure estimated tem. = 1130°C ± 50°C; Sample > 900°C
UC/15wt%PuC 1.0% O_2	25	96.4	Sintered and crushed fuel feed vibropacked; burn-up 4.4-5.7%; 1245°C = PCFT; from structure estimated temp. = 1152° ± 70°C; SAmple > 900°C

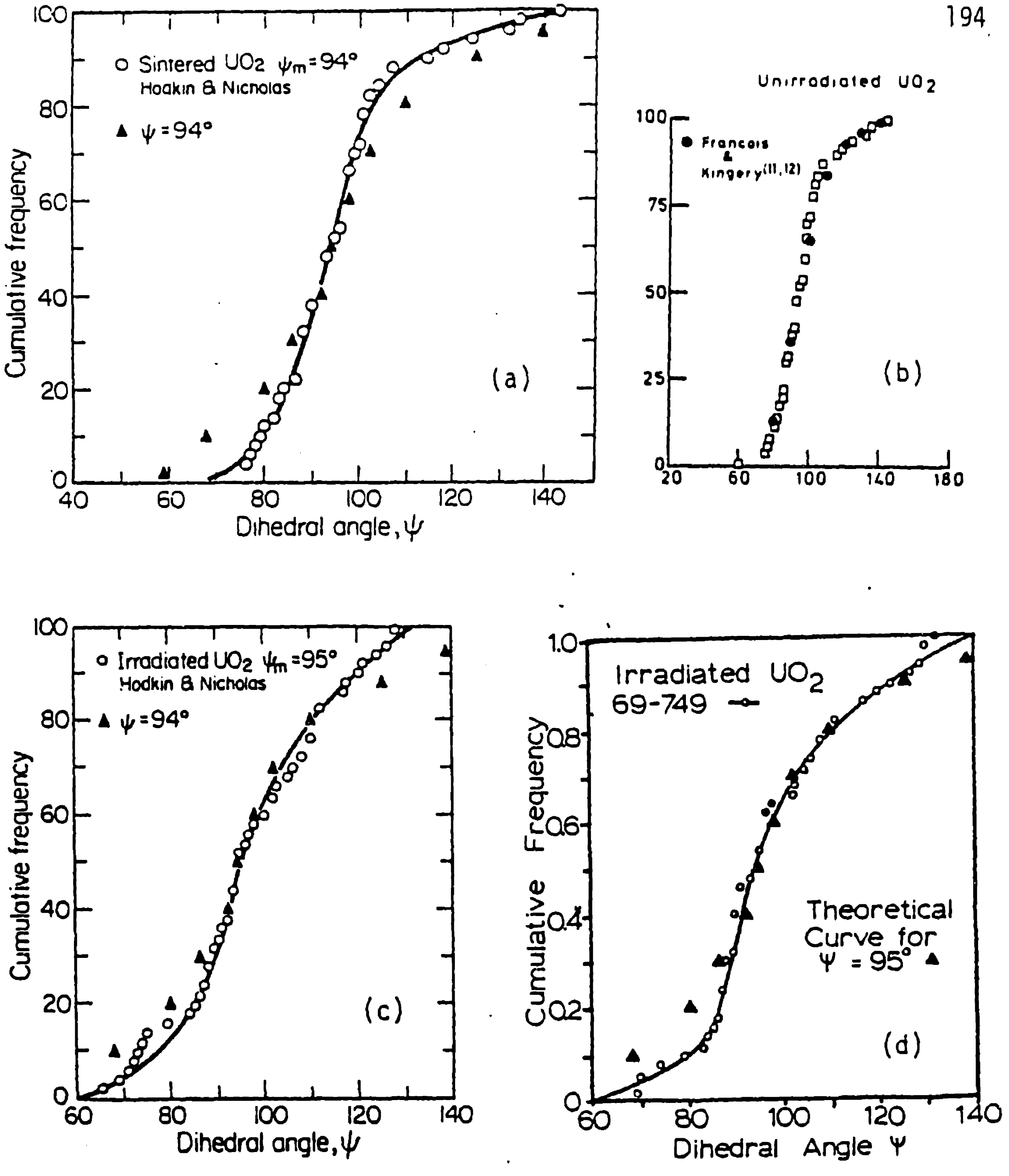

Figure IV-18 Cumulative distributions of apparent dihedral angles from planes of polish in porous nuclear ceramics (from Hodkin, 1980):(a,b)sintered UO$_2$; (c) sintered and irradiated UO$_2$, Sample 69-810; (d) sintered and irradiated UO$_2$, Sample 69-749; (e)sintered UO$_2$/5wt% PuO$_2$; and (f) sintered and irradiated UO$_2$/15wt% PuO$_2$. Hodkin data in (a) and (b) are identical.

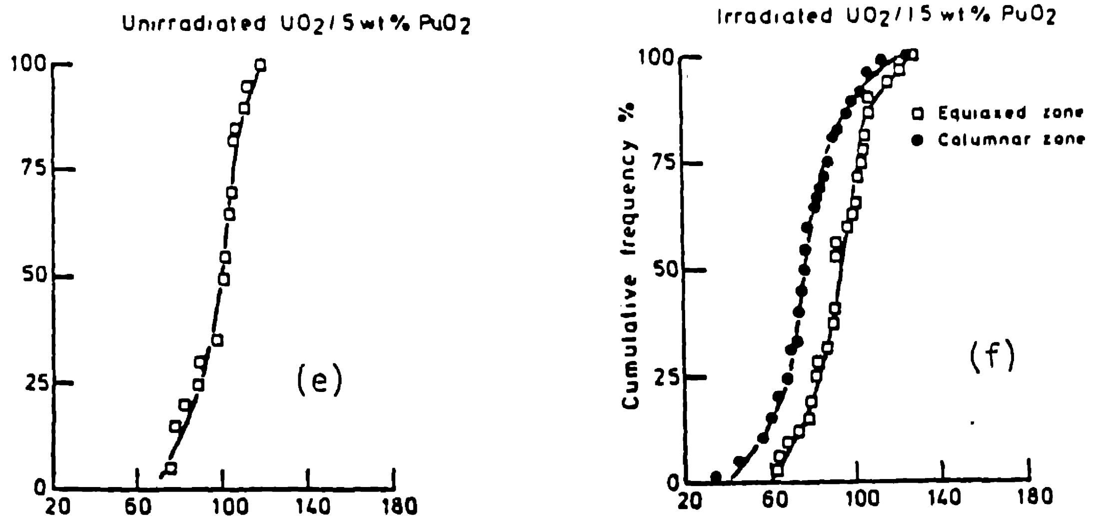

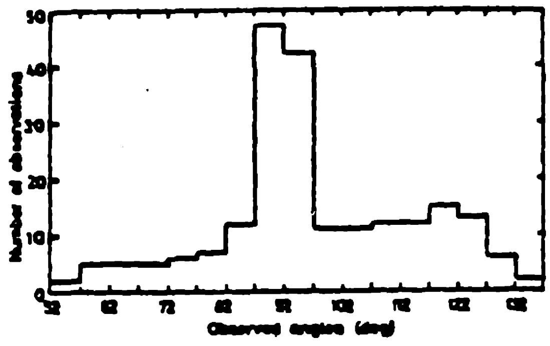

Figure IV-19 Histogram of apparent dihedral angles from internal pores in undoped β-SiC (from Suzuki and Hase, 1978).

In addition, boundary-pore separation had occurred in all samples leading to ambiguities in identifying which pores were on boundaries; this led to a decrease in the number of larger apparent angles. Thus, the procedure described in Section 2.2.2 for the deconvolution to obtain the distribution of true angles represented in a distribution of apparent angles cannot be applied in these cases. The shapes of the curves are used as indicators of multiple modes in the apparent distributions. Without examination of the microstructures, it is not possible to determine whether modes determined by only a few points are significant.

The curve for sintered, unirradiated UO_2 shows only one peak at the median value, ψ_m = 93.2°. This value is not significantly different from that determined by Kingery and Francois (1965), ψ_m = 92° (Figure IV-18(a)). For irradiated UO_2 samples, the following peaks were found: Sample 69-810: 73°, 92°, 110° and Sample 69-749; 90°, 96°; Figures IV-18 (c) and (d), the pores in the equiaxed region of irradiated UO_2 showed only one peak.

The dihedral angle medians for unirradiated UO_2/5 wt% PuO_2 (Figure IV-18 (e)) and the equiaxed region in irradiated UO_2/15 wt% PuO_2 (Figure 18(f)) are similar. In the columnar region of UO_2/15 wt% PuO_2 (Figure IV-18 (f)) the distribution is shifted to smaller angles as expected from the model for bloating due to internal gas evolution.

The distribution of apparent dihedral angles measured by Suzuki and Hase (1978) from polished sections of porous, undoped β -SiC heated 2170K is shown in Figure IV-19. The distribution appears multimodal; the maxima occur approximately at 92° and 122°. Greskovich et al. (1975) determined that additions of B and C, which enhance sintering of SiC, do not change the distribution significantly. There are no grooving data for SiC with which to compare these apparent angles.

For W, UO_2, UO_2/PuO_2 and UC/PuC the distributions from grooved surfaces are significantly different from the distribution of apparent angles in porous compacts. In the UO_2 and UC samples, there may be multiple modes in the distributions of apparent angles in porous compacts. In the UO_2 samples, multiple modes in the distributions appear during irradiation and concurrent gas evolution. For porous undoped SiC, multiple modes exist in the as-sintered state.

In all cases presented in this section, where grain boundary grooving and polished section data were both available, the dihedral angle distribution from porous sections were shifted to smaller angles relative to angles from grooved surfaces, in agreement with the theory of pore stability presented in Chapter I. The apparent dihedral angle distributions from porous sintered samples were broad, denoting a wide distribution of true angles, and frequently had multiple modes. After gas evolution during heat treatment more small dihedral angles are observed in polished sections and more modes are apparent.

IV.3 Experimental Procedures

3.1 Measurements from Grooved Surfaces

The grooved samples for measurements using the metal reference line technique were high purity MgO, undoped Al_2O_3, and MgO-doped Al_2O_3. The grooves on the MgO-doped Al_2O_3 samples were measured by both interferometry and the metal reference line technique.

The grooved MgO samples were prepared from high purity $MgCO_3 \cdot n\text{-}H_2O$ (99.995 wt % Mg, cation basis), produced as described in Chapter III. The hydrated carbonate was transformed to MgO at 1270K in air (specific surface area = 20 m^2/gm). The MgO powder was cold pressed in a WC die at approximately 700 MPa. and annealed at 1870 K in air for 48 h. The sample densities were approximately 99% ρ_{th}.

The fabrication and grooving heat treatments of the Al_2O_3 samples* are listed here for facile reference but do not constitute work performed for this research project. The undoped Al_2O_3 samples (nominally 99.99% Al_2O_3) were prepared from mixtures of ball-milled α- and γ-Al_2O_3 of different specific surface areas (Sample 1: 1m^2/gm and Sample 2: 30m^2/gm). The powder was isostatically pressed at 300 MPa, prefired at 2173K for 4h, and vacuum fired ($< 2 \times 10^{-5}$ torr) at 1820K for 95h to greater than 99.6% ρ_{th}. Disks of high density MgO-doped Al_2O_3 were cut from an 8mm. diameter rod supplied by the General Electric Company. The MgO concentration of the samples was above the solubility limit; $MgAl_2O_4$ precipitates were evident.

All grooving samples were polished using a succession of diamond pastes of grit sizes from 15µm to 0.25µm with a solution of ethanol and ethylene glycol. The depth of material removed was kept to a minimum but was not measured directly. A thickness of greater than one grain diameter was probably removed for all samples.

For the grooving anneals, the MgO-doped Al_2O_3 samples were packed in a 5 wt% MgO-95 wt% Al_2O_3 pre-equilibrated powder mixture. The undoped Al_2O_3 and MgO samples were packed in the parent powder to suppress evaporation from the surfaces and to provide a barrier to furnace contaminants. Details of the sample-powder grooving configuration are presented elsewhere (Dynys, 1982).

The MgO samples were grooved at 1520 K in air for 18 hrs. The MgO-doped and undoped Al_2O_3 samples were annealed at 1873 K in air for 3 hours

---

and 1 hour respectively.

The results of interferometric measurements of the MgO-doped Al_2O_3 were reported by Dynys. The dihedral angle values were originally calculated using Equation (IV-6). The data used here have been corrected using the Tolman-Wood correction factor described in Equation (IV-7).

Chromium gratings were deposited onto the thermally grooved oxide surfaces by the photoresist technique described in Section IV.2.2.1. A chromium grating on the grooved surface of MgO-doped Al_2O_3 at a tilt angle of 10° is seen in Figure IV-20. The SEM experiments were performed on the AMR 1400 and 1000A microscopes at specimen stage tilts from 0° to 80°. The specimen stage tilt was calibrated by measuring a line of known length from 0° to 80°. The apparent dihedral angles at large tilt angles were measured directly from SEM micrographs and the true dihedral angles calculated from the stage tilt angle and the angle between the boundary and the metal gratings at the groove root. The SEM optics and the projection geometry are shown in Appendix AII.

3.2 Measurements from Porous Sections

Apparent angle distributions from internal pores were measured for three MgO samples and one MgO-doped Al_2O_3 sample. The sample histories and the angle measurement techniques are listed in Table IV-7. The microstructures of MgO-1 and MgO-3 are described in detail in Chapter II. Representative microstructures of MgO-1 and MgO-3 are shown in Figure II-5 and II-11, respectively. The microstructures of the as-hot pressed MgO-2 is shown in Figure IV-21 (a). After annealing at 1670K for 1h, the density of MgO-2 had decreased to 96% ρ_{th} and the grain size increased by a factor of 5, as seen in Figure IV-21 (b). The high density Al_2O_3

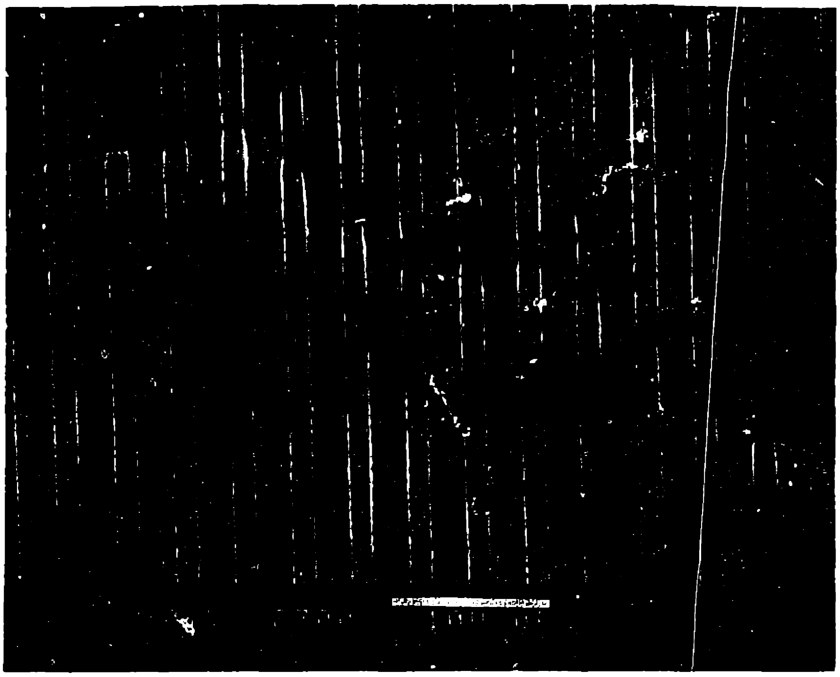

Figure IV-20 Chromium grating on surface of MgO-doped Al_2O_3 at a tilt angle of 10°.

Table IV-7

Sample Histories and Angle Measurement Techniques for MgO and MgO-doped Al_2O_3

Sample	Thermal History	Measurement Technique
MgO-1	hot pressed $Mg(OH)_2$-derived MgO annealed at 1670 K $\rho \sim 0.95 \rho_{th}$	polished sections observed by optical microscopy and SEM
MgO-2	hot pressed $MgCO_3$-derived MgO $\rho \sim 0.99 \rho_{th}$ annealed at 1670K $\rho \sim 0.90 \rho_{th}$	fracture surfaces examined by SEM
MgO-3	settled $MgCO_3$-derived MgO compacts sintered at 1670 K $\rho \sim 0.98 \rho_{th}$	fracture surface examined by SEM
MgO-doped Al_2O_3	sintered compacts deformed 4% to maximum stresses of 55 to 76 MPa at 1670K	thin sections observed by TEM

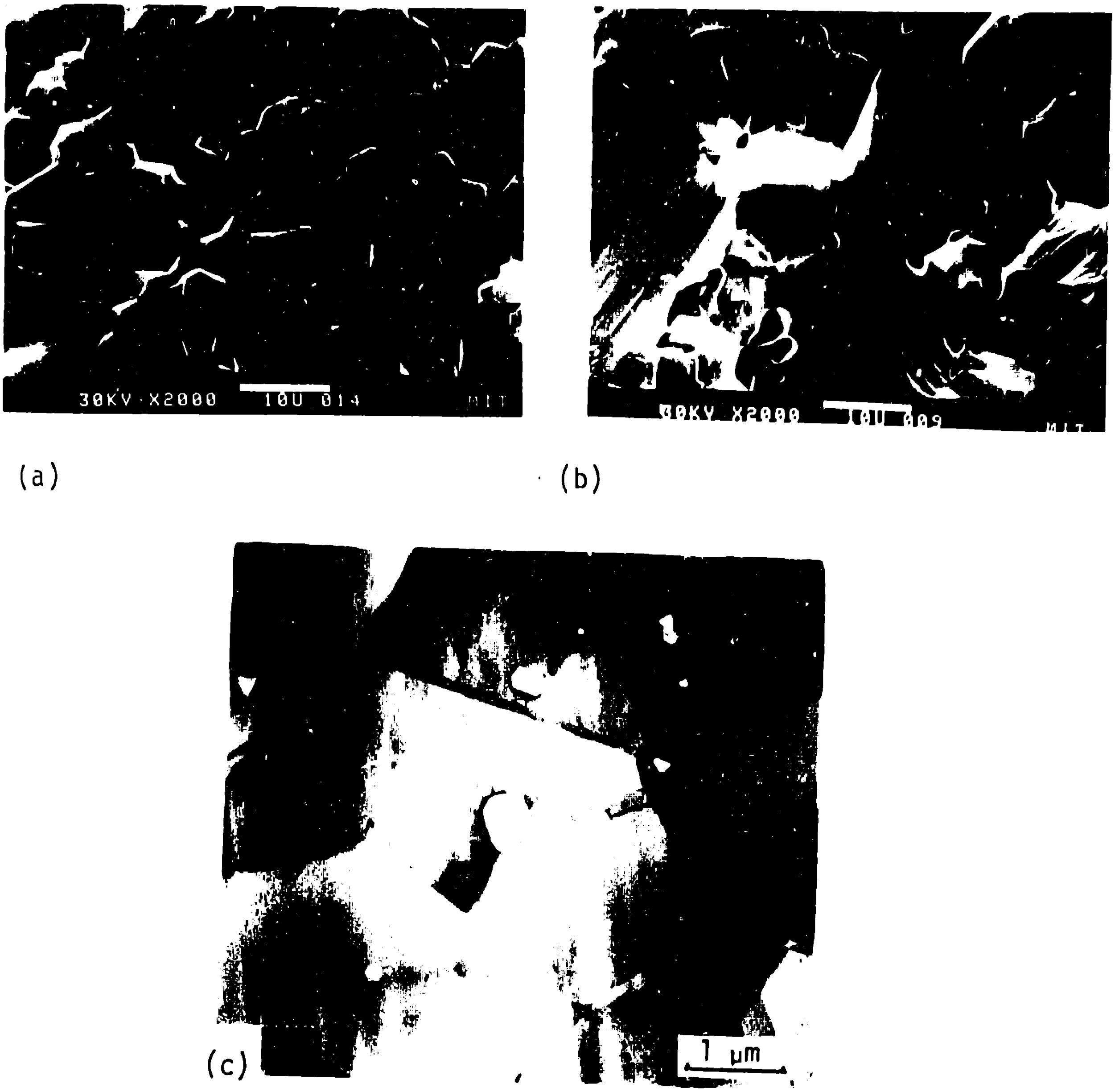

(a)

(b)

(c)

Figure IV-21 Microstructures of (a) as-hot pressed MgO; (b)hot-pressed and annealed MgO after 1 h at 1670K; and (c) strained MgO-doped Al_2O_3 sample (from Heuer et al., 1980).

samples* were deformed 4% to maximum stresses of 55 to 76 MPa at 1670K and subsequently thinned to form TEM foils (Heuer, Tighe, and Cannon, 1980). A typical microstructure of the cavitated samples is shown in Figure IV-21 (c).

The dihedral angle distributions of MgO-1 were measured from optical micrographs at 500X of polished, unetched surfaces. Dihedral angles of MgO-2 and MgO-3 were measured from SEM micrographs of fracture surfaces. Fracture was primarily intergranular. No assessment was made of the deviation of the apparent dihedral angle, which is determined, in part, by the tilt of the pore -grain boundary intersection relative to the SEM projection plane, from the true dihedral angle. The apparent angles for the MgO-doped Al_2O_3 samples were measured from TEM micrographs.

IV.4 Results

4.1 Measurements of grooved surfaces

Representative surfaces of the MgO, Al_2O_3 and MgO-doped Al_2O_3 samples are shown in Figures IV-22 (a)-(c). Varying degrees of faceting were exhibited by the surfaces. Undoped Al_2O_3 faceted considerably more than MgO-doped Al_2O_3; both were more faceted than the MgO surfaces. Faceting in undoped and MgO-doped Al_2O_3 has been discussed in detail by Dynys (1982). Most grooves were asymmetrical, with average groove widths of 15μm, 0.5μm, and 1μm for the MgO-doped Al_2O_3, undoped Al_2O_3, and MgO surfaces, respectively. The grain sizes ranged from 10-30 μm for the MgO-doped Al_2O_3, 5-100 μm for the undoped Al_2O_3, and 10-40μm for the MgO samples. There was no correlation between the curvature of the boundary and symmetry of the observed groove.

---

*Courtesy, R. M. Cannon, A. H. Heuer, and N. J. Tighe

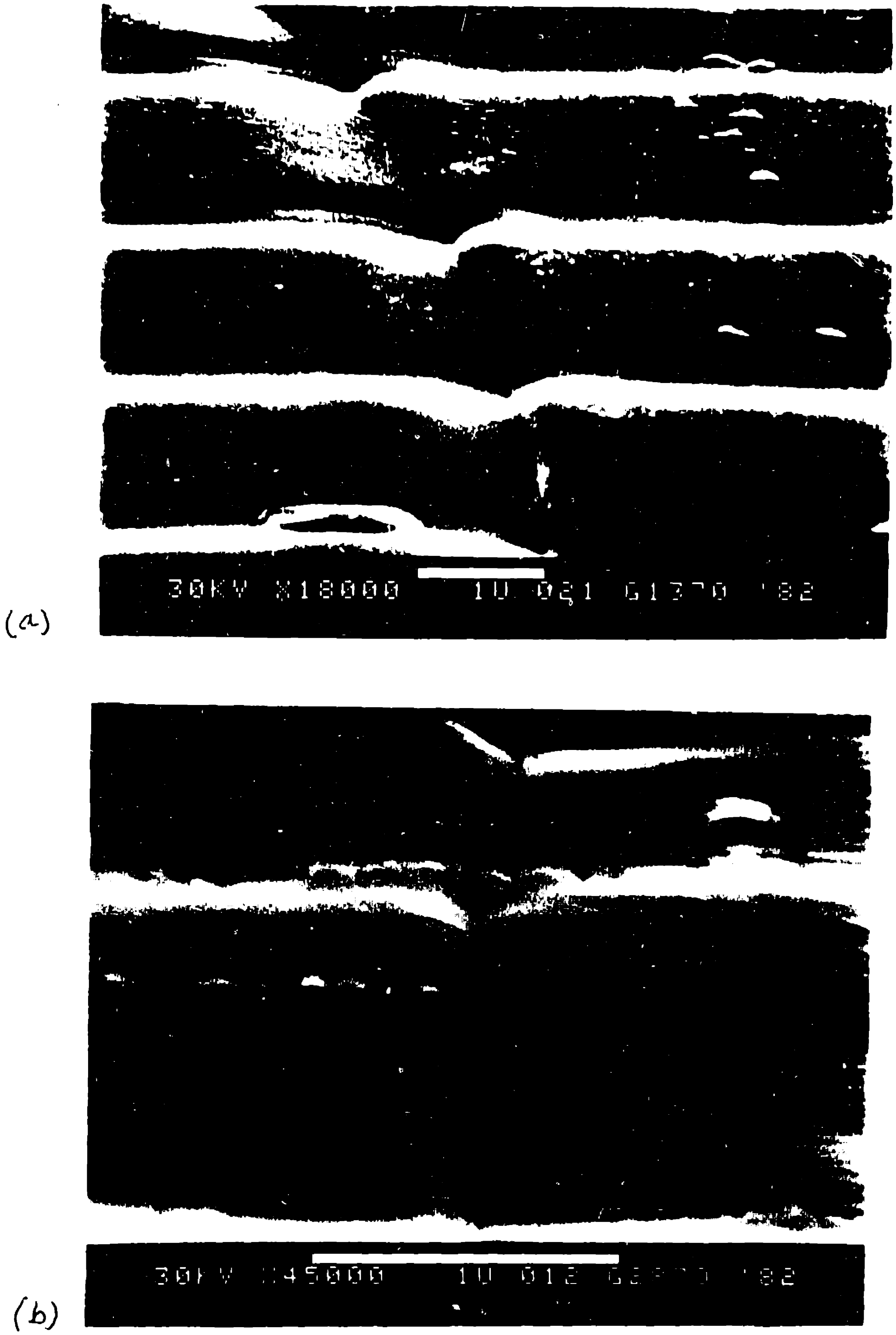

Figure IV-22 Representative surface with metal reference lines: (a) MgO; (b) Al_2O_3; and (c) MgO-doped Al_2O_3.

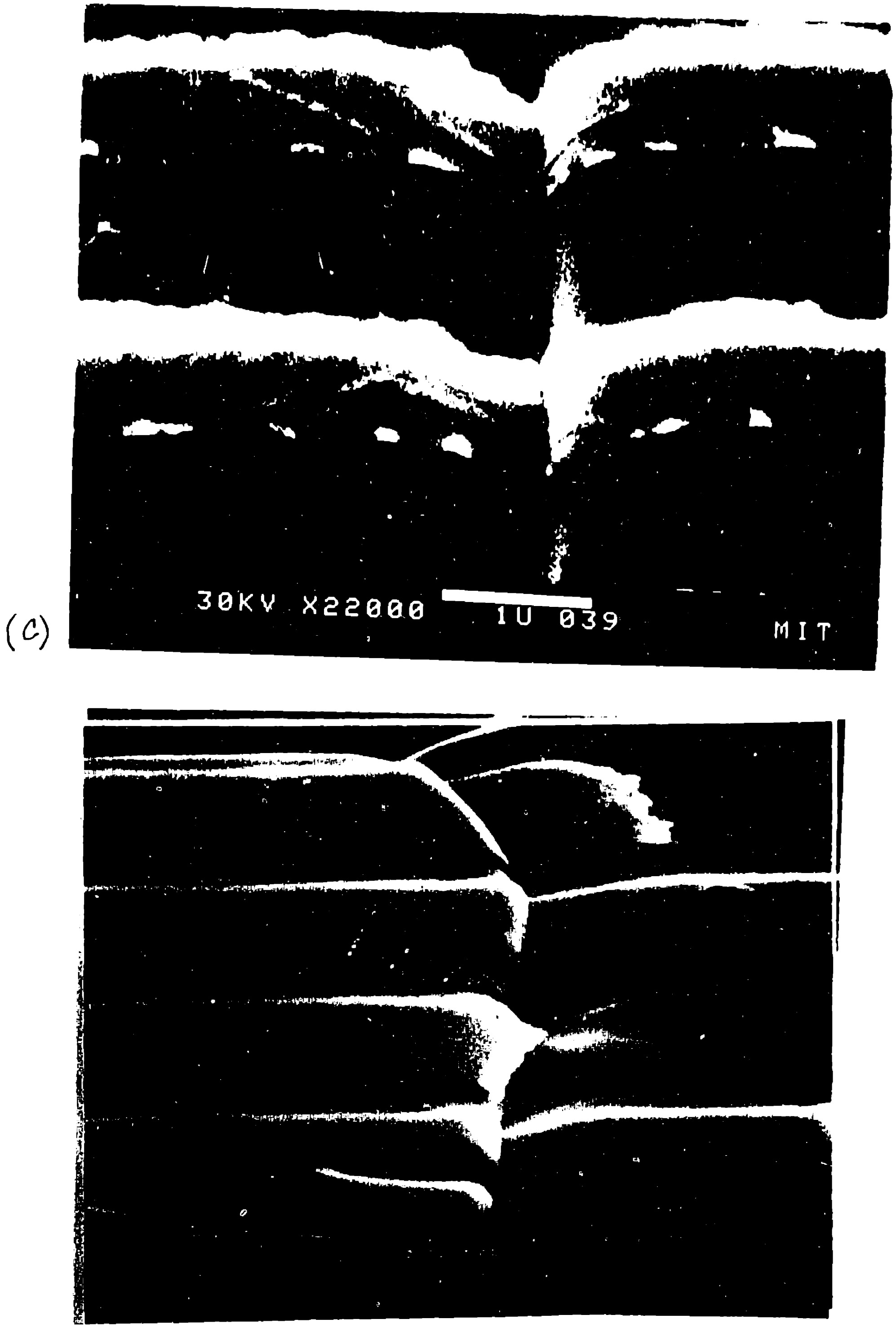

Figure IV-23 Example of poor metal-ceramic adhesion at grain boundary grooves.

An example of a MgO boundary groove not measurable by the metal reference line technique is shown in Figure 23. The metal grating is partially detached from the groove and the grain surfaces. In addition, boundary curvature obscures the groove root. In the sample described here, it is estimated that boundaries immeasurable due to such curvature make up less than 1% of the total.

The distribution of dihedral angles measured by the metal reference line technique and by interferometry are presented in Figures IV-24 (a)-(c). Using the reference line technique for MgO the dihedral angles range from 97° to 123° with the median, ψ_m = 112°. For undoped Al_2O_3 the angles are from 85° to 170°, with ψ_m = 115°; for MgO-doped Al_2O_3, the dihedral angles range from 95° to 142° with ψ_m = 117° using the reference line technique and from 110° to 144° with ψ_m = 130° using interferometry.

The partial angles Ψ_1 and Ψ_2, as defined in Figure 1 (d), were determined and are graphed in Figures IV-25 (a)-(b). The partial angles range from 28° to 87° for MgO, 29° to 76° for MgO-doped Al_2O_3, and 38° to 90° for undoped Al_2O_3

4.2 Measurements of porous compacts

The observed dihedral angles for pores in MgO are presented in Figure IV-26(a) with the data from grooved MgO surfaces. The plane of polish and fracture surface data range from 49° to 111°. For MgO-1 (Al-doped, hot pressed), ψ_m = 76°. For both MgO-2 (hot pressed) ψ_m = 90°. For MgO-3 (sintered), ψ_m = 87°. An additional peak was observed at 55° for MgO-3. The dihedral angles from thermal grooves vary from 97° to 123°, with ψ_m = 112°.

The observed angles from TEM foils of MgO -doped Al_2O_3 vary from 39° to 129°, with ψ_m = 70° and are shown in Figure IV-26 (b) with the data from grooved surfaces. An additional peak is observed at 55°. As with the UO_2

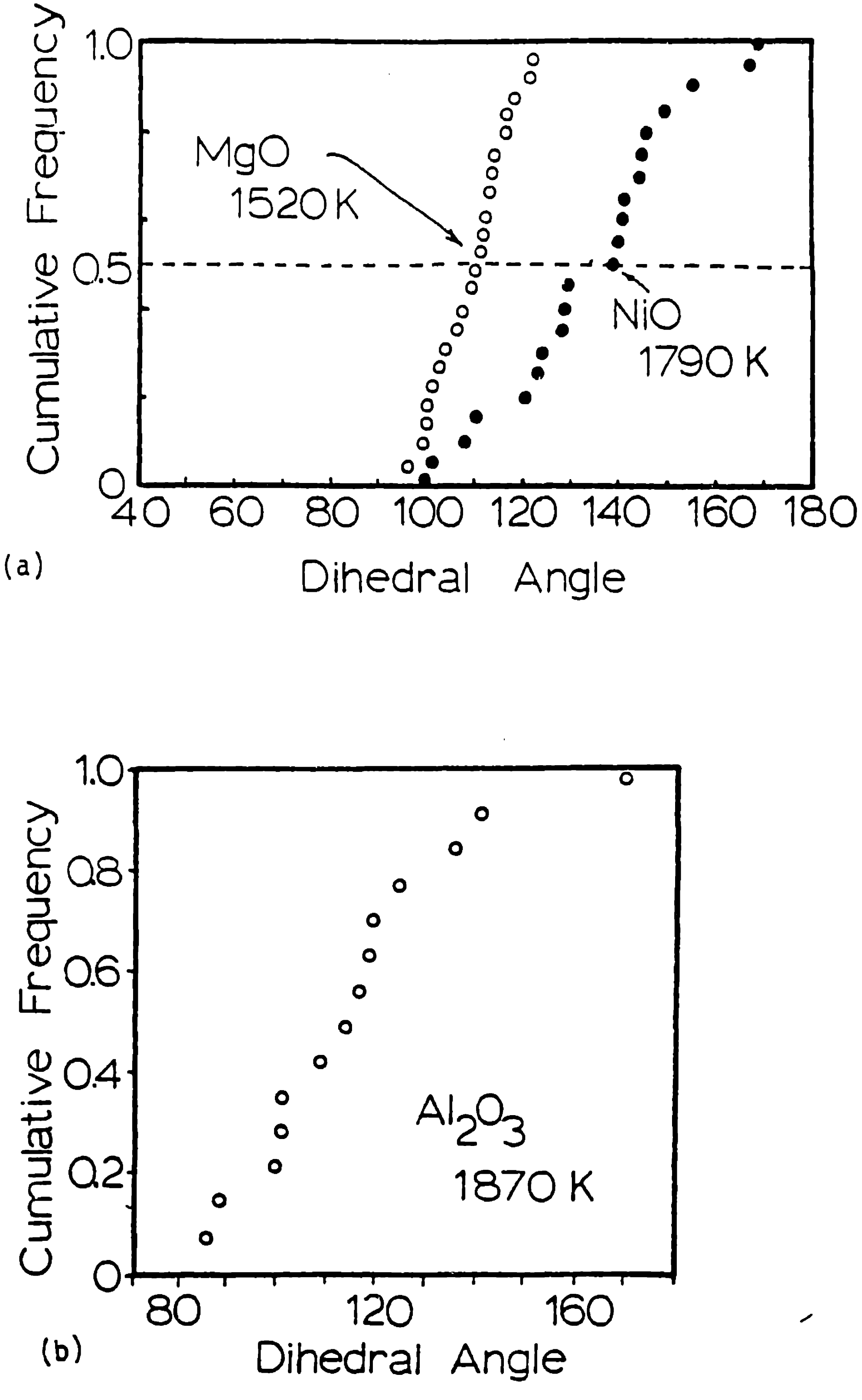

Figure IV-24 Cumulative distributions of dihedral angles measured by the metal reference line technique: (a) MgO; (b) Al_2O_3; and (c) MgO-doped Al_2O_3 along with angles detemined by interferometry on the same sampie.

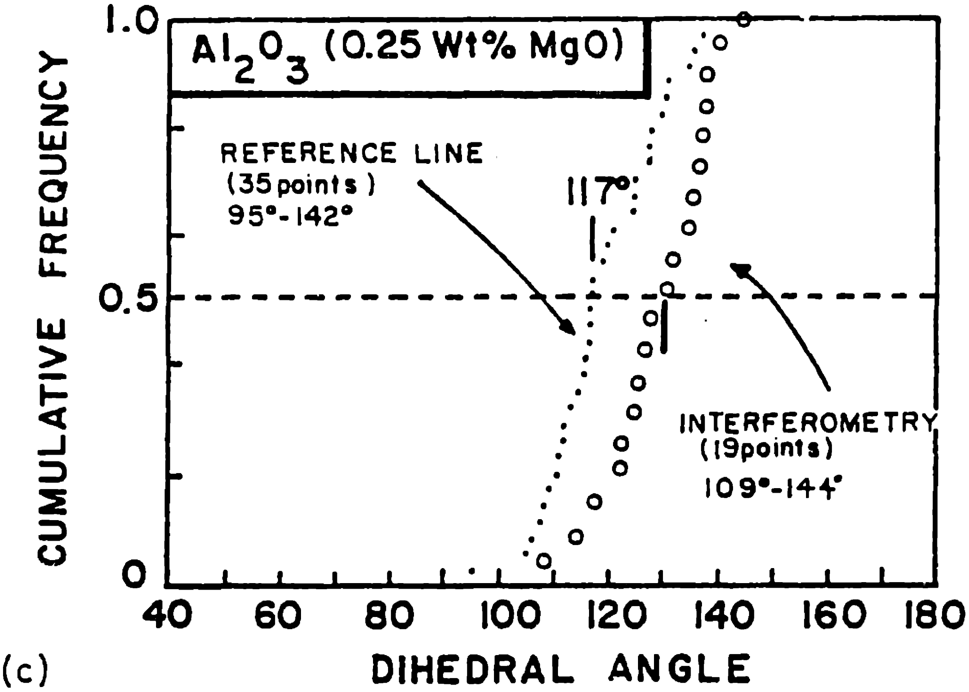

Al_2O_3 (0.25 Wt% MgO)
REFERENCE LINE
(35 points)
95°-142°
117°
INTERFEROMETRY
(19 points)
109°-144°
CUMULATIVE FREQUENCY
1.0
0.5
0
40
60
80
100
120
140
160
180
DIHEDRAL ANGLE

(c)

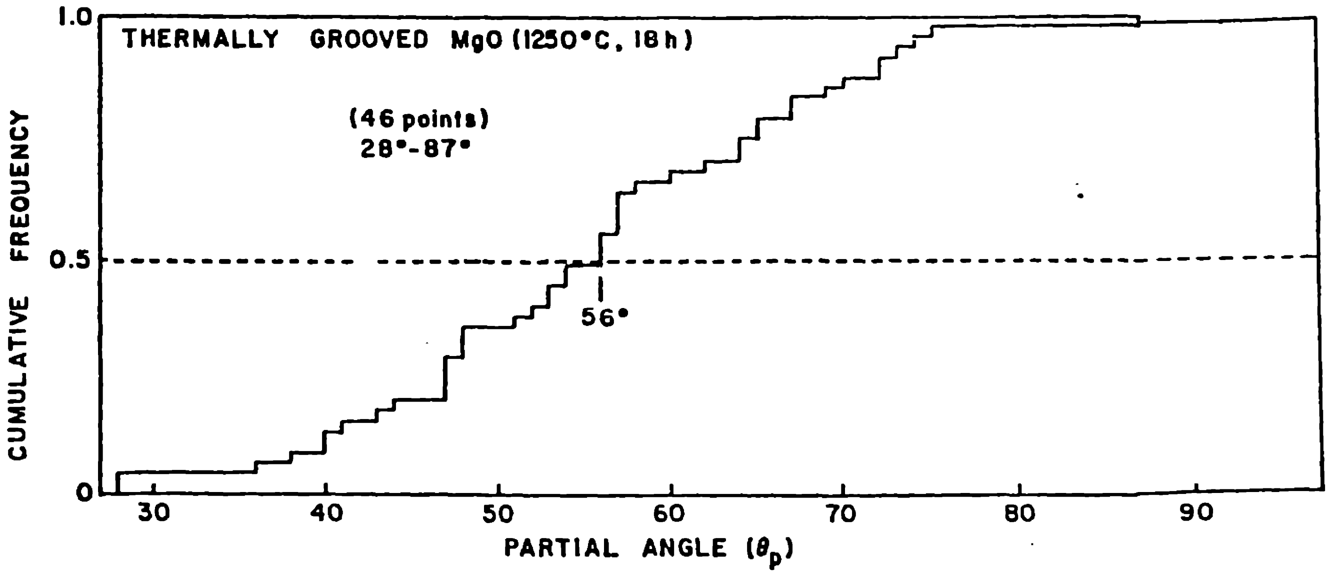

Figure IV-25 Cumulative distributions of partial dihedral angles as defined in Figure IV-1(d): (a) MgO and (b) Al_2O_3 and MgO-doped Al_2O_3.

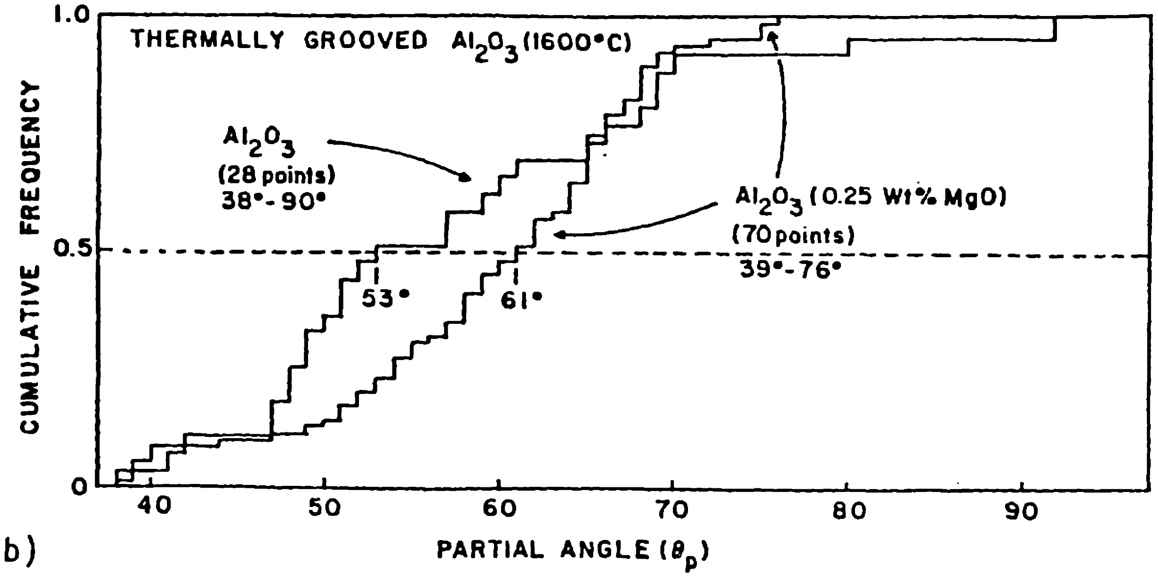
THERMALLY GROOVED Al_2O_3 (1600°C)
Al_2O_3
(28 points)
38°-90°
Al_2O_3 (0.25 Wt% MgO)
(70 points)
39°-76°
53°
61°
CUMULATIVE FREQUENCY
1.0
0.5
0
40
50
60
70
80
90
PARTIAL ANGLE (θ_p)

(b)

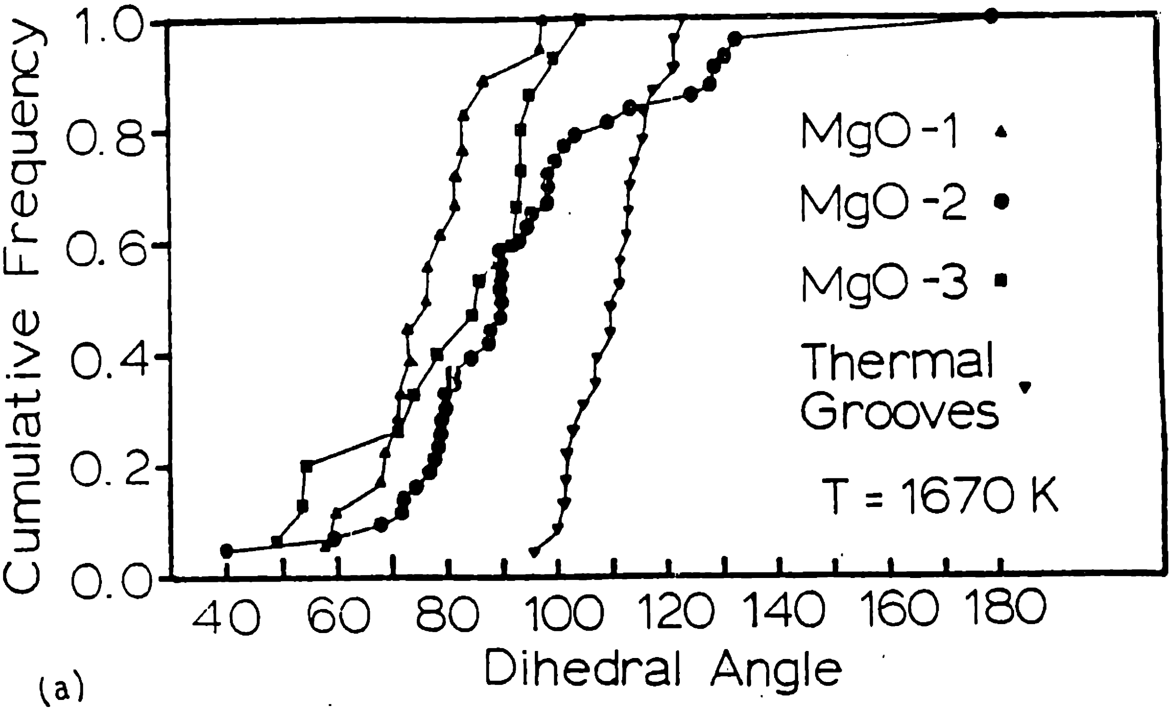

Figure IV-26 Distributions of Apparent dihedral angles in porous (a) MgO and (b) MgO-doped Al_2O_3.

data, the multiple modes in the MgO and Al_2O_3 distributions are determined by 1-2 data points and, therefore, cannot be considered as signficant as the general shape and the median value of the curves.

IV.5 Discussion

Of primary importance for interpretation of dihedral angle distributions is the effect of measurement technique on measured angles. In this study the same sample has been examined using the metal reference line technique and optical interferometry. The median value was shifted from 130° (interferometry) to 117° (metal reference line technique). By interferometry, 50% of the grooves had angles $< 130°$; by the metal reference line technique, 83% of the grooves were $< 130°$. Using Figure IV-3(a) a $\pm 2°$ degree error in measuring the angle produced by optical interferometry leads to a range of calculated angles from 93° to 124° for a true angle of 112°. It is suggested that measurements from interference micrographs are generally in error by $(+\Delta\psi')$ rather than $(-\Delta\psi')$ at small values of ψ', leading to the observed upward shift in angle.

The observed shift to larger angles can also be generated by measurements near but not at the groove root. The angle near the groove root is greater than or equal to the angle at the groove root. With the metal reference line technique, the higher resolution of SEM allows observation of the angles nearer to the groove root than with interferometry. Thus, the metal reference line technique represents a significant improvement over interferometry for measurements of small dihedral angles.

It has long been recognized that plastic deformation can introduce crytallographic texture into a dense body. Pressure forming operations of powder compacts, such as die pressing, hot pressing, and extrusion can, likewise generate subsets of random grain orientations in the compacts. All three materials used in this study were prepared by pressure forming operations (see Table IV-7). Therefore, it cannot be unequivocably stated that the boundaries and surfaces sampled in this study represent the total possible ranges. However, the observed distributions are broad, as expected from the variations of γ_s and γ_{gb} described in Sections IV.2.3 and 2.4 and are the most reliable data on ionics based on an analysis of measurement techniques. The effect of processing techniques is discussed further in Section IV.5.

The dihedral angle distribution for MgO at 1520K does not extend to angles greater than 123°. Some angles nearer 180° are expected in MgO both from calculations of the energies of low angle boundaries and from angle measurements for tilt boundaries in NiO. The dihedral angle distribution for MgO at 1520 K is presented with the dihedral angle data for NiO [011] tilt boundaries at 1790K, measured using interferometry. These NiO data were reported by Dhalenne et al. (1982) and corrected according to Equation IV-7. The NiO distribution varies from 101° to 170°. The dihedral angle values for NiO [001] tilt boundaries for $\theta = 7° - 37°$ are from 137° to 170°, a subset of the values for [011] tilt boundaries (Dhalenne et al., 1979). The range of angles from 139°-170° correspond to NiO low angle boundaries and twins for [011] tilt boundaries and to the entire range for [001] tilt boundaries. Using the 13° correction to convert interferometry data at low angles to 'true' angles, the low angle and twin data vary from 126° to 170°. The remaining NiO dihedral angles vary from 88° to 117°.

If the grain boundaries are randomly oriented, and low angle boundaries vary by $\sim$10° from perfect coincidence for all intersections, the percentage of low angle boundaries in the total population (not counting 'special' boundaries) is $\sim$ 5%. For a sample size of n, the probability that at least one low angle boundary is present in the sample is

$$P_n = 1 - \left(\frac{95}{100}\right)^n$$

For n = 25, 50 and 100, P_n = 78%, 92%, and 99.4%, respectively. Although only 25 data points are given in Figure IV-25 (a), the MgO sample surfaces were scanned to identify any large dihedral angle in the population ($\psi > 160°$). For the $\sim$ 200 grains examined, P_{200} = 99.96% for 5% low angle boundaries in the population. However, no large angles were found. This result implies that the percentage of <u>low-energy</u>, low-angle grain boundaries and <u>low energy</u> special boundaries in the population is less than 5% and is probably much less than 1%. If the MgO samples have random populations of grain orientations and, hence, 5% low angle boundaries, the measured distributions must also include dihedral angles representative of the remaining 4+% of the low angle boundaries, not just of the low energy, low angle boundaries. The only calculations of boundary energies in ionics have been performed for 'special' low angle boundaries, for symmetrical <001> tilt boundaries and (001) and (011) twist boundaries in rock-salt structures. Although there are no other data, experimental or theoretical, with which to estimate the energies and dihedral angles of asymmetrical low angle boundaries, it is suggested from the NiO and MgO data that most low angle boundaries in rock salt structure materials are of high energy relative to the symmetrical low angle boundaries and have dihedral angles and energies comparable to high angle boundaries.

From both the MgO and NiO dihedral angle data, low angle grain boundaries in fcc ionics are of higher relative energy (small dihedral angles) than in metals. As described in Section IV. 2.5.1, low angle boundaries in metals have associated dihedral angles from 160° to 180°. Since surface energy anisotropy in metals is small and the $\partial\gamma_i/\partial\psi_i$ terms are also small, this range represents the low angle grain boundary energies. In NiO, the low angle symmetrical <001> and <011> tilt boundaries have angles from 126° to 170° showing a wider range than metals. Because of surface energy anisotropy these data are not simply converted to value of γ_{gb}.

As shown in Figure IV.-27, the dihedral angle distribution for undoped Al_2O_3 (85° - 170°) is broader than the distribution for MgO-doped Al_2O_3 (95° - 142°). Disregarding the datum at 170° for undoped Al_2O_3, the distribution is still broader than for MgO-doped. The observed change in the distribution of dihedral angles with MgO additions is consistent with the thermodynamics of adsorption and segregation. It is also consistent with the observation by Dynys of a decrease in the amount of faceting in Al_2O_3 with MgO additions. Less faceting implies a decrease in the anisotropy in the Wulff plot and lower absolute energies for some surfaces. It is assumed in this analysis that the highest surface and grain boundary energies are most affected by MgO additions. When Equation (IV-2) applies, the highest values of ψ are determined by the highest values of γ_s and the lowest for γ_{gb}. Adding MgO decreases γ_s and, hence, decreases ψ. Likewise, lowest values of ψ are determined by the lowest values of γ_s and the highest values of γ_{gb}, leading to an increase in ψ. This combined effect on γ_s and γ_{gb} narrows the distribution. The distributions of the partial angles for the two materials, shown in Figure IV-25 (b), also show the

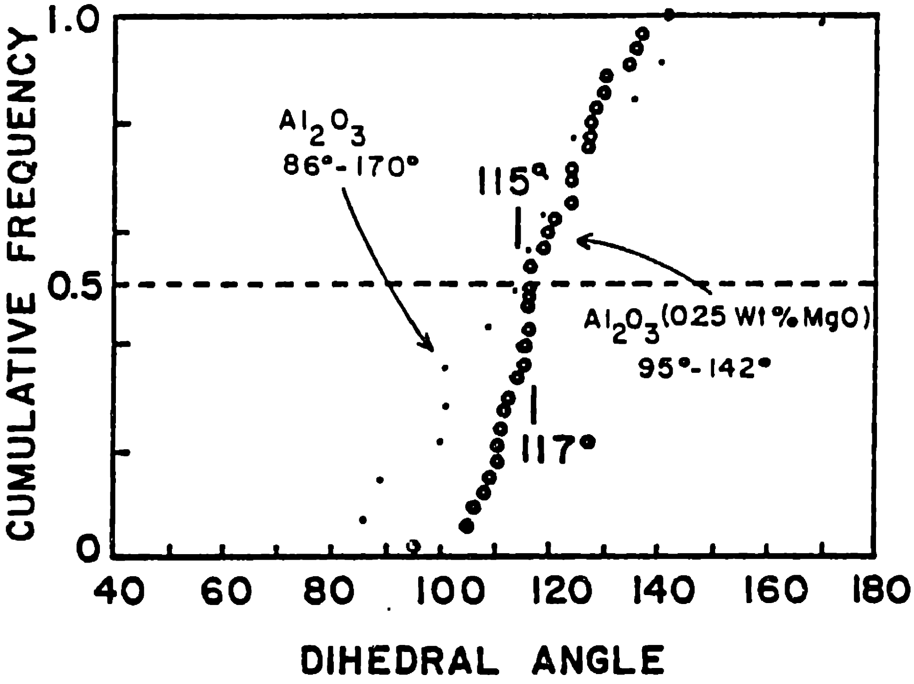

Figure IV-27 Dihedral angle distributions for undoped and MgO-doped Al_2O_3.

same differences in breadth as the ψ distributions.

The distribution for undoped Al_2O_3 samples at 1870K varies from 85° to 170° with $\psi m = 115°$ and $\bar{\psi} = 117°$. The range of these data includes the dihedral angle measurements for undoped Al_2O_3 of Shackelford and Scott (1968) for [$\bar{1}$100] tilt boundaries at 2070 K (143° - 159°) and of Gaddapati (1972) for polygonized boundaries and deformation twins at 2280 K (139°-170°). These boundaries are of lower energy than random high angle grain boundaries and are expected to have larger dihedral angles.

The value $\bar{\psi} = 117°$ differs significantly from Kingery's value of $\bar{\psi} = 152°$, measured by optical microscopy from polycrystalline undoped Al_2O_3 samples annealed at 2120 K. Although poor resolution and polishing could be blamed for the shift in $\bar{\psi}$, there are not enough data in this case to distinguish between differences in samples and in measurement techniques.

The asymmetry of the grooves, as determined by the partial angles graphed in Figure IV-25 (b) was more pronounced for the undoped Al_2O_3 (38°-90°) than for the MgO-doped Al_2O_3 (39°-76°). Although the range of dihedral angles measured by the metal reference line technique is narrowest for the grooved MgO surface (97°-123°), the asymmetry of the grooves was greatest for this sample (28°-87). The factors which influence the symmetry of the grain boundary grooves are: (1) boundaries not perpendicular to the surface; (2) differences in the surface energies of the two grain-vapor intersections; (3) the magnitudes of the surface energy and grain boundary energy "anistropy", the $\partial\gamma_i/\partial\psi_i$ terms; and (4) grain boundary migration.

There are no data to evaluate the first three factors. It is probable that the grain boundaries on the MgO samples were not perpendicular to the surface in light of the narrow distribution of dihedral angles and the broad distribution of partial angles. Dynys examined the changes in groove profiles with time for these Al_2O_3 samples and found no evidence of boundary migration. For the MgO samples there was no correlation between boundary curvature and measured dihedral angle or partial angles. Due to the myriad of factors determining groove symmetry, the partial angle data cannot be interpreted.

As discussed in Section I.2, relative pore stability is determined in part by the grain boundary to surface energy ratio and, hence, the dihedral angle. For four-sided pores in three dimensions, pores with dihedral angles equal to or less than 70.5° will be stable relative to pores with $\psi = 70.5°$. With all dihedral angles $\leq 70.5°$ is an ideal final stage microstructure.

In porous compacts with wide dihedral angle distributions, stable or growing pores will coexist with shrinking pores. As sintering proceeds, the apparent dihedral angle distribution shifts to smaller dihedral angles due to the stability differences among pores. Even for the case where all four-sided pores have $\psi \leq 70.5°$, there will be stability differences between pores with $\psi = 100°$ and with $\psi = 140°$, leading to differences in sintering rates. For the case of some four-sided pores with $\psi \leq 70.5°$, the pores must become three- or two-sided for sintering to continue. That is, the pore must separate from one or two boundaries without separation from all boundaries. In poorly packed green compacts (non-ideal, typical), n-sided pores, with $n > 4$, frequently occur. As n increases, the critical dihedral angle defining pore stability increases. For these cases, n must decrease for sintering to proceed.

If the pores become sufficiently large, no separation and no further densification will occur. Large local variations in porosity and boundary pinning will exist. Some regions will sinter to closed pore stage and undergo grain growth while other regions contain open pores. If the dihedral angle distribution is broad and the fraction of small angles is large, the probability of having a high density, large grain region adjacent to a samller grain size, porous region increases. The larger grain size region can then grow into the immobile porous region. This is the classic description of discontinuous grain growth.

For MgO-doped Al_2O_3, the dihedral angle distribution from grooved surfaces is narrower than for undoped Al_2O_3. The distribution of groove angles for MgO types are much narrower than for both Al_2O_3 sample types. From the analysis of the effects of dihedral angle distribution on sintering and grain growth presented above, the order in which these three materials will undergo discontinuous grain growth is undoped Al_2O_3 > MgO $\approx$ MgO-doped Al_2O_3. This is in good qualitative agreement with experiment.

The distributions of apparent dihedral angles for the porous MgO samples and the cavitated MgO-doped Al_2O_3 samples support the predicted microstructural evaluation based on dihedral angle variations. At high densities, the dihedral angle distribution is predicted to shift to small dihedral angles. As the density increases, the porosity is determined by the pores with low dihedral angles and by entrapped pores. In higher density samples undergoing grain growth, pores which effectively pin the boundaries or which migrate with the boundaries will dominate the distribution. Two-sided pores with the smallest dihedral angles were calculated by Hsueh, et al. to more efficiently pin and to migrate faster than pores of equal in-boundary radii but larger dihedral angle.

The average apparent dihedral angles for the MgO samples were observed to shift to 77° (MgO-1), 90° (MgO-2), and 82° (MgO-3). The median angles shifted to 70° (MgO-1), 90° (Mg)-2, and 88° (MgO-3), as compared with the $\psi_m = \bar{\psi} = 112°$ for the grooved surfaces. The sample MgO-1 which was Al-doped (500 ppm), hot pressed, and annealed at 1670K, has the highest density and the narrowest apparent dihedral distribution of the three sample types. There was no evidence of changing density or significant grain growth for the annealing times examined here. For the high density sample (MgO-1), the dihedral angles distribution is expected to be shifted to smaller dihedral angles relative to the distribution for sintered lower density material. The sample MgO-3 was sintered at the same temperature, had a much larger grain size and a slightly larger apparent dihedral angles. The sample MgO-3 has a broader dihedral angles distribution than MgO-1 and these two distributions overlap in the 40°-70° range. It is not certain whether the apparent mode at 45° for MgO-3 is significant. The MgO-1 and MgO-3 distributions are not significantly different from the theoretical curves for ψ = 75° and to ψ = 86°. Although it is certain that the apparent dihedral angles do not represent single true values, it is not possible to deconvolute the distributions into true angles as discussed in Section .

The sample MgO-2 was hot-pressed and, during annealing at 1670K, desintered due to internal gas pressure to < 90% ρth. The typical microstructure of the as-hot-pressed body is shown in Figure IV-22(c). Triple point pores and multi-sided pores are still apparent in the hot-pressed microstructure and have apparent dihedral angles in the 60°-90° range. After desintering to a high volume fraction porosity, the distribution of apparent dihedral angles was observed to be shifted to larger angles ($\overline{\psi}$ = 90°) relative to MgO-1 (77°) and MgO-3 (82°). At the initial stage of desintering, the original pores at triple points with low dihedral angles are expected to grow. As gas evolution and desintering proceed, the internal stress increases, leading to pore nucleation on grain faces and edges and to pore linkage along high energy (low ψ) boundaries. The distribution is predicted to broaden during desintering and to shift to higher ψ boundaries. This has occured in the MgO-2 samples.

The distrubtion of apparent angles for cavitated Al_2O_3 is significantly broader (39-119°) than for the MgO samples and may exhibit multiple modes. The pores/creep cavities were generally three-sided or four-sided in the TEM foils and were not observed in the as-hot pressed sample. The mode at 54° corresponds to the apparent angles at some three-sided pores where all 3 angles of the pore were $<60°$. These pores nucleated at the low stress used in these experiments and were still quite small and widely spaced for the creep times examined in this study. This distribution of apparent dihedral angles is broader than the distribution of surface groove angles and may represent a population containing angles less than 60°. This is in contrast to the distributions from porous MgO which overlappped with the distribution of surface groove angles.

IV.6 Summary

The surface-grain boundary dihedral angles span the following ranges for the materials and grooving techniques indicated: 97°-123° for MgO at 1520K, 85°-170° for undoped Al_2O_3 at 1870K, and 95°-140° for MgO-doped Al_2O_3 at 1870K. Using a metal reference-line technique, the grooves were observed to be generally asymmetrical, the distribution of angles broad, and the median values significantly lower than earlier results based on other techniques.

The distribution of dihedral angles from MgO-doped Al_2O_3 was narrower than for undoped Al_2O_3. The dihedral angle distribution of MgO is narrower (97°-123°) than from either Al_2O_3 surface. The lack of $\psi > 123°$ for MgO suggests that the energies of most low angle boundaries in MgO are not significantly lower than random high angle boundaries. However, the dihedral angle distributions for these three materials are probably affected by the sample fabrication techniques and the impurities present.

The observed angles from polished and fractured surfaces of sintered, hot-pressed and annealed, and hot-pressed and strained samples were shifted to lower values relative to the angles observed on grooved surfaces, as is theoretically predicted.

With a wide dihedral angle distribution, the sintering techniques in a material are expected to vary from one grain boundary to another and to be faster for larger dihedral angles. The stability of pores with respect to densification increases with decreasing dihedral angle. In addition, the mobilities of isolated pores with equal in-boundary radii are predicted to increase with decreasing dihedral angle. For uniform sinterability, the dihedral angle distribution should be narrow. For uniform resistance to pore-boundary separation, the lower limit of the distribution should be narrow. For uniform resistance to pore-boundary separation, the lower limit of the distribution should be high enough to avoid pore growth but low enough to give highly mobile pores. Although the median dihedral angles are similar for the three materials (111° for MgO, 115°, for Al_2O_3, and 117° for MgO-doped Al_2O_3), the breadths of the distributions are significatnly different and lead to a predicted ranking of sinterability: undoped Al_2O_3 < MgO $\overset{\sim}{<}$ MgO-doped Al_2O_3.

Appendix AI Simultaneous Sintering and Coarsening Expressions

I Sintering by grain boundary diffusion/grain growth controlled by pore drag (surface diffusion controlled)

$$\Gamma = \frac{\dfrac{WD_s \Omega \gamma_{gb}}{16kT}}{\dfrac{11}{3}\,\dfrac{\delta D_{b} \Omega \gamma_s}{kT}} \qquad \text{(AI-1)}$$

$$r^4 - r_o^{\,4} = 4(K_s - S_b)\,(t - t_o) \qquad \text{(AI-2)}$$

$$\frac{G}{G_o} = \left(\frac{r_o}{r}\right)^{K_s/S_b - K_s} = \left(\frac{r}{r_o}\right)^{\Gamma/\Gamma - 1} \qquad \text{(AI-3)}$$

For 'normal' purity MgO

$$\delta D_b = 2.13 \times 10^{-8} \exp\,(-55.8 \text{ kcal/RT})$$

and

$$WD_s = 6.9 \times 10^{-3} \exp(-90 \text{ kcal/RT})$$

at 1623 K, $\Gamma = 0.15$. AT 1673K, $\Gamma = 0.20$.

<u>at 1673K</u>

V_{fo}	G_o	r_o	r	G	V_f	t
0.3	1μm	0.18μm	0.10	1.16μm	0.03	80.4
			0.05	1.38μm	2.3×10^{-3}	88.4
			0.01	2.06μm	5.5×10^{-6}	88.9
			0			88.98
	5μm	0.90μm	0.50	5.80	0.03	5.0×10^{4}
			0.25	6.89	2.3×10^{-2}	5.5×10^{4}
			0.10	8.66	7.4×10^{-5}	5.56×10^{4}
			0.01	15.4μm	1.3×10^{-8}	5.56×10^{4}

at 1623K

V_{fo}	G_o	r_o	r	G	v_f	t
0.3	1 μm	0.18 μm	0.10	1.11	0.035	122
			0.05	1.26	3×10^{-3}	134.5
			0.01	1.68	1.0×10^{-5}	135.3
	5 μm	0.90 μm	0.50	5.56	0.03	7.65×10^4
			0.25	6.30	3×10^{-3}	8.40×10^4
			0.10	7.43	1.2×10^{-4}	8.45×10^4
			0.01	11.24	3.4×10^{-8}	8.45×10^4

For high purity MgO at 1623K, Γ = 107. As indicated in Figure (AI-1), this indicates little densification compared with coarsening/grain growth.

II Sintering by lattice diffusion /

grain growth controlled by pore drag (surface diffusion limited.)

$$\Gamma = \frac{\dfrac{WD_s \Omega \gamma_{gb}}{16\ kT}}{\dfrac{2D_1 r\ \Omega\gamma_s}{kT}} = \frac{K_s}{S_1} = \frac{K}{S_1' r} \qquad \text{(AI-4)}$$

$$\frac{G}{G_o} = \left(\frac{r}{r_o}\right)^{\Gamma/\Gamma-1} = \left(\frac{r_o}{r}\right)^{\frac{K_s}{S_1-K_s}} \qquad \text{(AI-5)}$$

From Equation AI-4, Γ is less than 1 when $r > K/S_1'$. This implies that pores smaller than a critical size (r^*) are so mobile that sintering for pores $< r^*$ is insignificant compared with coarsening/grain growth. If grain boundary mobility controls grain growth rather than pore mobility, then these pores will sinter for $r < r^*$.

The expression for pore shrinkage rate is:

$$\frac{dr}{dt} = \frac{1}{r^3}(K_s - S_1) = \frac{1}{r^3}(K_s + S_1'r) \qquad \text{(AI-6)}$$

where $S_1' = -\frac{2D_1\Omega\gamma_s}{kT}$. Integration of (AI-6) yields:

$$\frac{r^3-r_0^3}{3S_1'} - \frac{K_s^2}{S_1'^3}(r-r_0) - \frac{K_s}{S_1'^2}(r^2-r_0^2) - \frac{K_s^3}{S_1^4}\log\left(\frac{K_s + S_1'r}{K_s + S_1'r_0}\right) = t - t_0 \qquad \text{(AI-7)}$$

For $r_0 = r^*$, the equation (AI-7) is undefined. For $r < r^*$, $t_0 > t$. Shrinkage only occurs for $r_0 > r^*$. At 1623K, $r^* = 1.5\mu m$. At 1673, $r^* = 1.9\mu m$.

For $r_0 = 3\mu m$, $r = 2.5\mu m$, $T = 1623K$, $(t-t_0) = 2.53 \times 10^8$ sec (8 yrs). For $r > r^*$, grain growth has slowed so that for $r_0 = 3\mu m$ and $r = 2.5\mu m$ at 1623K, $G/G_0 = 1.2$.

For the case of lattice diffusion controlled shrinkage and pore-drag (wD_s) controlled coarsening/grain growth, the pores and grains will coarsen until grain boundary mobility controlled grain growth or $r = r^*$. For large values of r^* and small values of S_1' as is the case here, the time to densify is long.

Table AI-1

Sintering/Grain Growth Equations for Various Rate Controlling Mechanisms

1. Sintering- Boundary Diffusion
   Grain Growth - Surface Diffusion

$$\frac{d \ln G}{d \ln r} = \frac{1}{1 - \frac{176}{3} \frac{\delta D_b}{w D_s} \frac{\gamma_s}{\gamma_b} g(v_f)}$$

2. Sintering - Lattice Diffusion
   Grain Growth - Surface Diffusion

$$\frac{d \ln G}{d \ln r} = \frac{1}{1 - 32 \frac{r D_l}{w D_s} \frac{\gamma_s}{\gamma_b} g(v_f)}$$

3. Sintering - Lattice Diffusion
   Grain Growth - Evaporation/Condensation

$$\frac{d \ln G}{d \ln r} = \frac{1}{1 - \frac{1}{r} \left(\frac{64 (2\pi m k T)^{1/2} D_l \gamma_s}{\alpha' \rho_v \Omega \gamma_b} \right) g(v_f)}$$

4. Sintering - Boundary Diffusion
   Grain Growth - Boundary Mobility Controlled

$$\frac{d \ln G}{d \ln r} = \frac{1}{1 - \frac{11}{3} \left(\frac{\delta D_b \Omega}{M_b \Omega k T} \frac{\gamma_s}{\gamma_b} \frac{G^2}{r^4} \right) g(v_f)}$$

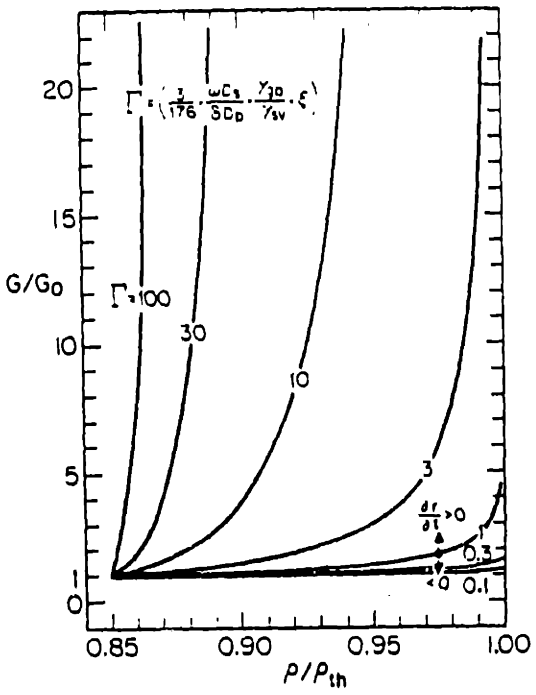

Figure AI-1 Grain size/ porosity evolution during final stage sintering as functions of Γ and starting grain size. (Cannon.)

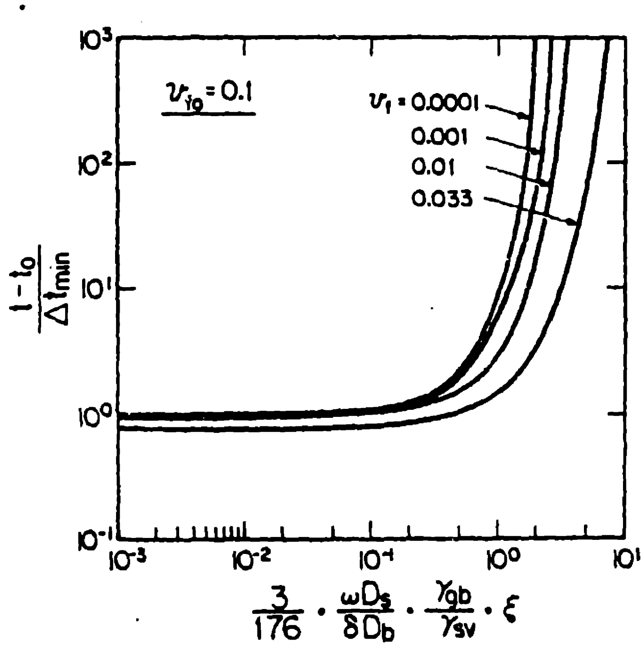

Figure AI-2 Time to sinter to various porosities as a function of Γ. (Cannon.)

Appendix II. SEM Reference Line Geometry

The following derivation was presented, in part, by Achutaramayya and Scott (1973).

The SEM specimen stage tilt angle is defined to be 0^0 when the electron beam is perpendicular to the sample surface and 90^0 when the beam is parallel to the sample surface. These are shown schematically in Figure AII-1.

When the SEM specimen stage tilt angle, ϕ, is 0^0 and the metal reference lines are horizontal to the SEM projection plane, the metal reference line appears straight at grain boundary intersections. This is line ABC in Figure AII-2. At $\phi = 90^0$, the groove is perpendicular to the SEM projection plane and the observed angle is the true angle. This is the triangle ADC. At ϕ between 0^0 and 90^0, the apparent angle is between 180^0 and the true angle. At an arbitrary less than 90^0, the apparent triangular construction for the groove is AEC. The partial angles corresponding to the dihedral angles are ψ_1 and ψ_2 for the true angles and ψ_1' and ψ_2' for the observed angles at specimen tilt angles ($0^0 < \phi < 90^0$).

When the reference line away from the grain boundary groove is horizontal on the projection plane, the relationship between the apparent angle and the true angle is defined by the angle, ϕ, to be:

$$BD \cdot \frac{AB}{BD} = \frac{AB}{BE} \cdot BE \qquad \text{(AII-1)}$$

Since $AB/BD = \tan \psi_i$, $AB/BE = \tan \psi_i'$, and $BE/BD = \sin \phi$.

$$\tan \psi_i = \sin \phi \tan \psi_i' \qquad \text{(AII-2)}$$

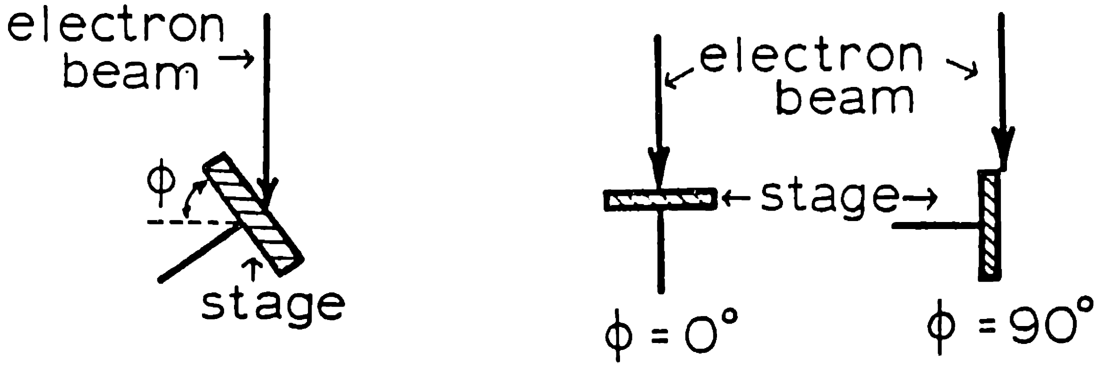

Figure AII-1 SEM specimen stage tilt geometry.

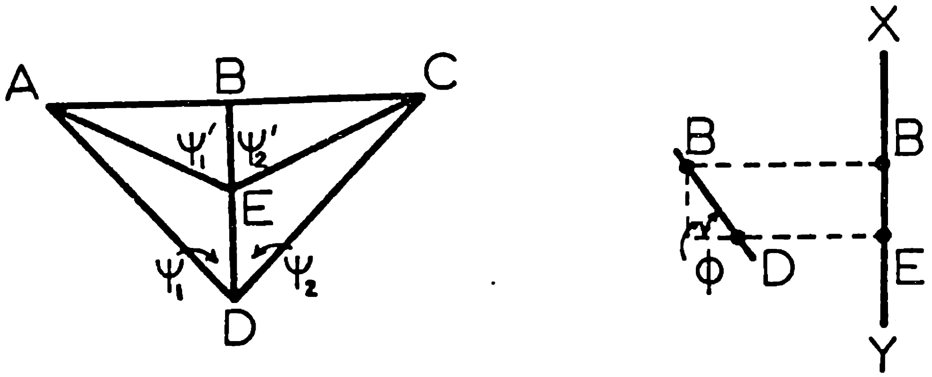

Figure AII-2 SEM reference line geometry

Appendix III. Error Analysis for Interferometry and the Metal Reference Line Technique

The following analysis was performed by Gjostein (1958) for interferometry but applies equally to the metal reference line technique.

The equation describing the relationship between the observed angle, ψ', in interferometry and the true angle, ψ, is:

$$\tan\frac{\psi}{2} = \frac{2a}{M\lambda}\tan\frac{\psi'}{2} \qquad \text{(AIII-1)}$$

In the metal reference line technique, the relationship between the true angle, ψ, and the observed angle, ψ', is:

$$\tan\frac{\psi}{2} = \sin\text{(tilt angle)}\tan\frac{\psi'}{2} \qquad \text{(AIII-2)}$$

These equations can be represented as:

$$\tan\frac{\psi}{2} = K\tan\frac{\psi'}{2} \qquad \text{(AIII-3)}$$

For $\psi/2 = \psi_i$ and $\psi/2 = \psi_i'$, the change in the calculated true angle with error in the measurement of ψ_i' is:

$$\frac{d\psi_i}{d\psi_i'} = K\left(\cos^2\psi_i\left(1 + \frac{\tan^2\psi_i}{K^2}\right)\right) \qquad \text{(AIII-4)}$$

For a 1^o measurement error in ψ_i' ($d\psi_i' = 1^o$), the error in ψ is calculated for K = 24 for interferometry and K = 0.866 for the metal reference line technique. These values are presented in

Table AIII-1. (The actual error in ψ is twice the value listed in Table AIII-1.) Only at $\psi > 160^{\circ}$ is interferometry the preferred technique.

Table AIII-1

Error in Calculated Angle with 1° Measurement

Error in Observed Angle

ψ_i	K = 24	K = 0.866
10°	23.3°	0.87°
20	21.2	0.90
30	18.0	0.94
40	14.1	0.99
50	9.9	1.04
60	6.0	1.08
70	2.8	1.12
80	0.76	1.15

Appendix IV

The hydrated magnesium carbonate was precipitated by adding an excess of a $(NH_4)_2CO_3(aq)$ solution dropwise into a stirred nitrate solution prepared by dissolving Mg* metal in reagent grade HNO_3. The resulting precipitate was washed with water, then acetone and ground with acetone using a porcelain mortar and pestle. The carbonate powder specific surface area of approximately 17 m^2/g. Chemical analysis of one powder batch is listed in Table II-1. The carbonate was transformed to the oxide at 1270 K in air for 2 h. The specific surface area increased to 27 m^2/g. The agglomerated oxide powder was suspended in ethanol and filter cast by vacuum filtration through an ashless filtered paper to form a preform for hot-pressing. The disk was vacuum-dried at 320 K for 25 h and preannealed at 1270 K for 10 h. The as-filtered density was approximately 20% of theoretical density. The disk was hot-pressed at 1620 K and 36 MPa to $\sim$99+% ρ_{th}. Subsequent annealings were performed at 1670 K in air at times from 2 h to 31 h. The as-hot pressed and annealed samples were examined by optical microscopy of polished sections and by SEM of polished and fracture surfaces.

---

*Atomergic Chemetals, Plainview, N.Y.

Results

The microstructure of the high density as-hot pressed sample is shown in Figure IV-21(a). The hot-pressed sample was gray, indicating carbon contamination or transition metal impurities, and highly translucent ($\sim$99+% ρ_{th}). Auger analysis of a fracture surface indicated elemental carbon (graphite) on the boundaries. Upon annealing at 1670 K, the samples became white and opaque.

During heat-treatment after hot-pressing, the average grain size and pore size increased and the density decreased. During the gas evolution and desintering, the pores remained attached to the boundaries. Upon further annealing, these samples resintered. Representative fracture surfaces of the $MgCO_3$-derived MgO before and after annealing are shown in Figure IV-21(b) and AIV-1. An exact measurement of density by immersion was precluded due to platinum contamination of the sample surfaces during annealing.

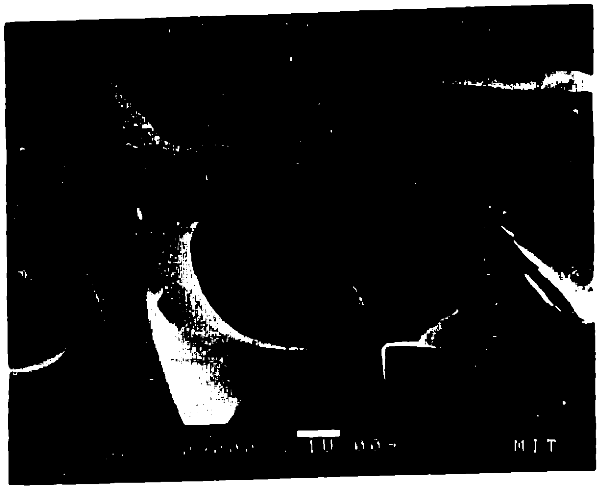

Figure AIV-1 Micrograph of MgO-2 samples.

Bibliography

Chapter I

R. J. Brook (1969) "Pore-Grain Boundary Interactions and Grain Growth", J. Am. Ceram. Soc. 52 (1) 56.

R. L. Coble (1961) "Sintering Crystalline Solids, I. Intermediate and Final Stage Diffusion Models", J. Appl. Phys. 22 (5) 787.

W. S. Coblenz, J. M. Dynys, R. M. Cannon, and R. L. Coble (1980) "Initial Stage Sintering Models, A Critical Analysis and Assessment", Sintering Processes, ed. G. C. Kuczynski, Plenum Press.

J. M. Dynys, R. L. Coble, W. S. Coblenz, and R. M. Cannon (1980) "Mechanism of Atom Transport during Initial Stage Sintering", Sintering Processes.

J. M. Dynys (1982) "Sintering Mechanisms and Surface Diffusion for Aluminum Oxide", Ph.D. Thesis, M.I.T.

H. Gleiter and B. Chalmers (1972) "High-Angle Grain Boundaries", Prog. in Mat. Sci., Vol. 16.

T. K. Gupta (1968) "Correlations between Grain Size and Density During Sintering", Westinghouse Scientific Paper 68-1B5-VALAM-P1.

T. K. Gupta (1975) "Crack Healing in Thermally Shocked MgO", J. Am. Ceram. Soc. 58 (3-4) 143,

T. K. Gupta (1978) "Instability of Cylindrical Voids in Alumina", J. Am. Ceram. Soc. 61 (5-6) 191.

C. H. Hsueh, A. G. Evans, and R. L. Coble, "Microstructure Development During Final/Intermediate Stage Sintering - I. Pore/Grain Boundary Separation", Acta Met. 30, 1269.

W. D. Kingery and B. Francois (1967) "The Sintering of Crystalline Oxides, I. Interaction Between Grain Boundaries and Pores", Sintering and Related Phenomena, ed, G. C. Kuczynski, N. Hooton, and C. Gibbon, Gordon and Breach, NY, 471

F. A. Nichols (1969) "Kinetics of Diffusional Motion of Pores in Solids", J. Nucl. Mat. 30, 148.

F. A. Nichols and W. W. Mullins (1985) "Surface-(Interface-) and Volume-Diffusion Contributions to Morphological Changes Driven by Capillarity" Trans. A.I.M.E. 233 (10) 148.

C. F. Yen and R. L. Coble (1972) "Spheroidization of Tubular Voids in Al_2O_3 Crystals at High Temperature",J. Am. Ceram. Soc. 55 (10) 507.

Chapter II

R. Altman (1961) "Vaporization of MgO and Its Reaction with Alumina", J. Phys. Chem. 67 (2) 366.

Y. M. Chiang, A. F. Henricksen, W. D. Kingery, and D. Finello (1981) "Characterization of Grain Boundary Segregation in MgO", J. Am. Ceram. Soc. 64 (7) 388.

R. S. Gordon (1975) Mass Transport Phenomena in Ceramics, ed. A. R. Cooper and A. H. Heuer, Plenum Press, NY, 445.

R. S. Gordon, D. D. Marchant, and G. W. Hollenberg (1970) "Effects of Small Amounts of Porosity on Grain Growth in Hot Pressed Magnesium Oxide and Magnesiowustite", J. Am. Ceram. Soc. 53, 399

T. K. Gupta (1971) "Kinetics and Mechanisms of Pore Growth in MgO", J. Mat. Sci. 6, 989.

K. Hamano and H. Kamizono (1977) "Etching Figures of Magnesia Specimens", Yogyo -Kyokai-Shi, 85 (1) 44.

C. A. Handwerker, M. M. O'Connor, R. M. Cannon, and R. L. Coble (1982) "Preparation and Characterization of High Purity MgO Powder Compacts", Powder Processing, ed. R. German and K. Lay, TMS-AIME Special Publication.

J. Henney and J. W. S. Jones (1968) "Surface Diffusion Studies on UO_2 and MgO," J. Mat. Sci. 3, 158.

A. F. Henriksen (1978) "Precipitation in MgO", Ph.D. Thesis, M.I.T.

J. D. Hodge and R. S. Gordon (1978) "Grain Growth and Creep in Polycrystalline Magnesium Oxide Fabricated with and without a LiF Additive", Ceram. Int. 4, 17.

H. Kamizono and K. Hamano (1978) "Relation between Pore Distribution and Grain Size of Magnesia in the Intermediate Stage", Yogyo-Kyokai-Shi, 88 (10), 48.

W. D. Kingery, W. L. Robbins, A. F. Henriksen, and C. E. Johnson (1976) "Surface Segregation of Aluminum (Spinel Precipitation) in MgO Crystals" J. Am. Ceram. Soc. 58, 239.

M. H. Leipold and C. M. Kapadia (1973) "Effect of Anions on Hot-Pressing of MgO", J. Am. Ceram. Soc. 56 (4) 200.

M. M. O'Connor "Effect of Powder Precursor and Alcohol Dispersant on the Surface and Compact Characteristics of MgO Powder", S. M. Thesis, M.I.T.

W. H. Rhodes, B. J. Wuensch, and T. Vasilos (1977a) "Relation Between Particulate Chemistry and Ceramic Properties", ONR Contract N00014-70-C-013 Report, 1 January 1970 - 31 December 1972, AVCO Corporation.

W. H. Rhodes and B. J. Wuensch (1972) "Relation Between Precursor and Microstructure in MgO", J. Am. Ceram. Soc. 56 (9) 495.

W. M. Robertson (1967) in Sintering and Relation Phenomena, ed. G. C. Kuczynski, N. A. Hooton, and C. F. Gibbon, Gordon and Breach, Science Publishers, Inc., N.Y.

R. T. Tremper, R. A. Giddings, J. D. Hodge, and R. S. Gordon (1972) "Creep of Polycrystalline MgO-FeO-Fe_2O_3 Solid Solutions", J. Am. Ceram. Soc. 57, 421.

D. Turnbull (1951) "Theory of Grain Boundary Migration Rates", Trans. A.I.M.E., 191, 661.

R. Vieira (1980) "Fast-Firing and Hot Pressing of MgO", Ph.D. Thesis, University of Leeds.

H. Watanabe, Z. Nakagawa, M. Hasegawa, and K. Hamano (1982) "Effects of Addition of Magnesium Basic Carbonate, Sulfate, Fluoride, and Oxalate on Sintering of Magnesia", Report of the Research Laboratory of Engineering Materials, Tokyo Institute of Technology, 7.

B. J. Wuensch, W. C. Steele, and T. Vasilos (1973) "Cation Self-Diffusion in Single Crystal MgO," J. Chem. Phys. 55, 5258.

Chapter III

ACS Committee on Environmental Improvement (1980) "Guidelines for Data Acquisition and Data Quality Evaluation in Environmental Chemistry", Anal. Chem. 52, 2242.

P. Adams (1972) "Glass Containers for Ultrapure Solutions," Ultrapurity, ed. M. Zief and R. Speights, Marcel Dekker, N.Y.

R. A. Brown (1965) "Sintering of Very Pure Magnesium Oxide and Magnesium Oxide Containing Vanadium", J. Am. Ceram. Soc. 44 (6) 483.

P. Chaudhari and J. W. Matthews (1971) "Coincidnece Twist Boundaries between Crystalline Smoke Particles", J. Appl. Phys. 42 (8) 3063.

A. Debska-Horecka, T. Pukas, and I. Stronski (1973) "The Preparation of High Purity MgO", J. Radioan. Chem.13, 21.

R. M. Dell and S. W. Weller (1969) "The Thermal Decomposition of Nesquehonite $MgCO_3 \cdot 3B_2O$ and Magnesium Ammonium Carbonate $MgCO_3 \cdot (NH_4)_2CO_3 \cdot 4H_2O$", Trans. Faraday Soc. 55, 2203.

F. Freund, G. Debras, and G. Demortier (1977) "Carbon Content of Magnesium Oxide Single Crystals Grown by the Arc Fusion Method," J. Crys. Growth, 38, 277.

F. Freund, H. Kathrein, H. Wengeler, R. Knobel, and G. Demortier (1980) "Atomic Carbon in Magnesium Oxide. I, Carbon Analysis by the $^{12}C(d,p)^{13}C$ Method", Mat. Res. Bull. 15, 1011.

A. M. Glaeser (1981) "Grain Boundary Migration in LiF", Sc.D. Thesis, M.I.T.

K. Hamano, K. Asano, Y. Akiyama, and Z. Nakagawa (1979) "Effects of Water Vapor Pressure on Sintering Magnesia", Report of the Research Laboratory of Engineering Materials, Tokyo Institute of Technology, 4.

T. Ikegama, S. I. Matsuda, Y. Moriyoshi, and H. Suzuki (1978) "Sintering Processes of a Sinterable and Non-sinterable BeO Powder", J. Am. Ceram. Soc. 61 (1-2) 532.

T. P. Ketcham (1982) "Fracture Toughness Enhancement and Synthesis of ZrO_2-bearing Ceramic Alloys", Ph.D. Thesis, M.I.T.

S. Musikant (1980) Advanced Optical Ceramics, Phase II, DIN: 805DR2172 Report, 31 August 1980, AVCO Corporation.

J. Stary (1964) The Solvent Extraction of Metal Chelates, Pergamon Press,

F. J. Welcher (1958) The Analytical Uses of Ethylenediaminetetraacetic Acid, Van Nostrand, Princeton.

M. Yan, H. K. Bowen, and R. M. Cannon (1976) "Grain Boundary Migration in Ceramics", Ceramic Microstructures '76, ed. R. M. Fulrath and J. A. Pask, 276.

Chapter IV

G. Achutaramayya and W. D. Scott (1973) "Measurement of Dihedral Angles by SEM", J. Am. Ceram. Soc. 56 (4) 230.

S. Amelincks, N. F. Binnendijk, and W. Dekeyser (1953) "Interferometric Measurements of Grain Boundary Grooves", Physica, 19, 1173.

R. W. Balluffi, P. D. Bristowe, and C. P. Sun (1981) "Structure of High Angle Grain Boundaries in Metals and Ceramic Oxides", J. Amer. Ceram. Soc. 64 (1) 23.

J. M. Blakely (1973) Introduction to the Properties of Crystal Surfaces, Pergamon Press.

B. V. Belogurov (1963) Institute for Powder Metallurgy and Special Alloys, Izd. Akad. Nauk Ukr. SSR, Kiev, 19.

D. G. Brandon (1966) "The Structure of High Angle Grain Boundaries", Acta Met. 14, 1479.

P. D. Bristowe and S. L. Sass (1980) "The Atomic Structure of Large Angle [001] Twist Boundary in Au Determined by a Joint Computer Modelling and X-Ray Diffraction Study", Acta Met., 28, 575.

R. M. Cannon, T. D. Ketcham, and T. W. Coyle (1982) "Toughened Optical Materials", to be published in SPIE Proceedings on Emerging Optical Materials.

P. Chaudhari and H. Charbnau (1972) "On the Energy of [100] Coincidence Twist Boundaries in MgO", Surface Sci. 31, 104.

P. Chaudhari and J. W. Matthews (1970) "Coincidence Twist Boundaries Between Crystals of MgO Smoke", Appl. Phy. Lett. 17 (3) 115.

P. Chaudhari and J. W. Matthews (1971) "Coincidence Twist Boundaries Between Crystalline Smoke Particles", J. Appl. Phys. 42, 3063.

W. R. Class and E. S. Machlin (1966) "Crack Propagation Method for Measuring Grain Boundary Energies in Brittle Materials", J. Am. Ceram. Soc. 49, 306.

R. R. Cowley, R. L. Segall, R. St. C. Smart, and P. S. Turner (1979) "Growth Twinning in Magnesium Oxide Smoke Crystals", Phil. Mag. A, 39 (2) 163.

G. Dhalenne, A. Revcolevshi, and A. Gervais (1979) "Grain Boundaries in NiO, I. Relative Energies of ⟨001⟩ Tilts", Phys. Stat. Sol. A, 56 (1) 267.

G. Dhalenne, M. Dechamps, and A. Revcolevschi (1982) "Relative Energies of ⟨011⟩ Tilt Boundaries in NIO", Comm. Am. Ceram. Soc. C11-C12.

C. B. Duke (1978) "Atomic Geometry of Semiconductor Surfaces", CRC Critical Reviews in Solid State and Materials Science, 8, 69.

R. L. Fullman (1951) "Interfacial Free Energy of Coherent Twin Boundaries in Cu", J. Appl. Phys. 22 (4) 448.

J. J. Gilman (1960) "Direct Measurements of Surface Energy of Crystals", J. Appl. Phys. 31 3208.

N. A. Gjostein (1958) "Absolute Energies and Structures of Grain Boundaries in Cu", Ph.D. Thesis, Carnegie Institute of Technology.

N. A. Gjostein and F. N. Rhines (1959) "Absolute Interfacial Energies of 001 Tilt and Twist Grain Boundaries in Cu", Acta Met. 7, 319.

A. M. Gokhale, C. V. Iswaran, and R. T. DeHoff (1981) "Stereology of Grain Boundary Precipitates", Metall. 14, 14.

C. Greskovich, J. R. Rosolowski, and S. Prochazka (1975) "Ceramic Sintering", Final Tech. Report ARPA Order #2698 (SRD-75-084).

D. Harker and E. R. Parker (1943) "Grain Shape and Grain Growth", Trans. ASM, 34, 156.

G. Hasson, J. Y. Boos, I. Herbeuval, M. Riscondi, and C. Goux (1972) "Theoretical and Experimetnal Determination of Grain Boundary Structures and Energies. Correlation with Various Experimental Results", Surface Sci. 31 (1) 115.

C. Herring (1951) Physics of Powder Metallurgy, 143.

G. Herrmann, R. Gleiter, and G. Baro (1976) "Investigation of Low Energy Grain Boundaries in Metals by a Sintering Technique", Acta Met. 24, 353.

A. H. Heuer, N. I. Tighe, and R. M. Cannon (1980) "Plastic Deformation of Fine Grained Alumina", J. Am. Ceram. Soc. 63, 53.

B. K. Hodgson and H. Mykura (1973) "Torque Terms and Grain Boundary Energy Measurement", J. Mat. Sci. 8 (4) 565.

E. N. Hodkin and M. G. Nicholas (1973) "Surface and Interfacial Properties of Stoichiometric UO_2", J. Nucl. Mat. 47, 23.

E. N. Hodkin and M. G. Nicholas (1977) "Surface and Interfacial Properties of Non-Stoichiometric Uranium Dioxide", J. Nucl. Mat. 67, 171.

E. N. Hodkin (1980) "The Ratio of Grain Boundary to Surface Energy of Nuclear Ceramics as Determined from Pore Geometries", J. Nucl. Mat. 88, 7.

E. D. Hondros and M. McLean (1970) "Structure and Properties of Metal Surfaces", CNRS, Paris.

M. C. Inman and H. R. Tipler (1963) "Interfacial Energy and Composition in Metals and Alloys", Met. Rev. 8, (3) 105.

W. D. Kingery (1954) "Metal-Ceramic Interactions: IV. Absolute Measurement of Metal-Ceramic Interfacial Energy and Interfacial Adsorption of Silicon from Iron-Silicon Alloys", J. Am. Ceram. Soc. 37, 42.

N. D. Lang and W. Kohn (1970) "Theory of Metal Surfaces: Charge Density and Surface Energy", Phys. Rev. 8, 1 (12) B4555.

M. C. Mackrodt and R. E. Stewart (1977) "Defect Properties of Ionic Solids: I. Point Defects at the Surfaces of Face-Centered Cubic Crystals", J. Phys. C: Solid State Phys. 10, 1431.

M. McLean and B. Gale (1969) "Surface Energy Anisotropy by an Improved Thermal Grooving Technique", Phil. Mag. 20, 1033.

M. McLean (1973) "Grain Boundary Energy of Cu at 1030°C", J. Mat. Sci. 8, 571.

L. E. Murr, R. J. Horylev, and G. I. Wong (19 "Measurement of Absolute Interfacial Energies in a NiCr Alloy", Surf. Sci. 26, 184.

L. E. Murr (1975) Interfacial Phenomena in Metals and Alloys, Addison-Wesley, London.

H. Mykura (1961) "The Variation of the Surface Tension of Ni with Crystallographic Orientation", Acta Met. 9, 570.

H. Mykura (1979) "Grain Boundary Energy and the Rotation and Foundation of Cu Spheres during Sintering onto a Substrate", Acta Met. 27, 243.

J. F. Nicholas (1968) "Calculations of Surface Energies as a Function of Orientation for Cubic Crystals", Aust. J. Phys. 21, 21.

P. Nikalopoulos, S. Nazare, and E. Thummler (1977) "Surface, Grain Boundary, and Interfacial Energies in UO_2 and UO_2-Ni", J. Nucl. Mat. 71, 89.

N. L. Peterson, C. L. Wiley, and J. Faber (1980) "Low Energy Grain Boundaries in NiO", Advances in Ceramics 1, 101.

B. O. Powell and D. P. Woodruff (1976) "Anisotropy of Grain Boundary Segregation in Cu-Bi Alloys", Phil. Mag. 34, 167.

D. W. Readey and R. E. Tech (1968) "Energies and Grooving Kinetics of [001] Tilt Boundaries in NiO", J. Am. Ceram. Soc. 51 (4), 201.

O. K. Riegger and L.H. Van Vlack (1960) "Dihedral Angle Measurements", Trans. A.I.M.E. 218, 933.

W. M. Robertson and P. G. Shewmon (1963) "Crystallography of Impurity Adsorption on Cu Surfaces", J. Chem. Phys. 39 (9) 2330.

H. Sautter, H. Gleiter, and G. Baro (1977) "The Effect of Solute Atoms on the Energy and Structure of Grain Boundaries", Acta.Met. 25, 467.

T. Schober and R. W. Balluffi (1970) "Quantitative Observation of Misfit Dislocation Arrays in Low and High Angle Twist Grain Boundaries," Phil. Mag. 21 (1), 109.

M. P. Seah and E. D. Hondros (1973) "Grain Boundary Segregation", Proc. Royal Soc. A335 (1601) 191.

J. F. Shackelford and W. D. Scott (1968) "Relative Energies of $[\bar{1}100]$ Tilt Boundaries in Al_2O_3", J. Am. Ceram. Soc. 51 (12) 688.

D. A. Smith, V. Vitek, and R. C. Pond (1977) "Computer Simulation of Symmetrical High Angle Boundaries in Al", Acta Met. 25, 475.

H. Suzuki and T. Hase (1978) "Some Experimental Considerations on the Mechanism of Pressureless Sintering of Silicon Carbide", Proc. Int. Symp. of Factors in Densification and Sintering of Oxide and Non-Oxide Ceramics, Japan

C. P. Sun and R. Balluffi (1979) "Observation of Intrinsic and Extrinsic Secondary Grain Boundary Dislocation in [001] High Angle Twist Boundaries in MgO" Scr. Met. 13, 757.

P. W. Tasker (1979a) "The Surface Properties of Uranium Dioxide", Surf. Sic. 78, 315.

P. W. Tasker (1979b) "Thw Surface Energies, Surface Tensions, and Surface Structure of Alkali Halide Crystals", Phil. Mag. A, 39 (2) 119.

P. W. Tasker (1979c) "The Stability of Ionic Crystals", J. Phys. C: Solid State Phys. 12.

P. W. Tasker (1980) "The Structure and Properties of Fluoride Crystal Surfaces", J. de Phys. C6, 488.

P. W. Tasker (1982) "The Surface Properties of Ionic Materials," Proc. of NATO ASI "Mass Transport in Solids", ed. Catlow and Beniere.

F. R. Tolman and J. G. Wood (1956) "Fringe Spacing in Interference Microscopes", J. Sci. Instr. 33, 236.

R. S. Wagner and B. Chalmers (1960) "Grain Boundaries in Germanium", J. Appl. Phys. 31, 581.

T. Watanabe, T. Murakami, and S. Karoshima (1978) "Misorientation Dependence of Grain Boundary Segregation", Scr. Met. 12, 361.

W. L. Winterbottom and N. A. Gjostein (1966) "Determination of the Anisotropy of Surface Energy of Metals. II: Experimental γ Plot of Gold", Acta Met. 14, 1041.

D. Wolf (1980) "Energies of [110] Coincidence Twist Boundaries, Stacking Faults, and Free Surfaces in Metal Oxides with NaCl Structure", Surfaces and Interfaces in Ceramic and Ceramic-Metal Systems, ed. J. A. Pask and A. G. Evans, Pergamon Press.

D. Wolf and R. Benedek (1981) "Energy of [001] Coincidence Twist Boundaries in Oxides with NaCl Structure", Advances in Ceramics 1, 107.

Autobiographical Note

I was born in 1951 in Memphis, Tennessee, the child of Ruth Walker and Howard Thiers Handwerker. I decided at the age of 9 to become a scientist and to attend MIT. I remained in the Heart of the Southland until 1969 when I came to Wellesley College and the Greater Boston Area and spent time studying in the company of Yankees. I earned my Bachelor of Arts degree in art history from Wellesley College in 1973 and decided to go back to school to learn science. After working as a systems programmer and studying as a special student at MIT for a year, I became a regular full-time undergraduate and earned an SB in Materials Science and an SM in Ceramics in 1978.

I am married to John E. Blendell and will be the mother of at least one child (due August 1983.)